Synthesis, Characterisation, Time-Resolved and Photocatalytic Studies of Inorganic Assemblies for Hydrogen Generation

Laura O'Reilly B.Sc.

Thesis submitted for the award of PhD

School of Chemical Sciences

Dublin City University

Under the supervision of

Dr. Mary T. Pryce and Prof. Johannes G. Vos

February 2019

Author's Declaration

I hereby certify that this material, which I now submit for assessment on the programme of study leading to the award of Doctor of Philosophy is entirely my own work, that I have exercised reasonable care to ensure that the work is original, and does not to the best of my knowledge breach any law of copyright, and has not been taken from the work of others save and to the extent that such work has been cited and acknowledged within the text of my work.

Signed: _____ ID No.: _____ Date: _____

Dedicated to my parents, Anne and Gerry,

for all their love, support and patience.

Thanks Mam and Dad, we did it!

Acknowledgements

Firstly, I would like to thank my supervisor Dr. Mary Pryce for really believing in me and encouraging me every step of the way. I would not have accomplished this without her blind faith in me and constant reassurance and answers to all my questions. All the opportunities and people I have met during this process, I attribute to you. Thank you. Thank you to my co-supervisor Prof. Han Vos, for all his knowledge and input and support and terms of endearment (I was known as the "bold one") over the last number of years. Thank you, Prof. Conor Long for all your help, support, calculations and stories. The three of you treated me as an extension of your family, making it so much easier to fully express my concerns or queriers and enjoy the Christmas parties and trips abroad. So many memories, thank you!

I would like to thank all those that I have collaborated and published with over the course of my PhD. Prof. Dr. Wesley Browne and his vast research group in Groningen, for opening your lab to me and making me so welcome. Dr. Qing Pan and Dr Annemarie Huijser for all the back and forth between us and your help and understanding throughout the process. Dr Elizabeth Gibson and her research group, especially Nils and Fiona, for all their help and support and friendliness over the years. To the team at RAL, specifically Igor, Ian and Mike, incredible experience I was lucky to visit three times during my PhD and each time I gained more and more invaluable knowledge. Also, thank you to Prof. Dr. Sven Rau, for the kind words of encouragement.

Thank you to all the staff at DCU, especially the support staff, Veronica, Ambrose, John, Damien, Vinny, Catherine, Mary, Mary and Julie. Thank you for all your unwavering help, support, patience, understanding and brightening my days at DCU. Each and everyone of you has helped me in so many different ways, you can't imagine. Special thanks to Ambrose for sneaking my free stuff and always checking in on me and giving me chocolate, you know how to make me smile!!

My lab family, thank you, there have been so many coming and goings but the support and craic never changed. I am so lucky to have had the group work so well, no matter who was still in DCU! From everyone I started this journey with, Jen (from my 4th year project to now, my superior to dearest friend), Nive, Liam, Suzanne, Finn,

Ahmed, those in between Kathi, Diana, Aoife, and to those I am finishing with Aoibhín, Martin, Puia, Michael, Tony, thank you. I thought I was lucky with the group I had when I started, but I know am with the group that is there now, thank you for dragging me over the line and dealing with my mess along the way.

To the others at DCU that enjoyed a drink and had the one too many, you lot kept me sane, especially in the last year or two! Chris, Ash, Colm, Aurélien, Darragh, Éadaoin, Steve, Guil, Jack, Sinead, Dave and everyone else I have shared a drink with over the years! Also, appreciate the times in the last few months Chris, Ash, Darragh, Éadaoin, Steve and Kae have been there as a listening ear, got on board with full blown rants, understood completely how I was feeling and always cheered me up in the end!!

Thank you to every single one of friends, I can't name you all, but thank you for fully understanding when I was on the missing list (mostly in the last few months). Each of you helped me unwind and have unbelievable craic! Mark and Nicole, thank you for always being there, from nights out, mornings after, holidays, walks, talks, tears and laughs, unconditional love and support from both of you. Nick and Fiona, from me finding out I got this opportunity when we were in Cambodia to passing my Viva, you are part of so many aspects of the last number of years, thank you!! Thank you to some of my oldest friends Rob, Gill and Michelle, for being there from day one and keeping me grounded and laughing with/at me over the years! Thanks to my team and mentors, Jonny, Gus and Gerry, at Scoil Uí Chonaill for giving me an outlet to clear my head!

I want to thank my family, my mam and dad for being so involved and supportive every step of the way and always positive and encouraging. My sisters, Claire and Sarah, for your support, love and listening and understanding, thank you. Thank you to my gran, Kitty, and the memory of my Grandad Joe and Gran O'Reilly. For Gran Kitty's unconditional love and unconditional support, I can do no wrong!! Thank you to all the Kirwan's and family friends for their constant support and well-wishes!

Finally, I want to thank my long-suffering boyfriend and best friend Seán. Thank you for standing with me through all my meltdowns and celebrating the absolute joys. Thank you for being the person I want to share everything with, even the bits that put you to sleep! Thank you for supporting me so blindly and always wanting me to be healthy and happy. Thank you for everything. I am excited for the next nine years together, without one (or both) of us in college!

Table of Contents

Chapter 2

Chapter 3

Chapter 4

Chapter 5

Chapter 6 Future Work

Table of Figures

Chapter 1:

Chapter 2:

Chapter 3:

Chapter 4:

Chapter 5:

List of Key Abbreviations

Abbreviation	Explanation
SEAI	Sustainable Energy Authority of Ireland
UNFCCC	United Nations Framework Convention on Climate Change
GHG/s	Greenhouse gas/es
Mtoe	Million tonnes of oil equivalent
AIRS	Atmospheric Infrared Sounder
NASA	National Aeronautics and Space Administration
ppm	Parts per million
hv	energy from light
G°	Gibb's free energy
kJ/mol	Kilojoule per mole
PS	Photosensitiser
CAT	Catalyst
BL	Bridging ligand
SA	Sacrificial agent
NiO	Nickel oxide
PL	Peripheral ligand
DCU	Dublin City University
Bpy	2,2'-bipyridine
dceb	4,4′-di(carboxyethyl)bipyridine
bpyMeP	4,4'-bis(diethyl-(methylene)-phosphonate)-2,2'-bipyridine
tbbpy	4,4-di-tert-butyl-bipyridine
G_0 (or S_0)	singlet ground state
S_1 (S_2, etc.)	singlet excited state

T_1	triplet excited state
VR	vibrational relaxation
IC	internal conversion
ISC	inter-system crossing
MC	metal centred
LC	ligand centred
MLCT	metal to ligand charge transfer
LMCT	ligand to metal charge transfer
ILCT	intraligand charge transfer
CT	charge transfer
CTTS	charge transfer to solvent
MMCT	metal-to-metal charge transfer
LLCT	ligand-to-ligand charge transfer/inter-ligand transfer
PECs	Photoelectrochemical cells
e^-	electron
h^+	hole
SC	semiconductor
CB	conduction band
VB	valence band
n-SC	negative-type SCs
p-SC	positive-type SCs
DSSC	Dye-sensitised solar cell
DSC	dye-sensitised semiconductor
OER	oxygen evolution reaction
HER	hydrogen evolution reaction
HOMO	highest occupied molecular orbital
LUMO	lowest unoccupied molecular orbital

2,5-bpp/terpy	2,2':5',2"-terpyridine
2,6-bpp	2,2':6',2"-terperidine
phen	1,10-phenanthroline
ph_2phen/dpph	4,7-diphenyl-1, 10-phenanthroline
TON	turnover number
TOF	turnover frequency
TA	Transient absorption
TRIR	Time resolved infrared
RAL	Rutherford Appleton Laboratory
BODIPY	boron dipyrromethene
GSB	ground state bleach
ESA	excited state absorbance

Abstract

Laura O'Reilly

Synthesis, Characterisation, Time-Resolved and Photocatalytic Studies of Inorganic Assemblies for Hydrogen Generation

Chapter 1 introduces the research discussed in this thesis. An overview of state-of-the-art approaches to photocatalytic hydrogen evolution is included. The focus is on ruthenium-platinum/palladium intramolecular systems, with a goal towards immobilising the complexes onto surfaces. Included in this section are the techniques employed, throughout the research carried-out, to probe the steps leading to hydrogen generation.

Chapter 2 explores the intermolecular route towards hydrogen generation using a known photosensitiser, a Ru-diphenylphenanthroline (dpph) complex, $[Ru(dpph)_3](PF_6)_2$. This photosensitiser was irradiated under multiple reaction conditions, systematically investigating the effect of each on the turnover number. Substitution of one of the of ligands with a suitable bridging ligand (BL) was achieved ($[Ru(L)_3] \rightarrow [Ru(L)_2(BL)]$), enabling synthesis of a photocatalyst capable of intramolecular hydrogen production ($[Ru(L)_2(BL)PtI_2]$). These complexes were investigated for their hydrogen production capabilities. Time resolved studies spanning the pico- to –millisecond time scale were carried out both at DCU and with collaborators in the University of Twente.

Chapter 3 compares a known working terpyridine ruthenium photocatalytic assembly with a novel triazole-photocatalyst. Photocatalytic studies were performed, and in an attempt to probe the photochemical steps leading to hydrogen generation, time resolved transient absorption and time resolved infrared were carried out. The experiments were conducted both in solution and following adsorption of the ruthenium-platinum/palladium complexes onto NiO. Together with collaborators at the University of Newcastle photoelectrocatalytic hydrogen evolution studies were performed.

Chapter 4 introduces the use of Ru-M complexes as photosensitisers for photocatalytic CO_2 reduction studies, where M = Re-carbonyl moiety. This chapter also introduces intramolecular assemblies based on porphyrin-Re-carbonyls were assessed for their ability to reduce CO_2 to CO. Time-resolved and photocatalytic studies were conducted.

Chapter 5 gives a brief literature review of boron-dipyrromethene based monomeric and polymer compounds. These compounds were assessed for their ability to generate singlet oxygen. Time-resolved IR studies together with transient absorption measurements were performed to probe the mechanism leading to formation of this cytotoxic species.

Chapter 6 contains concluding remarks and future work for each chapter.

Chapter 1

1 Introduction

Chapter 1 acts as an insight to the work included in this thesis. Introducing the basis for and the science behind the presented investigations. The status of the climate change crisis, current measures combating global warming and rising energy demands are among the discussions of this chapter. Also included is an overview of recent progress in the advancement of photocatalytic approaches to hydrogen evolution, focusing on ruthenium-platinum/palladium intramolecular systems, with a goal to immobilise the complexes on semiconductor surfaces and using a photoelectrochemical approach to generate hydrogen. To further understand the mechanisms leading to hydrogen generation, time resolved techniques spanning the sub-pico – nanosecond timescale are discussed. Current research achievements in p-type dye-sensitised photochemical cells are included. In addition, the techniques employed to investigate the complexes used throughout this thesis are introduced to the reader.

1.1 Current Energy Climate

In recent years, Ireland has seen a rise in the consumption of energy from renewable sources. This coincides with an increase in the total energy consumption, which is attributed to population growth and a buoyant economy, as we emerge from the recession (2008-2014). A 2016 report from the Sustainable Energy Authority of Ireland (SEAI), entitled Energy Statistics 1990-2015, highlights that Ireland is on track to achieve a target of a 16% contribution of renewable energy sources to the total energy consumption by 2020 (Figure 1.1 graphically depicts this progression).[1] This target was set by 2009 Renewable Energy Directive, to achieve an overall European target of 20% by 2020. Globally, efforts have been made to ensure the sustainability of our planet for new generations. World leaders came together in 1994 when the United Nations Framework Convention on Climate Change took effect,[2] then again in 1997 the Kyoto Protocol,[3] and more recently in November 2016 when the Paris Agreement entered into force.[4] This was the worldwide community making commitments to recognising and combating the earth's rapidly increasing temperatures. It indicates the level of effort and seriousness of the matter at hand. Although we (Ireland) are on the right path, we are not progressing fast enough. For instance, in the previously mentioned SEAI report, roughly 60% of Ireland's total greenhouse gas (GHG) emissions are energy related. Energy related CO_2 emissions increased by 5.8% in 2015 and with energy demands only rising, faster and more efficient methods of lowering these emissions are urgently required.[1] The latest SEAI report (2018) notes Ireland has since lowered CO_2 emissions from the 2015 increase.[5] Although, this decrease is promising, in the recent (2018) Climate Change Performance Index 2019 by Germanwatch, Ireland was found to be the 49th out of 55 countries, and the worst European country, for overall efforts towards fighting climate change.[6] The index considers four categories: "GHG Emissions", "Renewable Energy", "Energy Use" and "Climate Policy".

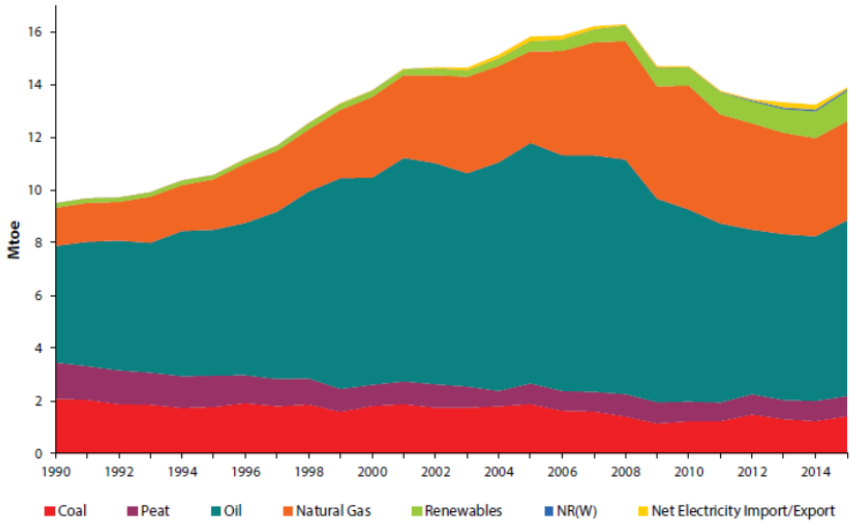

Figure 1.1: Graph of primary energy consumption by fuel in Ireland 1990 – 2015. (Mtoe equals million tonnes of oil equivalent).[1]

1.2 Green House Gases and Greenhouse Effect

The Earth's primary GHGs include carbon dioxide (CO_2), nitrous oxide (N_2O), methane (CH_4), ozone (O_3) and water vapour (H_2O). These, among others, are important in our atmosphere, as they keep the Earth warm with the greenhouse effect. As the gases absorb and emit thermal infrared radiation, their emissions are scattered in all directions, with some scattering in the direction of the Earth's surface, i.e. trapping the heat.[7] The impenetrability of this gaseous blanket increases with rising concentration of these gases, therefore intensifying the greenhouse effect. Figure 1.2 highlights the global increase of atmospheric CO_2 from ~375 ppm, in 2002, to 415 ppm, in 2016.

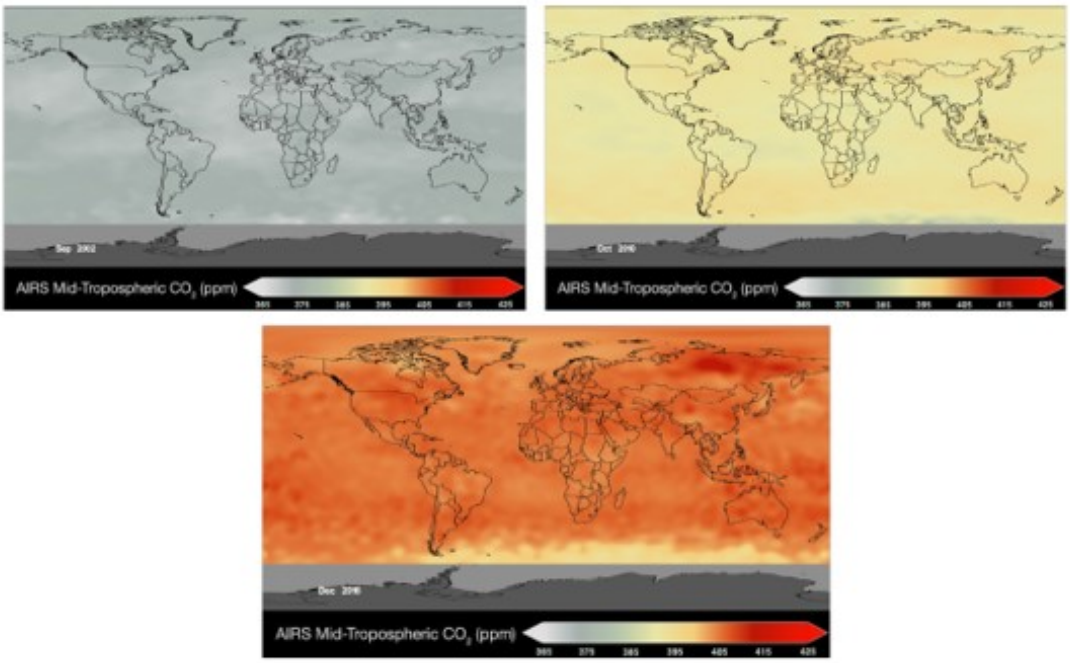

Figure 1.2: Atmospheric Infrared Sounder (AIRS) data collected by NASA of atmospheric CO_2 in 2002 (top left, ~375 ppm), 2010 (top right, ~395 ppm) and 2016 (bottom, 415 ppm)[8]

Anthropogenic influences, specifically the burning of fossil fuels, are a major contributor towards the increase in GHGs.[9] This is reflected in global temperatures rising at an alarming rate since the industrial revolution. Some of the damage includes, but is not limited to, the bleaching of coral on ocean beds[10] and melting of polar ice caps,[11] which in turn contributes to coastal flooding. Additionally, our excessive use of fossil fuels such as coal, oil and gas, as our main sources of energy, is not sustainable.

Natural supplies of fossil fuels are dwindling, attributing to a rise in the cost of fuel. Ireland, as an example, relies heavily on imported energy (approx. 95%) and therefore, is one of the most vulnerable countries in Europe to energy exploitations. Although, fracking offers a method to produce oil or gas, with the use of high pressure, Ireland has passed a ban on all onshore fracking to protect the local and global environments, furthering efforts to use cleaner energy sources.[12] Onshore fracking would alleviate any vulnerability, but as fracking does not address the release of harmful gases into the atmosphere upon their production and consumption, the Irish government have imposed this ban and, also, committed to stop public spending on fossil fuels, furthering efforts towards an energy independent country through the use of cleaner

sources of fuel.[13] From a financial standpoint, the threat of increased carbon taxing is a further incentive to explore other methods of producing energy with cleaner by-products. These are several pressing reasons to move away from our current sources of energy and progress towards clean, renewable sources and have been the motivation behind the intense research, from the international scientific community, for a solution to reduce GHG concentration and emissions.

1.3 Renewable Energy

Commonly known renewable energy sources include wind, tidal and solar sourced forms of energy. Each converting one form of energy to another, for example, wind turbines convert kinetic energy to another form, such as electric. Solar energy processes convert light to other forms of energy, photosynthesis in plants being the obvious example. These are intermittent sources, they do not produce a steady flow of energy. They can produce too little or too much (if the grid is at capacity) and in Ireland the grid can currently only take 20% of electricity generated by renewables. Therefore, wind turbines may be turned off during high winds. This is where energy storage becomes an issue.

1.4 Hydrogen Energy

Hydrogen is an ideal candidate for clean energy storage. On its consumption H_2 releases 286 kJ/mol and the only biproduct is water.[14] Thus, it is free of harmful emissions. Hydrogen is currently mostly generated from steam reformation, the Kværner process or partial oxidation, all of which are energy intensive and produce GHG emissions. Water splitting to produce hydrogen has been explored using electro and photo driving forces and the implementation of photo-/electro-catalysts has been found to reduce the energy required to split water (water splitting equation below, equation (1)). Using renewably sourced energy is paramount to making this process completely clean, energy efficient and financially viable to replace fossil fuels.

$$H_2O + h\nu \rightarrow H_2 + 0.5\ O_2 \qquad \Delta G^\circ = 238\ kJ\ mol^{-1} \qquad (1)$$

1.4.1 Leeds City Gate Project

In Leeds, in the UK, there is a project underway to have the city, with the population of 660,000 people, convert to using hydrogen energy. It is known as the H21 Leeds City Gate project.[15] Utilising the existing gas network routes and converting from natural gas pipelines to an all hydrogen gas network. In Ireland, our existing gas networks can only hold 5% hydrogen, so a similar upgrade would be required. One of the drawbacks of the project is that the hydrogen is generated by methane steam reformation, an energy intensive process, which releases GHGs. It is imperative, for a fully clean energy source, that the energy used to produce hydrogen, be obtained via renewable sources. The technology is currently not at the level of development to be considered economically viable, even if the chosen alternative releases harmful gases. The City Gate Project is also exploring the option of employing a carbon capture system, but once again, the technology is in its infancy.

1.5 Solar Driven Hydrogen Production

There is a considerable amount known about hydrogen and its abilities as a clean renewable energy candidate, as mentioned previously. This has spurred many investigations involving the production of hydrogen from water using cleaner and more energy efficient methods to advance the viability of a hydrogen economy. Renewable sources must be the initial energy supply for the process to improve overall efficiency. Solar energy (photons) is nature's source to generate chemical energy, inspiring many groups, some discussed in this thesis, to use solar energy as the driving force for their systems. Solar energy is also one of the most abundant sources of energy at our disposal, with more energy being provided by the sun's rays hitting the earth in an hour, than what is required to supply the world with energy for a year.[16] From the solar radiative spectrum, depicted in Figure 1.3, the visible region (~390-700 nm) is the largest portion of the sun's rays that hit the earth's surface. Therefore, there is great interest in exploiting the visible region for harvesting the sunlight's energy.

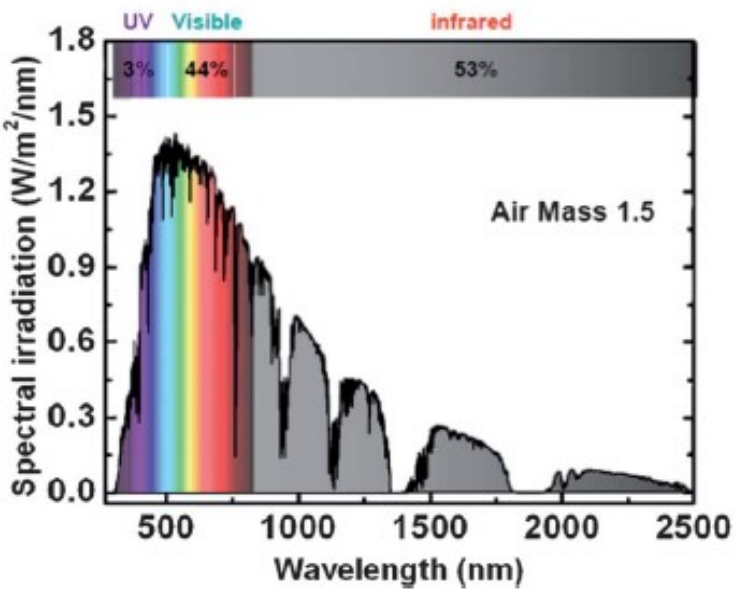

Figure 1.3: Spectrum of solar irradiance, based on the American Society for Testing and Materials for Terrestrial Reference.[17,18]

1.5.1 Catalysis and Photocatalysis

Catalysis is the increased rate of a chemical reaction with the use of a catalyst. The catalyst is used to reduce reaction times and is unchanged after the process has occurred. Catalysts work by reducing the energy requirements of a reaction (activation energy), allowing processes to occur easier, and therefore, faster. There are two types of catalysis relevant to this thesis, homo- and heterogeneous catalysis. Homogeneous catalysis involves the catalyst being in the same phase as the reactants, i.e. both are in the liquid phase. Whereas, heterogeneous catalysis involves the catalyst being in a different phase to the reactant, mostly the catalyst is in the solid phase and the reactants are in the liquid or gas phase.[19] Therefore, photocatalysis is the increased reaction rate with energy gained from a light source. For this thesis, the photocatalysis discussed is that of photocatalytic water splitting, known as an artificial photosynthetic process. Photocatalytic water splitting can then be subcategorised further by the two half-reactions. The main focus of this thesis is the hydrogen evolution half-reaction, with the intent of improving knowledge of the electron pathways undertaken after excitation and achieving some progression in this research area.

1.5.2 Photocatalytic Systems

There is an exhaustive list of parameters contributing to the overall workings of a photocatalytic system, most of which are explored in this thesis. This section covers some of the primary aspects required for high-functioning photocatalysts and photocatalytic systems for hydrogen evolution. First and foremost, photocatalysis relies on the use of an efficient photosensitiser (PS). Simply put, an efficient PS should strongly absorb light in the visible to near IR region, thus, benefiting from the abundance of photons available to be harnessed. Another main requirement is to efficiently supply the harnessed energy to the catalyst (CAT). In other words, ensuring as much of the absorbed energy as possible, reaches the catalytic unit and is not lost through other dissipation pathways (discussed later in this thesis). There are two approaches that systems can follow, either an inter- or intra-molecular approach (*vide infra*). The last main factor is to ensure the catalytic centre can utilise the supplied energy and reduce the activation energy of the reaction.

Figure 1.4 depicts the basic scheme of a homogenous photocatalytic hydrogen production system, following the electron pathways of (a) inter- and (b) intra-molecular approaches. From the figure, the intermolecular approach, described in (a), involves a separate PS and catalyst unit. The energy obtained by the PS must find its way to the catalytic centre and, in this scenario, the rate is determined by the diffusion constants and collision probability of PS and catalyst. Whereas, in (b) the intramolecular approach is portrayed with the presence of a bridging ligand (BL), linking the separate units to form a supramolecular photocatalyst. The difference between a supramolecule and a large molecule is most obvious when they are subjected to photons or electrons. A large molecule will experience delocalisation of a charge across entire species. Whereas, supramolecules experience an excited state forming on one of the subunits. When the subunits are in their separate precursor form, they have their own individual properties. This is due to the level of electronic interaction between the components of the molecule. Here, the energy is passed through the supramolecule via the BL to the catalyst. Although, the rate limiting factors of the intermolecular system, mention previously, are removed, there are processes, including recombination (back electron transfer), that contribute to reduced efficiency in intramolecular systems. This is where fine tuning of the electronic

properties through structural changes of the PS, BL, CAT, or even the peripheral ligand (PL) of the PS (ligands not directly attached to the catalyst) or CAT (ligands not directly attached to the PS), and a deep understanding of electron pathways, within the system, are fully appreciated. In solution experiments following either of the two approaches, a sacrificial agent (SA) replenishes the cycle of electron transfer, enabling the process to recur. This is done by the SA donating an electron to the excited photosensitiser (PS^*), enabling the photosensitiser to return to the ground state. Both inter- and intra-molecular approaches are investigated in this thesis. This is to confirm any enhancement, for photocatalytic hydrogen production, using intramolecular systems. The focus is the use of dinuclear supramolecular systems, investigating the parameters pertaining to their use for water splitting to generate hydrogen.

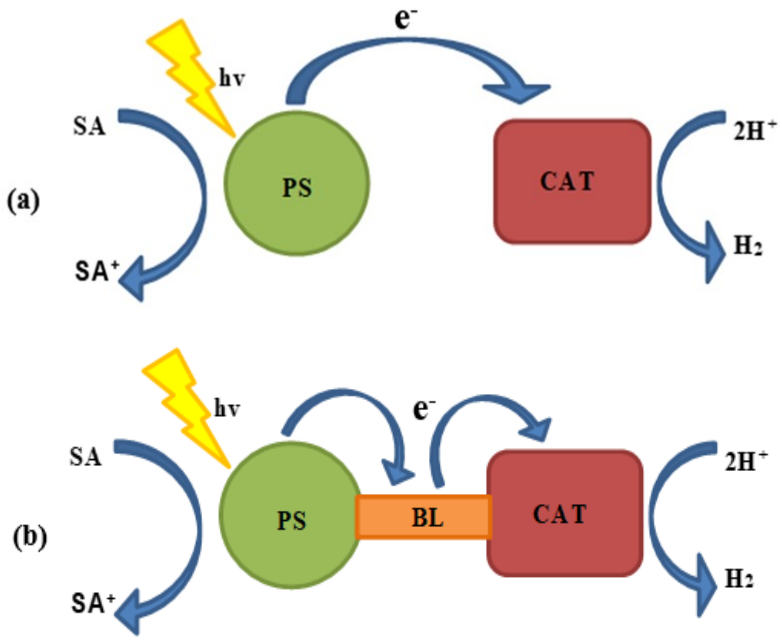

Figure 1.4: Schematic of (a) intermolecular system and (b) intramolecular system. In both (a) and (b) of the above figure, hv is the energy supplied by light, PS is the photosensitiser, e^- is the electron travelling, the arrows note the direction, CAT is the catalyst, SA is the sacraficile agent and SA^+ is the reduced sacrificile agent. In (b) BL is the bridging ligand.

1.5.3 Photoelectrocatalytic Systems

Previous work from the DCU group, and others, have investigated improvements made by moving from an inter to an intra approach.[20,21] The overall aim, is to move

away from working in solution with SAs, such as triethylamine, and use intramolecular systems immobilised on the surface of an electrode, such as nickel oxide (NiO). A simplified schematic representation of photoelectrocatalytic system for hydrogen generation, and the corresponding electron pathway, is depicted below in Figure 1.5. Note, in the schematic, the sacrificial agent is removed, as the cycle can be replenished by a bias applied to the electrode. The system remains a photo-driven catalytic process. Immobilising photocatalysts to semiconducting electrodes, opens a plethora of new parameters, associated with the overall efficiency of the system. Many of these parameters are covered later in this thesis. A further detailed description of photoelectrocatalytic systems and how they operate is given in the following sections.

Modifying the PL with anchoring groups to immobilise photocatalysts to electrodes, adds to the importance of the PL. In photoelectrocatalytic systems PL are referred to as the anchoring ligand, as these are the ligands that anchor the supramolecular photocatalyst to the electrode surface. In some instances, not all the PL ligands are anchored. When this is the case, the PL that is not anchored to the semiconducting material, is referred to as the ancillary or auxiliary ligand. Modifications of the peripheral groups has been investigated by our group, with the end goal of immobilising the photocatalyst to an electrode in a photoelectrocatalytic hydrogen generating system. Carboxylate or phosphonate functional groups have been studied for this purpose. Figure 1.6 shows an array of peripheral ligands discussed in this thesis. From left to right the figure displays the structures of bpy (2,2'-bipyridine), dceb (4,4′-di(carboxyethyl)bipyridine), bpyMeP (4,4’-bis(diethyl-(methylene)-phosphonate)-2,2’-bipyridine) and tbbpy (4,4-di-tert-butyl-bipyridine). Bpy, as a PL, has been used as a reference point, for many groups, as $Ru(bpy)_3$ is deeply understood, this is discussed in greater detail later in this chapter. In Figure 1.6, dceb and bpyMeP are the only two ligands equipped with anchoring groups for immobilisation. There are others anchoring groups utilised for immobilisation, that are not displayed in Figure 1.6. these include, but are not limited to, ligands furnished with carboxylic acid groups or even pyridine, where the nitrogen is capable of immobilising the complex.[22]

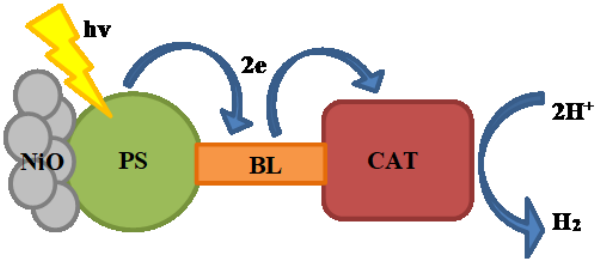

Figure 1.5: Schematic of intramolecular system immobilised on NiO electrode for photoelectrocatalysis

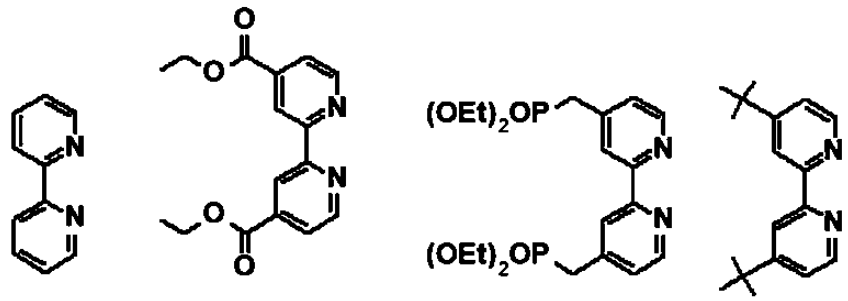

Figure 1.6: Structures of peripheral ligands discussed throughout the text

1.6 Photophysics and Photochemistry

The system depicted in Figure 1.5, is a basic blueprint of an ideal photoelectrocatalytic system, for hydrogen generation, with the driving energy acquired from a light source. Understanding and tuning the photophysics and photochemistry of the system are crucial to its overall efficiency. Photophysics, put simply, is the study of processes that occur to a molecule after the absorption of a photon without the presence of chemical reactions. Whereas, photochemistry involves the processes that occur to a molecule after the absorption of a photon resulting in chemical reactions.[23]

1.6.1 Jablonski Diagram

Photochemistry is based on the processes of photophysics such as those summed up by the schematic of the Jablonski Diagram, depicted in Figure 1.7, below. Briefly, the Jablonski Diagram involves the absorption of light leading to formation of excited states from a ground state (e.g. $G_0 \rightarrow S_1$) and the possible energy releasing pathways taken on return to the ground state. In Figure 1.7 it is clear the different electronic states are assembled vertically by increasing energy, the ground state being the lowest energy state, anything above ground state is considered an excited state. The electronic states are also grouped horizontally by their spin multiplicity. The ground state, denoted here by G_0 (may also be denoted as S_0), has a singular spin multiplicity, this is the same for the singlet excited state, hence its name, denoted below as S_1 and S_2 (S_2 being a singlet excited state of higher energy than S_1). The triplet state (T_1) follows this naming pattern, it has a spin multiplicity of three. After excitation, the transitions between excited states by non-radiative processes are as follows; vibrational relaxation (VR), between vibrational levels to lowest vibrational level of same electronic level, depicted in the figure as S_2: $v_2 \rightarrow v_1 \rightarrow v_0$, internal conversion (IC), between the lowest vibrational level of a higher electronic level to a lower electronic level of the same multiplicity, e.g. $S_2 \rightarrow S_1$ and/or inter-system crossing (ISC), between the lowest vibrational level of an excited electronic level to an excited electronic level of different multiplicity, e.g. $S_1 \rightarrow T_1$. The relaxation back to the ground state by radiative, as fluorescence (spin-allowed), illustrated by $S_1 \rightarrow G_0$ or non-radiative processes, such as phosphorescence (spin-forbidden, e.g. $T_1 \rightarrow G_0$), non-radiative decay to the ground state can occur due to quenching. Kasha's rule states that radiative emission occurs from the lowest electronic excited state.[24]

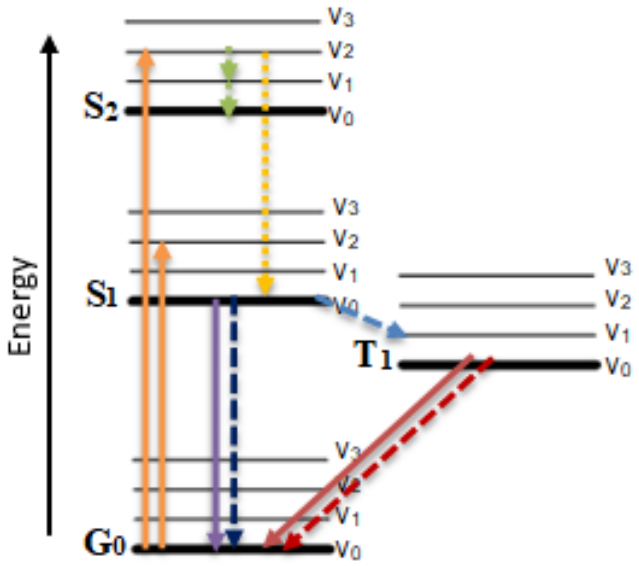

Figure 1.7: Schematic of the Jablonski Diagram. Absorbance is indicated by ascending solid orange arrows, radiative decay is indicated by descending solid arrows, non-radiative decay is indicated by descending dashed arrows.

1.6.2 Non-Radiative Decay Processes in Intermolecular Systems

Non-radiative decay processes can occur by both energy and electron transfer processes. In the case of intermolecular photocatalytic systems energy transfer is described as:

$$PS + CAT + h\nu \rightarrow {}^{*}PS + CAT \rightarrow PS + {}^{*}CAT$$

i.e. after irradiation, the excited PS transfers this excited energy to the CAT upon returning to the ground state.

Whereas, electron transfer can be described as either:

$PS + CAT + h\nu \rightarrow {}^{*}PS + CAT \rightarrow PS^{+} + CAT^{-}$ *(oxidative electron transfer)*

i.e. after irradiation, the excited PS transfers an electron to the catalyst.

$PS + CAT + h\nu \rightarrow {}^{*}PS + CAT \rightarrow PS^{-} + CAT^{+}$ *(reductive electron transfer)*

i.e. after irradiation, the excited PS receives an electron

1.6.3 Intercomponent Processes in Intramolecular Systems

In the supramolecular system PS-BL-CAT, intercomponent processes occur upon excitation. Optical electron transfer (charge transfer, CT) is a radiative process that can lead to the formation of new bands in an absorption spectrum when compared to the sum of the spectra of its components. Optical electron transfer is the delocalisation of a photon upon absorption and can be described as:

$$PS\text{-}BL\text{-}CAT + h\nu \rightarrow PS^{+}\text{-}BL\text{-}CAT^{-}$$

Photoinduced electron transfer, on the other hand, is when a photon is absorbed and localises on the PS, following this, an electron moves through the supramolecule in a non-radiative manner:

$$PS\text{-}BL\text{-}CAT + h\nu \rightarrow {}^{*}PS\text{-}BL\text{-}CAT \rightarrow PS^{+}\text{-}BL\text{-}CAT^{-}$$

The bridging ligand can also play a role, although, it is not entirely clear what role the bridging ligand has in a supraspecies. There is a relationship between the length of the BL and its electronic structure, with the degree of delocalisation between PS and CAT (when at the same centre-to-centre distance):

$$PS\text{-}BL\text{-}CAT + h\nu \rightarrow {}^{*}PS\text{-}BL\text{-}CAT \rightarrow PS^{+}\text{-}BL^{-}\text{-}CAT \rightarrow PS\text{-}BL^{+}\text{-}CAT^{-}$$

Intramolecular systems avoid the need for diffusion of the PS and CAT centres, as in bimolecular systems the components are attached. A disadvantage, however, of intra-systems is back transfer of an electron, also referred to as charge recombination (CR), a non-radiative process:

$$PS^{+}\text{-}BL\text{-}CAT^{-} \rightarrow PS\text{-}BL\text{-}CAT$$

Charge recombination competes with charge transfer and energy transfer. To avoid this process, the rate of CT must be faster than that of CR.

Energy transfer in supramolecular species is similar to energy transfer between individual components, in the way that the excited catalyst must be of equal or lower energy than the excited state of the photosensitiser, thereby allowing for facile, downhill electron transfer. There are two main energy transfer mechanisms: Föster-type[25] (coulombic, Figure 1.8) and Dexter-type[26] (exchange, Figure 1.9) energy transfer.

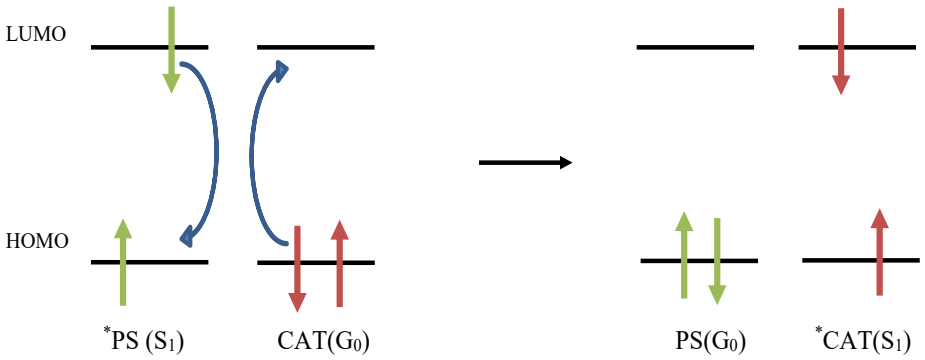

Figure 1.8: Schematic representation of Förster energy transfer mechanism

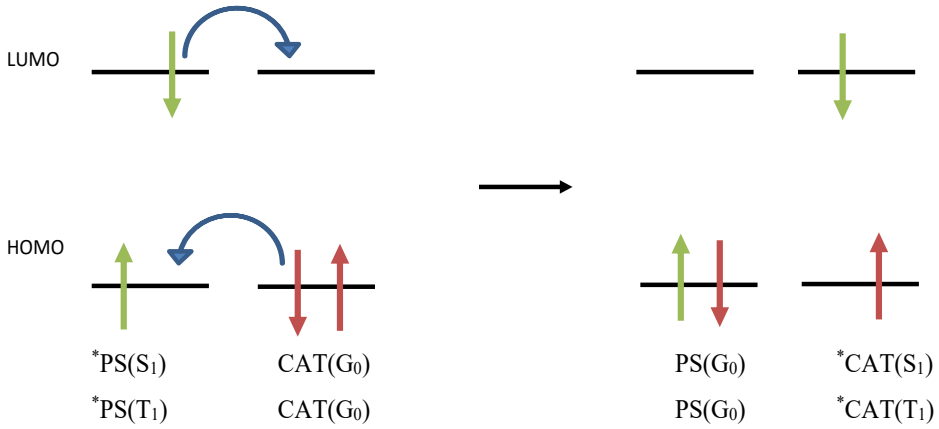

Figure 1.9: Schematic representation of Dexter energy transfer mechanism

The transfer mechanism used in photocatalytic systems is dependent on the parameters of the systems, such as, distance between PS and CAT and multiplicity of ground and excited states. The Förster mechanism involves long-range (1-10 nm) dipole-dipole interactions and collisions. The excited PS generates an electric field through an oscillating dipole. When the catalyst enters this field, through collision in solution as a separate molecule (inter) or collision from a change of orientation of the combined species (intra), the catalyst resonates and becomes excited. Electrons remain on their starting molecules or part of the supramolecule they were excited from. This mechanism is uncommon amongst transition metal complexes as it involves singlet-singlet ($S_1 \rightarrow G_0$) energy transfer, as this transition has the high oscillator strength

required for this mechanism. For metal complexes, such as our systems, singlet excited states do not last long enough for this mechanism type to take place. The presence of the heavy atom allows for the spin-forbidden process, ISC from the singlet to the triplet state to occur. This is due to the phenomenon of spin-orbit coupling (interaction of the spin and momentum). Therefore, the Dexter-type mechanism is the most frequent pathway for transition metals as these systems experience long-lived triplet excited states. The Dexter mechanism is a short-range (<1 nm) simultaneous exchange of two electrons and requires an overlap of PS emission spectrum with the CAT absorbance spectrum, i.e. the spectral features occur over a similar wavelength range and therefore, at similar energy. The energy transfer efficiency is dependent on the degree of this overlap.

1.6.4 Electronic Transitions

Molecular orbital theory is used to describe charge transfer between metal d orbitals of the PS and the bonding π or anti-bonding π^* ligand orbitals of the organic BL during photoexcitation in supramolecular organometallic systems, like the ones discussed in this thesis. The peripheral ligands can also be involved. The electronic transitions that arise from the movement of electrons between these orbitals are depicted below in Figure 1.10. When the charge is localised at the central metal, metal centred (MC), d-d transitions can occur. Similarly, ligand centred (LC) transitions from the bonding π orbital to the anti-bonding π^* orbital can occur. These types of transitions can be seen in the near-UV region, with neither MC or LC influencing the charge distribution between the metal and ligands. d-π^*, known as metal to ligand charge transfer (MLCT), and ligand to metal charge transfer (LMCT), are indicative of a redistribution of electron density and are seen in the visible region. There are other important transitions to consider, such as, intraligand charge transfer (ILCT), CT within the same ligand, charge transfer to solvent (CTTS), metal-to-metal charge transfer (MMCT), in complexes with more than one metal, and ligand-to-ligand charge transfer (LLCT), also known as inter-ligand chare transfer.

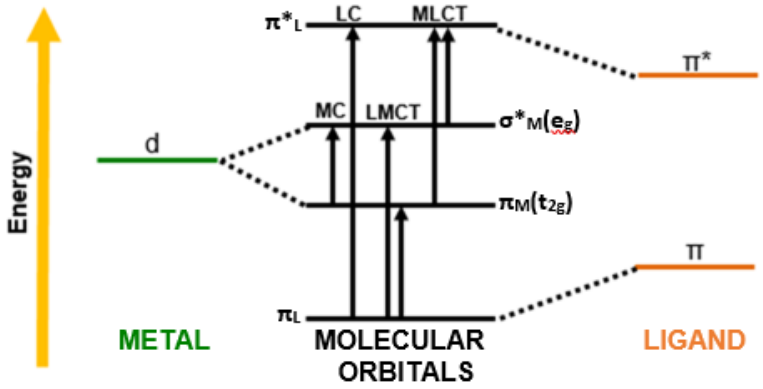

Figure 1.10: Simplified schematic energy level diagram of organometallic complexes using molecular orbital theory

1.7 Photoelectrocatalysis

Photoelectrochemical cells (PECs), are designed to split water into H_2 and O_2 simultaneously, as a one-step or a two-step (Z-scheme) process of artificial photosynthesis. In simple terms, PECs operate by firstly forming electron-hole (e^-, h^+) pairs, through the absorption of a photon by the photocatalyst. If this photon has enough energy to overcome the band gap (energy difference between the top of the valence band and bottom of the conduction band) of the semiconductor (SC), subsequently, electrons are generated in the conduction band (CB) and holes in the valence band (VB). Holes are travelling vacancies in the valence band. This can then lead to the reduction of water at the photocathode, with the use of a proton reduction catalyst, using the electrons generated and water oxidation at the photoanode, with an oxygen evolving catalyst, due to the holes generated. Figure 1.11 further illustrates the pathways taken, of the electrons and holes, to split water.

There has been a lot of research into improving the efficiency of the overall photoelectrocatalytic process, from designing photosensitisers that absorb further out in the visible region, to tuning the levels of the valance and conduction bands and subsequently the band gap width of semiconductors. The theoretical band gap minimum (minimum required amount of energy, at room temperature and pH 0) for water splitting being 1.23 eV (~1100 nm), as the bottom of the CB has to be more negative than the reduction potential of water (0 eV) and the top of the VB more positive than the oxidation potential of water (1.23 eV), to generate H_2 and O_2

respectively.[27] In one step photoexcitation systems, the CB and VB meet these criteria. Whereas, in two-step photoexcitation systems, there are two photoelectrodes, one meeting the band gap requirements for H_2 generation using the electrons from its CB and the other for O_2 production from the holes on its VB. A redox shuttle couple then utilises the photogenerated holes from the VB of the H_2 evolving photocatalyst, to oxidise the reductant, and subsequently the resulting oxidant is reduced back to reductant by the electrons from the CB of the O_2 producing photocatalyst. One-step and two-step photoexcitation processes are depicted in Figure 1.11 (a) and (b), respectively.

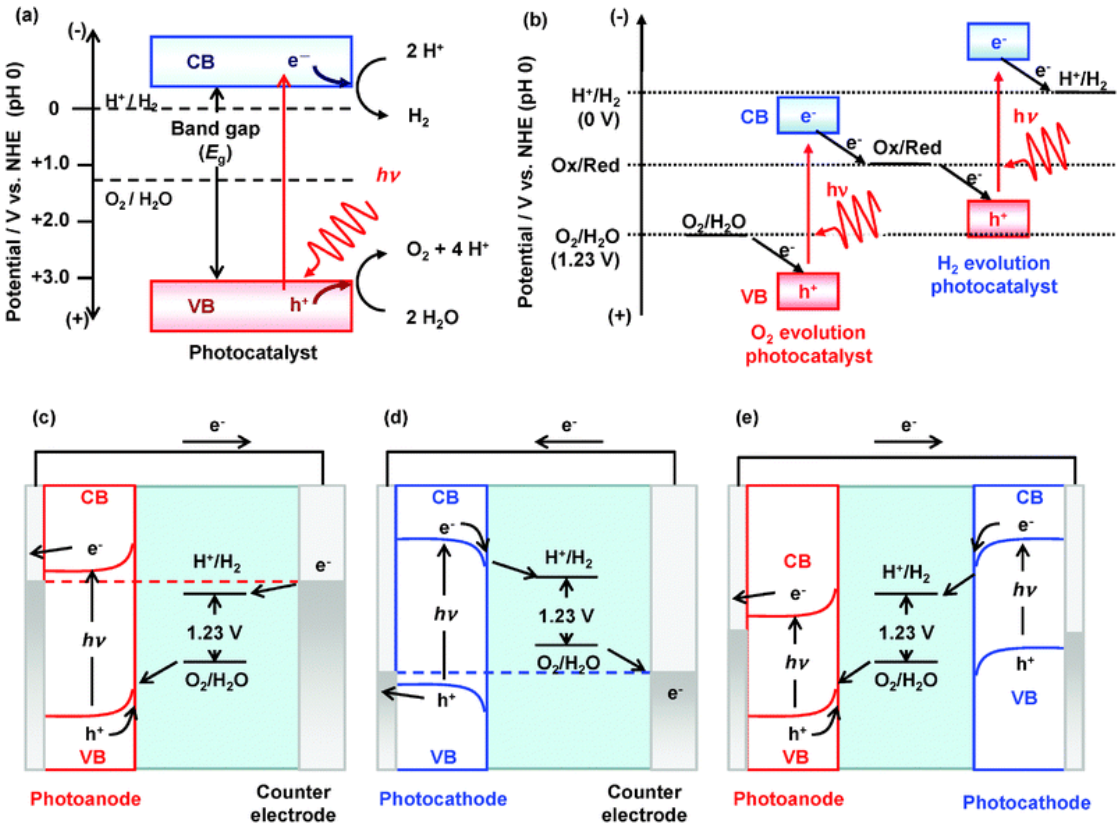

Figure 1.11: Schematic energy diagrams of photocatalytic water splitting systems with one-step (a) and two-step (b) photoexcitation, and PECs with n-type photoanode (c), p-type photocathode (d) and a tandem system using n- and p-SCs as anode and cathode, respectively (e)[28]

1.7.1 Semiconductors

The semiconducting electrodes of PECs can be doped with either acceptor or donor impurities. This changes the ratio of electrons to holes, shifting the Fermi level

accordingly, resulting in extrinsic semiconductors (SCs). The Fermi level is the level of the highest state filled with electrons. SCs can then be classed as p-type photocathode (Fermi level shifted towards VB) or n-type photoanode (Fermi level shifted toward CB). The potential of TiO_2 was first realised in 1969 with the Fujishima-Honda effect,[29] and then, in 1972, the Fujishima-Honda cell, was the first n-type PEC to split water, using TiO_2 n-type photoanode producing O_2 and Pt dark catalytic cathode producing H_2.[30] Figure 1.11 (c) and (d), represent the different SC types in PECs, the dashed line in both (c) and (d) represent their corresponding Fermi level. By following the charge flow, water is reduced and oxidised, at the photocathode and photoanode respectively. N-type (negative-type) SCs are doped with a donor type dopant, e.g. phosphorous. The dopant then donates its valance electrons to the SC, thus negatively charging the SC due to the presence of more electrons to that of holes. In p-type (positive-type) semiconductors, the positive charge is due to a higher concentration of holes (h^+), which are positively charged, and a lower concentration of negatively charged electrons (e^-). This is due to the SC being doped with an acceptor type dopant, e.g. boron. Electrons are easily elevated from the VB of the SC leaving holes present in the VB. Using mesoporous NiO films as a natural p-type semiconductor, has been proven to be repeatedly successful for hole injection due to its properties of mixed valence states (Ni^{2+} and Ni^{3+}), and a band gap of 3.47 eV.[31]

1.7.2 Dye-sensitised semiconductors (DSCs)

Dye-sensitised solar cells (DSSC) are frequently referred to as Gräzel cells, as Michael Gräzel and co-inventor Brian O'Regan pioneered this technology.[32] Original DSSCs were regenerative systems, typically n-type photoanodes sensitised with dyes that absorb light then exchanges electrons with aqueous electrolytes. Further development lead to widespread use of iodide redox couples for non-aqueous cells. The cathode is usually a platinum electrode, it is known as the dark catalytic cathode as the energy is not provided directly from light. The processes involved are the same as those mentioned previously. The PS, on the surface of the anodic electrode, absorbs light and is excited ($PS \rightarrow PS^*$). Then injection of the excited electrons into the CB of the anodic electrode occurs, with oxidation of the PS^+, which leaves it available to accept electrons from a reduced redox mediator, thus, oxidising the mediator and regenerating the ground state PS. The injected electrons, simultaneously, travel to the

counter electrode. There the oxidised redox couple is reduced, thereby completing the circuit. The mechanism for charge transport throughout an early developed p-type dye-sensitised semiconductor (p-DSC) system is the flip of a n-DSC. When the PS is excited, the PS donates holes to the VB of the p-SC, this is hole injection. Updated versions of the Gräzel cell combine this technology and the Fujishima-Honda cell, with the oxygen evolution reaction (OER) catalyst removing the need for the redox couple and splitting water. Similarly, a photoactive hydrogen evolution reaction (HER) catalyst is used instead of the redox mediator, for p-DSSCs.

In relatively recent years, research into p-DSCs for hydrogen generation has gathered momentum. The quest for an ideal tandem system, with combined optimised photoanode and cathode, np-junction DSSC, (Figure 1.11, (e)), as opposed to single-junction PECs, has many potential benefits which will progress photoelectrocatalysis to more efficient way of splitting water, producing hydrogen at the photocathode and oxygen at the photoanode. The efficiency of conventional n-DSSCs depends on several factors; the energy levels of the HOMO and LUMO of the PS, the Fermi level of the anodic electrode and the redox potential of the shuttle redox couple or the ease of energy transfer to the OER catalyst. Dye-sensitised photocathodes could be a means of increasing the efficiency of standard n-DSSCs. The theoretical maximum efficiency in DSSCs is increased by 10% when the Pt counter electrode is replaced by a dye-sensitised photocathode, such as, dye-sensitised NiO.[33]

There are only two reported working dye-sensitised tandem devices, by Sun and co-workers, and both employ separately immobilised PS and CAT components onto both the photoanode and photocathode. The first, in 2014, uses molecular Ru and a molecular Co CAT on the NiO photocathode, with Ru being used for both the PS and CAT at the TiO_2 photoanode.[34] The second system, in 2015, employs organic dyes as the PS for both photoanode and photocathode, this is the first account of where organic metal-free dyes have been used in tandem.[35] A cobaloxime type HER catalyst and the same Ru OER catalyst, as used in their first device, are co-immobilised to their corresponding semiconductors. The efficiencies of the two devices are supressed by the photocathodic side of the reaction. Many systems, discussed below, report desorption and/or degradation of the catalyst as a major contributor to low hydrogen evolution. This is where the idea of immobilising intramolecular species, for photocatalytic hydrogen generation on p-SC, comes into play. Intramolecular

complexes are extremely synthetically tuneable. Thus, complexes can be altered systematically to meet the requirements of efficient DSSCs. These requirements include, but are not limited to, the PS component absorbing strongly in the visible region, with a HOMO level shifted towards more positive position than that of the Fermi level of the p-SC and the electrode's VB must be between HOMO and LUMO of the PS, while the CB must be more negative than the PS's LUMO level. The PS element of the supramolecule, should have a long-lived excited state lifetime, while the bridging ligand's LUMO level is lower than that of the PS's LUMO level, then the HER component's LUMO level lower than the BL, for directional ease of electron flow. When immobilised on the surface of the electrode, the photocatalyst needs to be stable at the conditions of the system. A simplified schematic energy diagram depicting charge transfer in these systems is represented in Figure 1.12. In the schematic, **1** corresponds to illumination of the photosensitiser which results in the absorption of a photon and formation of an excited photosensitiser, **2** is hole injection on to the valance band of the electrode creating a charge separated state, **3** is directional electron transfer along the bridging ligand to the catalytic centre, regenerating the PS to the ground state, **4** is the catalytic process of the reduction of water, forming H_2.

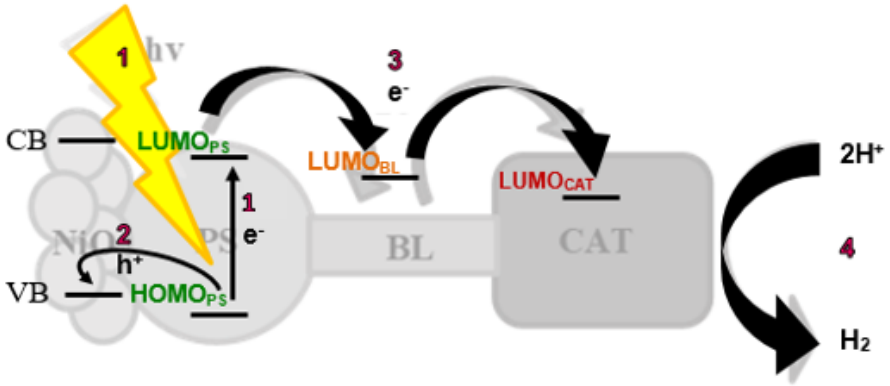

Figure 1.12: Simplified schematic drawing of charge transfer in supramolecular systems immobilised on NiO film electrodes

The work presented in the following chapters, focuses on the photocathodic, hydrogen-evolving, half of the water splitting reaction. Therefore, only p-DSC systems, with a p-type photocathode as the working electrode and a metal counter electrode, together with photocatalysts, with the sole function of generating hydrogen, are discussed in detail.

1.8 Photocatalysts

A vast amount of research has been and is on-going, to explore and design ideal photocatalytic systems. Many groups, including ours, follow a similar structure as to how investigations develop. Using design parameters, known from the literature (e.g. light absorption in the visible region, directional electron flow towards the catalyst, etc.), a possible complex is envisioned. The synthetic confines are researched and adapted as required, and then synthesis can proceed. Characterisation of the complex follows, along with studying the photophysical properties, electrochemical properties and other such behavioural properties. This then leads to photocatalytic solution experiments, determining and quantifying hydrogen production. Analysis of the system under hydrogen evolution conditions (as close to as possible) is performed, such as, stability of complex over time irradiated, rate of production over time, spectroelectrochemical experiments, etc. Then progressing to immobilising the photocatalyst onto the surface and accounting for the relative considerations once bound to the surface of a semiconducting electrode (e.g. stability of complex when immobilised). Below is a brief insight, into working ruthenium-platinum/palladium supramolecular photocatalysts for hydrogen generation on the surface of p-type photocathodes.

1.8.1 Polypyridyl Ruthenium(II) photosensitisers

Polypyridyl ruthenium(II) (Ru(II)) complexes have been extensively explored (more so in solution) for their capabilities as photosensitisers and in simulating natural photosynthesis. $[Ru(bpy)_3]^{2+}$ (bpy = 2,2'-bipyridine) was first used as a photosensitiser by Sauvage and co-workers, in the late 1970s.[36] The complex exhibits the attributes required for a working photosensitiser, such as strong absorption in the visible region and long-lived excited states allowing for electron transfer to other molecules. $[Ru(bpy)_3]^{2+}$ sparked global interest when it was discovered it could transfer electrons. Synthesis is relatively simple (depending on the ligands attached to the metal centre) and the tuneability of the Ru complex is limitless. Many derivatives have been synthesised with the intent of improving the capabilities of the photosensitiser.

The properties of the ligands (π-acceptor, σ-donor) dictate the properties of the Ru(II) complexes. The ligand properties can be assessed by investigating the free ligand and comparing to those of bpy. The reduction potential relates to the π-acceptor capabilities and the pK_a correlates to the σ-donor capabilities. Reduction potential and pK_a can be determined by cyclic voltammetry (CV) and acid-base studies, respectively. The substitution of one of the 2,2'-bipyridine ligand, in a tris-bipyridine Ru(II) PS, for a π-acceptor ligand ($[Ru(bpy)_2(L)]^{2+}$), such as 2,2'-bipyrazine (bpz), leads to absorption further out in the visible region, increasing the utilisation of the solar spectrum. Although this is an obvious advantage, one disadvantage is that π-acceptor type complexes can be less photostable. Photostability can be improved by increasing the energy gap between the triplet metal-to-ligand charge transfer (^{3}MLCT) and triplet metal-centred (^{3}MC) states, i.e. increasing the energy of this latter state, avoiding transitions to the ^{3}MC state, as population of this state can lead to ligand dissociation.[37] This can be done using a σ-donor, which shifts the ^{3}MC to higher energy. Ligands with strong σ-donor properties, such as, 1,2,4-triazole, can blue shift the absorbance and emission spectra. This is avoided by using the mixed ligand systems ($[Ru(bpy)_2(L)]^{2+}$). Many different, mono-, bi- and tridentate, organic ligands have been bound to the Ru centre by mono-, bis-, tris-, etc, substitution, with the intention of pushing the absorbance further into the red, enhancing the electron transfer capabilities and increasing charge separation and the lifetimes of excited states. The endless derivatives possible, from the initial tris complex, broadens its functionality. This has led researchers to investigate $[Ru(bpy)_3]^{2+}$, and its derivatives, for many different applications, such as, a PS for anode[38] and cathode,[39] in biodiagnostics and in environmental optical chemical sensors.

1.8.2 The Bridging Ligand, e.g. $[Ru(bpy)_2(L)]^{2+}$

The design of photocatalysts was then focused towards using the substitution of a bpy ligand, as an opportunity to incorporate ligands that are more suitable for binding a hydrogen catalyst, for intramolecular systems. For example, in the case of $[Ru(bpy)_2(L)]^{2+}$, where L is a suitable bridging ligand, i.e. capable of directing the flow of electron transfer from the photosensitiser towards the bound catalyst and that limits back electron transfer. Our group,[40] and many others,[41] strive to design and synthesise intramolecular supraspecies, as intramolecular tactics address some of the

limiting factors involved in intermolecular approaches, such as, diffusion rates and collision probability. The bridging ligand's properties, size, shape, flexibility, electronic nature, can be fine-tuned to aid the photocatalytic processes.

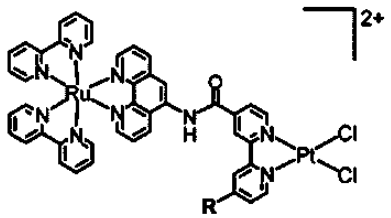

1a-d:
1a: R = COOH; 1b: R = COOEt; 1c: R = CH3; 1d: R = CN.

Figure 1.13: Structures of photocatalysts discussed throughout the text

Sakai and co-workers published, in 2006, the first RuPt, hydrogen generating photocatalyst depicted in Figure 1.13 **(1a)**.[42] Sakai noted the effect that simple structural changes had on the turnover number (TON). TON is used to describe the amount of hydrogen achieved by a system and is calculated by dividing the number of moles of hydrogen produced by the number of moles of catalyst employed by the system. The TON was affected by the simple increase of the electron-withdrawing ability of the substituent on the bridging ligand. As the withdrawing properties increased, the TON increased too, but remained low, i.e. TON of R = CH_3 < COOEt < COOH < CN, with R = CH_3, an electron donating group, being photo-catalytically inactive, to R = CN reaching a TON = 12.5.[43] The electron donating/withdrawing properties of the BL influences the driving force of the photoinduced electron transfer within the intramolecular system. When the PS is excited (PS^*), its emissive ^{3}MLCT state are quenched when a CAT is attached. This indicates electron transfer to the LUMO of an excited state, forming the charge separated (CS) state, which is favourable, at lower energy than the PS's emissive ^{3}MLCT. Sakai reports that when the BL has electron withdrawing substituents this is the case, and the CS state is on the side of the Pt CAT, easing electron transfer from the Ru PS. This is not the case for **1c** , when R = CH_3, the electron donating group, thus, hydrogen generation does not occur. Therefore, the stronger withdrawing effect of the CN group causes an increase in photocatalytic activity. This work also showed no colloids were formed during the photocatalytic experiments. Colloid formation may indicate the platinum centre had separated from the complex, meaning the photocatalyst had degraded and

was no longer the active catalyst. Sakai and co-workers also investigated different types of BL, discussed in the following sections, but few were photo-catalytically active.[44–46]

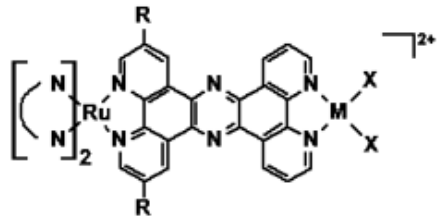

2a-e

Complex	N⌒N	R	M	X
2a	tbbpy	H	Pd	Cl
2b	tbbpy	Br	Pd	Cl
2c	tbbpy	H	Pt	Cl
2d	tbbpy	H	Pt	I
2e	bpyMeP	H	Pt	Cl

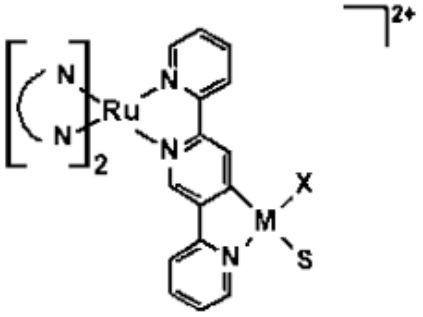

3a-d

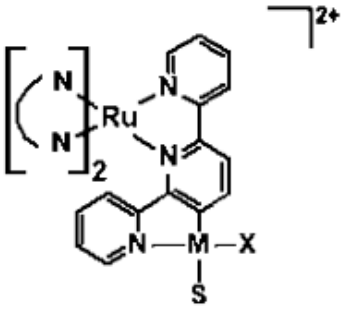

4: N⌒N = bpy, M = Pd, X = Cl
S = Solvent

3a: N⌒N = bpy, M = Pd, X = Cl;
3b: N⌒N = dceb, M = Pd, X = Cl;
3c: N⌒N = bpy, M = Pt, X = I;
3d: N⌒N = bpy, M = Pt, X = I;
S = Solvent

Figure 1.14: Structures of complexes discussed throughout the text (continued).

Rau and co-workers reported a photoinduced hydrogen evolution (PHE) active RuPd (Figure 1.14: **2a**) assembly, in the same year as Sakai and co-workers.[47] A TON of 56 was achieved in the presence of TEA (triethylamine) with acetonitrile as the solvent. In a later study (2010), water was added (10% vol) and the TON increased to 161.[48] This shows the reaction conditions can also affect the activity of the photocatalyst. The same study showed a correlation between the irradiation wavelength and catalytic activity, indicating that localisation of the initial excited state is important for PHE. For this complex, it was determined that the initial MLCT resided on the BL side of Ru, and this resulted in more efficient electron transfer and therefore higher TON. When the excitation wavelength is varied, and ligand-centred

transitions are excited on the peripheral ligands, the TONs for hydrogen are lower. Subsequently, in 2011, Rau and co-workers, altered the BL by bromine substitution (Figure 1.14: **2b**), to investigate the effect on TON. The addition of Br leads to a decrease in TON, it also has a lower water tolerance. TONs reached maxima after the addition of only ~7% vol. of water (TON ~94), and were lower than that of the initial compound (max TON ~238 with H_2O content of ~15 % and a TON ~175 when H_2O content is ~7%).[49]

Vos and co-workers reported similar conclusions in 2012, in that there is a solvent effect for individual complexes, along with the findings that a bridge based ^{3}MLCT produces more hydrogen than a PL (peripheral ligand) based ^{3}MLCT, with density functional theory (DFT) calculations supporting experimental findings.[40] DFT is routinely used to model experiments to both justify or to help explain experimental data. The 2012 study compared two very similar RuPd complexes with a different BL, one incorporating 2,2':5',2"-terpyridine (2,5-bpp) **(3a)** and the other, 2,2':6',2"-terperidine (2,6-bpp) **(4)**, (essentially, one straight BL (2,5-bpp) and one bent BL (2,6-bpp), as depicted in the figure above). Only the **3a** complex was observed to be photocatalytically active under the experimental conditions used, with no evidence for colloid formation.

1.8.3 The Catalytic component, e.g. $[Ru(bpy)_2(L)(M)(X)_2]^{2+}$

The catalytic centre is of obvious importance, as it facilitates hydrogen production from water splitting. An ideal catalyst should, fundamentally, enable directional electron transfer, use all electrons supplied by PS and be stable under catalytic conditions. If the photocatalyst is unstable under catalytic conditions this could lead to the breakdown of the complex and possible formation of colloids, and this is routinely investigated to rule out colloid involvement in the production of hydrogen. For example, in 2007, Hammarström and co-workers, used X-ray photoelectron spectroscopy (XPS) and transmission electron microscopy (TEM) to determine the degradation of dinuclear species (Figure 1.15: **5**) and the formation of colloidal Pd.[50] This led to Rau and co-workers to test the possibly of colloidal formation during photocatalysis experiments for a RuPd complex, **2a**, and investigate the use of Pt as the catalytic metal centre (Figure 1.14: **2c**).[51] Complex **2c** was previously reported,

in 1998, by Eisenberg and co-workers[52] but Rau and co-workers used X-ray absorption spectroscopy (XAS), and together with mercury (Hg) poisoning experiments, they confirmed that **2a (**RuPd) started to fall apart after 35 min of irradiation. Photocatalytic H_2 evolution experiments in the presence of Hg, showed no hydrogen was produced. This indicates colloidal Pd formation is the active catalyst in the previous photocatalytic experiments employing **2a** as the photocatalyst. Although lower TONs were achieved when **2c** was employed, in comparison to **2a**, the XAS experiments provided no evidence for colloid formation, and mercury poisoning did not affect the TON. From time-resolved transient absorption studies it was clear that the replacement of Pd with Pt had little effect on the mechanism of electron transfer. The original RuPd complex, **2a**, was thought to lose one of the Cl ligands (attached to the catalytic metal centre) to facilitate electron transfer and hydrogen generation. The latter study by Rau and co-workers demonstrated that this is not the case for complex **2c**, and the Cl ligands remained coordinated during photocatalysis.

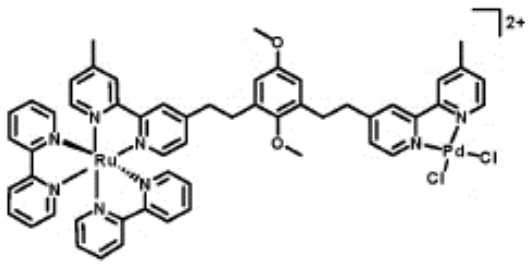

5

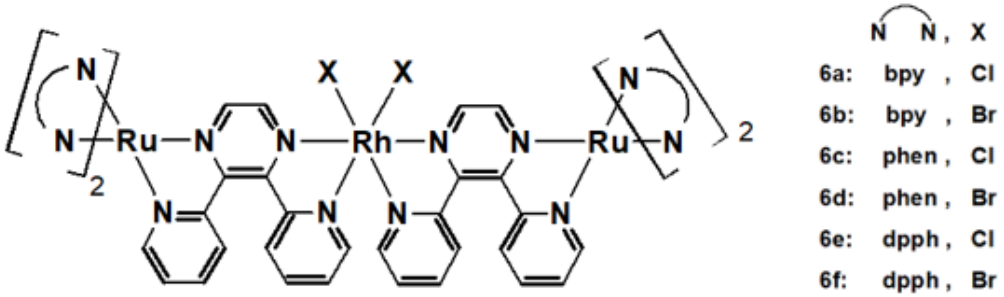

Figure 1.15: Structures of complexes discussed throughout the text (continued).

Brewer and co-workers reported in 2011 that with their RuRhRu trinuclear complexes (Figure 1.15: **6**), tuning of the peripheral groups on the catalytic metal increased photocatalytic activity. Substituting Cl for Br, reduced the emission, indicating

improved electron transfer. This was attributed to the reduced σ-donating properties of Br.[53,54] In these experiments the Brewer group investigated the effect of the peripheral ligands on the Ru end of the molecule, and this will be discussed in the next section. In the same year, Rau and co-workers investigated the effect of changing the halide group at the catalytic centre, in the RuPt photocatalyst, **2c**, with substituting Cl^- for an I^- anion (Figure 1.14: **2d**). The decision to increase electron density at Pt, was based on the premise proposed by Sakai and co-workers, that hydrogen is generated via water-proton and Pt d_z^2-orbital interactions, thus, increasing the electron-density should result in more viable interactions.[44] Although, the photophysics and principal catalytic behaviour remained the same, regardless of the halide attached, the TON, for **2d**, increased to 272 from 7, for **2c**.[55] The presence of iodine enhances electron density on the Pt metal, which they reported led to stabilisation of the intermediate species created during photocatalysis, and thereby indicating that minimal modifications at the catalytic centre, can have significant effects on the overall catalytic ability of the photocatalyst.

1.8.4 The Peripheral Ligands, e.g. $[Ru(PL)_2(L)(M)(X)_2]^{2+}$

The importance of the peripheral ligands at the Ru light-absorbing centre, has been known for some time. Rau and co-workers reported wavelength dependent photocatalytic activity for a RuPd complex.[48] Brewer explored the effect of varying the halide on the catalytic centre (discussed above). In the same year (2011), Brewer also demonstrated that altering the PL at the Ru photosensitiser (together with the catalytic halides), effects the TON (structures are given in Figure 1.15). They studied PL = bpy **(6a** and **6b)**, phen (1,10-phenanthroline) **(6c** and **6d)** and ph_2phen (4,7-diphenyl-1, 10-phenanthroline) **(6e** and **6f)** as PLs on the Ru centre.[53] After 5 hrs of irradiation for the complexes $[\{(PL)_2Ru(dpp)\}_2RhBr_2]^{5+}$ (dpp = 2,3-bis (2-pyridyl)pyrazine), H_2 was generated, with TONs of 20, 31 and 140 in the order of PL = phen **(6d)** < bpy **(6b)** < ph_2phen **(6f)**. The photophysical features do not follow this trend. When PL = phen **(6d)**, the rate constant is largest for deactivation of the ^{3}MLCT through interaction of the excited state complex and the sacrificial agent DMA (*N*,*N*-dimethylaniline), and this inhibits formation of the reduced catalyst. The increased levels of H_2 with ph_2phen as PL **(6f)**, are thought to be due to the steric demands of

this PL protecting the reduced catalytic species from other side reactions, as the excited state rates reported, do not fluctuate significantly between the different PLs.

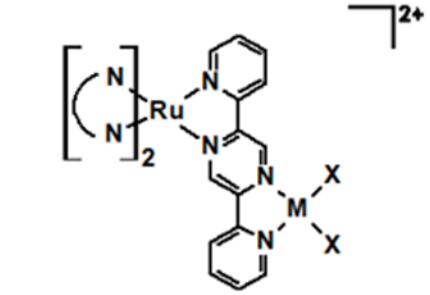

7a-c

7a: N⌒N = bpy, M = Pt, X = Cl
7b: N⌒N = bpy, M = Pd, X = Cl
7b: N⌒N = dceb, M = Pd, X = Cl

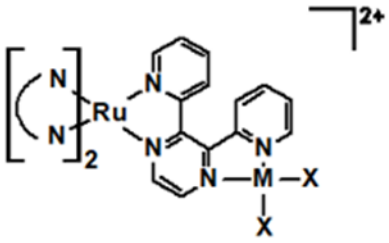

8a-c

8a: N⌒N = bpy, M = Pt, X = Cl
8b: N⌒N = bpy, M = Pt, X = I
8c: N⌒N = dceb, M = Pt, X = I

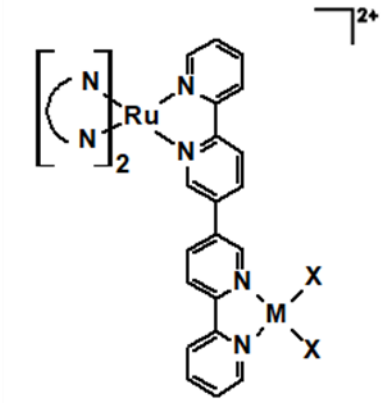

9a-d

Complex	N⌒N	M	X
9a	bpy	Pd	Cl
9b	dceb	Pd	Cl
9c	bpy	Pt	Cl
9d	dceb	Pt	Cl

Figure 1.16: Structures of complexes discussed throughout the text (continued)

The same year (2011), Vos and co-workers examined the effect of the PL using a similar compound to Sakai's RuPt complex with a di(pyridine-2-yl)pyrazine BL (2,5-dpp) **(7a).**[45] Vos reported the use of $PdCl_2$ at the catalytic metal, and then compared the photocatalytic activity for two PLs, bpy **(7b),** and dceb (4,4'-di(carboxyethyl)-2,2'-bipyridine) **(7c)**.[56] These studies showed the bpy analogue is inactive, whilst, the dceb analogue proved to be active with a TON of 400 after 18 h irradiation at 470 nm. Other work done by the DCU group, in 2015, included another of Sakai's RuPt complexes, with a 2,3-dpp BL **(8a)**,[44] which was inactive under their catalytic

conditions and also under our conditions. This work involved changing the halide on the catalytic centre from Cl to I **(8b)** and then the PL was changed from bpy to dceb in the PtI_2 complex **(8c)**. The new $[Ru(dceb)_2(2,3\text{-dpp})PtI_2]^{2+}$ complex, **8c**, was found to be an active photocatalyst, achieving a TON of 44.[21] The early-time photodynamics were investigated by transient absorption and resonance Raman (in acetonitrile). These results showed little difference between Cl or I ligands at the catalytic centre, but very different results are observed for bpy and dceb analogues, thereby indicating that the location of the excited state following excitation differs for the two complexes (discussed in more detail in Chapter 2). This study also notes that further time-resolved investigations should be carried out in catalytic conditions, i.e. with the addition of SA and a proton source. The use of sacrificial agents in photocatalytic experiments in time-resolved studies, would enable a better understanding of the electron dynamics involved during hydrogen generation. The use of dceb, to improve catalytic activity, has the bonus feature of using the esters as anchoring groups for chemiabsorption on the electrodes. This approach eliminates the need for SA, thus lowering the risk of decomposition of the photocatalyst.

Rau and Dietzek and co-workers, in 2015, changed the peripheral ligands on **2c** from 4,4'-bis(tert-butyl)-2,2'-bipyridine (tbbpy) to 4,4'-bis(diethyl-(methylene)-phosphonate)-2,2'-bipyridine (bpyMeP) **(2e)**.[57] The intention being to deprotect the phosphonate groups for subsequent anchoring and enabling immobilisation of the complex onto the surface of an electrode, such as commonly used in DSSCs. Their choice of anchoring ligand was based on research published by Odobel et al, (discussed later in this chapter, 1.11.2).[58] They also note that the use of phosphonate anchoring groups does not alter the localisation of the electron after excitation, compared to systems furnished with COOH/COOEt anchoring groups.[21] Dietzek and co-workers report that complex **2e** is a more active photocatalyst when compared with **2c** (37 vs 7 TON), although lower TON are achieved than similar complexes employing a $PdCl_2$ catalytic moiety, such as, **7c**, with TON of over 400 reported.[56] $PtCl_2$ was selected over $PdCl_2$ due to the risk of colloidal Pd formation during irradiation.[51]

In 2016, Vos and co-workers looked to continue studies on the effect of the catalytic activity of a photocatalyst upon the introduction of PtI_2, using **3a**,[59] as Rau and co-

workers had published with **2d**.[55] This study also looked at the effect of the PL on the TON for hydrogen generation. The $[Ru(PL)_2(2,5\text{-bpp})MXS]^{2+}$ complexes were investigated under catalytic conditions, using acetonitrile, TEA (triethylamine) and H_2O, where PL = bpy or dceb; S = solvent; M = Pd or Pt; X = Cl or I (the corresponding structures are given in Figure 1.14). This work showed an improvement in TON to 720 for the $[Ru(dceb)2(2,5\text{-bpp})PtI_2]^+$ dinuclear species **(3d)**, from 100 in the bpy analogue **(3c)**.[59] Huijser and co-workers, in collaboration with the DCU group, examined these complexes by DFT calculations and fs-ps transient absorption spectroscopy.[60] The results from this work show that the lowest lying (smallest energy gap from ground state) ^{3}MLCT state changes from the BL to PL, when the PL bpy ligands are exchanged for dceb. The same is reported for the LUMO of the ground state. A comparison of transient absorption spectral features, of the bpy and dceb analogues, showed a difference in the states populated, with the increased intensity of the spectral features pertaining to the BL for **3c** and to the PL for **3d**. This assignment was found to agree with DFT calculations which showed that the electron density in **3c** resides on the BL and on the PL for **3d,** following inter-system crossing (ISC) to the triplet state. This indicates that the electron flow is orientated towards the PL and away from the catalytic centre, when PL = dceb. Here, the PL is thought to act as the electron pool, contrary to original theories of the BL acting as the electron reservoir being the most efficient pathway for electron flow to the catalyst.

In 2017, the DCU group have extended their investigations in this area, and studied the effect of lengthening the distance between the metal centres, as the location of both metals on the central ring was thought to enable back electron transfer and recombination, thus, reducing the photocatalytic efficiency.[61] This study assessed inter- and intra- (Figure 1.16: **9a-d**) molecular approaches, and compared hydrogen production with photocatalytic systems of alternating BL, PL and the M. The novel complexes, of this study, were designed using bisbpy (2,2':5',3":6",2"'-quaterpyridine) as the BL; bpy and dceb as PL; and Pd and Pt as M. The study also reported the effect of water concentrations on catalytic activity during photocatalysis. The contribution includes photophysical characterisation and DFT calculations of the novel complexes. It is a comprehensive paper that considers all that has been reported over the last decade, in a bid to optimise photocatalysts for hydrogen generation by light driven water splitting. Experimental findings support previous findings in that

the addition of ester groups onto the peripheral bpy alters the flow of electrons and the PL acts as an electron reservoir.[60] The report is in agreement with other studies that Pd as the catalytic metal yields higher TONs than Pt (Cl is the halide employed for a more direct comparison of PdCl and PtCl, rather than create an additional difference with the introduction of I as the catalytic ligand).[51] The paper, also, further confirms each complex's catalytic activity is solvent dependent.[40] Although, the novel dceb compounds, in the article, achieved high TON they were lower than that of the $[Ru(dceb)_2(2,5\text{-bpp})PtI_2]^{2+}$ **(3d)**, which yielded a TON of 720 after 18 h.[59] Investigating the substitution of the Cl halide for I and the effect on the TON and early-time photodynamics, would be an interesting study.

1.9 Other Working Photocatalysts

There are many groups focused on progressing the research of photocatalysts for H_2 generation for large scale deployment, as discussed above. The photocatalysts discussed in previous sections, focus mainly on ruthenium-based photosensitisers with platinum or palladium catalytic centres systems (with some Ru-Rh-Ru trinuclear complexes). However, give a comprehensive overview of the various systems reported in the literature, this section touches on other system designs reported recently.

Vos and co-workers have worked with similar design parameters, using Ir as the light absorber.[62] There is also continuous work, within the DCU group, to design and synthesise more sustainable and environmentally friendly photocatalysts, with the use of organic compounds or first row transition metals.[63] Park and co-workers developed an Ir PS that achieved TONs of a staggering 510000, with a Pt catalyst, in DMF/DMA/H_2O solution after 18 days.[64] Park's group have also investigated anchoring Ir PS and Pt CAT on to molecular organic frameworks (MOFs), and this system is described as "self-healing", with steady TON and TOF (turnover frequency) seen up to nearly 7 days.[65] Yu and co-workers have reported high TONs of over 1500 for a photocatalytic IrPt supramolecule.[66]

Others, such as, Artero and Sun, and their groups, have worked towards employing cobaloxime as the catalytic component of the photocatalyst, with Ru as the light absorbing unit.[67–69] TONs achieved are comparable to many systems employing a noble metal as the catalytic metal centre. Song and Sun, and their corresponding

groups, have reported using Zn or Mg porphyrin-cobaloxime or iron hydrogenase mimics, as photocatalysts.[70,71] Song and co-workers also employed a metal-free PS component, in the form of a free-base porphyrin.[70] These noble-metal-free systems produce low levels of hydrogen, but they are a step in the right direction for large-scale deployment.

1.10 NiO as a p-type Semiconductor

Current research on p-SC is based, almost solely, on NiO nanoparticle films. Ni is a first-row transition metal and is cheap and abundant. As mentioned previously, it has the properties required for hole injection, making it a suitable photocathodic material. Dye-sensitised NiO photocathodes are currently being more heavily investigated. The focus of the work in this thesis is using supramolecular photocatalysts (discussed above) anchored on to the NiO surface for photoelectrocatalytic hydrogen generation, referred to as dye sensitised photoelectrochemical cells (DSPECs). With an abundance of different groups working in this area and preparing their own NiO, along with commercially available NiO, there are many inconsistencies in the production of NiO films, with many different preparation methods to create the NiO mesoporous films, e.g. electrodeposition. As part of the COST Action CM1202 on Supramolecular water splitting workshop, Gibson and co-workers set out to investigate if the inconsistencies in preparation affected the film's characteristics. Gibson and co-workers compared sources of NiO and examined their photoelectrochemical properties using different preparation methods, while maintaining the same PS and CAT.[33] They found similar results leading to the conclusion that these different parameters have little effect on the system. The study concluded all types of preparation made working p-DSCs. To improve the overall functionality of p-DSCs, they suggest focusing on improving both the current generated by, and the voltage applied to, the device. This is beyond the scope of this thesis but, it is important to highlight other features that contribute to the efficiency of the device.

There are also different approaches for employing PS and CAT systems, i.e. using separate PS and CAT, with the catalyst in solution and the PS immobilised on the electrode surface, co-immobilisation, layer-by-layer grafting or immobilising supramolecular photocatalysts directly via the PS component. Each approach has their

individual advantages and drawbacks, discussed below. Other features to be taken into consideration include; choice of anchoring group; number of anchoring sites; difference in length of anchoring group from PS; and for cases where PS and CAT are separated, the different ancillary ligands. As discussed previously, when one or more PLs are anchored, also known as anchoring ligands, the PLs not anchored to the SC and not attached directly to the catalytic centre (BL), are known as the ancillary ligand.

1.11 Immobilisation of Photocatalysts on Semiconductors

There has been a surge of interest in dye-sensitised p-type systems in recent years, but very few reported photoelectro-catalytically active p-DSCs. The aforementioned, solution-based studies have contributed positively to the creation of active p-type photoelectrochemical cells (p-PECs). There are several new factors to consider when moving from homogenous, solution systems, to working with immobilised complexes, on the surface of electrodes, in aqueous conditions. These new considerations are discussed below, tied in with the few, thus far, tested p-DSPEC water splitting systems for hydrogen generation.

1.11.1 Solution to Surface

In 2012, Sun and co-workers introduced the use of a water reduction catalyst (WRC), cobaloxime, to their working system of an immobilised organic dye on the surface of a NiO semiconductor.[72–74] The PS and CAT homogenous system proved to be photocatalytically active with the inclusion of a sacrificial agent, TEOA, in a MeOH/H_2O solution.[75] This led them to deposit the catalyst onto the electrode to remove the requirement for a SA. A downside of this system was the desorption of the catalyst leading to its instability. In 2013, Wu and co-workers attempted to address this issue by immobilising a supramolecular Ru-cobaloxime complex. This was the first publication reporting the use of a supramolecule for the photoelectrocatalytic generation of hydrogen. This photocatalyst was generated after the immobilisation of the photosensitiser component on to the NiO film, followed by the soaking of the film in solution containing the catalyst, which would then bond to a pyridyl group on an ancillary ligand.[76] This method of assembling differs from the approach taken in this thesis, where the supramolecule is synthesised, then immobilised on to the surface as

one. Our approach allows for direct control over PS to CAT ratio. Wu reports an increased stabilisation and the elimination of desorption issues with their assembly. The Wu group also contribute stability to the increased electron density of the anchoring ligand, when compared to $Ru(bpy)_2(dcb)Cl_2$, (dcb = 4,4′-$(COOH)_2$bpy). They propose that nucleophilic attack by water molecules at the binding sites of the anchoring groups to the surface of the NiO film is limited due to this increased electron density. In addition, the anchoring ligand had previously been investigated by Wu and co-workers, and the optimal distance between the anchoring group and the PS centre was determined, which provided electron transfer and minimal charge recombination.[77] This is vital for an efficient system. A further increase in stability is achieved by the atomic layer deposition (ALD) of a monolayer of alumina coated on the NiO prior to sensitisation. This slows down the CR between the reduced PS and the holes of the NiO by forming a barrier, and subsequently, permit directional electron transfer from the PS to the CAT, enhancing photocurrent density. The principles from these investigations are considered by us and others, discussed below, when looking at photocatalysts on the surface.

1.11.2 Working in Acidic Conditions

Odobel and co-workers reported a Ru phosphonate complex, immobilised on NiO and Rh catalysts in solution, to study the successful electron transfer between the PS and CAT in acidic conditions, with the formation of a Rh hydride.[78] Previous investigations by this group looked at the effect of four different anchoring ligands on the photoconversion efficiencies of the devices, biscarbodithioic acids, carboxylic acids, methyl phosphonic acids and catechol.[58] They found carboxylic acids to have the highest affinity for NiO, but all displayed similar photocurrent efficiencies (in order carboxylic acids > phosphonic acids > catechol > biscarbodithioic acids), except the complex with biscarbodithioic acids as anchoring groups. This study also suggests utilising a more π-accepting ancillary ligand in comparison to that of the anchoring ligand pushing the absorption further out and creating greater charge separation, thus, increasing CR times. Phosphonates as anchoring groups facilitate polarisation of the charge and have a high binding affinity, therefore, have been selected as the anchoring group for following studies by many research groups. Unfortunately, the intermolecular RuRh system was not photocatalytically active for hydrogen

generation but shed light on the possibility of using acidic solution for hydrogen production.

The Fermi level of a semiconductor (doped or otherwise) is affected by interfacial interactions with electrolyte. Once immersed in electrolyte solution the Fermi levels of both materials equilibrate causing a phenomenon known as band bending (migration of charge carriers from one material to the other). The initial distribution ratio of charge carriers on the semiconductor is known as the flat band position and the flat band potential is the potential applied to the semiconductor in electrolyte solution to return the band edges to their flat band position. NiO has a pH dependent flat-band potential due to protonation and deprotonation on the NiO at the interface of NiO to the solution, thus, leading to a pH-dependent driving force for hole injection. When measured by photocurrent onset, NiO has a flat band potential of 0.47 V vs. NHE (normal hydrogen electrode) at pH 7[31] or by the Mott-Schottky method, 0.53 V vs. NHE.[79] Odobel looked at the effect of acid on the flat band potential of NiO, in their system of CH_3CN solution with 0.1 M $(Bu_4N)PF_6$ electrolyte, in the absence of acid, the flat band potential was recorded at 0.484 V vs. NHE. In the presence of $5x10^{-2}$ mM of *p*-cyanoanilinium acid, the flat band potential of NiO shifted to 0.764 V vs. NHE. Wu and co-workers report an active system using an organic PS that is hydrophobic at the anchoring end and hydrophilic at the free end. This creates a bilayer between the NiO and the acidic media, increasing stability in acidic conditions for 16 h with no degradation of the NiO film.[80] The stability of the PS in extreme acidic conditions, enables a Mo-S cluster to be employed as the CAT. This approach also eliminates proton accumulation on the surface of NiO, therefore, bending of the valence band of the NiO semiconductor is inhibited and the hole injection driving force remains the same in the presence and absence of acid.

1.11.3 Stabilisation of PS and CAT of p-DSCs

Reek and Detz and co-workers used the co-immobilisation of their organic PS and Ni-based CAT, to simplify synthetic routes compared with supramolecular systems. They reported that their system was inactive for photo-evolution of hydrogen and postulated the formation of aggregates of the complexes on the films, charge recombination or instability of the CAT.[81] Reisner and co-workers, in the same year (2016), used a

different approach of co-immobilisation/supra-assembly, with a Ni-based catalyst, on NiO mesoporous films. They employed a Ru tris-bipyridine derivative as the PS and used Zr^{4+} ions to link the phosphonate anchoring groups of the PS to the CAT in a layer by layer assembly.[39] This style of deposition maintains NiO-PS and PS-CAT interactions, but reduces CAT-NiO interactions, encouraging directional electron transfer. They found, that straight co-immobilisation was less preferential to the layer-by-layer approach, with an increase in stability and higher photocurrents seen for the latter. Unfortunately, only low levels of hydrogen were achieved. The group postulated this to be due to poor charge transfer dynamics within the system. Meyer and co-workers report the novel system design of a "donor-dye-catalyst", immobilised by layer-by-layer assembly on inverse opal, nanostructured indium tin oxide film.[82] Their system was also victim of the desorption and degradation of the catalyst under irradiation.

Hammarström and co-workers investigated co-immobilisation of coumarin 343 dye (a benchmark dye for DSC) and an iron hydrogenase biomimic. Hammarström, previously investigated, bio-inspired iron catalysts by transient absorption.[83] Upon moving to aqueous conditions, it was deemed necessary to change the anchoring group from a carboxylic acid to a phosphonate group, in an effort, for a more stable immobilisation, as desorption of the carboxy-anchor catalyst was prevalent.[84] They, also, lengthened the distance from the anchoring group to the catalyst, in an attempt, to extend charge recombination times, between the reduced CAT and NiO holes. The original shorter distance suggests there was fast recombination occurring and disabling electron hopping transfer mechanism, thus, preventing any significant photocurrent. Although transient absorption measurements, for both PS-CAT mixes, proved sufficient electron transfer between the PS and CAT, when the phosphonate CAT and PS mix were examined by photoelectrochemical experiments, a gradual decrease in photocurrent ensued. GC-MS and attenuated total reflection infrared (ATR-IR) studies proved the decomposition of CAT with the release of CO ligands, contributing to the decrease in photocurrent over time and, therefore, reduced photoelectro-evolution of hydrogen. The desorption of the CAT from NiO under irradiation remained an issue also contributing to a decrease in activity. Stability of the PS and CAT on the surface is still a major issue.

Wasielewski and co-workers, in 2017, applied atomic layered deposition (ALD) of alumina oxide, as a means of increasing stability of their PS, an organic dye, on the surface of a NiO electrode.[85] Although, TA time-resolved studies showed ALD of Al_2O_3 did improve the stability of the dye by decreasing degradation. This means aggregate formation of the dye molecule on the NiO surface is avoided and CR times are lengthened, therefore supporting hole injection. Although these are promising improvements, only a TON 1.5 of hydrogen were produced with their best system. They suggest implementing ALD of Al_2O_3, before immobilising the PS, as it creates a type of barrier situation, and reducing the likelihood of competitive process of charge recombination from the NiO and dye and increases hole collection. This behaviour was previously observed in 2013 by Wu and co-workers, as discussed above.[76]

1.11.4 Covalently bonded Supramolecular Assemblies

Artero and co-workers, in 2016, were the first to use a noble-metal free, covalently bonded supramolecular system immobilised on NiO to produce hydrogen.[86] Using an organic PS covalently bound to a cobaloxime unit. They utilised a coadsorbent, chenodeoxycholic acid (CDCA), to avoid compound aggregation on the NiO film. XPS was investigated for the system after hydrogen evolution experiments, as the Faradaic hydrogen yield was low, thought to be due to competing processes, including the formation of Ni^0 and change of ratio of Ni^{III} and Ni^{II} ions, although, PS-CAT degeneration was not ruled out. They stress the urgency to address these processes, as they may be the cause for low efficiency in many other systems. In 2017, Hammarström and Tian and co-workers investigated another supramolecule, similar to the complex Artero's group reported, in which the immobilised (on NiO electrode) organic PS was in situ covalently bonded to a cobaloxime-type CAT.[87] This system, also, generates miniscule amounts of hydrogen. They assumed that the extinction coefficient of the complex in solution is similar to that on NiO. In theory, the concentration of the dye present on the surface of the active area of the electrode, can be estimated, thus, the TON calculated. A TON of 0.05 was achieved, despite the system displaying suitable CT properties to photoelectrocatalytically produce hydrogen. They propose, that the second electron CT, to the CAT, has a lower driving force, leading to meagre CT of the second electron. They also suggested that, the low TON for hydrogen could be due to the inadequacy of a Co CAT component as a water

reduction catalyst (WRC) on the surface. Their final remarks are that creating new dyes and/or using alternative HER catalysts, more suitable for the charge transfer mechanism required, would in turn increase photocurrent ability, therefore, improving the H_2 evolution capability.

1.12 Time-resolved Spectroscopic Techniques used throughout this Thesis

Time-resolved spectroscopic techniques are used in every chapter of this thesis to monitor the electron pathways taken within the photocatalytic hydrogen generating systems investigated. These techniques can lead to the assignment of excited states and provide the kinetic dynamics of electron transfer within a system by examining the spectro-temporal evolution. The systematic alteration of the complex structure leads to a deeper understanding of these dynamics, which can galvanise the progression of synthetically optimised systems. A description of the techniques used is provided below, in this introductory chapter. Relevant literature examples of the techniques being applied can be found in the pertaining chapters, where the complexes prepared in this thesis are investigated using these techniques.

1.12.1 Transient Absorption Spectroscopy (TA)

Transient absorption spectroscopy (TA) is a well-recognised technique used to follow the evolution of the excited state species in the UV-Near IR region. TA is a pump-probe technique, this involves a pump pulse (laser pulse) exciting the sample from the ground state, the dynamics of this excitation are then probed by a secondary laser pulse at a set time-delay. The time-delays can be recorded over a wide timeframe depending on the system, from early (fs-ns) to late (ns-ms) timescale. The data collected generates a spectrotemporal map detailing the evolution and decay of the transients formed and the kinetic traces can be extracted from this map. This map shows the difference of the absorption of the sample, which appears with negative and positive absorption features, over time. The negative features, known as the ground state bleach (GSB), are attributed to the electronic absorbance of the ground state that is no longer present as it has been excited to higher energy by the initial laser pulse. Whereas the positive features are attributed to the excited state absorbance (ESA). TA is used in this thesis to investigate complexes in solution and immobilised to the surface of a p-type

semiconductor, NiO. Measurements were recorded across a wide time window and three different systems. The ULTRA system at the Central Laser Facility, Rutherford Appleton Laboratories in the U.K. boasts an ultrafast (<200 fs) time resolution TA spectrometer. The Huijser Research Group, Twente provided measurements on their early-time (ps) TA spectrometer. The Pryce Research Group has an Edinburgh Instruments Laser system, operating on the nanosecond to late (ms) timescale. These instruments differ in their setup but function essentially by the same pump-probe mechanism discussed previously.

1.12.2 Time-resolved Infrared Spectroscopy (TRIR)

Time-resolved infrared spectroscopy (TRIR) is a long-standing technique that monitors differences in the infrared region of a complex after excitation. TRIR fundamentally functions using the same principles as TA, with a pump-probe mechanism and follows the temporal evolution of the excited state species but probes the infrared for changes instead of the UV-NIR. Early-time TRIR is used in tandem with TA in this thesis on complexes in solution immobilised on the surface of NiO films. TRIR monitoring the mid-IR region, as carboxy groups on the dceb ligand absorb in this region, may add to the information gained through TA experiments. IR bands are sensitive to minor variations in their environment. It is then reasonable to postulate that further information can be acquired by probing the IR region for processes too sensitive to be featured in the UV-NIR region.

1.13 Scope of Thesis

Research into suitable molecular photocatalysts for sensitising p-semiconductors (p-SC) is pertinent to the progression of this area. This is an opportunity to move away from noble metals. The use of cheaper and more readily available materials lowers the overall costs and raises the economic viability of the technology. The design of PSs that absorb further out in the visible region, increases the exploitable energy, that is already available, (solar irradiance spectrum (Figure 1.3)). Employing intramolecular photocatalysts that can absorb photons and transfer the energy to a connected catalyst to produce H_2, on semiconductors, thereby rendering the use of sacrificial agents redundant. Theoretically, a tandem system or half reaction cell, becomes more

efficient adhering to an intramolecular approach and therefore more plausible to be utilised commercially. This is made possible by the systematic modification of the structure of the intramolecular photocatalyst, for optimal performance when immobilised on the surface of SCs, as the ratio of PS to catalyst is controlled.

A notable requirement for an efficient p-type dye-sensitised photocathode is down to the photocatalyst's dynamic processes. Ensuring the photocatalyst employed has a long-lived (μs) photoinduced charge-separated state that decelerates charge recombination between the reduced dye and the hole of the valence band of the NiO, allowing for sufficient time for catalysis to occur. Comprehending early-time dynamics of photocatalysts on the surface of electrodes is vital to the further development of these systems and key to improving efficiency.

In this thesis, PS/catalysts and photocatalysts were synthesised and assessed for their ability to generate hydrogen in solution and when immobilised on NiO electrodes. Complexes synthesised are based on known proficient photosensitisers and hydrogen evolving catalysts, i.e. ruthenium-polypyridyl-platinum/palladium system. Ultimately the aim is to immobilise the photocatalytic units on to p-semiconductor, and to broaden our understanding of the requirements for efficient p-DSCs and the cell's electron transport pathway using photoelectrochemical characterisation and time-resolved studies. As rare metals are utilised, the systems investigated are not commercially viable for large-scale development. They are, though, extremely useful for advancing our understanding of the integral aspects previously mentioned.

This chapter provides an overview into the literature surrounding photocatalysis of intramolecular complexes and the progression of our understanding of such systems made to date. Along with an insight into the relatively novel research of p-type dye sensitised photoelectrocatalysis and the challenges met in the development of intramolecular complexes for this photoelectro- approach. This chapter also included an introduction to the time resolved techniques used to investigate the complexes discussed in this thesis, e.g. time-resolved infrared (TRIR) and transient absorption (TA).

In chapter two, the effect of the experimental environment i.e. the parameters of the system, on photocatalytic hydrogen production using an intermolecular approach with a working photosensitiser, is investigated extensively. This study highlights the

difficulties of comparing/screening PS+Cat/photocatalysts systems under a single set of experimental parameters. This chapter also includes work recently published involving the development of novel inter- and intra-molecular complexes, based on diphenyl-phenanthroline peripheral ligands. These complexes are synthesised, characterised and their photocatalytic hydrogen generation abilities are studied. In addition, fs-transient absorption measurements were conducted by our collaborators in Twente and ns-TA was carried out in DCU to provide an understanding of electron transfer within the complexes over a broad timeframe.

While in chapter 3 the high TON achieving supramolecule, **3d** (discussed previously), along with a novel photocatalyst, utilising the dceb peripheral ligands, were synthesised, characterised and further investigated by time-resolved experiments, in the Rutherford Appleton Laboratory (RAL). The experiments were conducted both in solution and on the surface of a NiO film. Collaboration of the Gibson group, from Newcastle University, U.K., allowed for photoelectrocatalytic hydrogen evolution studies to be performed, including other photoelectrochemical characterisation techniques. This study also contributes to changing the perception of how we currently screen possible photocatalysts (in solution-based experiments). It is not the most efficient process to optimise systems under solution conditions if the end goal is to immobilise photocatalyst on the surface of a semiconductor.

Chapter 4 follows on from chapter 3, in that the dinuclear Ru-triazole-Pd hydrogen evolution photocatalyst is repurposed by the substitution of the Pd-catalyst for a Re-carbonyl catalyst in efforts to synthesise a CO_2 reduction photocatalyst. Chapter 4 also looks to moving away from the employment of rare metals in photosensitisers (ruthenium), and towards a more sustainable photocatalyst, e.g. porphyrins. Novel photocatalysts are synthesised and characterised and investigated by ns-TA and for their photocatalytic CO_2 reduction abilities.

Chapter 5 includes a brief literature review of boron dipyrromethene (BODIPY) based complexes, with a focus on time resolves techniques, and the ES generated. BODIPY-based complexes, including halogen-free- and diiodo-monomeric BODIPY complexes and their polymeric analogues, were investigated by both time-resolved IR and transient absorption. The results found the early-time electron transfer pathways taken within each class of complex were very different.

Chapter 6 contains concluding remarks and future work for each chapter and the overall research topic studied in this thesis.

References

[1] M. Howley, M. Holland, *Energy-in-Ireland-1990-2015*, **2016**.

[2] *United Nations Framework Convention on Climate Change*, **1992**.

[3] *United Nations Framework Convention on Climate Change, "Kyoto Protocol,"* **1997**.

[4] *United Nations Framework Convention on Climate Change, "Paris Agreement"*, **2016**.

[5] M. Howley, *Energy in Ireland 2018 Report*, **2018**.

[6] J. Burck, U. Hagen, F. Marten, N. Höhne, C. Bals, *Climate Change Performance Index (2019)*, Germanwatch, **2018**.

[7] R. K. Pachauri, A. Reisinger, *IPCC, 2007: Climate Change 2007: Synthesis Report. Contribution of Working Groups I, II and III to the Fourth Assessment Report of the Intergovernmental Panel on Climate Change*, **2007**.

[8] "Carbon dioxide concentration | NASA Global Climate Change," can be found under https://climate.nasa.gov/vital-signs/carbon-dioxide, **2018**.

[9] C. E. Boroneant, *Climate Change, Human Systems, and Policy Vol.I Anthropogenic Climate Influences*, EOLSS, **2009**.

[10] T. P. Hughes, A. H. Baird, D. R. Bellwood, M. Card, S. R. Connolly, C. Folke, R. Grosberg, O. Hoegh-Guldberg, J. B. C. Jackson, J. Kleypas, et al., *Science* **2003**, *301*, 929–933.

[11] S. C. B. Raper, R. J. Braithwaite, *Nature* **2006**, *439*, 311–313.

[12] *Petroleum and Other Minerals Development (Prohibition of Onshore Hydraulic Fracturing) Act*, **2017**.

[13] *Fossil Fuel Divestment Bill*, **2016**.

[14] National Research Council, National Academy of Engineering, *The Hydrogen Economy: Opportunities, Costs, Barriers, and R&D Needs*, The National Academies Press, **2004**.

[15] Northern Gas Networks, *H21 Executive Summary*, **2016**.

[16] W.-Y. Wong, *J. Organomet. Chem.* **2009**, *694*, 2644–2647.

[17] H. Zhou, Y. Qu, T. Zeid, X. Duan, *Energy Environ. Sci.* **2012**, *5*, 6732–6743.

[18] C. A. Gueymard, *Sol. Energy* **2004**, *76*, 423–453.

[19] I. Chorkendorff, J. W. Niemantsverdriet, *Concepts of Modern Catalysis and Kinetics*, Wiley-VCH, Weinheim, **2007**.

[20] Y. Halpin, M. T. Pryce, S. Rau, D. Dini, J. G. Vos, *Dalton Trans.* **2013**, *42*, 16243–16254.

[21] T. Kowacs, Q. Pan, P. Lang, L. O'Reilly, S. Rau, W. R. Browne, M. T. Pryce, A. Huijser, J. G. Vos, *Faraday Discuss.* **2015**, *185*, 143–170.

[22] K. Ladomenou, T. N. Kitsopoulos, G. D. Sharma, A. G. Coutsolelos, *RSC Adv.* **2014**, *4*, 21379–21404.

[23] V. Balzani, F. Scandola, *Supramolecular Photochemistry*, Ellis Horwood, **1991**.

[24] M. Kasha, *Discuss. Faraday Soc.* **1950**, *9*, 14–19.

[25] T. Förster, *Ann. Phys.* **1948**, *437*, 55–75.

[26] D. L. Dexter, *J. Chem. Phys.* **1953**, *21*, 836–850.

[27] C. Jiang, S. J. A. Moniz, A. Wang, T. Zhang, J. Tang, *Chem. Soc. Rev.* **2017**, *46*, 4645–4660.

[28] T. Hisatomi, J. Kubota, K. Domen, *Chem. Soc. Rev.* **2014**, *43*, 7520–7535.

[29] A. Fujishima, K. Honda, S. Kikuchi, *J. Soc. Chem. Ind. Jpn.* **1969**, *72*, 108–113.

[30] A. Fujishima, K. Honda, *Nature* **1972**, *238*, 37–38.

[31] F. P. Koffyberg, F. A. Benko, *J. Electrochem. Soc.* **1981**, *128*, 2476–2479.

[32] B. O'Regan, M. Grätzel, *Nature* **1991**, *353*, 737–740.

[33] C. J. Wood, G. H. Summers, C. A. Clark, N. Kaeffer, M. Braeutigam, L. Roberta Carbone, L. D'Amario, K. Fan, Y. Farré, S. Narbey, et al., *Phys. Chem. Chem. Phys.* **2016**, *18*, 10727–10738.

[34] K. Fan, F. Li, L. Wang, Q. Daniel, E. Gabrielsson, L. Sun, *Phys. Chem. Chem. Phys.* **2014**, *16*, 25234–25240.

[35] F. Li, K. Fan, B. Xu, E. Gabrielsson, Q. Daniel, L. Li, L. Sun, *J. Am. Chem. Soc.* **2015**, *137*, 9153–9159.

[36] J. M. Lehn, J. P. Sauvage, *Nouv J Chem* **1977**, *1*, 449–450.

[37] Y.-J. Tu, S. Mazumder, J. F. Endicott, C. Turro, J. J. Kodanko, H. B. Schlegel, *Inorg. Chem.* **2015**, *54*, 8003–8011.

[38] M. Orlandi, R. Argazzi, A. Sartorel, M. Carraro, G. Scorrano, M. Bonchio, F. Scandola, *Chem. Commun.* **2010**, *46*, 3152–3154.

[39] M. A. Gross, C. E. Creissen, K. L. Orchard, E. Reisner, *Chem. Sci.* **2016**, *7*, 5537–5546.

[40] G. S. Bindra, M. Schulz, A. Paul, R. Groarke, S. Soman, J. L. Inglis, W. R. Browne, M. G. Pfeffer, S. Rau, B. J. MacLean, et al., *Dalton Trans.* **2012**, *41*, 13050–13059.

[41] M. Schulz, M. Karnahl, M. Schwalbe, J. G. Vos, *Coord. Chem. Rev.* **2012**, *256*, 1682–1705.

[42] H. Ozawa, M. Haga, K. Sakai, *J. Am. Chem. Soc.* **2006**, *128*, 4926–4927.

[43] C. V. Suneesh, B. Balan, H. Ozawa, Y. Nakamura, T. Katayama, M. Muramatsu, Y. Nagasawa, H. Miyasaka, K. Sakai, *Phys. Chem. Chem. Phys.* **2013**, *16*, 1607–1616.

[44] H. Ozawa, Y. Yokoyama, M. Haga, K. Sakai, *Dalton Trans.* **2007**, *0*, 1197–1206.

[45] Y. Yamada, K. Sakai, T. Tsubomura, **1993**.

[46] K. Sakai, H. Ozawa, *Coord. Chem. Rev.* **2007**, *251*, 2753–2766.

[47] S. Rau, B. Schäfer, D. Gleich, E. Anders, M. Rudolph, M. Friedrich, H. Görls, W. Henry, J. G. Vos, *Angew. Chem. Int. Ed.* **2006**, *45*, 6215–6218.

[48] S. Tschierlei, M. Karnahl, M. Presselt, B. Dietzek, J. Guthmuller, L. González, M. Schmitt, S. Rau, J. Popp, *Angew. Chem. Int. Ed.* **2010**, *49*, 3981–3984.

[49] M. Karnahl, C. Kuhnt, F. Ma, A. Yartsev, M. Schmitt, B. Dietzek, S. Rau, J. Popp, *ChemPhysChem* **2011**, *12*, 2101–2109.

[50] P. Lei, M. Hedlund, R. Lomoth, H. Rensmo, O. Johansson, L. Hammarström, *J. Am. Chem. Soc.* **2008**, *130*, 26–27.

[51] M. G. Pfeffer, B. Schäfer, G. Smolentsev, J. Uhlig, E. Nazarenko, J. Guthmuller, C. Kuhnt, M. Wächtler, B. Dietzek, V. Sundström, et al., *Angew. Chem. Int. Ed.* **2015**, *54*, 5044–5048.

[52] W. Paw, W. B. Connick, R. Eisenberg, *Inorg. Chem.* **1998**, *37*, 3919–3926.

[53] T. A. White, J. D. Knoll, S. M. Arachchige, K. J. Brewer, *Materials* **2011**, *5*, 27–46.

[54] T. A. White, S. L. H. Higgins, S. M. Arachchige, K. J. Brewer, *Angew. Chem. Int. Ed.* **2011**, *50*, 12209–12213.

[55] M. G. Pfeffer, T. Kowacs, M. Wächtler, J. Guthmuller, B. Dietzek, J. G. Vos, S. Rau, *Angew. Chem. Int. Ed.* **2015**, *54*, 6627–6631.

[56] G. S. Bindra, M. Schulz, A. Paul, S. Soman, R. Groarke, J. Inglis, M. T. Pryce, W. R. Browne, S. Rau, B. J. Maclean, et al., *Dalton Trans.* **2011**, *40*, 10812–10814.

[57] M. Braumüller, M. Schulz, D. Sorsche, M. Pfeffer, M. Schaub, J. Popp, B.-W. Park, A. Hagfeldt, B. Dietzek, S. Rau, *Dalton Trans.* **2015**, *44*, 5577–5586.

[58] Y. Pellegrin, L. Le Pleux, E. Blart, A. Renaud, B. Chavillon, N. Szuwarski, M. Boujtita, L. Cario, S. Jobic, D. Jacquemin, et al., *J. Photochem. Photobiol. Chem.* **2011**, *219*, 235–242.

[59] T. Kowacs, L. O'Reilly, Q. Pan, A. Huijser, P. Lang, S. Rau, W. R. Browne, M. T. Pryce, J. G. Vos, *Inorg. Chem.* **2016**, *55*, 2685–2690.

[60] Q. Pan, L. Freitag, T. Kowacs, J. C. Falgenhauer, J. P. Korterik, D. Schlettwein, W. R. Browne, M. T. Pryce, S. Rau, L. González, et al., *Chem. Commun.* **2016**, *52*, 9371–9374.

[61] N. Das, G. S. Bindra, A. Paul, J. G. Vos, M. Schulz, M. T. Pryce, *Chem. – Eur. J.* **2017**, *23*, 5330–5337.

[62] S. Soman, G. S. Bindra, A. Paul, R. Groarke, J. C. Manton, F. M. Connaughton, M. Schulz, D. Dini, C. Long, M. T. Pryce, et al., *Dalton Trans.* **2012**, *41*, 12678–12680.

[63] J. C. Manton, C. Long, J. G. Vos, M. T. Pryce, *Dalton Trans.* **2014**, *43*, 3576–3583.

[64] D. R. Whang, S. Y. Park, *ChemSusChem* **2015**, *8*, 3204–3207.

[65] D. Kim, D. R. Whang, S. Y. Park, *J. Am. Chem. Soc.* **2016**, *138*, 8698–8701.

[66] Z.-T. Yu, Y.-J. Yuan, X. Chen, J.-G. Cai, Z.-G. Zou, *Chem. – Eur. J.* **2015**, *21*, 10003–10007.

[67] A. Fihri, V. Artero, M. Razavet, C. Baffert, W. Leibl, M. Fontecave, *Angew. Chem.* **2008**, *120*, 574–577.

[68] A. Fihri, V. Artero, A. Pereira, M. Fontecave, *Dalton Trans.* **2008**, *0*, 5567–5569.

[69] C. Li, M. Wang, J. Pan, P. Zhang, R. Zhang, L. Sun, *J. Organomet. Chem.* **2009**, *694*, 2814–2819.

[70] P. Zhang, M. Wang, C. Li, X. Li, J. Dong, L. Sun, *Chem. Commun.* **2010**, *46*, 8806–8808.

[71] L.-C. Song, L.-X. Wang, M.-Y. Tang, C.-G. Li, H.-B. Song, Q.-M. Hu, *Organometallics* **2009**, *28*, 3834–3841.

[72] P. Qin, H. Zhu, T. Edvinsson, G. Boschloo, A. Hagfeldt, L. Sun, *J. Am. Chem. Soc.* **2008**, *130*, 8570–8571.

[73] P. Qin, M. Linder, T. Brinck, G. Boschloo, A. Hagfeldt, L. Sun, *Adv. Mater.* **2009**, *21*, 2993–2996.

[74] P. Qin, J. Wiberg, E. A. Gibson, M. Linder, L. Li, T. Brinck, A. Hagfeldt, B. Albinsson, L. Sun, *J. Phys. Chem. C* **2010**, *114*, 4738–4748.

[75] L. Li, L. Duan, F. Wen, C. Li, M. Wang, A. Hagfeldt, L. Sun, *Chem. Commun.* **2012**, *48*, 988–990.

[76] Z. Ji, M. He, Z. Huang, U. Ozkan, Y. Wu, *J. Am. Chem. Soc.* **2013**, *135*, 11696–11699.

[77] Z. Ji, G. Natu, Z. Huang, O. Kokhan, X. Zhang, Y. Wu, *J. Phys. Chem. C* **2012**, *116*, 16854–16863.

[78] C. E. Castillo, M. Gennari, T. Stoll, J. Fortage, A. Deronzier, M.-N. Collomb, M. Sandroni, F. Légalité, E. Blart, Y. Pellegrin, et al., *J. Phys. Chem. C* **2015**, *119*, 5806–5818.

[79] T. O. Rouse, J. L. Weininger, *J. Electrochem. Soc.* **1966**, *113*, 184–190.

[80] K. A. Click, D. R. Beauchamp, Z. Huang, W. Chen, Y. Wu, *J. Am. Chem. Soc.* **2016**, *138*, 1174–1179.

[81] B. van den Bosch, J. A. Rombouts, R. V. A. Orru, J. N. H. Reek, R. J. Detz, *ChemCatChem* **2016**, *8*, 1392–1398.

[82] B. Shan, A. K. Das, S. Marquard, B. H. Farnum, D. Wang, R. M. Bullock, T. J. Meyer, *Energy Environ. Sci.* **2016**, *9*, 3693–3697.

[83] A. M. Brown, L. J. Antila, M. Mirmohades, S. Pullen, S. Ott, L. Hammarström, *J. Am. Chem. Soc.* **2016**, *138*, 8060–8063.

[84] L. J. Antila, P. Ghamgosar, S. Maji, H. Tian, S. Ott, L. Hammarström, *ACS Energy Lett.* **2016**, *1*, 1106–1111.

[85] R. J. Kamire, M. B. Majewski, W. L. Hoffeditz, B. T. Phelan, O. K. Farha, J. T. Hupp, M. R. Wasielewski, *Chem. Sci.* **2017**, *8*, 541–549.

[86] N. Kaeffer, J. Massin, C. Lebrun, O. Renault, M. Chavarot-Kerlidou, V. Artero, *J. Am. Chem. Soc.* **2016**, *138*, 12308–12311.

[87] P. B. Pati, L. Zhang, B. Philippe, R. Fernández-Terán, S. Ahmadi, L. Tian, H. Rensmo, L. Hammarström, H. Tian, *ChemSusChem* **2017**, *10*, 2480–2495.

Chapter 2

2 Intermolecular to Intramolecular Photocatalytic Systems

Chapter 2 provides a detailed intermolecular hydrogen generation study using a known Ru diphenylphenanthroline (dpph) complex, $[Ru(dpph)_3](PF_6)_2$, as the photosensitiser (PS). This PS was irradiated under various reaction conditions, by altering the solvent, catalyst, sacrificial agent, varying the water content and ratios of the photosensitiser to catalyst (Cat), systematically. Substitution of one of the of diphenylphenanthroline ligands for a suitable bridging ligand (BL), in this case terpyridine (terpy) led to the isolation of $[Ru(dpph)_2(BL)]$, and the subsequent intramolecular photocatalyst ($[Ru(dpph)_2(2,5\text{-bpp})PtI_2]$). The complexes were investigated for their inter/intra-molecular hydrogen production capabilities. A closer look at electron transfer within these new systems was carried out with collaborators in University of Twente, Netherlands. These studies included both early and late timescales. We investigated the ns to μs timescale, and our collaborators focused on the fs to ps timescale.

Hydrogen-Generating Ru/Pt Bimetallic Photocatalysts Based on Phenyl-Phenanthroline Peripheral Ligands
Laura O'Reilly, Qing Pan, Nivedita Das, Kasper Wenderich, Jeroen P. Korterik, Johannes G. Vos, Mary T. Pryce, Annemarie Huijser
ChemPhysChem, **2018**, 19, 3084-3091

2.1 Aim

As no standard reporting method exists for photocatalytic hydrogen generation, one of the objectives of this chapter, was to analyse the effect of different experimental parameters on the amount of hydrogen detected. The parameter that were varied included; .solvent medium, sacrificial agent, percentage of water added, catalyst, ratios of PS to CAT, and irradiation source. This investigation was performed to emphasise how subtle changes can dramatically influence the amount of hydrogen generated, therefore highlighting the difficulty in directly comparing systems in the literature. Generally, when photocatalysts are screened for their ability to generate hydrogen, either the turnover number (TON), turnover frequency (TOF) or volume of hydrogen is reported. The latter part and main aim of this chapter was to synthesise a novel intramolecular photocatalyst and then investigate its hydrogen evolution capabilities, and using time resolved studies the photodynamic processes spanning the early (fs–ps) to late (ns–μs) timescales were probed.

2.2 Introduction

2.2.1 Intermolecular studies using $[Ru(bpy)_3]^{2+}$ complexes as a photosensitiser

Chapter 1 gave an overview of photocatalytic supramolecular hydrogen generating systems, which focused predominantly on Ru-Pt/Pd supramolecular systems. These assemblies have stemmed from intermolecular studies, in the hope to improve catalytic activity and eliminate the drawbacks associated with an intermolecular approach, such as the reduced efficiency because of diffusion limitations and the stability of each of the components. Ruthenium polypyridyl complexes have been hugely successful in generating hydrogen from water by both inter- and intramolecular approaches. In this thesis the supramolecular system is always compared to the intermolecular technique, to ensure there is an improvement in the catalytic activity.

$[Ru(bpy)_3]^{2+}$ (where the counter ion is Cl_2 or $(PF_6)_2$) has been extensively investigated as a photosensitiser, for photocatalytic intermolecular hydrogen generation, under many different conditions. In 1977, Lehn et al. used the photosensitiser in combination with colloidal Pt and triethanolamine (TEOA) as the catalyst and sacrificial agent, respectively and reported quantifiable levels of hydrogen production.[1] The table below summarises the most common experimental conditions reported from 1977 to present, using $[Ru(bpy)_3]^{2+}$ as the PS. In these examples, varying amounts of hydrogen were reported. Direct comparison is difficult among these experiments, as they were performed by a range of research groups, using different setups and experimental conditions, and furthermore the hydrogen generated was reported in different ways (quantum yield, TON, TOF or the volume of hydrogen). However, these studies emphasise the influence of the experimental setup on the hydrogen production ability of a working photosensitiser.

Table 2.1: Hydrogen evolution experiments using $[Ru(bpy)_3]^{2+}$ as photosensitiser in aqueous solution

Catalyst	Sacrificial Agent	Electron Donor	Solvent	Hydrogen Reported	Ref.
Colloidal Pt	TEOA	$[Rh(bpy)_3]^{3+}$	Aq. Soln	22.4 ml/32 h	[1]
Colloidal Pt	TEOA	MV^{2+}	Aq. Soln	0.4 ml/0.5 h	[2]
Colloidal Pt	EDTA	MV^{2+}	Aq. Soln	12 L/24 h	[3]
Co(II) $(Me_6[14]dieneN_4)(H_2O)_2^{2+}$	Ascorbic acid	-	Aq. Soln	ϕH_2 1×10^{-5} *h*	[4]
RuO_2	Ascorbic acid	MV^{2+}-EDTA	Aq. Soln	1 mmol/2 h	[5]
$PdH(Pet_3)_3$	Ascorbic acid	-	Aq. Soln	1 ml/9 h	[6]
2Fe2S[a]	Ascorbic acid	-	CH_3CN/ H_2O	4.3 TON /3 h	[7]
$[Fe_2(\mu\text{-}Cl_2bdt)(CO)_6]$[b]	Ascorbic acid	-	DMF/ H_2O	200 TON (4 μmol) /2.5 h	[8]
$[Co(mnt)]_2$[c]	Ascorbic acid	-	CH_3CN/ H_2O	9000 TON (~2.4 ml) /12 h	[9]
$[(CF_3PY5Me_2)Co(H_2O)](CF_3SO_3)_2$[d]	Ascorbic acid	-	Phosphate buffer pH 7	0.6 ml/2 h	[10]
$[Co(CR)Cl_2]^+$[e]	NaHA and Ascorbic acid	-	H_2O	1002 TON (12.27 ml) /21 h	[11]
$[Co(L1)](PF_6)_2$[f]	Ascorbic acid	-	Acetate buffer	16300 TON /2 h	[12]
$[Co(dmgH)_2(DMAP)Cl]$[g]	TEOA	-	DMF/ HBF_4	2600 TON /20 h	[13]

a: [{(μ-$SCH_2)_2NCH_2C_6H$}{$Fe(CO)_3$} {$Fe(CO)_2P(Pyr)_3$}]
b: Cl_2bdt=3,6-dichlorobenzene-1,2-dithiolate
c: mnt = maleonitriledithiolate
d: PY5Me2 = 2,6-bis(1,1-di(pyridin-2-yl)ethyl)pyridine)
e: CR = 2,12-dimethyl-3,7,11,17-tetra-azabicyclo(11.3.1)-heptadeca-1(17),2,11,13,15-pentaene
f: N,N-bis-(6-(2,2'-bipyridyl)methyl-N-2-(methyl)pyridine)
g: DMAP=4-dimethylaminopyridine; dmgH=dimethylglyoxime
h: φH_2 = quantum yield of hydrogen production. In simplified terms, φ is the ratio of number of photons emitted to number of photons absorbed.

It is important to note that, although direct comparison of photocatalytic systems (even when using similar parameters) in various laboratories globally is difficult, there has been significant progress in this area of research in terms of identifying the optimal PS and catalytic unit. Ideally there should be a set of principles/standards to aide in the progression of photocatalytic systems, however there is no one standard reporting method. Furthermore, there has been a shift in recent years towards investigating the effect of structural changes on electron pathways (with the aid of time resolved

studies) and the corresponding effect on TONs. This can lead to novel design approaches, that may contradict previous design strategies.[14] To devise a standard reporting procedure is difficult, as a vast number of parameters can be varied in each experimental setup, which contributes to the overall performance of the system, and frequently, optimisation of the setup is unique to each photocatalyst assembly. In this chapter, the mononuclear Ru tris-dpph complex (dpph = 4,7-diphenyl-1,10-phenanthroline), was investigated as a PS for hydrogen generation, due to the long-lived lifetime created by this ruthenium complex. By altering a range of parameters within the experimental setup, such as, the catalyst, solvent, sacrificial agent, water content, PS:Cat ratio and headspace volume, it is clear that each parameter contributes to the overall performance of the system (determined by TON in this case). Following systematic variation, the TON for photocatalytic hydrogen production under the different experimental conditions are given in Table 2.2. These studies were performed not to create a standard or set of principles, but merely to highlight the difference in the amount of hydrogen produced with subtle variations in the experiment, and the difficulty in comparing systems directly when developing new photosensitisers. There are also questions raised about screening methods conducted to determine the progression of a photocatalyst from a homogeneous to a heterogeneous environment.

2.2.2 Intermolecular to Intramolecular approach

As discussed, in detail, in Chapter 1, the move from inter- to intra-approaches to photocatalytic hydrogen generation is underway and is necessary for technology development and scale up. A vast amount has been learned about intra-molecular systems, with a focus on ruthenium-platinum/palladium assemblies.

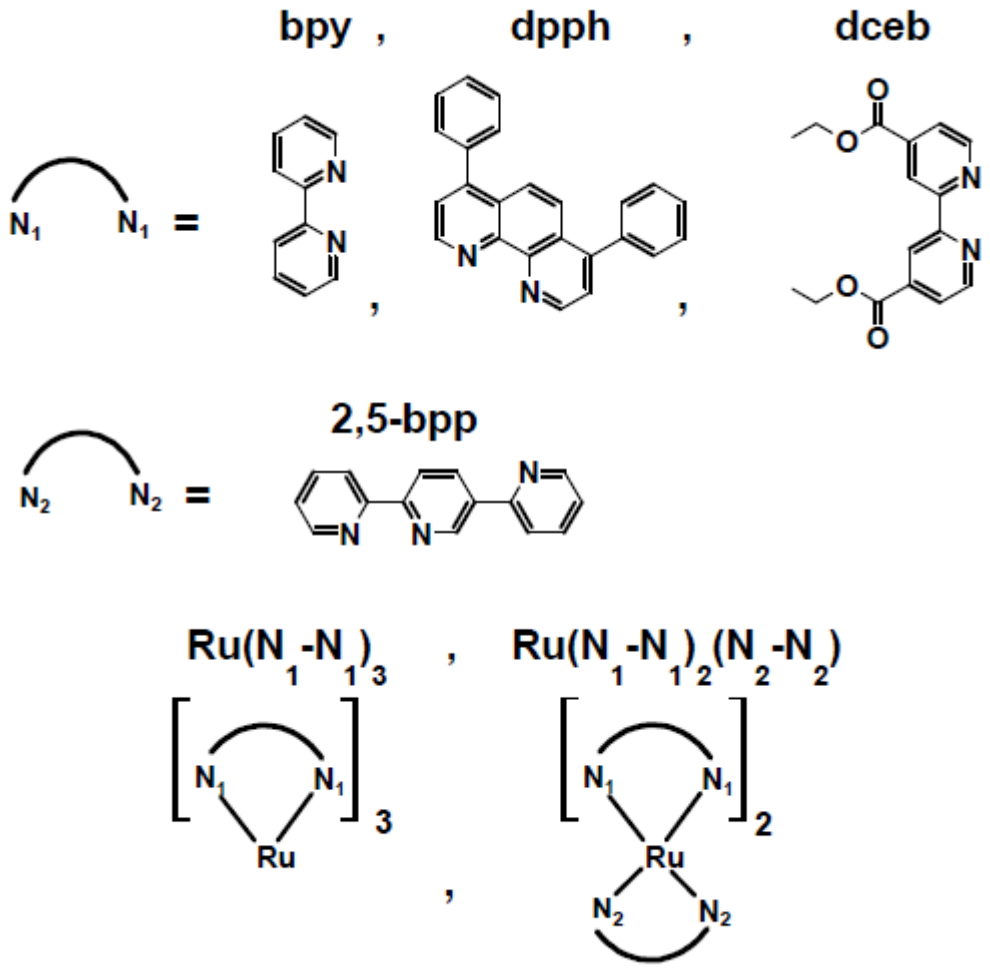

Figure 2.1: Structures of some intermolecular complexes used as precursors to bimetallic supraspecies discussed and/or investigated in this chapter; [Ru(bpy)$_3$]; [Ru(dpph)$_3$]; [Ru(dceb)$_3$]; [Ru(bpy)$_2$(2,5-bpp)]; [Ru(dpph)$_2$(2,5-bpp)]; [Ru(dceb)$_2$(2,5-bpp)] (bpy = 2,2'-bipyridine; dpph = 4,7-diphenyl-1,10-phenanthroline; dceb = 4,4'-di(carboxyethyl)bipyridine; and 2,5-bpp = 2,2',5',2''-terpyridine). All with PF_6 as the counter ion, unless otherwise stated.

Investigations, by the DCU group, with collaborators in Austria, The Netherlands and Germany, have suggested that efficient electron flow within a photocatalyst does not necessarily translate to directional flow of electrons from the photosensitising moiety towards the bridging unit and then to the catalyst.[14] However, this had been the general way of thinking for many years and it dictated photocatalyst design to fit this narrative.[15] The photocatalyst, discussed briefly in Chapter 1, **Ru(dceb)$_2$(2,5-bpp)PtIX** (4,4′-di(carboxyethyl)bipyridine; dceb), together with its precursor, have carboxy-ester groups on the peripheral bpy ligands, which have an electron withdrawing effect on the complex. The addition of these functional groups leads to an increase in TON compared to the bipyridine counterpart. Early-time transient absorption investigations, conducted by our collaborators in Twente, enabled us to determine that this photocatalytic species does not follow the same trend as that previously assumed, (electron transfer directly from the PS unit to the catalytic centre), but instead following excitation the electron resides on the peripheral carboxy units, which act as "an electron reservoir". The electron then moves towards the catalytic unit, where hydrogen is expected to be generated from water. These studies, led to the thinking, that an increase in the electron withdrawing properties of the peripheral unit may, in turn, lead to an increase in lifetime and thus, TON. Therefore, the dceb peripheral ligand was substituted for 4,7'-diphenyl-1,10'-phenanthroline ligand (dpph) and its ability to produce hydrogen photocatalytically was investigated using, both inter- (in Figure 2.1) and intra-approaches (Figure 2.2).

2.2.3 Transient absorption spectroscopy

In chapter 1 transient absorption spectroscopy (TAS) was discussed and the information that can be gained from the technique. This chapter recaps some of the relevant aspects, for the ease of the reader.

Transient absorption (TA) spectroscopy is a hugely important technique in this area of research. Ultrafast TA allows for the determination of the electron pathways within a complex by monitoring the spectral changes following excitation. The timescale for experiments can range between the sub-picosecond to the microsecond, after the laser pulse. In this chapter, both the very early times (fs-ps) and later times (ns-μs) are investigated for $[Ru(dpph)_2(2,5\text{-}bpp)](PF_6)_2$ (depicted above) and the corresponding RuPt intramolecular complex (below).

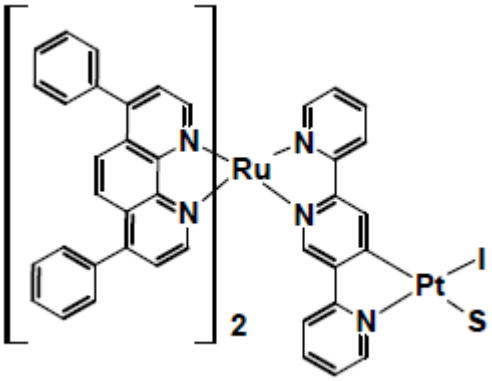

Figure 2.2:Structure of novel $RuPt(PF_6)_2$ dinuclear photocatalyst. S = solvent.

In 1997, McCusker and co-workers investigated the excited state properties of $[Ru(bpy)_3]^{2+}$ by fs-TA.[16] They reported the evolution of the Franck-Condon state, a singlet metal-to-ligand-charge-transfer (^{1}MLCT) state, to the ^{3}MLCT (triplet MLCT) of the Ru-complex occurred within ~300 fs. The fs-TA highlighted that after the population of the Franck-Condon state no intermediate states were defined till the final triplet state. Using ns-TA, McCusker and co-workers monitored the spectrotemporal progress of the ground state bleach (GSB), from the initial ^{1}MLCT state to the final ^{3}MLCT state, to confirm the spectral features recorded at early time points (>300 fs) were of triplet character. As the GSB remained in the same position and maintained its shape after 300 fs and up into the ns timescale, they were able to conclude the

^{3}MLCT was formed (via inter-system crossing (ISC) from or near the initial Franck-Condon state. The ^{3}MLCT evolution was concurrent with vibrational relaxation (VR) and solvent reorganisation (known to occur over ~100 fs timeframe). These ultrafast photodynamic processes highlighted the importance of early time investigations for developing efficient photocatalysts. Their study, among other ultrafast electron transfer dynamic studies (injection of an electron into a DSSC)[17] casted doubt on the common practice of disregarding of higher level excited states, as it was thought the energy would relax to the lowest energy excited state and ISC would occur from the lowest energy excited state. Studies like theirs proved that other pathways could be manipulated on these early timeframes, leading to possibly more efficient use of absorbed photons. Thus, limiting these early-time electron relaxation pathways would contribute to an increased quantum yield.

The DCU group together with collaborators (Huijser et al.), have probed the photophysical processes, at early time bases following photoexcitation, using transient absorption spectroscopy, for the mononuclear species; $[Ru(bpy)_2(2,5\text{-bpp})]$ (Ru_{bpy}) and $[Ru(dceb)_2(2,5\text{-bpp})]$ (Ru_{dceb}), and the dinuclear species; $[Ru(bpy)_2(2,5\text{-bpp})PdClS]$ ($RuPd_{bpy}$), $[Ru(bpy)_2(2,5\text{-bpp})PtIS]$ ($RuPt_{bpy}$) and $[Ru(dceb)_2(2,5\text{-bpp})PtIS]$ ($RuPt_{dceb}$) where S = solvent; all complexes have $(PF_6)_2$ acting as the counter ion.[14,18,19] These complexes were discussed in chapter 1, and will be further discussed in this chapter in the context of the TA results reported. In the TA spectra for all complexes, in Figure 2.3, the negative bands are the ground state bleaches (GSB), whereas, the positive bands are excited state absorbances (ESA) of the photoexcited species generated following excitation with the laser pulse.

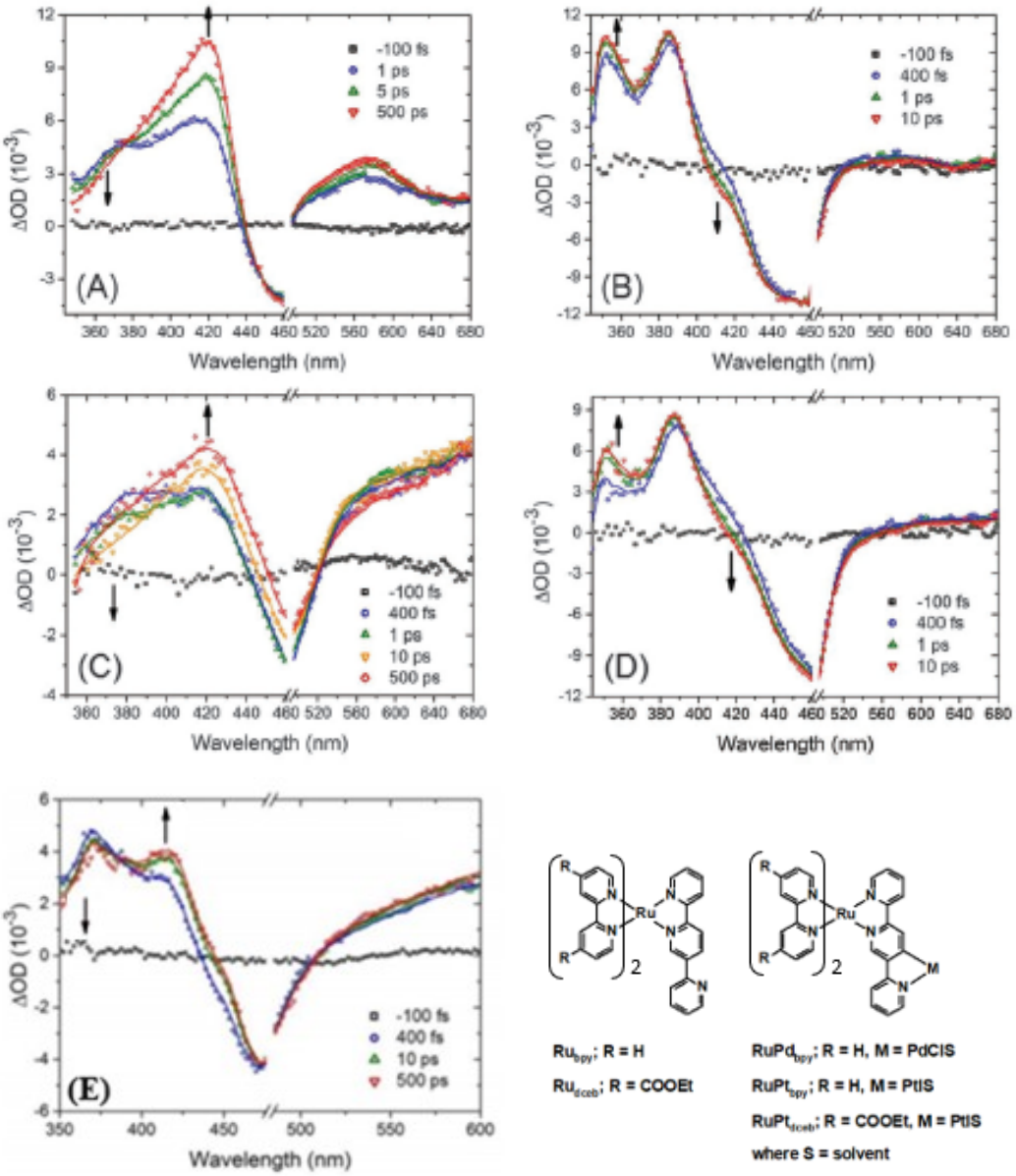

Figure 2.3: TA spectra of Ru_{bpy} (A) and Ru_{dceb} (B) monomers and $RuPt_{bpy}$ (C), $RuPt_{dceb}$ (D) and $RuPd_{bpy}$ (E) in acetonitrile, excited at 480 nm and the coresponding structures of the complexes investigated.[14,18,19]

The spectral profile for the ESA features in the TA spectra, for complexes **A, C** and **E** (see Figure 2.3): appear similar for the range of Ru_{bpy} complexes studied. The ESA at ~370 nm is related to the reduced bpy anion, bpy^{-} and the ESA at ~420 nm is assigned to the reduced terpyridine anion, 2,5-bpp^{-}. Both ESA features are considered intraligand transitions (ligand centred (LC), π-π*). The broad ESA >500 nm is attributed to the transitions of triplet ligand-to-metal charge transfer (^{3}LMCT) of the formally oxidised Ru(II) from the bridging ligand (BL, 2,5-bpp). The addition of Pd

(Figure 2.3: **E**) causes a redshift in this broad ESA, most likely due to the influence of Pd on this ^{3}LMCT transition. The investigation of the decay kinetics of ESA and GSB features (the negative features recorded ~450-500 nm), for $RuPd_{bpy}$, suggests that directional electron transfer from the $^3MLCT_{bpy}$→$^3MLCT_{2,5\text{-}bpp}$→catalytic centre occurs after the initial population of ^{1}MLCT (singlet metal-to-ligand charge transfer) of both bpy and 2,5-bpp ligands followed by ultrafast (~100 fs) intersystem crossing (ISC) to the ^{3}MLCT, leading to vectorial electron flow, depicted in Figure 2.4. Also note, vibrational cooling of the bpy is a competing process with interligand transfer from bpy to 2,5-bpp.

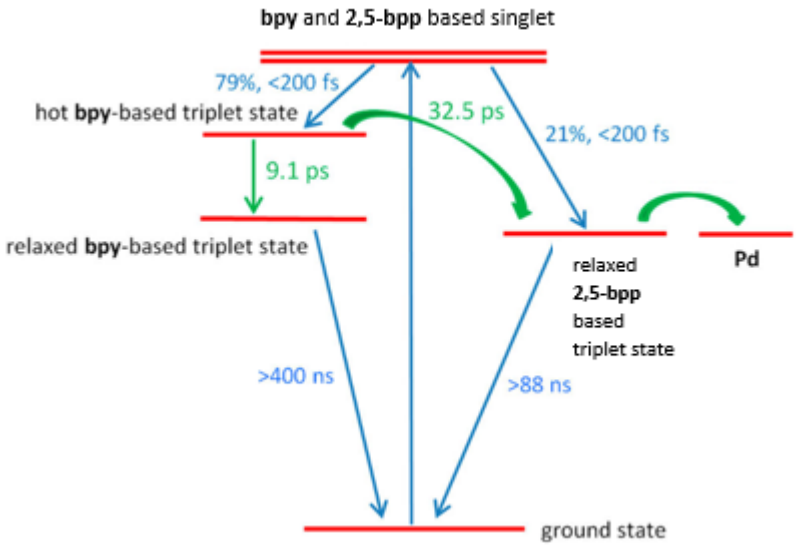

Figure 2.4: Scheme of electron transfer in $RuPd_{bpy}$[18]

Substitution of Pd by Pt at the catalytic centre (Figure 2.3: **C**), leads to further intricacy of the photodynamics. The reduced absorbance of the ESA features at <430 nm, attributed to the bpy and 2,5-bpp reduced anions, are assigned to a third triplet excited state, denoted as T_3 by Huijser et al.[18] This third excited state appears to quench the population of the surrounding ^{3}MLCT excited states as the absorbance intensity is lower at wavelengths < 430 nm, but a higher amplitude is observed for signals recorded at wavelengths greater than 530 nm. They speculated that the electron flow at this point, depicted in Figure 2.5, is a result of redistribution of the charge involving the T_3 state and the 2,5-bpp-Pt-I moiety. When $RuPt_{bpy}$ is excited at higher wavelengths, this T_3 state is more readily populated, hence the bpy and 2,5-bpp

^{3}MLCT are only slightly populated as their corresponding ESA signals are significantly reduced.[20]

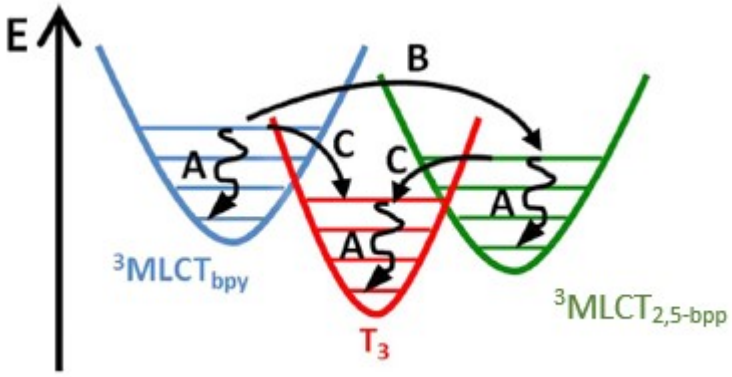

Figure 2.5: Scheme of electron pathway for $RuPt_{bpy}$ with a new T_3 state present after the addition of Pt. A = vibrational cooling (VC); B = ILCT (inter ligand charge transfer); C = charge transfer to the delocalised T_3 state [19]

Following the introduction of the ester functional groups to the terminal bpy ligands (dceb) the TA spectra recorded are altered significantly (in terms of the profile and kinetics of the TA spectra obtained),when compared to Ru_{bpy}, as seen in Figure 2.3(**B** and **D**). The ESA at 350 nm and the less intense ESA at 420 nm was assigned to the reduced dceb ligand and bridging, 2,5-bpp anion, respectively. An additional feature is present at 385 nm and was assigned to a $^3MLCT_{dceb}$. Due to the overlapping of the ESA features at 350 nm and 420 nm with 385 nm, the kinetics do not follow suit at 385 nm with that at 350 nm or 420 nm. In contrast to the bpy analogues, the addition of the ester groups on the dceb ligand leads to a reverse in the initial direction of the electron flow. Within 1 ps of excitation, the TA spectra display what is interpreted as $^3MLCT_{2,5\text{-bpp}} \rightarrow {}^3MLCT_{dceb}$ internal conversion (IC), illustrated in the amplitude of the ESA band at ~350 nm increasing alongside the decreasing intensity of the ESA ~420 nm. This bridge to peripheral ligand transfer is ultrafast, occurring on the sub-ps timescale. The addition of the Pt maintains this altered flow of electrons. The lack of kinetic interference has been seen previously for the equivalent bpy supramolecular assemblies, discussed above, when the catalytic centre is covalently bound to the mononuclear precursor. In Figure 2.6, the simplified, concluding scheme of electron transfer in $RuPt_{dceb}$ is represented. This gives an understanding to the increased TON achieved for the photocatalyst employing the dceb ligand, as the electron pathways differ vastly to the bpy analogues. A study from Dietzek et al. found that upon

mimicking the second reduction process (required for hydrogen generation) after the electrochemical reduction of the bridging ligand, the reduced bridge inhibits, rather than promotes, receiving the second electron.[21] For the dceb analogues, the electron resides on the peripheral dceb, as opposed to the bridging ligand, thus, possibly allowing for the second electron to be received and increasing TONs.

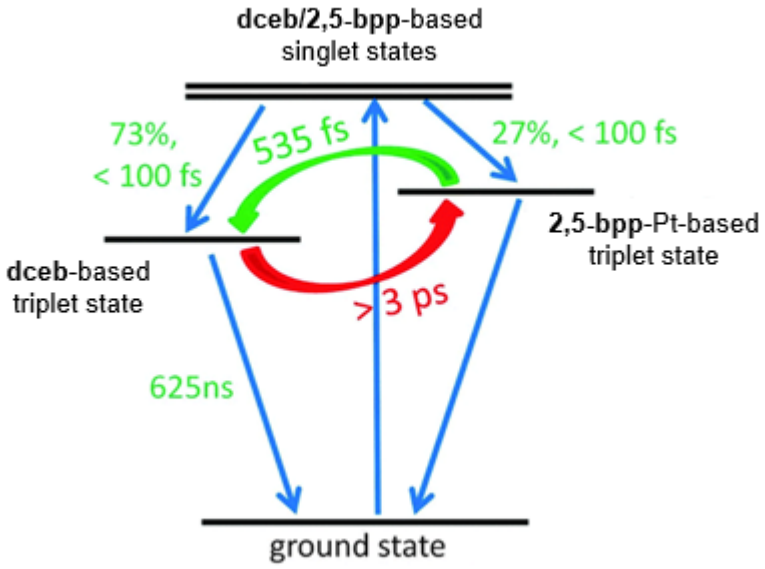

Figure 2.6: Scheme of a simplified photophysical model for $RuPt_{dceb}$[14]

2.2.4 4,7-diphenyl-1,10-phenanthroline as a peripheral ligand

The development of the intramolecular complex investigated in this chapter stemmed from the knowledge gathered from the previously discussed studies, where the dceb peripheral ligand led to an enhancement in hydrogen generation, with the time resolved studies clearly showed the different photodynamics following excitation and longer lifetimes when compared to that of the bpy analogue. $[Ru(diphenylphenanthroline)_3]^{2+}$ compounds have long lifetimes, and therefore diphenylphenanthroline was chosen as the peripheral ligand. For the bridging unit, 2,5-bpp was selected, as it is capable of accepting electron density from terminal ligands. Previous studies, by the DCU group, employing this BL in photocatalytic assemblies produced greater amounts of hydrogen vs. the 2,6-bpp analogue or either of the di(pyridine-2-yl)pyrazine ligands (2,3-dpp, 2,5-dpp).[15,22,23] Both Pt and Pd catalytic centres are used throughout the literature, as discussed. This is due to their

low over potential for proton reduction.[24] The catalytic centre, PtIS (S=solvent), was selected as Rau et al. demonstrated its superiority over PtClS or PdClS.[25] The TA spectra above, of the dceb complexes, gave photophysical evidence to the thinking that the peripheral ligands have an influence on the early time electron dynamics, which in turn, impact the overall capabilities of the photocatalyst to generate hydrogen. The use of dpph as the terminal ligand in this chapter was influenced by these previously discussed studies. Using phenanthroline ligands provide a higher level of conjugation and the presence of the phenyl rings on dpph extends the π-conjugation consequently prolonging lifetimes of the ^{3}MLCT states, reaching higher extinction coefficients in the visible region and emission quantum yields of almost unity.[26–29] The presence of the phenyl groups also encourage steric hindrance, therefore, decreasing non-radiative rates of decay contributing to long excited state lifetimes. Also, as previously conveyed in Chapter 1, Brewer et al. saw an large increase in hydrogen production activity for their RuRuRh complexes with dpph peripheral ligands versus bpy and 1,10-phenanthroline (phen).[28] Brewer et al. also saw slight increases in hydrogen generation with their tri- and tetra-metallic complexes using a Pt catalytic centre (RuRuPt, Ru_2RuPt), following replacement of the phen ligand with dpph.[30] The work in this chapter further investigates the effect of varying the peripheral ligand, and in this case introducing dpph ligands into the systems previously reported by the DCU group.

2.3 Experimental

2.3.1 Materials

All photocatalysis experiments where complexes were assessed for the generation of hydrogen were conducted under a nitrogen atmosphere. All solvents were dried and degassed prior to use for photocatalysis. The following preparations were made for solvents used in photocatalytic experiments: acetonitrile and triethylamine were distilled over CaH_2; anhydrous THF was distilled over benzophenone and Na metal; ethanol was dried over magnesium turnings; methanol was distilled over magnesium turnings and iodine. Triethanolamine was used as purchased. All solvents were supplied by the Aldrich Chemicals Co. All solvents used in UV-vis absorption, fluorescence, TA and time-resolved photoluminescence experiments were of spectrophotometric grade and were used without further purification. For ns-TA and time-resolved photoluminescence experiments, spectrophotometric grade acetonitrile was subjected to 3 cycles of freeze-pump-thaw technique to remove gas and water present, under an Argon gas atmosphere (argon purchased from BOC ltd).

2.3.2 Equipment

^{1}H NMR and ^{13}C NMR were recorded on a Bruker AC 400 spectrophotometer in deuterated solvents and were calibrated according to the deuterated solvent peak. All UV spectra were measured on an Agilent 8453 UV-Vis 91 spectrophotometer in a 1 cm quartz cell using spectrophotometric grade solvents. Emission spectra were recorded using a LS50B luminescence spectrophotometer using a 1 cm quartz cuvette and spectrophotometric grade solvents. Time-resolved photoluminescence and ns transient absorption data were recorded using an Edinburgh Instruments LP980 Transient Absorption Spectrometer.

The set-up for the TAS system located in the laboratories at Twente consists of a fs-TA setup consists of an amplified Ti:Sa system (Coherent, Legend Elite), which produces 800 nm laser pulses at 5 kHz repetition rate.[18] Part of this 800 nm output was directed into an optical parametric amplifier (Coherent, Opera) to generate the 490 nm, 515 or 525 nm pump beam used for photoexcitation. A fraction of the remaining part of the fundamental 800 nm beam was guided through a delay stage and

focused onto a CaF_2 crystal to generate a broadband white light continuum extending into the UV till ca. 350 nm used as the probe. The CaF_2 crystal was mounted on a continuously moving stage to avoid thermal damage. The remaining 800 nm fundamental was removed by using two 700 nm short pass filters. The experimental time resolution equals ca. 100-150 fs. The polarizations of the pump and probe beams were set at magic angle (54.7°). The probe pulses were sent into a 35 cm spectrograph coupled to a home built 256 pixels diode array detector. The differential absorbance between pump on and off was determined by chopping the pump beam at 2.5 kHz.[31] The data were analysed using the open-source program Glotaran.

2.3.3 Time-resolved studies

Samples for the fs-TAS set up were prepared by dissolving the complexes in anhydrous acetonitrile (Sigma-Aldrich, purity >99.9 %), followed by bubbling with dry N_2 for ~20mins and sealing. The samples were either excited at 490 nm, at 515 nm or at 525 nm, and had optical density (OD) values of 0.30, 0.14 and 0.10, respectively. The pump power was kept relatively low ($3\pm1\times10^{14}$ photons/(cm^2 pulse) for λ_{exc} = 490 nm, $5\pm1\times10^{14}$ photons/(cm^2 pulse) for λ_{exc} = 515 nm and $7\pm1\times10^{14}$ photons/(cm^2 pulse) for λ_{exc} = 525 nm) and was verified to be in the linear regime.

The samples for ns-TAS were prepared in anhydrous acetonitrile (Sigma-Aldrich, purity >99.9 %) and degassed by 3 cycles of freeze-pump-thaw. The samples had a typical absorbance (OD) at 355 nm equal to 0.3-0.4 OD.

2.3.4 Photocatalytic Hydrogen Generation

All photocatalysis experiments were conducted under a nitrogen atmosphere and in triplicate. All solvents were dried and degassed prior to use, unless otherwise stated. Triethanolamine was used as purchased and mixed with an appropriate amount of the required dried solvent (for ease of handling due to the viscosity), the amount of solvent used was accounted for, to keep the final amount as described. This mixture was then subjected to Schlenk conditions. Deionised water was used throughout.

A stock solution was made up with the photocatalyst in the required solvent:water ratio at a specified concentration. In the case of intermolecular studies, the same was

conducted, with the appropriate amount of catalyst added to the stock. This mixture was degassed and flushed with nitrogen, again, before the required amount was transferred to the corresponding, nitrogen filled vial. In a separate Schlenk tube, the sacrificial agent was prepared and then added to the vial. Vials were prepared in a separate Schlenk chamber and had been subjected to Schlenk conditions and maintained in a nitrogen atmosphere. The vials used were gas tight and had a septum on the cap to allow for a gas tight needle and syringe to withdraw 1 ml of headspace and inject onto the GC. Once prepared vials were sealed and stored in the dark until triplicate samples were ready for photolysis. The samples were exposed to a 470 nm (blue) LED array for a stated amount of time. Samples were placed in the dark after irradiation and injected on to a Shimadzu Gas Chromatograph with a BID detector. Standards were used to calibrate the peak area of the measured samples, to enable calculation of the number of moles of hydrogen generated after the experiment. The standards used were a mix of gases at 0.01% (100 ppm), 0.1% (1000 ppm), 1% (10000 ppm) and 5% (50000 ppm).

2.3.5 Synthesis

2,2':5',2"-terpyridine,[15] $[Ru(dpph)_3](PF_6)_2$, *cis*-$[Pt(DMSO)_2Cl_2]$[32] and *cis*-$[Pt(DMSO)_2I_2]$,[33] were prepared using literature methods, *cis*-$[Ru(dpph)_2Cl_2].2H_2O$, $[Ru(dpph)_2(2,5\text{-bpp})](PF_6)_2$,[15] and $[Ru(dpph)_2(2,5\text{-bpp})PtIH_2O](PF_6)_2$ were prepared using modified literature methods.[33]

cis-$[Ru(dpph)_2Cl_2]\cdot 2H_2O$. 690 mg (2.84 mmol) of $RuC1_3\cdot H_2O$, 2 g (6 mmol) of dpph and 2 g LiCl in 50 mL DMF were heated at reflux temperature for 8 h. Subsequently, the solution was allowed to cool to room temperature. Upon the addition of 100 mL of acetone, the reaction mixture was stored at – 4 °C overnight. The product was collected by filtration and washed with ice water and 50 ml Et_2O, yielding a dark purple solid. Yield: 1.6 g (1.4 mmol, 64 %). ^{1}H NMR (400 MHz, $(CD_3)_2SO$): 10.44 (2H, d), 8.27 (2H, d), 8.23 (2H, d), 8.1 (2H, d), 8.05 (2H, d), 7.86 (4H, d), 7.74 (4H, t), 7.72 (2H, d), 7.56 (10H, m) 7.41 (2H, d).

$[Ru(dpph)_2(2,5\text{-bpp})](PF_6)_2$. A solution of EtOH: H_2O (15 ml, 3:1) and 2,2':5'2" -terpyridine (30 mg, 0.14 mmol) was heated until the ligand was fully dissolved. *cis*-$[Ru(dpph)_2Cl_2]\cdot 2H_2O$ (80 mg, 0.095 mmol) dissolved in 5 mL EtOH was slowly added

to the hot mixture. The reaction was heated at reflux temperature for a further 6 h. The reaction mixture was then allowed to cool to room temperature. Following this, the EtOH was removed in *vacuo*. The remaining H_2O solution was filtered, and the product was precipitated by the addition of aqueous NH_4PF_6 to the mother liquor. The precipitate was collected by filtration and washed with H_2O and Et_2O and recrystalised from acetone and Et_2O, affording a red solid. Yield: 68 mg (0.05 mmol, 55 %). ^{1}H NMR (400 MHz, $(CD_3)_2SO$): 9.00 (2H, t), 8.82 (1H, dd), 8.47 (1H, d), 8.44 – 8.32 (5H, m), 8.30 – 8.21 (5H, m), 7.99 – 7.93 (3H, m), 7.92 – 7.87 (3H, m), 7.85 (1H, d), 7.81 (1H, d), 7.72 – 7.60 (20H, m), 7.56 (1H, td), 7.38 (1H, qd). Elem anal. calculated for $C_{43}H_{43}F_{12}N_7P_2Ru$: C, 58.7; H, 3.4; N, 7.6. Found: C, 58.42; H, 3.43; N, 7.36.

$[Ru(dpph)_2(2,5\text{-bpp})PtIH_2O](PF_6)_2$. $[Ru(dpph)_2(2,5\text{-bpp})](PF_6)_2$ (82 mg, 0.064 mmol) and *cis*-$[Pt(DMSO)_2I_2]$ (49.9 mg, 0.082 mmol) were dissolved in 20 mL EtOH: acetone mixture (1:1) and heated at reflux temperature for 7 days. The product formed as a precipitate and was collected by filtration and washed with cold H_2O. Yield: 47 mg (0.028 mmol, 45 %) As proton NMR is not always useful in the characterisation of these assemblies, due to the large number of aromatic protons, and isomers produced,[34] ESI high resolution mass spectrometry was used to characterise this compound, $[Ru(dpph)_2(2,5\text{-bpp})PtIH_2O](PF_6)_2$, found m/z = 1338.1249.

2.4 Results and Discussion

2.4.1 Intermolecular studies of $[Ru(dpph)_3](PF_6)$

A range of conditions were studied for hydrogen generation using the intermolecular approach, and with an overall summary of the results in Table 2.2, below, using $[Ru(dpph)_3](PF_6)_2$ as the photosensitiser. When TEOA was used as a sacrificial agent, zero to low TONs for hydrogen generation was observed for all catalysts tested (Exp. 1). Upon changing the sacrificial agent to TEA, TON increased to the 100s for most of the catalysts studied (Exp. 2), except Exp. 2G, where no hydrogen was detected. Nonetheless, a significant increase in TONs was observed for the other systems tested, on exchanging the sacrificial agent from TEOA to TEA. Such a variation in results upon swapping one sacrificial agent for another is an immediate indicator of the shortcomings of screening systems under one set of parameters. Changing the SA changes the pH of the solvent mix, the solubility of the photocatalyst in this mix. These are just examples that can affect the electron transitions between the SA and the photocatalyst. Different solvents were investigated but solubility issues occurred for most of the solvent choices and accurate TONs could not be determined (Exp. 3). Altering the percentage of water present (Exp. 4) had a direct correlation with TONs, up until a certain percentage, beyond which solubility issues arose. Also, a larger vial size was tested, with a water percentage of 20% (Exp. 3DL). This experiment was to establish if an increased headspace allowed for higher turnover numbers as there would be less pressure building up within the vial during irradiation, and therefore less likely that the gas will be forced into the solvent or escape. This was not the case as lower TONs were observed for the larger vial. It is possible that the light source did not irradiate the entire solution, which may have resulted in lower TONs. Changing the ratio of photosensitiser to catalyst (Exp. 5) showed no improvement on the 1:1 system. In addition to the samples that were irradiated under all the different experimental conditions, samples were also placed in the dark, and no hydrogen was detected in any of these samples.

Table 2.2: Table of experimental parameters and resulting TONs achieved, using [Ru(dpph)$_3$](PF$_6$)$_2$ as the photosensitiser

Exp.	Catalyst	No. of Moles of CAT	Ratio of PS:CAT	S.A.	Sol.	H_2O %	Vial Size	TON
S.A.	***TEOA***							
1C	$Pt(DMSO)_2Cl_2$	1.4E-07	1:1	TEOA	CH_3CN	10	5	2
1D	$K_2[PtCl_4]$	1.2E-07	1:1	TEOA	CH_3CN	10	5	1
1E	$C_{26}H_{24}Cl_2CoP_2$	9.7E-08	1:1	TEOA	CH_3CN	10	5	<1
1F	$C_{26}H_{24}CoI_2P_2$	1.1E-07	1:1	TEOA	CH_3CN	10	5	<1
1G	$Pt(DMSO)_2I_2$	1.0E-07	1:1	TEOA	CH_3CN	10	5	9
S.A.	***TEA***							
2A	$Pt(DMSO)_2I_2$	9.2E-08	1:1	TEA	CH_3CN	10	5	203
2B	$K_2[PtCl_4]$	8.2E-08	1:1	TEA	CH_3CN	10	5	286
2C	$Pt(DMSO)_2Cl_2$	7.9E-08	1:1	TEA	CH_3CN	10	5	161
2D	$Pt(bpy)Cl_2$	insoluble	1:1	TEA	CH_3CN	10	5	-
Sol.	***Solvent***							
3A	$Pt(DMSO)_2I_2$	1.1E-07	1:1	TEA	THF	10	5	<1
3B	$Pt(DMSO)_2I_2$	insoluble	1:1	TEA	EtOH	10	5	-
3C	$Pt(DMSO)_2I_2$	insoluble	1:1	TEA	MeOH	10	5	-
H_2O	***%H_2O***							
4A	$Pt(DMSO)_2I_2$	1.1E-07	1:1	TEA	CH_3CN	20	5	271
4B	$Pt(DMSO)_2I_2$	6.3E-08	1:1	TEA	CH_3CN	1	5	92
4C	$Pt(DMSO)_2I_2$	7.1E-08	1:1	TEA	CH_3CN	35	5	340
4D	$K_2[PtCl_4]$	4.7E-08	1:1	TEA	CH_3CN	20	5	575
4F	$K_2[PtCl_4]$	3.4E-08	1:1	TEA	CH_3CN	35	5	134
4G	$K_2[PtCl_4]$	insoluble	1:1	TEA	CH_3CN	50	5	-
4DL	$K_2[PtCl_4]$	1.5E-07	1:1	TEA	CH_3CN	20	20	455
Ratio	***PS:CAT***							
5A	$Pt(DMSO)_2I_2$	2.4E-07	3:1	TEA	CH_3CN	20	5	323
5B	$Pt(DMSO)_2I_2$	8.2E-08	1:3	TEA	CH_3CN	20	5	112
5C	$K_2[PtCl_4]$	4.9E-08	3:1	TEA	CH_3CN	20	5	467
5D	$K_2[PtCl_4]$	1.7E-08	1:3	TEA	CH_3CN	20	5	116

Although these results appear to be promising with TONs > 500, nearly all systems showed signs of Pt-colloid formation (possibly due to photolysis). When colloids are formed, these are the active catalyst and then calculating TON based on the precursor catalyst is incorrect, and it is difficult to obtain consistent colloid formation. Therefore, when assessing systems for hydrogen when Pt is used as the catalytic centre, colloid

formation is a possibility in photocatalytic mixtures using either inter- or intra-molecular approaches.

2.4.2 Moving from inter- to intra-molecular assemblies for hydrogen generation

Novel mono- and di-nuclear complexes were successfully synthesised, characterised and investigated for their hydrogen production abilities. Using the precursor *cis*-$[Ru(dpph)_2Cl_2].2H_2O$, a terpyridine BL was attached, resulting in the novel monomer $[Ru(dpph)_2(2,5\text{-bpp})](PF_6)_2$ (**Ru_{dpph}**). This enabled the addition of a Pt catalytic centre by cyclometallation at the end of the BL to make the dinuclear species $[Ru(dpph)_2(2,5\text{-bpp})PtIH_2O](PF_6)_2$ (**$RuPt_{dpph}$**).

2.4.2.1 UV-Vis Spectroscopy

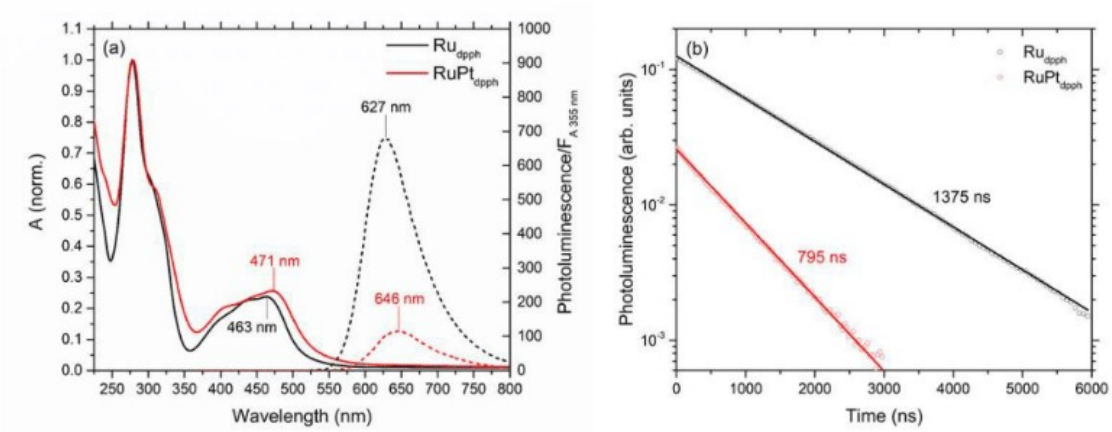

*Figure 2.7:(a) Spectra of the absorbance (solid line) and emission (dashed line) (a) and (b) the corresponding photoluminescence for **Ru_{dpph}** (black) and **$RuPt_{dpph}$** (red) in anhydrous degassed acetonitrile*

The electronic absorbance spectra of the both mono and dinuclear species, given in Figure 2.7 (a), display strong absorption bands from 250-350 nm which is indicative of the dpph ligand-centred transitions (π-π*).[30] Based on earlier work, the shoulder, at ~315 nm is assigned to the ligand-centred π-π* transitions of the bridging ligand, 2,5-bpp.[18] The broad ^{1}MLCT band, present at ~380-550 nm, undergoes a slight bathochromic shift (maxima at 463 nm vs. 471 nm), on the addition of the Pt moiety.[35] This indicates that cyclometallation with Pt slightly modifies the electronic levels of the ground states. This is also reflected in the difference between the

photoluminescence properties of the decay of the lowest ^{3}MLCT states, of the two complexes (mono- and di-nuclear), to their ground state. This is discussed below. The electronic absorption spectra obtained are typical for Ru(II) polypyridyl complexes and resemble many of the spectra reported for similar complexes discussed in this chapter.

2.4.2.2 Photoluminescence Spectroscopy

When comparing the photoluminescence spectra of the two complexes, (Figure 2.7), it is apparent there are changes in the excited state upon the addition of the Pt centre. A red shift of ~20 nm is observed in the emission spectra, on comparing **Ru$_{dpph}$** to **RuPt$_{dpph}$** which indicates a reduced gap between the excited and ground states. It is also apparent that the Pt centre has a quenching effect on the emission for the dinuclear complex. The photoluminescence lifetime (time taken for the emission of the species to decay) is also reduced, from 1375±20 ns for **Ru$_{dpph}$** to 795±8 ns for **RuPt$_{dpph}$**. This quenching effect has been reported for other similar complexes, such as, **Ru$_{dceb}$** vs **RuPt$_{dceb}$**, as seen in Table 2.3, below.[33] Also, Brewer et al. reported a reduction in lifetimes (110 ns to 77 ns) upon the addition of a Pt moiety to their trinuclear complexes to form tetranuclear species involving Ru_3Pt and dpph peripheral ligands.[30,35] These are photophysical traits for dinuclear complexes and are proof of cyclometallation of the complex with the Pt moiety.

Table 2.3: Comparison of lifetimes between mono- and di-nuclear complexes in degassed acetonitrile

Complex	Lifetime (ns)
Ru$_{dceb}$	1040
RuPt$_{dceb}$	624
Ru$_{dpph}$	1375
RuPt$_{dpph}$	795

2.4.2.3 Time-Resolved Studies

2.4.2.3.1 Transient Absorption Spectroscopy (TA)

Both the sub-ps and ns timescales were investigated to gain an insight into the photophysical properties of both the monomer and dinuclear assembly following photoexcitation. The fs-TA studies were performed by collaborators in Twente on both **Ru$_{dpph}$** and **RuPt$_{dpph}$** using a range of excitation wavelengths, including 490 nm, 515 nm and 525 nm. The ns-TA were performed in DCU on the two complexes at 355 nm.

2.4.2.3.1.1 Femtosecond to Picosecond Timescale (fs-ps)

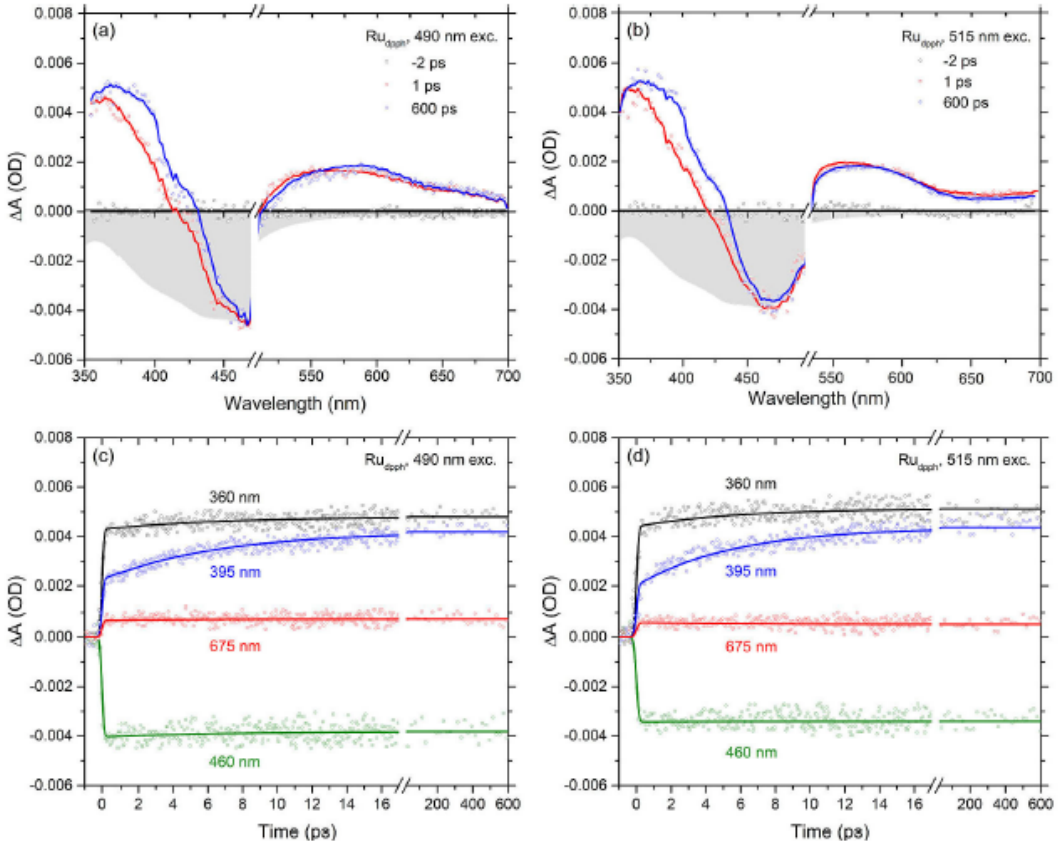

Figure 2.8: fs-TA spectra at various time delays for mononuclear [Ru(dpph)$_2$(2,5-bpp)] in anhydrous acetonitrile following excitation at (a) 490 nm and (b) 515 nm. The grey area represents the scaled and inverted steady-state absorbance spectrum. Kinetic traces at key probe wavelengths are shown in (c) following excitation at 490 nm and (d) following excitation at 515 nm. The solid lines present a global analysis fit line based on a one-component sequential model.[31] Experiments were performed in Twente.

Displayed in Figure 2.8 are the fs-TA spectra and kinetic traces, conducted by our collaborators, of the mononuclear species **Ru$_{dpph}$**, measured using an excitation wavelength (λ_{exc}) of 490 nm in Figure 2.8(a). The spectra are assigned to the triplet excited state as intersystem crossing occurs within the response of the instrument, <100 fs.[36,37] A scaled, inverted steady-state absorbance spectrum (grey area) is in the background of the negative region of Figure 2.8(a). The overlapping signal between 430 nm and 500 nm, in the foreground, is assigned to GSB. In the positive region, three ESA signals can be distinguished. The broad ESA band at greater than 500 nm is likely due to ligand-to-metal charge transfer transitions,[18,38] possibly with contributions from both the reduced 2,5-bpp[18] and dpph[39] ligands. A second broad ESA band centered at ~420 nm and partially overlapping with the GSB is likely due to ligand-centered transitions of the reduced 2,5-bpp ligand, as seen previously with **Ru$_{dceb}$**, as seen in Figure 2.3.[14] A third ESA band around ~355 nm is only partially resolved, and possibly due to ligand-centered transitions of the reduced dpph ligands.[40] These ESA signals indicate that after ISC both ^{3}MLCT states localised on the peripheral ligands and on the bridging ligand are populated.

Displayed in Figure 2.8(b) are the TA spectra generated following excitation of the mononuclear species at 515 nm. Altering the excitation wavelength can change the location of the Franck-Codon state and therefore, the population ratio of the subsequent triplet state (^{3}MLCT$_{dpph}$ and ^{3}MLCT$_{2,5\text{-}bpp}$). This has been previously discussed in the above text in relation to similar Ru complexes.[18] The resulting spectra generated following excitation at 515 nm are quite similar to those recorded when the sampled was excited at 490 nm. A notable difference is the shape of the ESA at >500 nm. It is possible experiments at longer wavelengths would lead to more obvious spectrotemporal features, however these experiments were not performed due to the low absorbance of the sample.

The kinetic traces given in Figure 2.8(c and d) depict the TA signals at specific wavelengths corresponding to the ESA and GSB bands evolution over time. The kinetics recorded at 460 nm relates to that of the GSB signal. The GSB appears within the instrumental response time of ca. 100 fs and then remains constant, showing that excited state decay is insignificant in the sub-ns experimental time window, in agreement with the long photoluminescence lifetime observed. The discreet broad band ~420 nm, assigned to the bridging ligand, 2,5-bpp, ^{3}MLCT state, increases on an

early timescale. The low number of probe photons generated by the CaF_2 crystal further in the UV (around 350-360 nm) does not allow to observe a potential simultaneous decrease of the ESA signal associated to $^3MLCT_{dpph}$ states. A global fit based on a one-component sequential model[31] yields time constants of 6.5±0.2 ps for λ_{exc} = 490 nm and 5.6±0.2 ps for λ_{exc} = 515 nm. This model combines inter-ligand internal conversion (ILIC) and vibrational cooling (VC) as $^3MLCT_{dpph} \rightarrow {}^3MLCT_{tpy}$ ILIC.

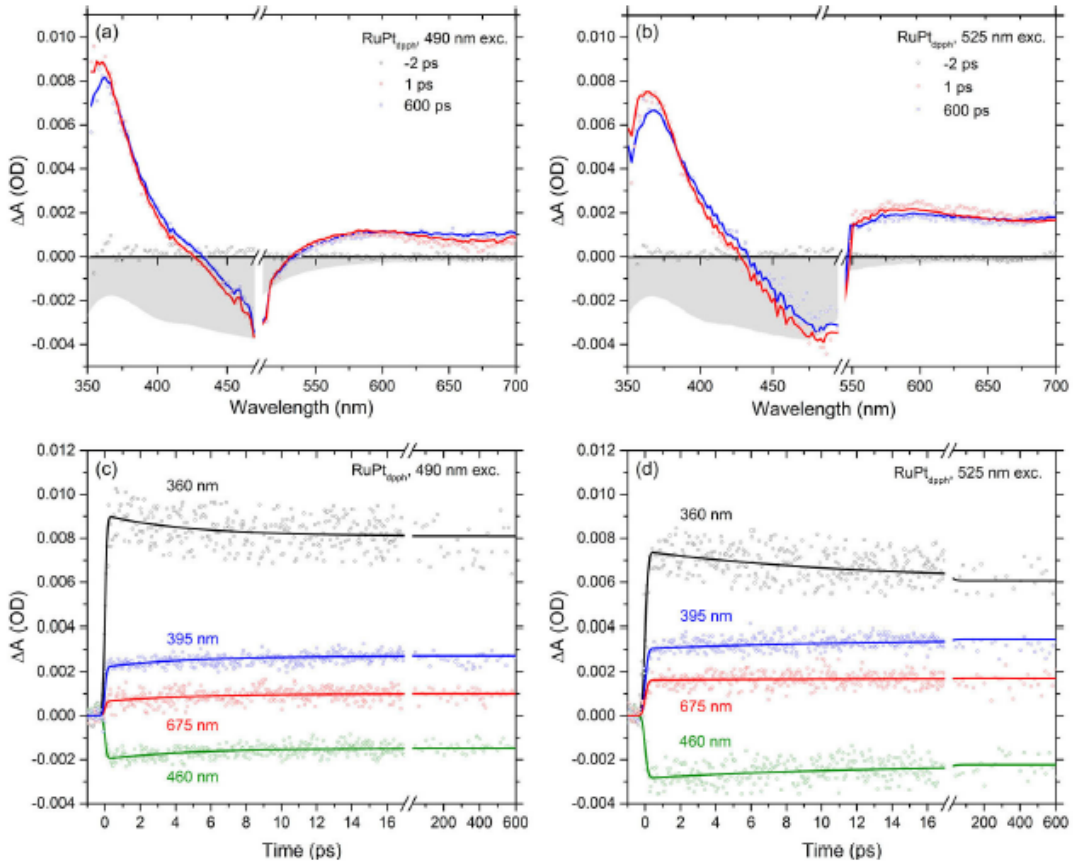

Figure 2.9: fs-TA spectra at various time delays for dinuclear [Ru(dpph)$_2$(2,5-bpp)PtIS] (S = solvent) in anhydrous acetonitrile following excitation at (a) 490 nm and (b) 525 nm. The grey area represents the scaled and inverted steady-state absorbance spectrum. Kinetic traces at key probe wavelengths are shown in (c) following excitation at 490 nm and (d) following excitation at 525 nm. The solid lines present a global fit based on a one-component sequential model.[31] Recorded in Twente.

Displayed in Figure 2.9 are the corresponding data collected for **RuPt$_{dpph}$** when excited at 490 nm (a and c) and 525 nm (b and d). The minimal differences between the spectra collected for the mono- and di-nuclear species highlight that the features

present for the dinuclear complex are related to Ru-based transitions. Assignment of the spectral features remain the same, with their shape and positioning shifting slightly upon the addition of the Pt centre. The first ESA, possibly due to the ligand-centred transitions of reduced peripheral ligands, is redshifted to 360 nm and remains, at lower intensity, after internal conversion (IC quantum yield less than unity). The broad band at ~420 nm, assigned to the ligand-centred transitions of the reduced bridge, it seems slightly redshifted/broadened and less intense. This feature does not follow the same evolutionary pathway as the mononuclear, as there isn't as many obvious changes visible. This is possibly due to the delocalisation of electron density over the bridging ligand and the Pt centre attached. The broadening of this band leads to further overlapping with the GSB and explains the ~5 ps component observed in the kinetic traces at 460 nm. The broad band, found at wavelengths greater than 500 nm, was assigned to the transitions of the 2,5-bpp-Pt-I, delocalised T_3 state, as seen for $RuPt_{bpy}$, discussed above.[19] Time constants were gained using global analysis with the one component sequential model, acquiring the following; 4.9±0.2 ps for λ_{exc} = 490 nm, 5.6±0.3 ps for λ_{exc} = 515 nm and 12.3±0.8 ps for λ_{exc} = 525 nm. This data likely represents the inter-ligand internal conversion from the dpph ligands to the 2,5-bpp bridge and/or Pt centre. The time constants increase with increasing excitation wavelength. This is indicative of the energy levels of the ligands increasing creating a larger energy barrier, this is further explained below.

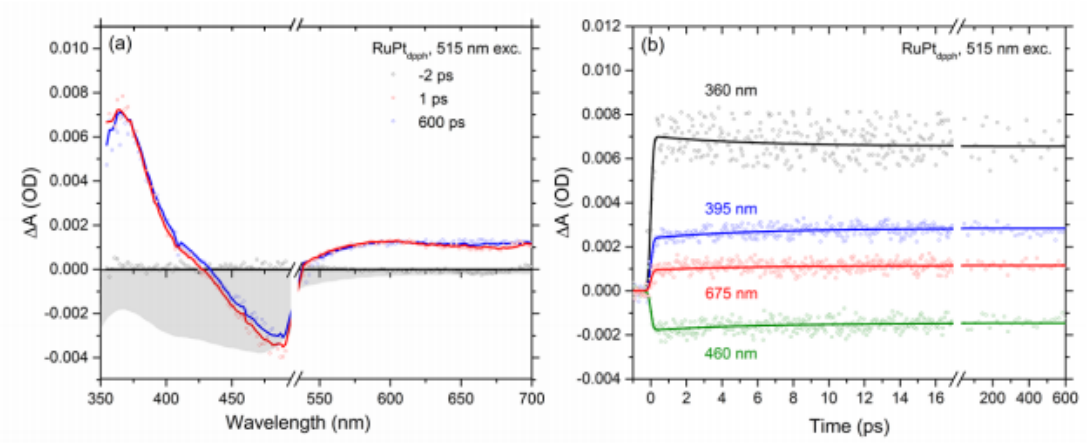

Figure 2.10: fs-TA spectra at various time delays for ***RuPt$_{dpph}$*** *in anhydrous acetonitrile following excitation at (a) 515 nm. The grey area represents the scaled and inverted steady-state absorbance spectrum. Kinetic traces at key probe wavelengths are shown in (b). The solid lines present a global fit based on a one-component sequential model. Recorded in Twente*

Data recorded following photoexcitation at 515 nm, depicted in Figure 2.10, illustrate similar population patterns as seen following excitation at 490 nm (Figure 2.9(a)). It is only when moving to an excitation wavelength that is slightly further redshifted (λ_{exc} = 525 nm) that the electron population distribution is altered and favours population of the T_3 state from the peripheral dpph ^{3}MLCT state.

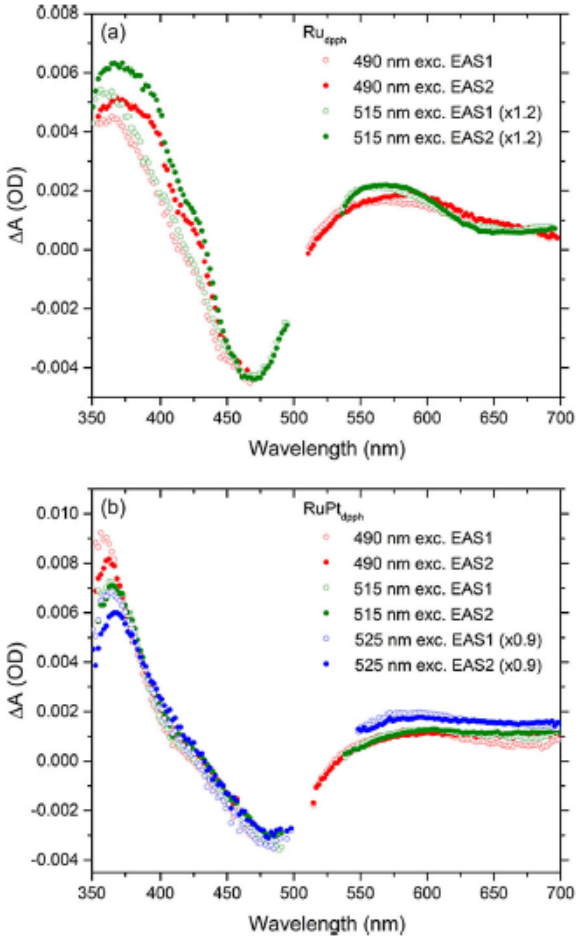

Figure 2.11: Evolution associated spectra (EAS) for ***Ru$_{dpph}$*** *(a) and* ***RuPt$_{dpph}$*** *(b) for excitation at various wavelengths. EAS1 is representative of the TA spectra prior to inter-ligand internal conversion and EAS2 describes the TA spectra afterwards (provided in the main text, dependant on excitation wavelength). A few EAS spectra have been scaled by the factor indicated in the legend to achieve similar GSB intensities.*

The above evolution associated spectra (EAS), for mono- (a) and dinuclear (b) complexes, are a means of describing the role of the photoexcitation energy for the species. EAS1 illustrates the TA spectra before internal conversion and EAS2 describes afterwards. Minor changes are seen when a different excitation wavelength

is applied to **Ru$_{dpph}$**, therefore, indicating there is only a minor role played by the excitation wavelength. In Figure 2.11(a), the ESA features at <440 nm are not as distinct at higher wavelengths (lower energy), and the ESA broad signal at >500 nm has a change of shape. Consequently, the excited states in **Ru$_{dpph}$** are likely not equilibrated, whereas, in similar Ru(II) complexes a Boltzmann distributed population of ^{3}MLCT states is detected in ~100 ps and does not follow a wavelength dependency.[39] In Figure 2.11(b), the differences are the spectra are more evident, which may indicate wavelength dependency, therefore, unequilibrated excited states are reflected in the EAS of **RuPt$_{dpph}$**. When the spectra are compared, the ESA signal at <440 nm appear lower intensity, whereas in the region >500 nm the intensity of the transient signals recorded increased upon lowering the excitation energy (increased λ_{exc}) applied. This effect is unlikely due to an increase in population of ^{3}MLCT$_{2,5\text{-bpp}}$ states with λ_{exc}, as an increase in signal around 420 nm is absent. An increase of amplitude at ~530 nm possibly reflects an increase in population of the delocalised T_3 state of the bridging ligand and catalytic moiety, 2,5-bpp-Pt-I.[19] This would also explain the excitation energy dependence observed for the **RuPt$_{dpph}$** complex, although this does not account for all of the data collected. The T_3 for **RuPt$_{dpph}$** is populated within 100 fs, whereas the T_3 state for **RuPt$_{bpy}$** quenches the ^{3}MLCT within ~1 ps. Also, the ~100 ps process found for **RuPt$_{bpy}$**, attributed to the electron density centred over the bridge-catalytic moiety, is not observed for **RuPt$_{dpph}$**.

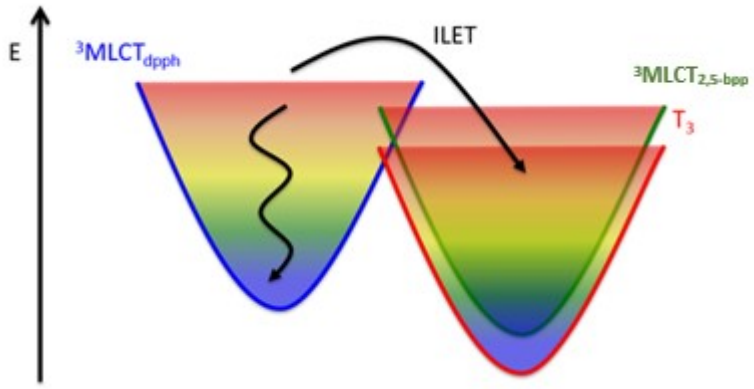

*Figure 2.12: Processes in **RuPt$_{dpph}$** following ultrafast intersystem crossing into the triplet manifold. For simplicity the singlet potential energy surfaces and the ground state are not shown. The time values for internal conversion are determined by a competition between inter-ligand electron transfer (ILET) and vibrational relaxation, and are hence photoexcitation energy dependent*

Figure 2.12 depicts a photophysical model for **RuPt$_{dpph}$.** As previously noted, ultrafast ISC from the Franck-Codon state to populate the triplet MLCT states of both the bridge (2,5-bpp) and terminal (dpph) ligands occurs within 100 fs. In the case of **RuPt$_{dpph}$** it also leads to the population of a third triplet state, denoted T_3. From the recorded time constants, it was deduced that increasing the excitation wavelength is likely to increase the electron density of the T_3 state (expected to be lower in energy) and lower population of the $^3MLCT_{dpph}$ (higher in energy in comparison to T_3), and this is portrayed in the above figure. As the electron follows the easiest downhill pathway, the energy levels of the triplet states determine the direction of the electron transfer. The lower population of ^{3}MLCT state is most likely due to the increased energy barrier, as excitation energy is lowered. In addition to this, the competing process, VR, which is known to occur over 5-15 ps,[18,38] contributes to the energy barrier over time. This is described as non-equilibrated population of excited states and although it does not fit the mono-exponential photoluminescence decay observed for the **RuPt$_{dpph}$** species, it can be explained by either a dominant emissive state or the states bearing comparable lifetimes.

2.4.2.3.2 Nanosecond to Microsecond Timescale (ns-µs)

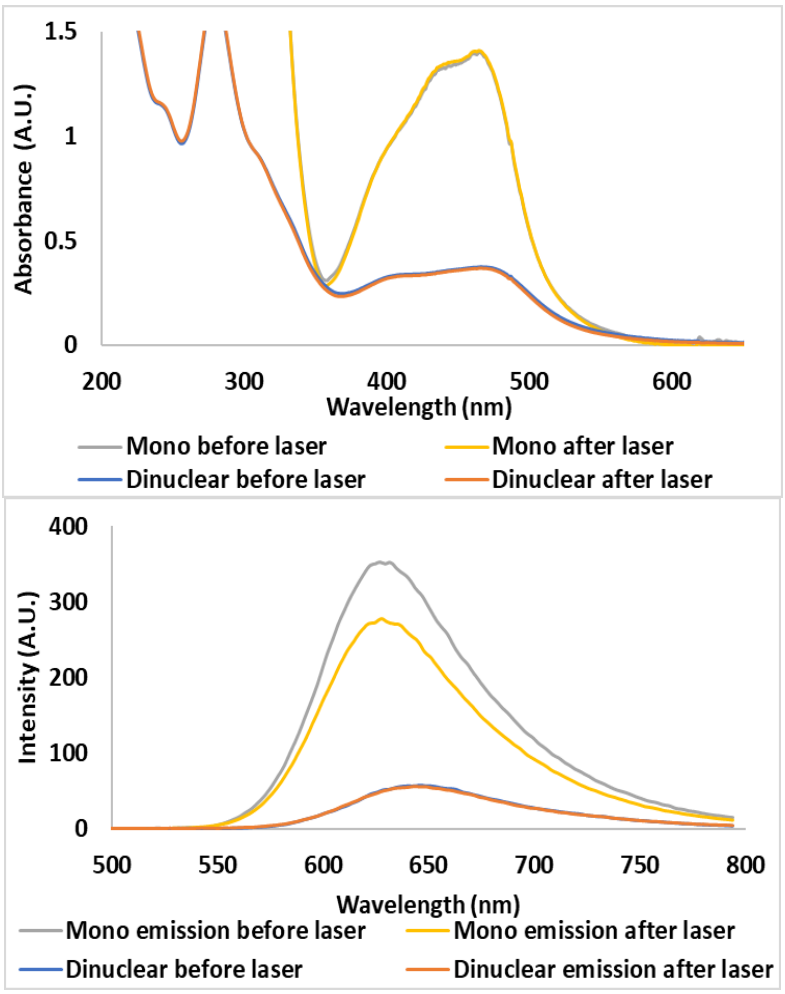

Figure 2.13: Electronic absorbance spectra (top) and emission spectra (bottom), following excitation at 355 nm. The same optical density was used for excitation of both the mono- and dinuclear species, which were before and after laser flash photolysis studies in acetonitrile after 3 cycles of freeze-pump-thaw

The above spectra show (Figure 2.13) the absorbance (top) and the emission (bottom) of the Ru and RuPt dpph complexes before and after laser flash photolysis experiments following excitation at 355 nm (samples were adjusted so that the optical density was ~0.27 at the excitation wavelength for both samples). The absorbance and emission spectra after the experiments are the same as those recorded prior to pulsed photolysis indicating that the samples do not decompose. The integration of the emission spectra (between 500 nm to 780 nm) emphasise the area of the emission achieved for the dinuclear complex (integral = 5812). This is <20% of what is achieved for the mononuclear species (integral = 33910). The integral, therefore, provides a value of

~80% for the quenching effect caused by the addition of the Pt catalytic centre on $RuPt_{dpph}$.

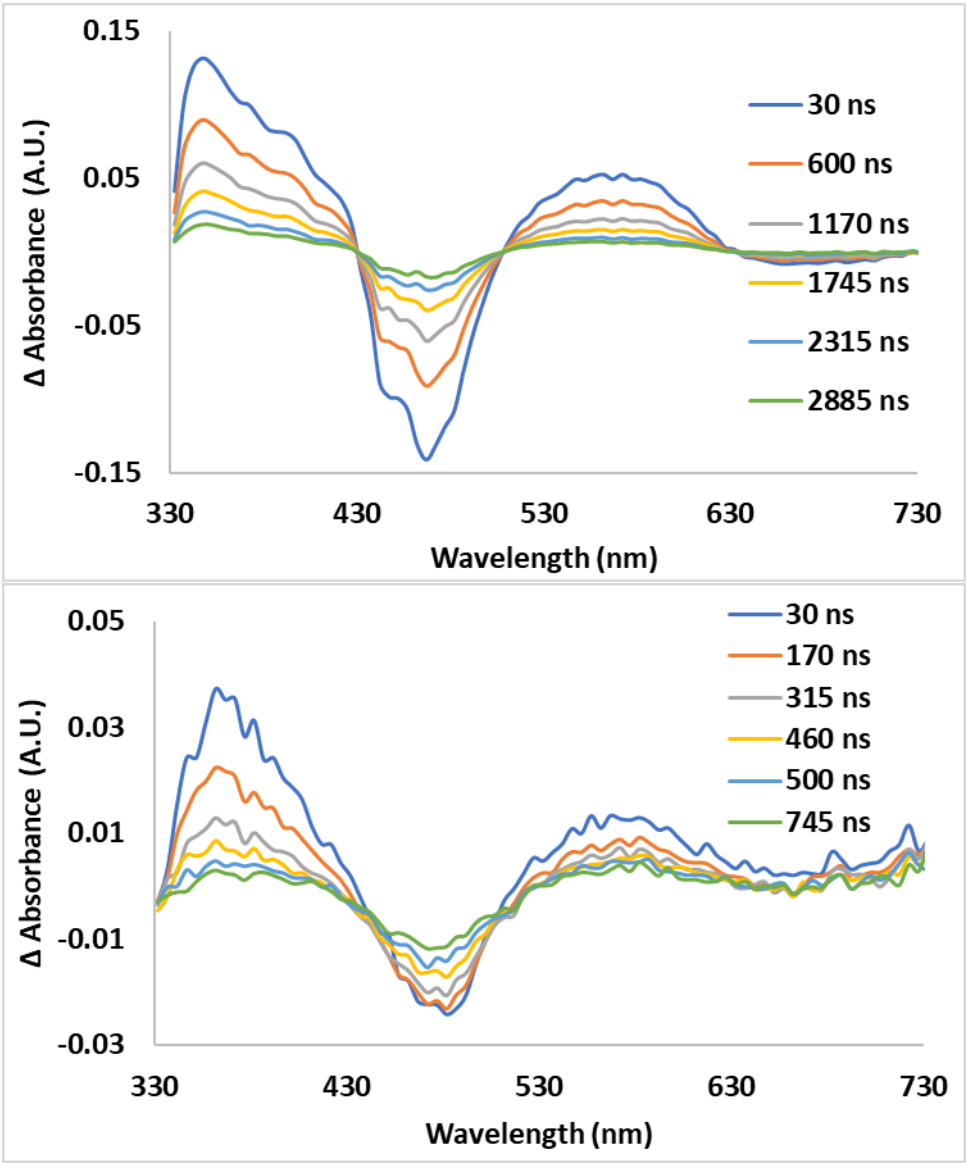

Figure 2.14: ns-TA spectra of mono- ***Ru****$_{dpph}$ (top) and the di-nuclear complex* ***RuPt****$_{dpph}$ (bottom) at certain timepoints following excitation at 355 nm in FPT prepared by freeze-pump-thaw under nitrogen in acetonitrile, OD at λ_{exc}= 0.27.*

The above spectra (Figure 2.14) represent the *ns*-TA for the triplet excited states for the two complexes when excited at 355 nm. The spectral features observed for **Ru$_{dpph}$** (top) and **RuPt$_{dpph}$** (bottom), both ESA (<430 nm and >500 nm) and GSB (430 nm – 500 nm), reflect that of what was recorded for these complexes on *fs*-TA, in Twente. The signals have therefore been assigned to the same species. The broad band at >500 nm, seen in each of the above spectra, is assigned to a ^{3}MLCT with contributions from

both the peripheral and the bridging ligand. The signal ~420 nm, previously noted in the *fs*-TA, is masked in the *ns*-TA spectra. The absence of ~420 nm peak in the spectra pertaining to $RuPt_{dpph}$ is explained by the weak signal intensity of the data recorded leading to quite noisy spectra. Note the difference in scale of the y-axis between the two graphs, the UV recorded for the complexes (Figure 2.13) provides confirmation that the absorbance at the λ_{exc} is equivalent in mono- and di-nuclear at ~0.27 A.U. The decay of the ESA and recovery of the parent in the GSB are clearly visible in these time-resolved spectra. For the mononuclear **Ru_{dpph}** complex the ESA at <430 nm, and the GSB appear to recover concurrently. Time constants for all the spectral features present, in both mono and di-nuclear complexes, are found to follow a mono-exponential decay (or recovery in the case of the GSBs). The ESA at ~352 nm following excitation of the **Ru_{dpph},** decays according to the photoluminescence lifetime (~1375 ns) within error, with τ = 1465 ns. The GSB at ~472 nm recovers over 1307 ns while the broad band, at ~562 nm, decays over 1348 ns. The same can be said for the **$RuPt_{dpph}$** complex, with a shorter lifetimes observed, compared to the mononuclear species, as expected due to the presence of the Pt-centre. This was consistent with the lifetime of the photoluminescence (~795 ns).

2.4.2.4 Time-Resolved Photoluminescence Spectroscopy

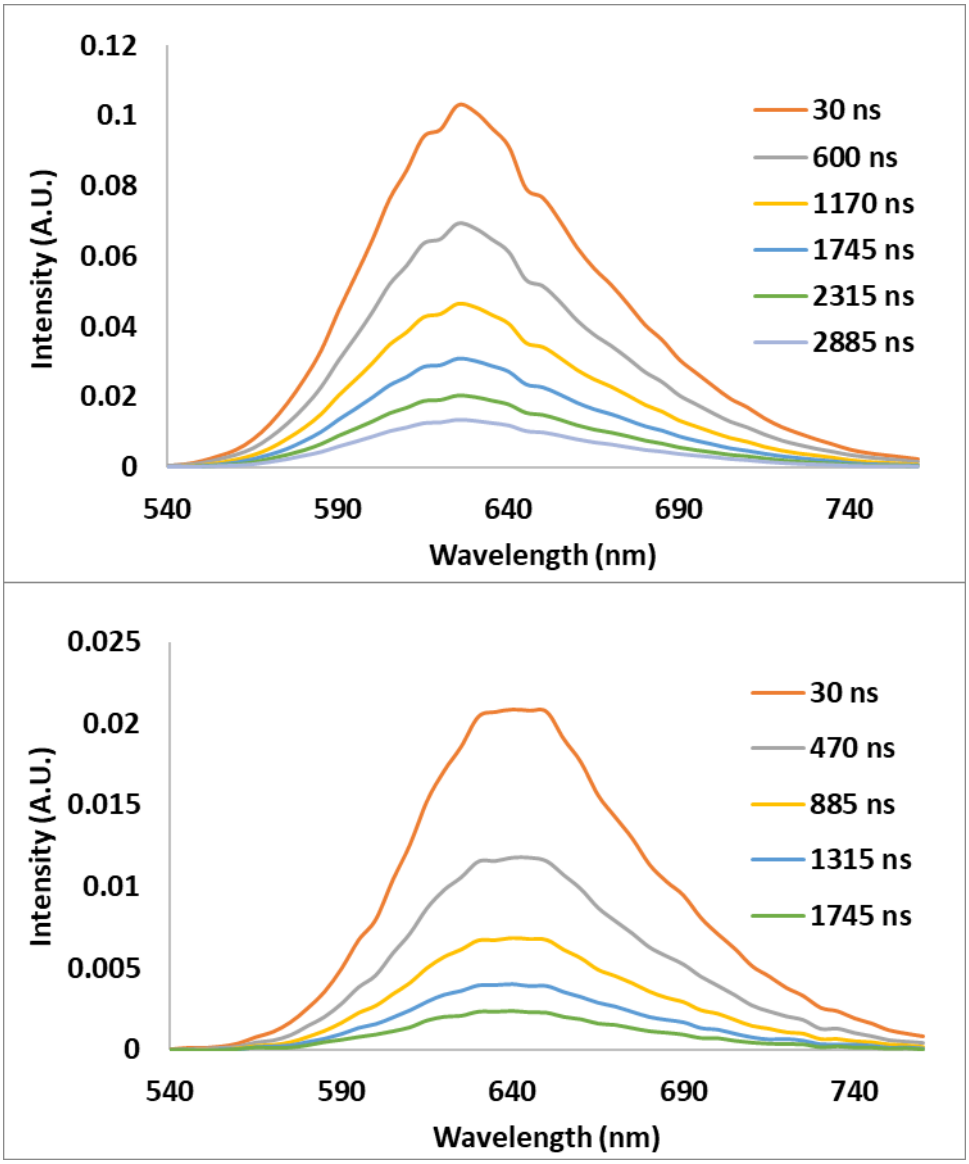

Figure 2.15: ns-time resolved emission spectra of mono- ***Ru$_{dpph}$*** *(top) and di-nuclear species* ***RuPt$_{dpph}$*** *(bottom) at certain timepoints following excitation at 355 nm in FPT prepared by freeze-pump-thaw under nitrogen in acetonitrile, OD at λ_{exc}= 0.27.*

In conjunction with the ns-TA experiments (Figure 2.14) the time resolved photoluminescence spectra, in Figure 2.15, were recorded and the lifetimes (Figure 2.7) for **Ru$_{dpph}$** and **RuPt$_{dpph}$**. While the lifetimes were briefly introduced when discussing the pico-second TA results, the time resolved photoluminescence were not discussed. The spectra displayed in Figure 2.15, are typical of those of ruthenium complexes. The emission maximum for the mononuclear and dinuclear complex occur at 627 and 646 nm, respectively, which is in agreement with the emission spectra in

Figure 2.7. The time constants recorded for both complexes, were; Ru_{dpph}: λ_{max} = 625 nm, τ = 1375 ns, $RuPt_{dpph}$: λ_{max} = 645 nm, τ = 795 ns, which is in agreement with the TA results discussed above.

2.4.3 Photocatalytic Hydrogen Generation Experiments

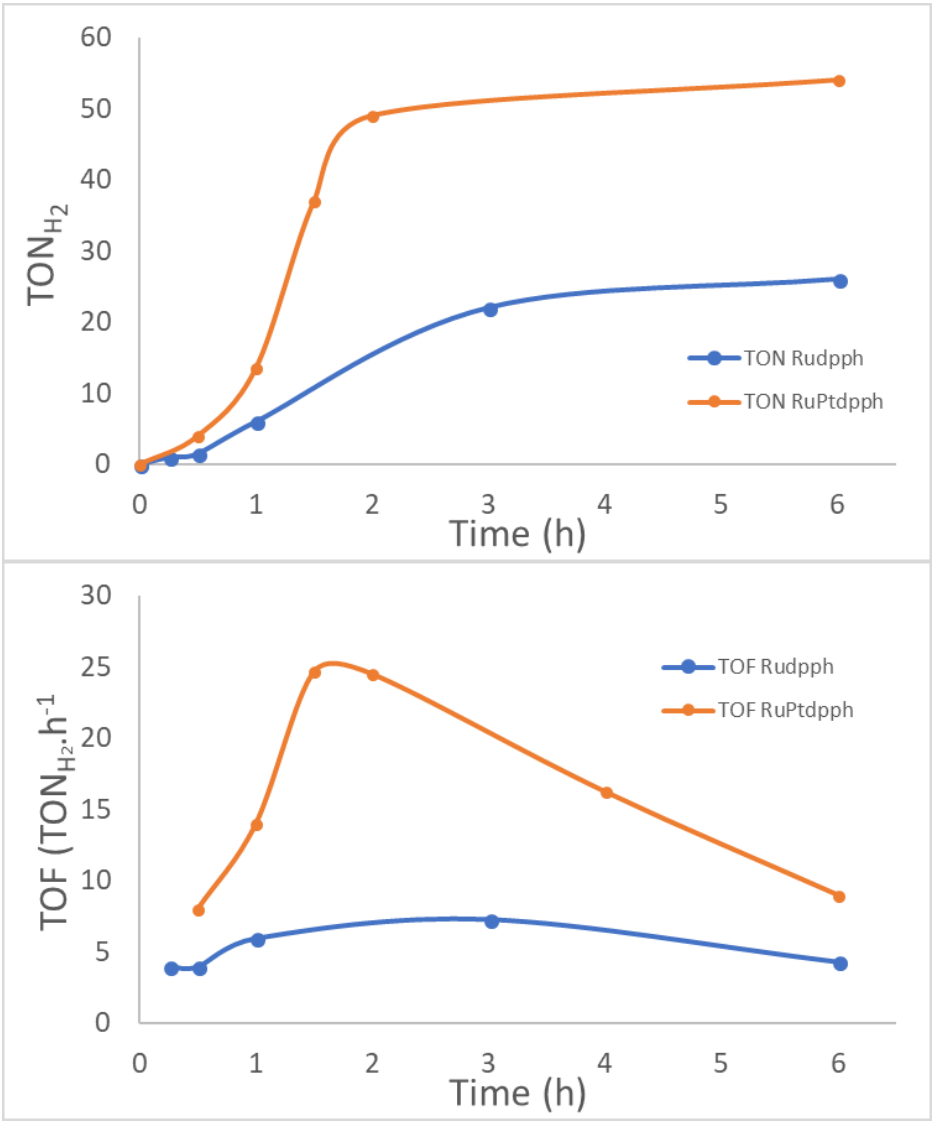

Figure 2.16: Photocatalysis results following irradiation with a 470 nm LED light source for multiple time points of both ***Ru_{dpph}*** *(blue line) and* ***$RuPt_{dpph}$*** *(orange line) in 60% acetonitrile, 10% water and 30% TEA (concentration of Ru_{dpph}/$(Pt(DMSO)_2I_2)$ or $RuPt_{dpph}$ ~$1.7x10^{-5}$ M). TON vs time (h) (top) and turnover frequency (TOF) (bottom). TON is calculated by the number of moles of hydrogen generated divided by the number of moles of catalyst present. TOF is the TON per hour.*

The photocatalysis experiments was conducted using the DCU group's standard method, to enable direct comparison of the complex following inter- and intra-

molecular approaches, with **Ru_{dpph}** vs **$RuPt_{dpph}$** and also vs other photocatalysts discussed in this chapter. Samples were irradiated using a 470 nm LED light source for 6 hours, yielding modest TONs of 26 for **Ru_{dpph},** with $Pt(DMSO)_2I_2$ as the catalyst, and a TON of 54 for **$RuPt_{dpph}$**. No hydrogen was detected with control samples which were left in the dark. The TOF of **$RuPt_{dpph}$** complex surpasses the capabilities of **Ru_{dpph}**, however they still remain modest values. In the TOF graph (right), there is a clear lag phase in the initial generation of hydrogen with the intermolecular approach, which has previously been observed for other intermolecular experiments. This lag phase was not evident for the **$RuPt_{dpph}$** complex, as it overcomes this by removing diffusion limitations and therefore is a more efficient photocatalyst. The stability of **$RuPt_{dpph}$** is however limited to ~1.5 h, which may be due to the presence of the sacrificial agent. As a result, the overall H_2 TON value plateaus after ~2 hrs.

2.5 Conclusion

Ru- and Pt-based complexes were employed in this chapter as they have been successfully used for the photogeneration of hydrogen from water. This enabled comparison of the photocatalytic activity of the complexes synthesised in the conditions applied to other similar working systems. Thus, growing the library of knowledge surrounding photocatalytic hydrogen evolution systems. Time-resolved studies are an extremely useful experimental tool to explore the inner workings of photocatalytic systems. The information gained from both early-time and later-time enables essential guidelines to be drafted.

In summary, a Ru tris-dpph-photosensitiser together with a catalytic unit has been examined to assess hydrogen evolution by varying the parameters of the intermolecular approach such as, solvent, catalyst, sacrificial agent, water percentage, ratio of PS to catalyst and varying headspace volume. A wide range of TONs for hydrogen evolution were achieved in this set of experiments, adding evidence to how the environment of the PS (and the catalysts) is as important as the properties of the PS and should also be taken into consideration.

Novel mono- and di-nuclear complexes were successfully synthesised, characterised and investigated for their hydrogen generation abilities. Along with this, the complexes were examined by ultrafast transient absorption spectroscopy, ranging from the fs to μs timescale. These studies concluded that the behaviours of these complexes reflect that of other similar systems such as Ru/RuPt$_{bpy}$. The longer ^{3}MLCT lifetimes achieved, did not yield higher TONs for hydrogen generation, which may be due to the stability of the photocatalyst.

The studies conducted in this chapter highlight the environmental and structural influence on the photocatalytic activity of a system. Although, it may be logical to synthetically optimise a photocatalyst to an environment that is simple to upscale, such as, a photocatalyst immobilised on the surface of an electrode in aqueous conditions. First, the processes and pathways of electrons within working photocatalysts need to be understood in detail. Therefore, a greater understanding is gained when comparing the electron dynamics within complexes when in solution vs. bound to an electrode. This type of investigation, such as, that carried out in this chapter, is integral to

progression of photocatalytic hydrogen generation technology towards global implementation as an alternative fuel source.

References

[1] J. M. Lehn, J. P. Sauvage, *Nouv J Chem* **1977**, *1*, 449–450.

[2] K. Kalyanasundaram, J. Kiwi, M. Grätzel, *Helv. Chim. Acta* **1978**, *61*, 2720–2730.

[3] J. Kiwi, M. Grätzel, *Nature* **1979**, *281*, 657–658.

[4] G. M. Brown, B. S. Brunschwig, C. Creutz, J. F. Endicott, N. Sutin, *J. Am. Chem. Soc.* **1979**, *101*, 1298–1300.

[5] E. Amouyal, P. Keller, A. Moradpour, *J. Chem. Soc. Chem. Commun.* **1980**, *0*, 1019–1020.

[6] J. R. Fisher, D. J. Cole-Hamilton, *J. Chem. Soc. Dalton Trans.* **1984**, *0*, 809–813.

[7] Y. Na, M. Wang, J. Pan, P. Zhang, B. Åkermark, L. Sun, *Inorg. Chem.* **2008**, *47*, 2805–2810.

[8] D. Streich, Y. Astuti, M. Orlandi, L. Schwartz, R. Lomoth, L. Hammarström, S. Ott, *Chem. – Eur. J.* **2010**, *16*, 60–63.

[9] W. R. McNamara, Z. Han, C.-J. (Madeline) Yin, W. W. Brennessel, P. L. Holland, R. Eisenberg, *Proc. Natl. Acad. Sci.* **2012**, *109*, 15594–15599.

[10] Y. Sun, J. Sun, J. R. Long, P. Yang, C. J. Chang, *Chem. Sci.* **2013**, *4*, 118–124.

[11] S. Varma, C. E. Castillo, T. Stoll, J. Fortage, A. G. Blackman, F. Molton, A. Deronzier, M.-N. Collomb, *Phys. Chem. Chem. Phys.* **2013**, *15*, 17544–17552.

[12] F. Lucarini, M. Pastore, S. Vasylevskyi, M. Varisco, E. Solari, A. Crochet, K. M. Fromm, F. Zobi, A. Ruggi, *Chem. – Eur. J.* **2017**, *23*, 6768–6771.

[13] O. Schott, A. K. Pal, D. Chartrand, G. S. Hanan, *ChemSusChem* **2017**, *10*, 4436–4441.

[14] Q. Pan, L. Freitag, T. Kowacs, J. C. Falgenhauer, J. P. Korterik, D. Schlettwein, W. R. Browne, M. T. Pryce, S. Rau, L. González, et al., *Chem. Commun.* **2016**, *52*, 9371–9374.

[15] G. S. Bindra, M. Schulz, A. Paul, R. Groarke, S. Soman, J. L. Inglis, W. R. Browne, M. G. Pfeffer, S. Rau, B. J. MacLean, et al., *Dalton Trans.* **2012**, *41*, 13050–13059.

[16] N. H. Damrauer, G. Cerullo, A. Yeh, T. R. Boussie, C. V. Shank, J. K. McCusker, *Science* **1997**, *275*, 54–57.

[17] J. M. Rehm, G. L. McLendon, Y. Nagasawa, K. Yoshihara, J. Moser, M. Grätzel, *J. Phys. Chem.* **1996**, *100*, 9577–9578.

[18] Q. Pan, F. Mecozzi, J. P. Korterik, D. Sharma, J. L. Herek, J. G. Vos, W. R. Browne, A. Huijser, *J. Phys. Chem. C* **2014**, *118*, 20799–20806.

[19] Q. Pan, F. Mecozzi, J. P. Korterik, J. G. Vos, W. R. Browne, A. Huijser, *ChemPhysChem* **2016**, *17*, 2654–2659.

[20] S. Tschierlei, M. Karnahl, M. Presselt, B. Dietzek, J. Guthmuller, L. González, M. Schmitt, S. Rau, J. Popp, *Angew. Chem. Int. Ed.* **2010**, *49*, 3981–3984.

[21] L. Zedler, J. Guthmuller, I. R. de Moraes, S. Kupfer, S. Krieck, M. Schmitt, J. Popp, S. Rau, B. Dietzek, *Chem. Commun.* **2014**, *50*, 5227–5229.

[22] G. S. Bindra, M. Schulz, A. Paul, S. Soman, R. Groarke, J. Inglis, M. T. Pryce, W. R. Browne, S. Rau, B. J. Maclean, et al., *Dalton Trans.* **2011**, *40*, 10812–10814.

[23] T. Kowacs, Q. Pan, P. Lang, L. O'Reilly, S. Rau, W. R. Browne, M. T. Pryce, A. Huijser, J. G. Vos, *Faraday Discuss.* **2015**, *185*, 143–170.

[24] H. Ozawa, M. Haga, K. Sakai, *J. Am. Chem. Soc.* **2006**, *128*, 4926–4927.

[25] M. G. Pfeffer, T. Kowacs, M. Wächtler, J. Guthmuller, B. Dietzek, J. G. Vos, S. Rau, *Angew. Chem. Int. Ed.* **2015**, *54*, 6627–6631.

[26] T. A. White, S. L. H. Higgins, S. M. Arachchige, K. J. Brewer, *Angew. Chem. Int. Ed.* **2011**, *50*, 12209–12213.

[27] S. L. H. Higgins, T. A. White, B. S. J. Winkel, K. J. Brewer, *Inorg. Chem.* **2011**, *50*, 463–470.

[28] T. A. White, J. D. Knoll, S. M. Arachchige, K. J. Brewer, *Materials* **2011**, *5*, 27–46.

[29] K. F. Mongey, J. G. Vos, B. D. MacCraith, C. M. McDonagh, C. Coates, J. J. McGarvey, *J. Mater. Chem.* **1997**, *7*, 1473–1479.

[30] J. D. Knoll, S. L. H. Higgins, T. A. White, K. J. Brewer, *Inorg. Chem.* **2013**, *52*, 9749–9760.

[31] L. O'Reilly, Q. Pan, N. Das, K. Wenderich, J. P. Korterik, J. G. Vos, M. T. Pryce, A. Huijser, *ChemPhysChem* **2018**, *19*, 3084–3091.

[32] J. H. Price, A. N. Williamson, R. F. Schramm, B. B. Wayland, *Inorg. Chem.* **1972**, *11*, 1280–1284.

[33] T. Kowacs, L. O'Reilly, Q. Pan, A. Huijser, P. Lang, S. Rau, W. R. Browne, M. T. Pryce, J. G. Vos, *Inorg. Chem.* **2016**, *55*, 2685–2690.

[34] S. L. Hopkins, L. Stepanyan, N. Vahidi, A. Jain, B. S. J. Winkel, K. J. Brewer, *Inorganica Chim. Acta* **2017**, *454*, 229–233.

[35] J. K. White, K. J. Brewer, *Chem. Commun.* **2015**, *51*, 16123–16126.

[36] A. T. Yeh, C. V. Shank, J. K. McCusker, *Science* **2000**, *289*, 935–938.

[37] A. Cannizzo, F. van Mourik, W. Gawelda, G. Zgrablic, C. Bressler, M. Chergui, *Angew. Chem.* **2006**, *118*, 3246–3248.

[38] S. Wallin, J. Davidsson, J. Modin, L. Hammarström, *J. Phys. Chem. A* **2005**, *109*, 4697–4704.

[39] C. W. Stark, W. J. Schreier, J. Lucon, E. Edwards, T. Douglas, B. Kohler, *J. Phys. Chem. A* **2015**, *119*, 4813–4824.

[40] M. Kovács, K. L. Ronayne, W. R. Browne, W. Henry, J. G. Vos, J. J. McGarvey, A. Horváth, *Photochem. Photobiol. Sci.* **2007**, *6*, 444–453.

Chapter 3

3 Homogenous to Heterogenous Photo-driven Systems

Chapter 3 compares a working hydrogen evolution photocatalyst, [Ru(dceb)$_2$(2,5-bpp)PtI(CH$_3$CN)](PF$_6$)$_2$ (RuPt$_{2,5\text{-bpp}}$), to a novel photocatalyst utilising a triazole bridging ligand (3,5-bis(2-pyridyl)-1,2,4-triazole = bpt) and a PdCl catalytic centre (RuPd$_{bpt}$). Both complexes were synthesised, characterised, and photocatalytic hydrogen evolution experiments were performed. Early-time photodynamics, in solution and on the surface of NiO films, were studied and compared to similar systems, using time-resolved IR and transient absorption techniques. These studies were conducted using the ULTRA facility at the Rutherford Appleton Laboratories (RAL) in the U.K. in collaboration with Elizabeth Gibson's Research Group, from Newcastle University, U.K. The Gibson group further investigated the complexes by photoelectro-characterisation techniques and their capability as p-type dye sensitised solar cells (p-DSSCs).

Photoelectrocatalytic H_2 evolution from integrated photocatalysts adsorbed on NiO
N. Põldme,* L. O'Reilly,* I. Fletcher, J. Portoles, I. V. Sazanovich, M. Towrie, C. Long, J. G. Vos, M. T. Pryce, E. A. Gibson
Chemical Science **2019** *10* (1), 99-112

*contributed equally to this paper and our joint first author.

3.1 Aim

An overall aim, of this chapter, was to develop ruthenium-platinum/palladium p-type dye sensitised photocathodes. The focal aim, following years of research in this area conducted using ruthenium-platinum/palladium photocatalysts in solution, was to immobilise the complexes on the surface of a p-type semiconductor, such as, NiO, thus enabling a photoelectrocatalytic approach towards hydrogen generation. A novel supramolecular photocatalyst, was synthesised, and compared with a known photocatalyst which yielded high TON for hydrogen in solution. The early-time photodynamics pathways for both complexes were probed both in solution and also on the surface of NiO films. The utilisation of established time resolved techniques including time-resolved IR (TRIR) where we monitored the carbonyl-ester groups, of the sensitised NiO films, together with transient absorption spectroscopy allowed us to probe the electron pathways in these systems, with view to progress to novel non-noble metal containing complexes capable of photo-driven hydrogen evolution.

3.2 Introduction

3.2.1 The Complexes $RuPt_{2,5\text{-bpp}}$ and $RuPd_{bpt}$

Chapter 1 provided a literature review into p-type dye-sensitised solar cells (p-DSSCs). The parameters and complications involved with heterogenous systems (as opposed to homogeneous) were highlighted in chapter 1 of this thesis. Chapter 2 summarised the literature relevant to the electron pathways taken within Ru-Pt/Pd assemblies monitored by transient absorption studies in solution. In this chapter, the focus is on the early-time photodynamics of the photocatalysts once immobilised on to the surface of a NiO film. The mononuclear (intermolecular PS) and dinuclear (intramolecular photocatalyst) of each species are investigated in solution and on the surface of NiO films for comparison. The work in this chapter has led to a publication, involving two of the focal complexes of this chapter. The systems discussed in the paper are the first published dye sensitised photocathodes employing Ru-Pt/Pd intramolecular photocatalysts with peripheral ester groups anchoring the complexes to NiO semiconductors.

One of the complexes studied in this chapter has already been discussed in the two previous chapters, $[Ru(dceb)_2(2,5\text{-bpp})PtI(CH_3CN)](PF_6)_2$. In Chapter 1, this photocatalyst is denoted as **3d** and it is introduced as the RuPt complex that achieves the high TON of hydrogen, generated under homogeneous conditions (TON of 650 after 6h) at DCU.[1] In Chapter 2 the complex is referred to as $RuPt_{dceb}$. Chapter 2 discusses previous time-resolved studies using $RuPt_{dceb}$, conducted by the DCU group and with collaborators from Twente.[2] These studies are used, in Chapter 2, as a reference point for comparison to that recorded for $RuPt_{dpph}$.[3] These studies were used to understand the electron transfer pathways that led to the high TON observed for hydrogen generation. In this chapter $RuPt_{dceb}$ is known as $RuPt_{2,5\text{-bpp}}$ to distinguish it from the other photocatalysts investigated within this chapter, as all these complexes utilise the dceb ligand, allowing for the immobilisation onto the NiO surface.

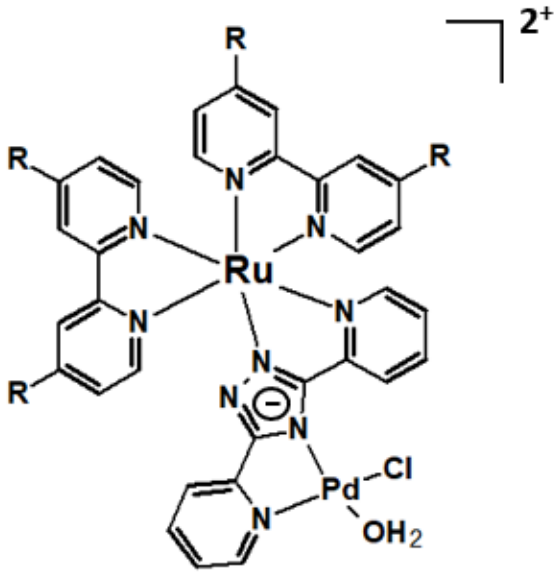

Figure 3.1: Structure of $[Ru(dceb)_2(bpt)PdCl(H_2O)]^{2+}$ where bpt = 3,5-bis(2-pyridyl)-1,2,4-triazole. The complex is denoted as $RuPd_{bpt}$ throughout the text. The negative charge on the pyridine ring indicates the complex is deprotonated. The counter ion is $(PF_6)_2$. R = CO_2Et.

The other principal complex, featured in the publication, is the novel Ru-triazole-Pd photocatalyst ($[Ru(dceb)_2(bpt)PdCl(H_2O)](PF_6)_2$, where bpt = 3,5-bis(2-pyridyl)-1,2,4-triazole), denoted $RuPd_{bpt}$, and depicted in

Figure 3.1. Ruthenium-triazole systems have been widely investigated by many, including extensive work by Vos and co-workers, due to their interesting spectroscopic, photophysical and electrochemical properties and pH chemistry.[4–11] Triazole ligands are typically strong σ-donors that create larger ligand field splitting avoiding population of the ^{3}MC. Triazole type ligands are also weak π-acceptors causing a blue shift in absorbance compared to that of the $Ru(bpy)_3$ parent complex. The blue shift usually observed in the absorbance spectra for triazole complexes can be counteracted by either substitution on the triazole with strong π-acceptor type substituents, such as, pyrazine-type units or in mixed ligand systems, e.g. $[Ru(bpy)_2(\text{triazole-type ligand})]^{n+}$. Although, the Hbpt ligand employed in Ru_{bpt} and $RuPd_{bpt}$ furnishes the triazole with pyridine, a weak π-acceptor, the implementation of the carboxy-esters make the dceb ligand a better π-acceptors with lower π* energy than bpy, which is manifested in a red shift in absorbance.[12]

There are two possible coordination sites for the Hbpt ligand. In Figure 3.1, the $Ru(dceb)_2$ unit is coordinated to the nitrogen on the pyridyl and the N_1 of the triazole ring, whereas, the Pd-moiety is coordinated to the nitrogen on the second pyridyl ring and the N_4 of the triazole ring. The coordination site also plays a role on the properties of the system, with the N_1 coordination found to be a stronger σ-donor than the N_4 site, attributing to a red shift in the UV-vis absorbance spectrum. In general, when synthesising mononuclear Ru-triazole species, coordination of the Ru-motif to the N_1 or N_4 or the dinuclear RuRu complex can be formed. Therefore, care is taken with the synthesis to limit or separate the unwanted complexes. The presence of large substituents on the triazole ring, such as the pyridine on the Hbpt ligand, reduces the likelihood of N_4 coordination. The properties of Ru-triazole complexes are also determined by the protonation state of the triazole ring.[5] Deprotonation of the N_4 on the triazole ring renders the bpt ligand a stronger σ-donor and this is observed in a further red shift in the UV-vis absorbance spectra. Upon addition of the second metal the Hbpt bridge is deprotonated, therefore, it is also important to investigate the deprotonated mononuclear complex for comparative purposes. Vos and co-workers have also investigated the interaction between two metal centres on a polypyridyl-triazole bridge.[13–15] They established that a strong interaction exists between two $Ru(bpy)_2$ units connected via a bpt bridge, and this is due to the negative charge on the deprotonated triazole ring.[6] In a separate publication, Vos and co-workers explored the early-time photodynamics of the $[Ru(dcb)_2\text{-bpt-}Ru(bpy)_2]^{3+}$ complexes immobilised on the surface TiO_2, a metal oxide typically used as an anodic electrode for the half-reaction of water oxidation.[16] In this study carboxylic acids were the anchoring group utilised on one of the $Ru(bpy)_2$ units (dcb) and discusses electron injection to the TiO_2 as oppose to hole injection to the NiO discussed here. The hetero-dinuclear complex, $RuPd_{bpt}$ in Figure 3.1, employs a palladium catalytic centre, used in many previous systems.[12,17–19] Rau and co-workers reported higher TON when using a Pd centre, although instability in solution lead to colloid formation.[20] Although, this may be the case when the complex is in solution, in this chapter, the immobilisation of the RuPd complex on to the surface of NiO was thought to possibly increase the stability of the photocatalyst.[16,21,22]

3.2.2 Time-resolved Transient Absorption of p-DSSCs

Chapter 2 provided a brief literature review of relevant time-resolved transient absorption (TA) investigations of charge transfer within Ru-complexes in solution. This chapter presents a synopsis of the literature surrounding TA used to investigate the electron transfer dynamics of hole injection and recombination between immobilised Ru-complexes and the NiO film. Although there are many transition metal complexes or organic dyes used in p-DSSCs, some of which were discussed in Chapter 1, Ru-polypyridyl complexes are the focus of this chapter. This work uses Ru-M based photocatalytic assemblies, exploiting the tuneability of this class of complex which have long-lived triplet excited states and electron absorption spectra that extend to the visible region. Along with the ease of combining the PS unit with a catalytic centre for full control over PS:Catalyst ratio and direct electron transport pathways from the PS to catalytic centre. These properties enable a full investigation of the contributing factors involved in the photoelectrocatalytic hydrogen generation process.

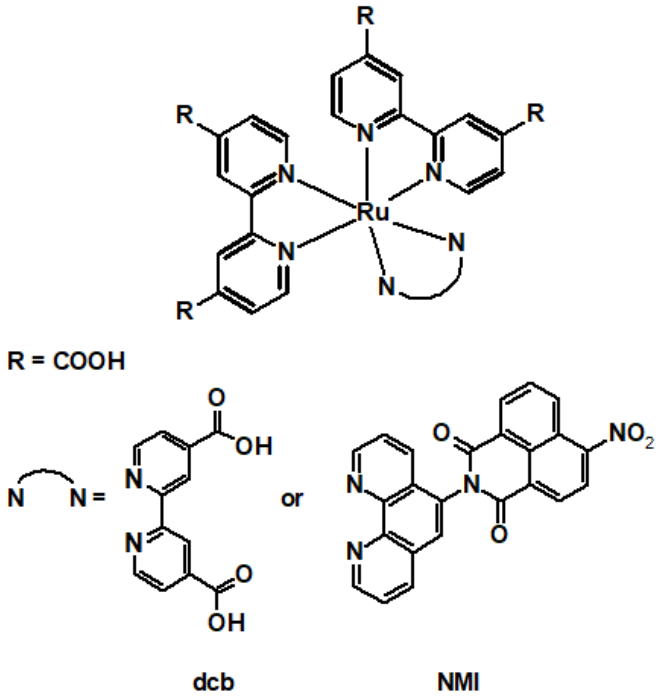

Figure 3.2: Structures of Ru-complexes subsequently immobilised to NiO for TA investigations conducted by Hammarström and co-workers[23] Discussed in the text below.

In 2012, Hammarström and co-workers synthesised a ruthenium polypyridyl complex with a *N*-(1,10-phenanthroline)-4-nitronaphthalene-1,8-dicarboximide (NMI) electron accepting ligand and immobilised it to p-type semiconductors, NiO.[23] Dyes employed up to this point were predominately organic dyes with high rates of recombination of the photogenerated charge separated state.[24–26] Studies on such organic dyes had shown the use of an electron accepting unit, located away from the NiO surface, which increased the lifetime of the charge separated state. Their $Ru(dcb)_2$(phen-NMI) complex, depicted in Figure 3.2, was designed to improve the efficiency of p-DSSCs by exploiting the charge transfer mechanics of ruthenium polypyridyl complexes (referenced throughout this thesis) and combine them with an electron acceptor unit, that would "pull" the excited electron away from the NiO surface, thus reducing the recombination rates.[27] Nanosecond TA studies confirmed this extended lifetime when comparing $[Ru(dcb)_3]^{2+}$ with $[Ru(dcb)_2(phen\text{-}NMI)]^{2+}$ (where lifetimes increasing from ~5μs to ~43 μs) and other organic dyes (phosphorous porphyrin had recovered by 90% after 8 ns).[24] Although, sub-picosecond TA could provide more detailed information it was not carried out with these systems.

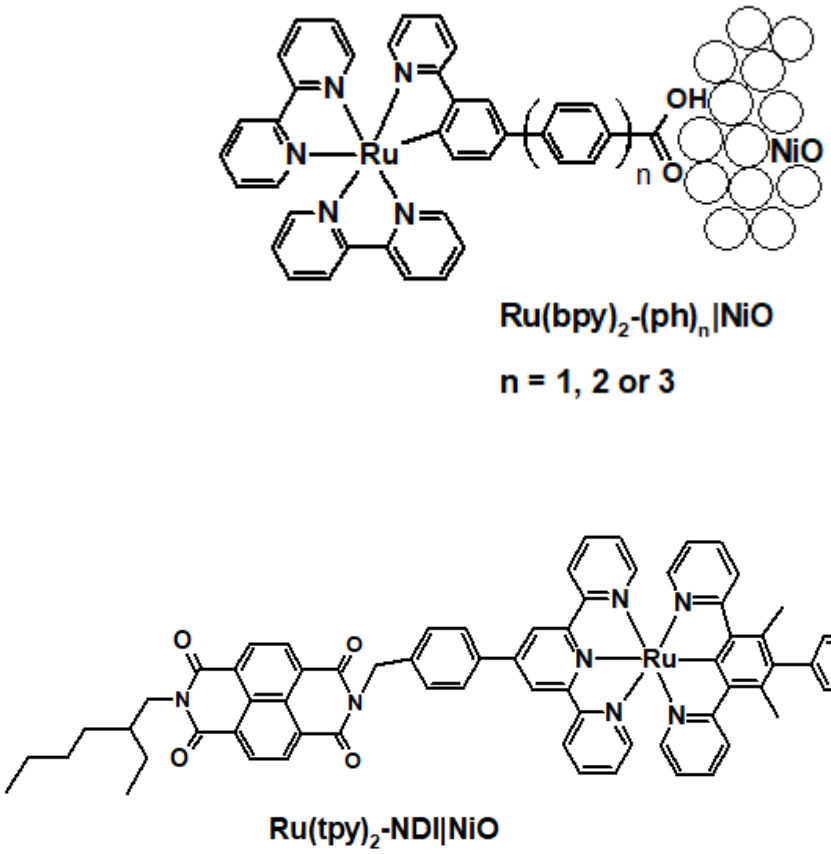

Figure 3.3: Structure of Ru-complexes immobilised to NiO investigated by TA spectroscopy, conducted by Wu and co-workers[28,29]

Also, in 2012, Wu and co-workers used TA, on the fs to sub-nanosecond timescale, to examine the effect on the recombination kinetics by adjusting the distance between the anchoring group and metal centre of the PS. They immobilised a Ru-complex to NiO films/electrodes using a carboxylic acid anchoring group on a phenylpyridine type ligand cyclometalated to the Ru metal of the PS unit ($Ru(bpy)_2$-$(ph)_n$|NiO, depicted in Figure 3.3).[28] TA investigations of the complexes in solution (CH_3CN) were used as a reference. The TA spectra of the solution and NiO immobilised samples, showed comparable ground state bleaching (GSB) but unique excited state absorption (ESA) features, which were contributed to hole injection in the immobilised systems. Their study found that hole injection occurred with all complexes within ~0.5 ps and increasing the length of the anchoring ligand lead to an increase in the lifetime of the charge separated state, with a decrease in initial recombination rates from 10 ps to 50 ps ($Ru(bpy)_2$-$(ph)_1$|NiO to $Ru(bpy)_2$-$(ph)_3$|NiO) (there is longer lived charge separation, <2 ns, but this surpasses the timeframe of the experiment). The slower rates improved the performance of the system, but the recombination rates remained magnitudes faster than that seen for systems on photoanodic surface, such as TiO_2, which occurs on the millisecond timescale.[30] Fast recombination is a consistent efficiency limiting factor surrounding p-DSSCs with a NiO surface.[24–26]

To combat these fast recombination rates (holes on NiO and electron on the PS), Wu and co-workers (2013) altered the ancillary ligand by extending the terpyridine ligand on a $[Ru(tpy)_2]^+$ photosensitiser with a naphthalenediimide (NDI) unit ($Ru(tpy)_2$-NDI|NiO, depicted in Figure 3.3).[29] The NDI unit acts as an acceptor for the excited electron, creating greater charge separation by 'pulling' the electron away from the hole on the NiO, thus reducing recombination. This work was inspired by similar studies conducted by Hammarström and co-workers discussed above.[23,27] TA experiments involving the $Ru(tpy)_2$-NDI|NiO system, verified a reduction in recombination rates when compared to the Ru-analogue without the NDI unit (~450 ps vs ~370 ps) but remained faster than previously reported Ru-complexes on TiO_2. By 2014 the Wu group achieved the highest efficiency for immobilised Ru-complexes on NiO for p-DSSCs with efficiency of 0.104% with their complex $Ru(phbpy)_2$-N on NiO.[31] TA confirmed reduced charge recombination times with this complex.

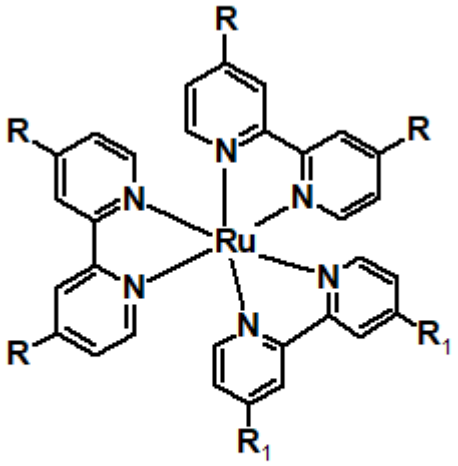

$Ru(dceb)_3$: R = R_1 = COOEt

$Ru(bpy)_2(dcb)$: R = H, R_1 = COOH

Figure 3.4: Structures of Ru-complexes subsequently immobilised to a NiO surface for TA studies conducted by Dietzek and co-workers[32]

In 2015, Dietzek and co-workers used TA to investigate recombination rates for a series of Ru complexes when the number of anchoring groups on a Ru-photosensitising unit is varied, together with altering the ancillary ligand, by introducing better π-accepting ligands.[33] Their study was based on prior findings from Odobel and co-workers[34] and other studies conducted by Dietzek and co-workers[32] on Ru-bpy complexes (both are discussed in Chapter 1). Dietzek's 2015 studies compare similarly structured Ru-bpy derivatives, one complex uses a 4,4'-dicarboxy-2,2'-bipyridine (dcb) anchoring ligand on $[Ru(bpy)_2(dcb)]^{2+}$ complex, and the other complex is a Ru-tris[4,4'-bis(ethylcarboxy)-2,2'-bipyridine] ($Ru(dceb)_3$), (both use $(PF_6)^{2-}$ as the counter ion and are presented in Figure 3.4). Total reflection-Fourier transform infrared spectroscopy (ATR-FTIR) was used to ensure samples were bound to the surface of NiO film. The characteristic IR bands for the anchoring groups employed in their systems include ν(C=O), seen as a broad band 1700 cm^{-1} and ν(COO) a double band at 1600 cm^{-1}. The comparison of these IR bands of the samples in solution (CH_3CN) vs. bound to the NiO surface, indicated that for $Ru(bpy)_2(dcb)|NiO$ the stretching vibration for the C=O bond at 1600 cm^{-1} broadened and the $\nu_{C=O}$ at 1700 cm^{-1} vanished. This indicates the complex was successfully adhered on the surface of the NiO. In the case of $Ru(dceb)_3|NiO$, the $\nu_{C=O}$ at 1600 cm^{-}

^{1} band is also broadened, confirming binding to the surface. The band at 1700 cm^{-1} is unchanged, therefore, there are unbound ester groups present. Transient absorption studies conducted on the complexes immobilised to NiO nanoparticles, indicated that unbound carboxy-esters, positively influence the hole injection dynamics of the system. This is due to the carboxy-esters lowering the ^{3}MLCT state, thereby allowing the electron density to reside, mainly, on the unbound ester ligands, thus, easing hole transfer. The TA and DFT study by Huijser and co-workers, in collaboration with the DCU group, on a $RuPt_{2,5\text{-bpp}}$ complex, (discussed previously in chapter 2), describes a similar outcome of electron density residing on the PL.[2] Similarly, as discussed, the simple introduction of carboxy-esters, to an inactive photosensitiser (**7b → 7c** or **8b → 8c**, complex structures are found in Chapter 1**)**, produced a photocatalytically active complex. Having previously illustrated the importance of PL, this relays the significance of ancillary ligands to the photophysics of immobilised complexes on NiO and the subsequent CT dynamics of the system.

In the same year (2015), Hammarström and co-workers reported the ns-TA results, conducted with their $Ru(dcb)_2$(phen-NMI)|NiO system (discussed earlier), and how varying the bias applied effects the recombination rates.[35] Their experiments indicated that at a negative bias (vs Ag/Ag^+) the band gap states on the NiO fill with the electrons supplied, thus lowering the recombination rates. This was the first study to conclude an alternative pathway for recombination through the holes available in the band gap of the NiO, known as trap states. Trap states are essentially areas on a semiconductor that can cause recombination. There are deep and shallow trap states depending on how deep they lie in the band gap of the semiconductor. Deep traps states can be exploited in fast switch systems by enhancing recombination rates, or they can be detrimental, as they are here, and in the case of n-DSSCs, reducing the overall efficiency of the system.[36,37] The Hammarström group previously determined that the presence of the NMI ligand on their Ru-complex, slows charge recombination. This is due to the NMI ligand localising the electron further away from the NiO surface, thus, avoiding interfacial recombination.[23] Recombination rates are reduced further when a negative bias is applied as the second recombination pathway is closed, elongating the charge separation state.

In 2017, Artero and co-workers noted the above discussed findings and investigated the effect on the early-time photodynamics of Ru-compounds furnished with a number

of phosphonate anchoring groups (2 or 4 groups).[38] They employ a non-conjugated methyl spacer, thus, limiting the electronic interference between the anchor and the complex (opposite to that observed with the addition of carboxy groups, e.g. dceb). They also studied the effect of altering the ancillary ligand by introducing better π-accepting ligands (substitution of bpy for dppz). The addition of the anchoring groups has little effect on the dynamics (vs the complex without the methylphosphonate groups) when studied by TA in acetonitrile solution, owing to the methyl spacer limiting the interaction. The ESA features differ between bpy based and dppz based complexes, with the electron localising over the dppz ligand. TA experiments performed using RuP_4dppz suggested that the charge localised on the dppz ligand is stable, attributing to a high amplitude of the charge separated state up to the ns-timeframe of the temporal window then that of their bpy systems. All the complexes studied exhibited a multiexponential lifetime, with fast hole injection and a biphasic process of recombination. The pathways determining the two recombination rates are depicted in Figure 3.5. Artero reports the faster rate is related to the recombination of charge from the anchored ligand with the NiO and the longer-lived species is due to the charge being located away from the NiO surface on the ancillary ligands, as seen by Hammarström and Wu, discussed above. The Artero group stress that TA studies across wider timeframes (fs-ms) with an applied potential is necessary to further understanding and therefore progress within this research topic.

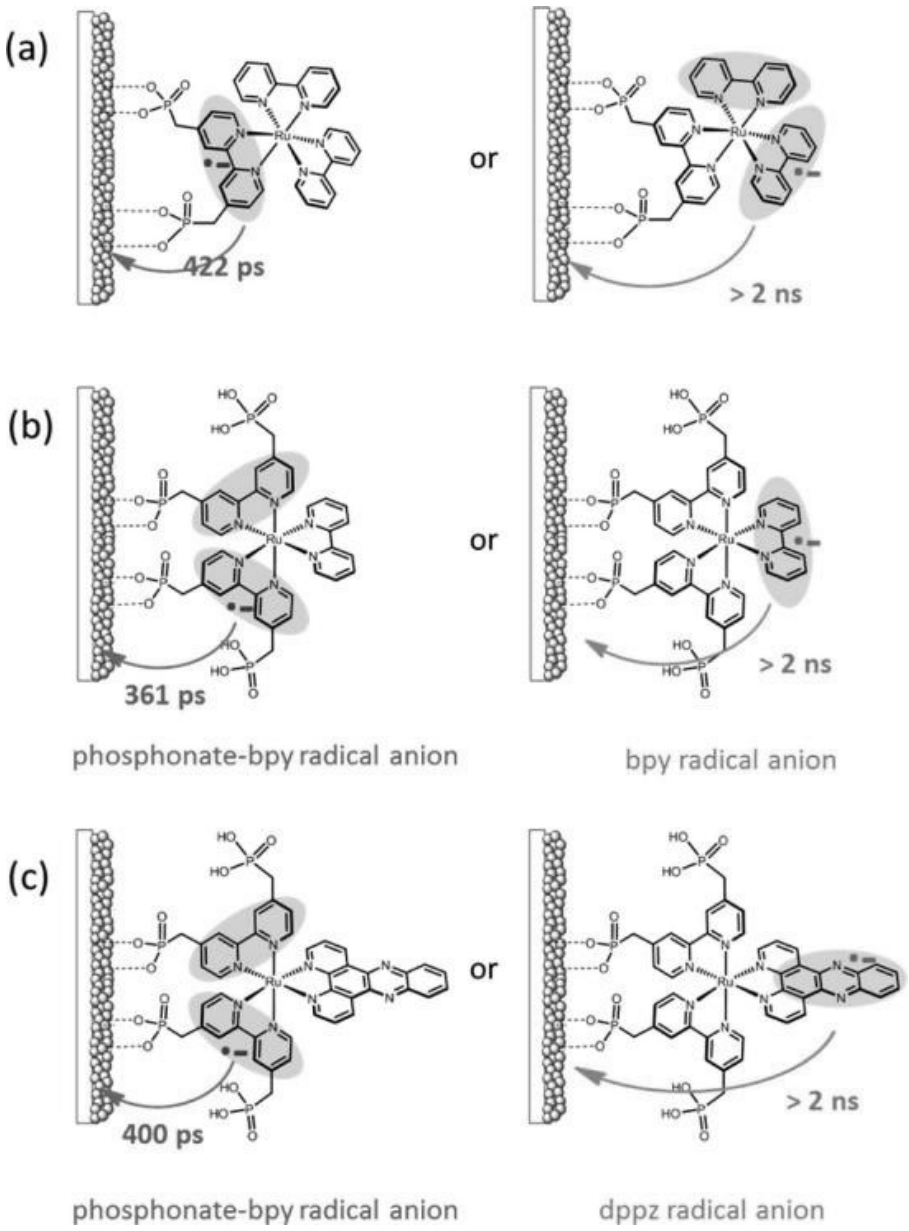

Figure 3.5: Schematic representation of (a) RuP_2bpy (b) RuP_4bpy and (c) RuP_4dppz PS and how they may be immobilised to the NiO surface and the photophysical scheme of different pathways of charge recombination for each system.[38]

The above studies all report the lack or minimal presence of the reduced PS as an indication of fast recombination after hole injection to the NiO. They also state that low hole mobility through the NiO maintains the injected hole at the interface of the anchored complex on the NiO film. More recently (2017), Papanikolas and co-workers have challenged this thinking and have found that fast recombination is not due to low hole mobility within the NiO film but the presence of trap states formed within the manufacturing process.[39] As discussed above, Hammarström and co-workers determined these trap states as a secondary recombination pathway.[35] The

Papanikolas group further probed this pathway using TA studies on the ps-timescale with RuP_2bpy, a complex that initially localises the electron density on the anchoring ligand, thus contributing to fast recombination (Figure 3.5 (a)). TA was employed to investigate the early-time photodynamics under different applied potentials, from positive to negative, causing vacant electronic states to be filled at more negative potentials, and altering the Fermi level of the semiconductor and closing this pathway of recombination with the trap states, enabling testing for low hole mobility within the NiO film. They concluded that this pathway was the main cause of fast recombination rates and that the introduction of an external negative bias closes this pathway leading to charge separated states on the millisecond scale for many complexes already investigated. They insist closer attention to the surface structure and interfacial electronic communication is paramount to the future progress of DSSCs.

3.2.3 Time-resolved Infrared Spectroscopy (TRIR) for DSSCs

The research performed in this chapter investigates the unbound ester groups in solution by TRIR and explores if kinetic information can be obtained using $\nu_{C=O}$ (in the ester group) as reporter ligands for the electron dynamics of the system. In conjunction with TRIR studies, TA studies were also performed. For the first time, in 1997, Heimer and Heilweil used ps-TRIR as a direct method of investigation into the charge transfer dynamics of electron injection of a Ru-complex onto TiO_2.[40] Utilising the intense IR bands of the carboxy ester groups on the $Ru(dceb)_2(bpy)$ complex immobilised to TiO_2 films, the $\nu_{C=O}$ stretching vibrations were utilised for kinetic data. Unfortunately, once on TiO_2 no excited state features were observed following excitation, so extrapolating kinetic information was not possible, but this study opened the door to this direct method of investigation. TRIR spectroscopy has been reported since to investigate immobilised complexes on both n-type and p-type materials. The work in this chapter describes how TRIR is used to directly probe electron dynamics on early-timescales using the dual functioning carboxy-ester anchoring groups as signallers in the mid-IR region.

3.3 Experimental

3.3.1 Materials

All experiments were conducted following the procedures described in Chapter 2, unless otherwise stated below. For solution ps-TA and ps-TRIR studies and for dye loading on the NiO films deuterated acetonitrile was used.

3.3.2 Equipment

All spectroscopic and photophysical techniques were recorded and processed as described in Chapter 2, unless otherwise stated below.

For ps-TA and TRIR measurements, the spectra were recorded using the ULTRA instrument at the Central Laser Facility in the Rutherford Appleton Laboratory in the U.K. The laser setup consists of two Ti:sapphire amplifiers of 1 kHz (pump) and 10 kHz (probe), which were synchronised with a 65 MHz oscillator. The pump laser was tuned to 470 nm by optical parametric amplification (OPA, Light Conversion, TOPAS). For TA spectroscopy, the probe pulse was provided by a white light continuum (WLC), which was generated by focusing 800 nm into CaF_2. The mid-IR probe pulses were generated using OPA with difference frequency mixing. The IR probe beam was split to form reference and probe beams which were passed through spectrographs onto MCT array detectors (IR Associates). High speed data acquisition systems (Quantum Detectors) allowed 10 kHz acquisition and processing of the probe and reference pulses to generate a pump-on pump-off infrared absorption difference signal. Spot sizes in the sample region were *ca*. 150 and 50 mm for the pump and probe, respectively, with a pump energy of 50 nJ. For all measurements, the pump polarisation was set to magic angle relative to the probe.

3.3.3 Time-resolved studies

The NiO films were prepared by the Gibson group by spraying a saturated solution of $NiCl_2$ in acetylacetone onto the surface of the CaF_2 window (Crystran), which was preheated to 450 °C on a hot plate; this was then allowed to cool slowly to room temperature to give a compact film of NiO. The mesoporous layer was then deposited

on top of the compact layer using the F108-templated precursor solution described below; the excess was removed by doctor blade. The film was sintered at 450 °C for 30 min, and an additional layer of precursor solution was applied and sintered to increase the film thickness. CaF_2|NiO windows were then left soaking overnight in a solution of a Ru-complex dissolved in deuterated acetonitrile. The windows were then rinsed and allowed to dry. All spectra were recorded in solution cells (Harrick Scientific Products Inc.) with CaF_2 windows. For samples prepared in solution, a 200 μm path length was used. In all experiments, the cell was rastered to minimise localised sample decomposition but maintaining the distance between the cell and the laser beam.

3.3.4 Quantum chemical methods

Quantum chemical methods were conducted by Prof. Conor Long. The calculations were used to gain theoretical insight to the electronic structure of both the ground singlet state and the lowest energy triplet states of the $RuPd_{bpt}$ complex discussed in this chapter. Three model systems were employed as the rotational energy required is higher for the methyl group (C-C bond) than that of the ester (C-O), $[Ru(bpy)_2(bpt)PdCl](PF_6)_2$, $[Ru(dmcb)_2(bpt)PdCl](PF_6)_2$, and $[Ru(dmcb)_2(bpt)PdCl(H_2O)](PF_6)_2$. Density functional theory (DFT) modelled the ground state structures and time-dependent density functional (TD-DFT) methods were used to characterise the low lying electronic excited states. B3LYP[41–43] was used with the doublezeta quality LanL2DZ basis set.[44–46] The same general approach was used for all complexes. Initial structures were generated by molecular mechanics methods and these were optimised at the B3LYP/LanL2DZ model chemistry. Either the presence of acetonitrile or water was included during calculations, following the Polarisable Continuum Method (PCM) approach.[47–49] All calculations were performed using the Gaussian 16, Revision A.03 programme suite.[50] Molecular structures and electron-density difference maps were visualised using GaussView 03.[51] Calculations were performed on the Fionn system at the Irish Centre for High End Computing.

3.3.5 Synthesis

dceb = 4,4'-di(carboxyethyl)-2,2'-bipyridine,[52] cis-$[Ru(dceb)_2Cl_2]$,[53] *cis*-$[Pt(DMSO)_2I_2]$,[1] cis-$[Pd(DMSO)_2Cl_2]$, $[Ru(dceb)_2(2,5\text{-bpp})](PF_6).2H_2O$, and $[Ru(dceb)_2(2,5\text{-bpp})PtI(CH_3CN)](PF_6)_2$, were prepared using literature methods. Solvents obtained were used without further purification.

$[Ru(dceb)_2(bpt)](PF_6)$ $2H_2O$. 84 mg (0.37 mmol) of 3,5-bis(2-pyridyl)-4-hydro-1,2,4-triazole (Hbpt) were dissolved in 60 mL EtOH/water (3:1) and heated for 20 minutes. 200 mg (0.26 mmol) of $[Ru(dceb)_2Cl_2]$ in ethanol was slowly added over 30 minutes. The reaction was brought to reflux temperature for a further 6 h, with a total volume of 100 ml. Subsequently, the ethanol was removed in *vacuo.* Following this, 40 mL of water was added to the reaction mixture. The red aqueous reaction mixture was filtered and an aqueous solution of NH_4PF_6 was added in excess to the filtrate and a precipitate formed. The precipitate was washed with diethyl ether and collected by filtration. For further purification, the filtrate was recrystallised with acetone/H_2O (3:1), yielding a black/brown solid. Yield: 212 mg (0.17 mmol, 65%). **^{1}H-NMR** (600 MHz, CH_3CN-d3) δ[ppm] = 1.35 - 1.45 (m, 12 H), 4.39 - 4.49 (m, 8 H), 7.27 (t, 1 H), 7.52 (dd, 1 H), 7.57 (td, 1 H), 7.72 (d, 1 H), 7.82 (dd, 1 H), 7.84 – 7.89 (m, 2 H), 7.93 (d, 1 H), 7.99 – 8.05 (m, 3 H), 8.10 (d, 1 H), 8.13 – 8.19 (m, 2 H), 8.24 (dd, 1 H), 8.51 (dd, 1 H), 8.97 (s, 1 H), 9.00 (s, 1 H), 9.02 – 9.05 (d, 2 H). **Elemental analysis** for $C_{44}H_{45}F_{12}N_9O_{10}P_2Ru$ Calc: C 42.2%, H 3.6%, N 10.1%. Found: C 42.12%, H 3.18% and N 10.28%.

$[Ru(dceb)_2(bpt)PdClH_2O](PF_6)_2.H_2O$. 28mg (0.11 mmol) of cis-$Pd(DMSO)_2Cl_2$ and 65 mg (0.05 mmol) of $[Ru(dceb)_2(bpt)](PF_6)_2$ $2H_2O$ were added to 15 mL of hot EtOH and stirred under nitrogen until dissolved. The reaction was brought to reflux temperature for 24 h. A precipitate formed, and the solution was allowed to cool to room temperature. The precipitate was collected by vacuum filtration and washed with cold EtOH and diethyl ether. Yield: 58 mg (0.04 mmol, 84%). **^{1}H-NMR** (400 MHz, acetonitrile-d3) δ[ppm] = 1.35 - 1.45 (m, 12 H), 4.39 - 4.49 (m, 8 H), 7.29 (t, 1 H), 7.50 (d, 2 H), 7.65 (t, 1 H), 7.70 (d, 1 H), 7.75 – 7.82 (m, 3 H), 7.83 (d, 1 H), 7.89 (d, 1 H), 7.95 – 8.05 (m, 2 H), 8.27 (d, 1 H), 8.36 (t, 1 H), 8.51 (d, 1 H), 8.95 – 9.08 (m, 3 H), 9.18 (d, 1 H), 9.60 (d, 1 H), 11.12 (d, 1 H). **Elemental analysis** for

$C_{44}H_{44}F_{12}N_9O_{10}P_2RuPdCl$ Calc: C 38.0%, H 3.2%, N 9.1%. Found: C 37.08%, H 2.71% and N 9.03%.

3.4 Results and Discussion

3.4.1 Studies of mono- and di-nuclear Ru-bpt/2,5-bpp complexes

3.4.1.1 Synthesis

Complexes $RuPd_{bpt}$ and $RuPt_{2,5\text{-}bpp}$ and their respective mononuclear precursors (Ru_{bpt} and $Ru_{2,5\text{-}bpp}$) were successfully synthesised using methods in the literature or modified versions. The complexes were characterised by ^{1}H-NMR and elemental analysis. The triazole complexes were also tested for their photocatalytic hydrogen production abilities and all complexes were investigated for their early-time photodynamics in CH_3CN and on the surface of NiO. Fiona Black, from Dr. Elizabeth Gibson's research group at Newcastle University, prepared the CaF_2|NiO windows for the time-resolved studies. Nils Põldme, also from the Gibson group, carried out photoelectrochemical characterisation on the dinuclear complexes. Prof. Conor Long, from DCU, conducted quantum mechanical calculations on model RuPd triazole complexes.

The results discussed focus on the synthesis of the novel triazole complexes. The dinuclear species, $RuPd_{bpt}$ and $RuPt_{2,5\text{-}bpp}$, complexes immobilised on NiO were used in the photoelectro-chemical/catalytic experiments. The early-time photodynamics studies include Ru_{bpt}, $RuPd_{bpt}$, $Ru_{2,5\text{-}bpp}$ and $RuPt_{2,5\text{-}bpp}$ and a series of other Ru-monomer and Ru-Pt/Pd dinuclear complexes that have been previously explored for hydrogen generation in solution (introduced to the reader in Chapter 1). The TRIR data for these complexes is not discussed in this thesis, as further experiments will be performed in Newcastle using these complexes immobilised on NiO.

3.4.1.2 ^{1}H-NMR and COSY-NMR Spectroscopy

As mentioned previously, the coordination site of the $Ru(dceb)_2$ unit on the triazole ring is a contributing factor to the spectroscopic and photophysical attributes of the mononuclear complex and subsequently the dinuclear species. Therefore, it is important to determine the coordination site of the novel mononuclear triazole complex, $[Ru(dceb)_2(bpt)](PF_6)_2$ depicted in Figure 3.6, prior to the addition of the

second metal centre. Spectroscopic techniques, such as, ^{1}H-NMR and COSY-NMR were applied to elucidate the structure of the complex.

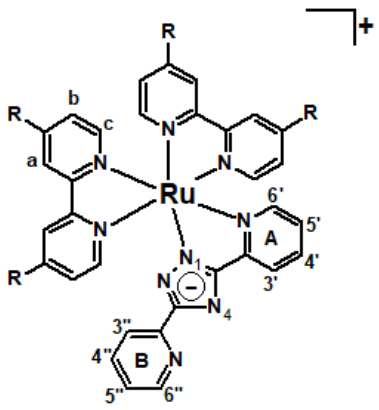

Figure 3.6: Structure of the mononuclear species[Ru(dceb)$_2$(bpt)](PF$_6$), R = COOEt.

The ^{1}H NMR spectra generated for the Ru$_{bpt}$ complex gives the typical features of the dceb protons when the Ru(dceb)$_2$ moiety is bound to the third ligand (Ru(dceb)$_2$(LL)), both in the aromatic region, attributed to the bpy based protons, and in the aliphatic region, based on the ethyl groups present.[1] There are also two distinct sets of the pyridyl protons, typical for the now asymmetric triazole ligand when bound to a Ru(L)$_2$ unit.[6,16] The ^{1}H NMR of the free Hbpt ligand is shown in Figure 3.7. This was then compared to the ^{1}H NMR of Ru$_{bpt}$ in CD$_3$CN (Figure 3.7: bottom) and that of similar complexes in the literature, which confirmed assignment of the doublet at 8.5 ppm to the H6" on the free pyridyl ring (ring B, in Figure 3.6). As expected the H6' proton is shifted upfield as Ru is coordinated to this ring (ring A), and the H6' proton feels the ring current of the spatially adjacent dceb ligand.[54] Assignment of the remaining protons is easily carried out using the COSY-NMR of Ru$_{bpt}$, shown in Figure 3.8. A comparison of the chemical shifts of the assigned peaks for the Ru$_{bpt}$ complex in the ^{1}H NMR with that of the free ligand and with the chemical shifts reported in the literature for Ru-bpt N$_1$ bound complexes, made it possible to determine that the coordination site was via the N$_1$ of the triazole ring, and the triazole ring is deprotonated in the complex. As mostly negative shifts are seen for all the pyridyl protons due to the anionic charge on the triazole ring which results in a slightly upfield shift.[6] Further confirmation that the triazole ring is deprotonated comes from the ^{1}H NMR of the complex with the addition of a base (NaOD). No shifts occur to the peaks as the complex is already deprotonated.

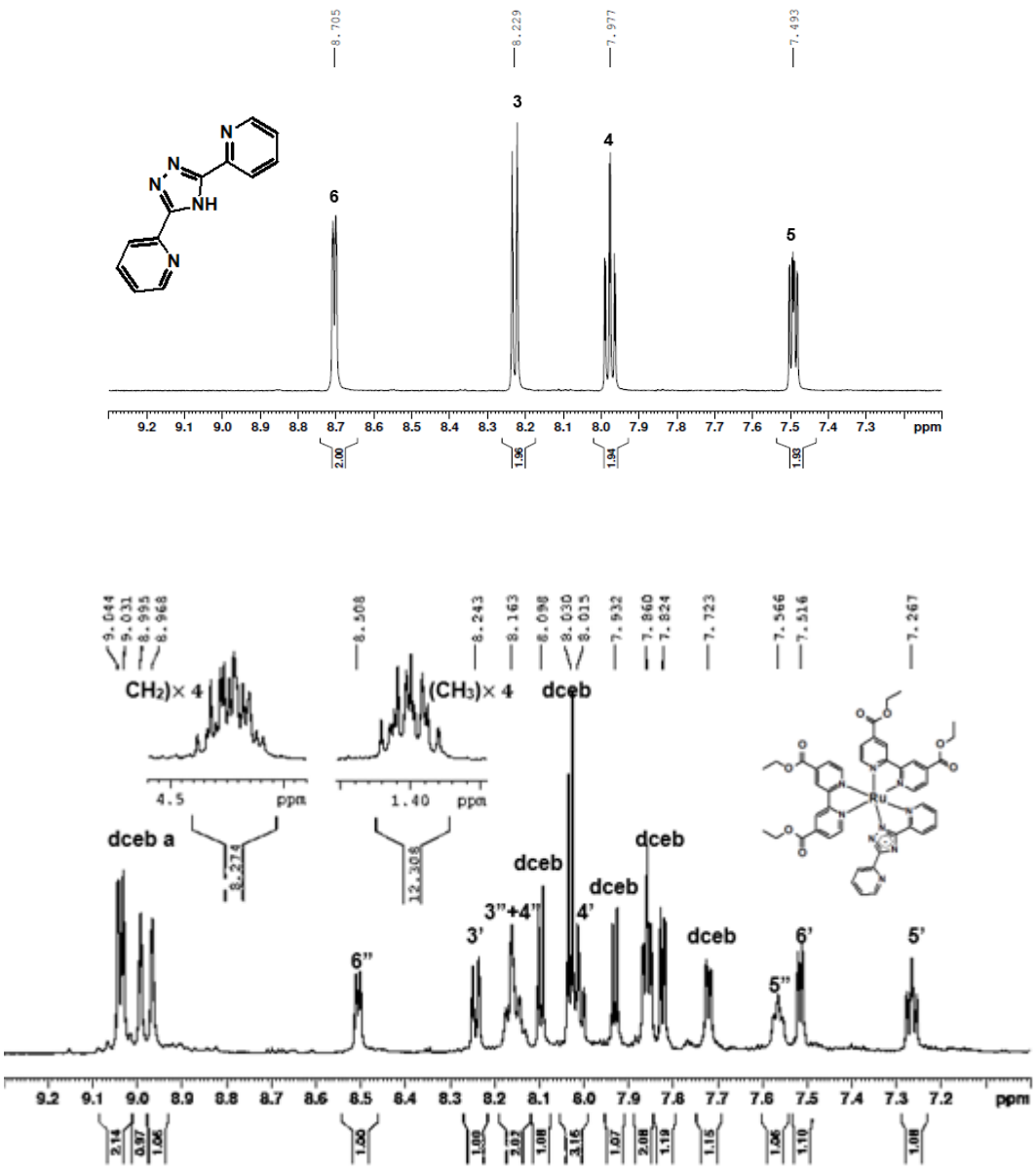

Figure 3.7: ^{1}H NMR spectra of Hbpt in CD_3CN (top) and Ru_{bpt} in CD_3CN (bottom)

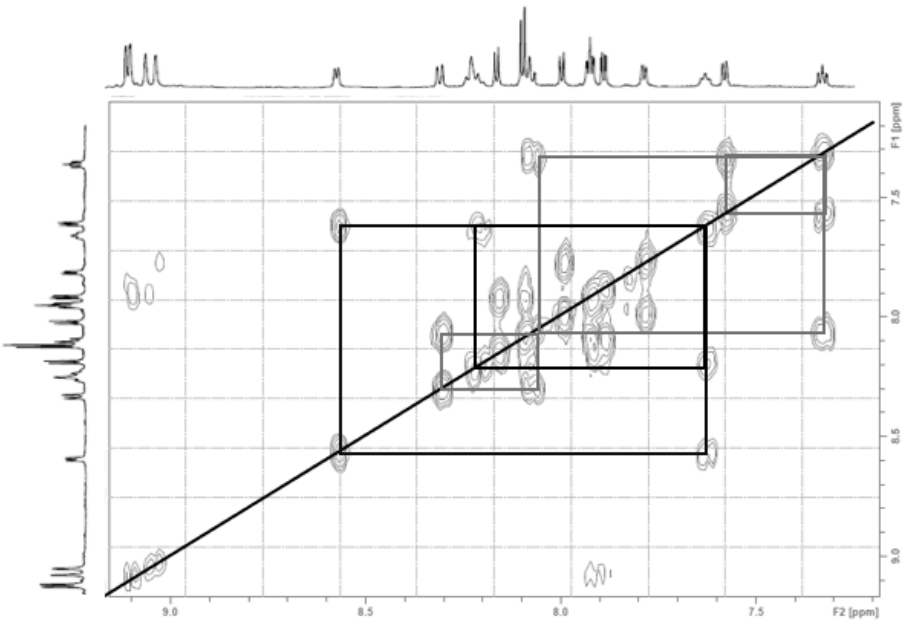

Figure 3.8: COSY-NMR spectrum of Ru_{bpt} in CD_3CN

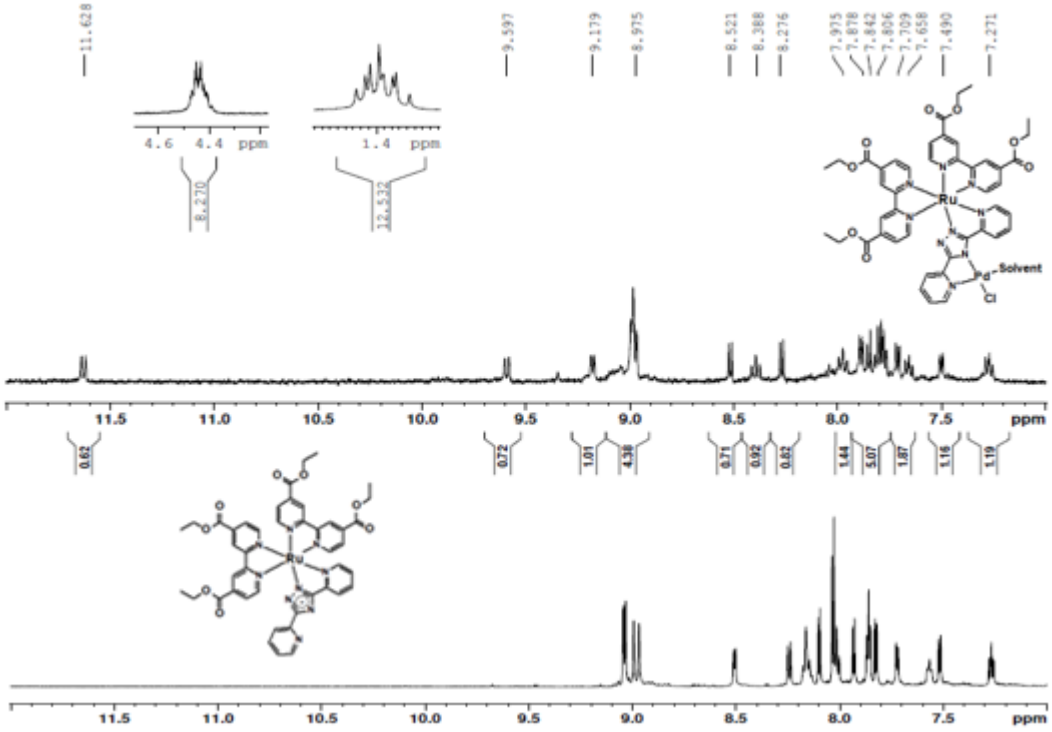

Figure 3.9: ^1H NMR spectrum of $RuPd_{bpt}$ in CD_3CN (top) and Ru_{bpt} (bottom) ^1H NMR spectrum for comparison.

The ^1H NMR spectrum of the dinuclear bpt complex, in Figure 3.9, follows a similar splitting pattern to that of other Ru-Pd/Pt dinuclear complexes reported in the literature.[1] A number of proton resonance are shifted downfield following

complexation with the Pd moiety. The ^{1}H NMR spectrum also proves the dceb ligand remains intact during the synthesis and purification.

3.4.1.3 UV-Vis Spectroscopy

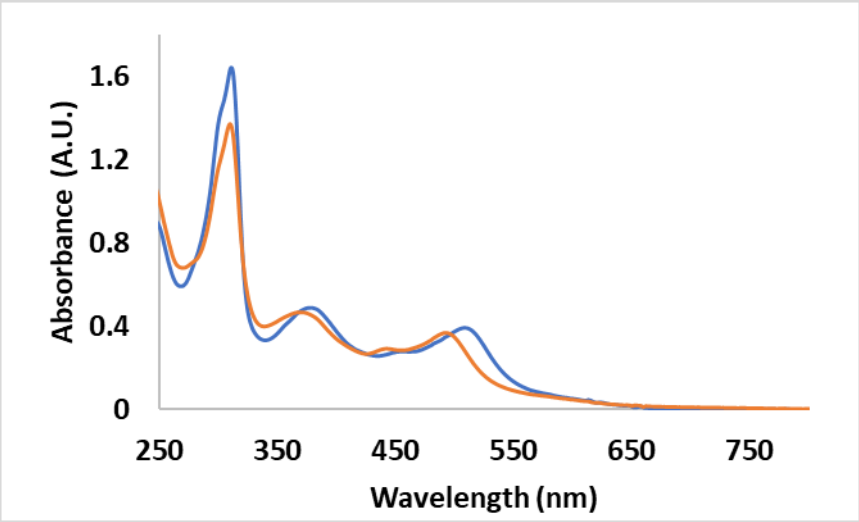

Figure 3.10: Electronic absorbance spectra of Ru_{bpt} (blue line) and $RuPd_{bpt}$ (orange line) in acetonitrile with an OD of ~0.37 at 355 nm.

The electronic absorption spectra of the deprotonated triazole Ru_{bpt}, in Figure 3.11 (blue line), reflects that of similar heteroleptic Ru-complexes, with one or more of the ligands containing carboxy-ester/acid groups.[55–60] The withdrawing effect of the carboxy-esters on the peripheral dceb ligands will contribute to a reduced HOMO-LUMO gap, observed as a bathochromic shift in the electronic absorption spectra *vs* $Ru(bpy)_2(L)$, where L is a triazole-type ligand.[61] Amedjkouh and co-workers reported that the asymmetry of the ligands also contributes to this bathochromic shift, as seen with a series of complexes involving $[Ru(dceb)_2(ppy)]PF_6$ type complexes, where ppy = phenylpyridine and is cyclometalated to the Ru-unit.[60] The asymmetry of the deprotonated triazole contributes to the additional features in the visible region with the Ru_{bpt} system when compared to the absorbance spectra of homoleptic complex, $Ru(dceb)_3$.[33] The strong σ-donor properties of the bpt ligand is also a factor in the redshift of the absorbance compared to other $Ru(dceb)_2(L)$ type complexes, such as the 2,5-bpp ligand of the $Ru_{2,5\text{-}bpp}$ studied in this chapter. The band from ~250-340 nm is attributed to the ligand centred (LC) π-π* transitions of the dceb and bpt ligands. The features present at >340 nm, are assigned to the ^{1}MLCT transitions of the complex with the lower energy absorption possibly due to Ru-dceb based transitions as the

TD-DFT calculations suggest (discussed further below). These assignments agree with the literature and the same assignments can be made for the dinuclear $RuPd_{bpt}$ species (orange). The electronic absorbance of the $RuPd_{bpt}$ complex undergoes a hypsochromic shift when compared to Ru_{bpt}. This is comparable with similar complexes with bpt type ligands as the anionic charge is delocalised over the two metal centres, reducing the electron density on the ruthenium metal centre, thus causing a blueshift of the ^{1}MLCT features.[61]

As discussed above, Ru-triazole complexes have multiple stages of protonation. The UV-Visible spectrum was used to further confirm the protonation state of the complex. The absorbance was monitored upon the addition of a base (TEA, as is used in the photocatalytic experiments), and no changes were observed. Upon deprotonation a redshift is expected, due to the increased σ-donating properties of the anionic ligand. This is additional evidence that the bridging ligand in the $RuPd_{bpt}$, complex is in the deprotonated state.[62–64] This deprotonation enables efficient electronic communication between the metal centres as in other dinuclear bpt systems, such as, the homo- (RuRu) and hetero-metallic (Ru/Os) bpt complexes.[16]

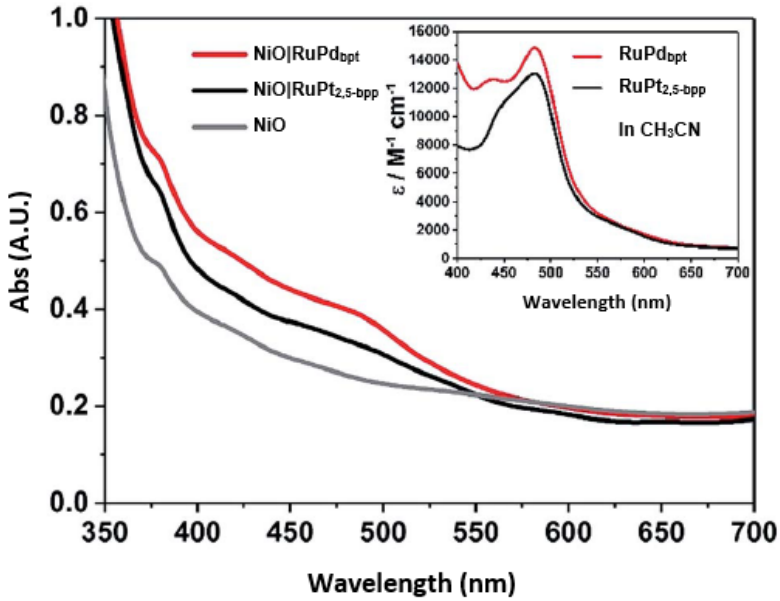

Figure 3.11: Electronic absorbance spectra of $RuPd_{bpt}$ and $RuPt_{2,5\text{-}bpp}$ immobilised to NiO and bare NiO. The insert is the that of the complexes in solution (CH_3CN).

Figure 3.11 represents the electronic absorption spectra of the dinuclear bpt and 2,5-bpp species studied in this chapter. The spectra also provide an example of the changes

experienced in the absorbance spectra for complexes dissolved in solution (insert) and when immobilised on the surface of a semiconductor, in this case NiO. The absorbance spectra of the complexes are broadened and blue-shifted (10 nm) once on the surface of the NiO vs. when in solution. The extinction coefficient is assumed to remain the same when on the surface as it is in solution and is used to determine the amount of photocatalyst grafted onto the NiO. These values are of similar orders of magnitude with other photocatalyst loading in the literature.[65]

3.4.1.4 FTIR Spectroscopy

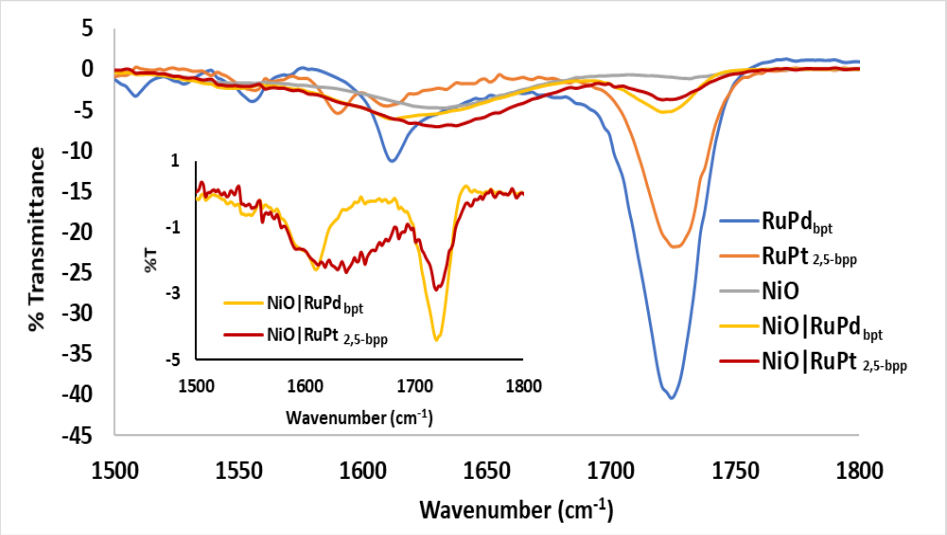

Figure 3.12: Graph of the FTIR spectra of $RuPd_{bpt}$ and $RuPt_{2,5\text{-}bpp}$ in KBr and on NiO and bare NiO. Insert is of the samples immobilised to NiO minus the bare NiO.

Prior to immobilisation, both complexes exhibit typical features in the IR for the carboxy-esters on the dceb, with the carbonyl band at 1724 cm^{-1} for the triazole dinuclear species and 1726 cm^{-1} for the terpyridine analogue, as seen in Figure 3.12. After immobilisation, these bands both shift to 1720 cm^{-1}, a possible indication of an interaction with the NiO surface and the ester moiety. The insert in the Figure 3.1 highlights that the IR bands related to the ester remain present, even after immobilisation, allowing for the band, now at 1720 cm^{-1}, to be monitored by TRIR. IR bands are significantly more sensitive to environmental changes than UV-Visible bands.

3.4.1.5 ps-Transient Absorption Studies

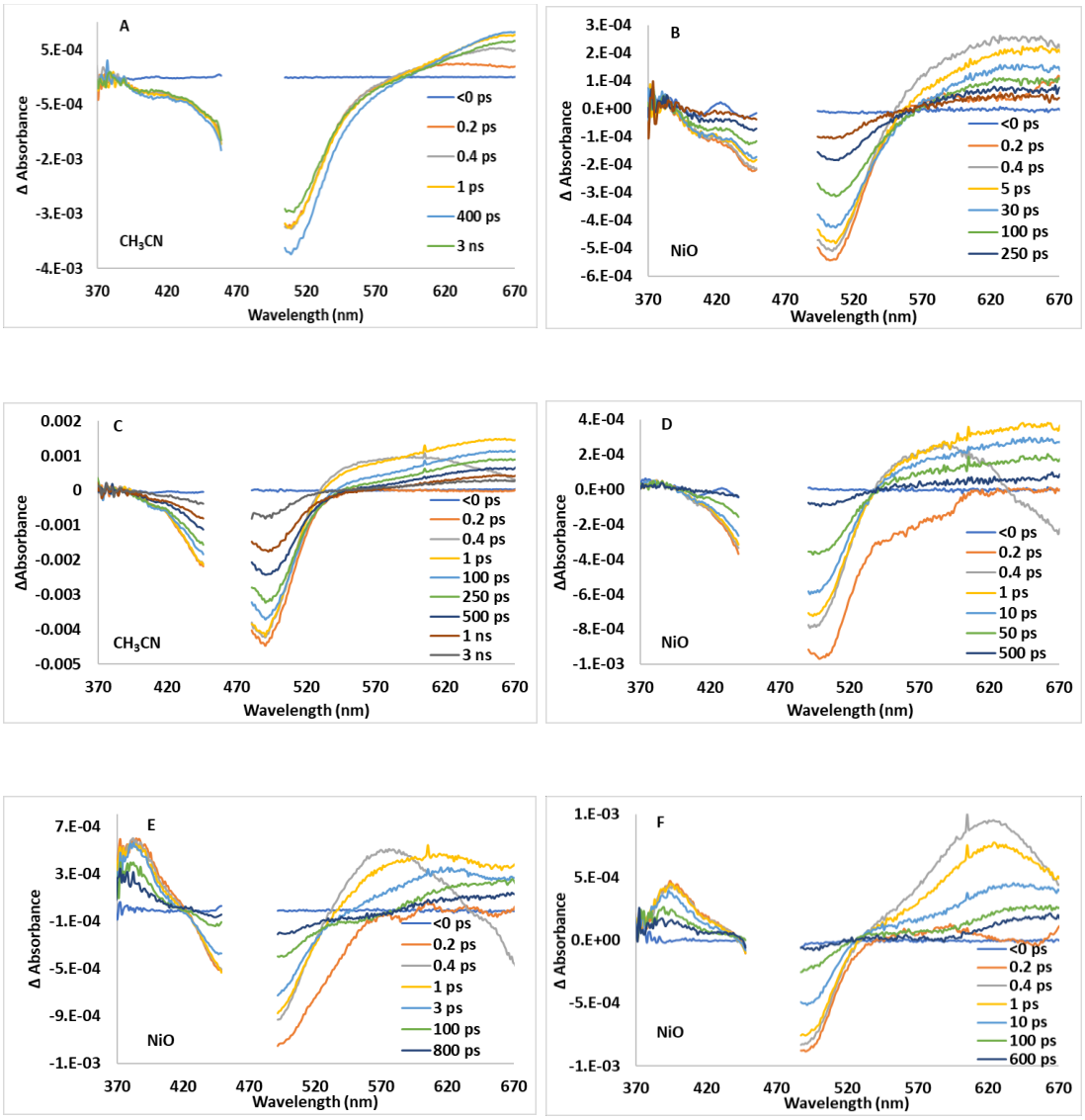

Figure 3.13: Graphs of the absorbance difference TA spectra of Ru_{bpt} in CH_3CN (A) and On NiO (B), $RuPd_{bpt}$ in CH_3CN (C) and on NiO (D), $Ru_{2,5\text{-}bpp}$ (E) and $RuPt_{2,5\text{-}bpp}$ (F) on NiO. All with an excitation wavelength of 470 nm. The break in the graphs is the notch from the laser pulse.

Transient absorption studies were conducted on a series of Ru complexes (both mononuclear and dinuclear assemblies). Figure 3.13 provides the difference spectra of the focal complexes from this chapter. Solution (CH_3CN) based experiments were also conducted with $RuPt_{2,5\text{-bpp}}$, using both TRIR and TAS but the results are not presented here as this complex was previously studied by Pan et al. using TAS and was discussed in Chapter 2. The spectra obtained were consistent with previous reports.[2] All spectra exhibit a typical MLCT GSB, centred ~490 nm (or ~510 nm in the case of the triazole mononuclear complex), that appears within the instrumental response and an excited state absorbance >520 nm. This ESA broadens and experiences a redshift as it decays after 1 ps in nearly all cases, except for the triazole monomer **A** as the feature grows in and shifts to the red, up to 400 ps, concurrent with a further depletion and shift to the red of the bleach. Both features persist beyond the 3 ns experimental window. In Ru_{bpt} (A in Figure 3.13) this ESA is most likely due to ^{3}LMCT, as seen with $Ru_{2,5\text{-bpp}}$ and other mononuclear complexes in solution.[2,3] In the resulting difference spectra for $RuPd_{bpt}$, (C in Figure 3.13), the ESA band is blue-shifted compared to its equivalent for Ru_{bpt} (A in Figure 3.13, where Ru_{bpt} is in solution). The blueshift of the ESA is most likely due to the blueshift the absorbance experiences with the addition of the Pd moiety, therefore less overlapping of the GS and ES bands occurs. There is an expected decrease in the lifetime of the triplet state upon the addition of the Pd metal centre, observed as the ESA band decays within the 3 ns window and redshifts by ~40 nm as it decays.[66] Decay associated spectra (DAS) for $RuPd_{bpt}$ in solution, shown in Figure 3.14 (left), proved the lifetime to be a biexponential process, τ_1 = 137 ps, τ_2 = 1830 ps. The lifetime of $RuPd_{bpt}$ is consistent with other triazole complexes.[62]

The most notable point for the triazole complexes (A, B, C and D in Figure 3.13), is the lack of the ESA band ~380 nm normally attributed to ligand centred transitions, typically observed for Ru-polypyridyl complexes and seen in the spectra for the immobilised $Ru_{2,5\text{-bpp}}$ based complexes (E and F in Figure 3.13).[3,66] Lees et al noted this absence in the difference spectra pertaining to similar Ru-triazole based complexes immobilised to TiO_2.[16,62] In their photoanodic systems the electron transfers from the complex to the TiO_2 surface occurred within the instrumental response, possibly explaining the absence of any ESA bands attributed to the Ru-complex. In the TA spectra, reported by Lees et al. conducted in aqueous solution at pH 7, for the complex $[Ru(dcb)_2(L)]$ (where L = 3-(2-hydroxyphenyl)-5-(pyridin-2-

yl)-1,2,4-triazole) an ESA feature ~380 nm (broader and less defined than typically seen) was observed. When comparing the UV-Visible spectrum of their Ru-triazole complex dissolved in aqueous solution pH 7 and in CH_3CN, there is a notable redshift of the absorbance in the visible MLCT region when dissolved in acetonitrile. The feature ~380 nm becomes more defined and mirrors what is observed in the electronic absorbance spectrum of Ru_{bpt} (Figure 3.10, blue line). It is possible, that in acetonitrile-based TA experiments of Ru-carboxy-triazole complexes, with similar electronic absorbance spectra that display this additional MLCT features ~380 nm, the GSB of this feature overlaps with the ESA of the same wavelength. Therefore, in the case of the Ru_{bpt} monomer examined in this chapter, minimal GSB is observed. For the dinuclear $RuPd_{bpt}$ complex, the amplitude of the bleach and the ESA may be equal and cancel each other out, leading to an absence of features in this region. TD-DFT calculations (discussed in detail below) conducted, by Prof. Long, on complexes analogous to $RuPd_{bpt}$ suggest the initial triplet state is a Ru-to-bpt ^{3}MLCT and not Ru-to-dceb. This could also possibly explain the absence of the ESA normally observed ~380 nm for Ru-complexes.

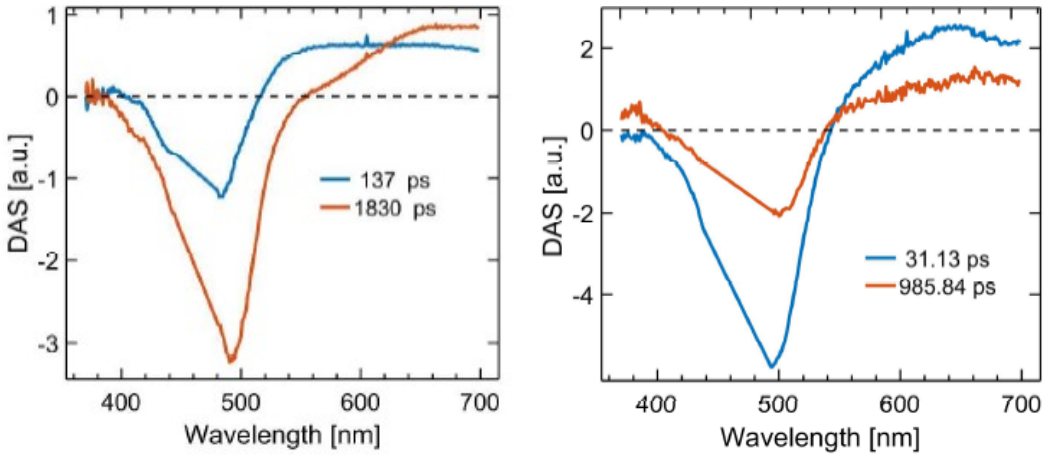

Figure 3.14: Decay associated spectra (DAS) of $RuPd_{bpt}$ in CH_3CN (left) and immobilised to NiO (right)

It is very apparent from the TA spectra that there is a significant reduction in lifetime once samples are immobilised on to the NiO surface (B, D, E and F in Figure 3.13). The early-time excited state features mirror those of the solution-based experiments with the overlying ESA for the reduced Ru-moiety, consistent with hole injection to the NiO surface. The difference spectra (D in Figure 3.13) for NiO|$RuPd_{bpt}$ displays a biexponential lifetime , $\tau_1 \approx 30$ ps and $\tau_2 \approx 1000$ ps. The DAS, Figure 3.14 (right),

indicates that the shorter lifetime (τ_1) is attributed to the reduced complex and τ_2 is assigned to the ^{3}MLCT as the shape resembles that of the complex in acetonitrile (Figure 3.14, left). Whereas, the DAS for NiO|$RuPt_{2,5\text{-bpp}}$ in Figure 3.15, show three species present which all involve the reduced dceb ligand with a feature at ~380 nm.[66] The components of the multiexponential lifetime are $\tau_1 \approx 2$ ps, attributed to hole injection and the reduced Ru-complex forming,[33] $\tau_2 \approx 80$ ps, most likely due to LMCT of the 2,5-bpp ligand[2] and $\tau_3 \approx 4$ ns, assigned to the ^{3}MLCT lifetime as is similar to that of the solution experiments.

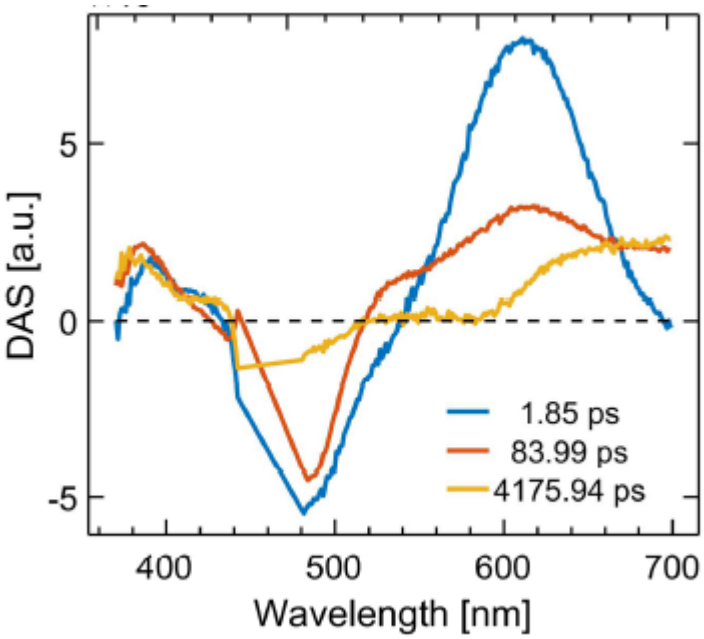

Figure 3.15: DAS for $RuPt_{2\text{-}5bpp}$ immobilised to NiO

3.4.1.6 Preliminary ns-TA Studies

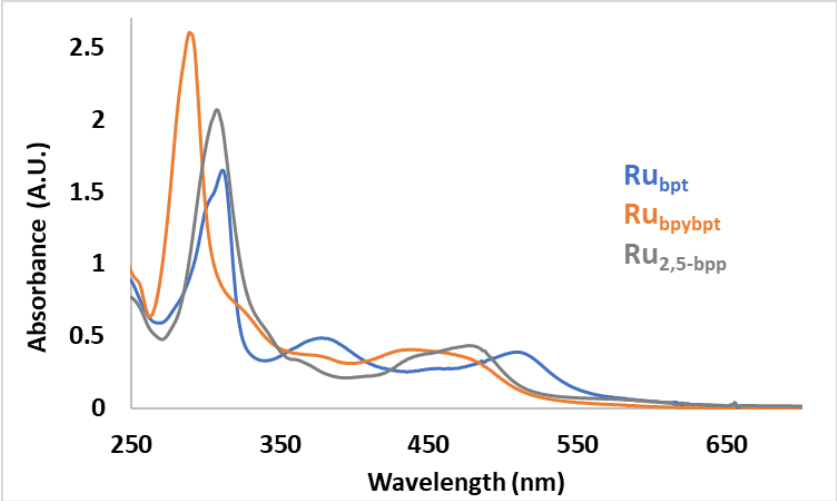

Figure 3.16: Electronic absorbance spectra of Ru_{bpt}, Ru_{bpybpt} and $Ru_{2,5\text{-}bpp}$ in acetonitrile before ns-TA experiments, absorbance at 355 nm is ~0.4 for all complexes.

The electronic absorbance spectra pertaining to the complexes examined by ns-TA, which include; Ru_{bpt}, Ru_{bpybpt} and $Ru_{2,5\text{-}bpp}$, are displayed in Figure 3.16. The preliminary ns-TA spectra are displayed in Figure 3.17 (Ru_{bpt} (top row), Ru_{bpybpt} (middle row) and $Ru_{2,5\text{-}bpp}$ (bottom row)). ns-TA was conducted in aerated acetonitrile (left column) and with the addition of TEA (right column), this was to investigate any possible changes to the excited state dynamics in the presence of a base. It was also of interest to examine the spectral features present at higher energy and a wider temporal window. These experiments follow the ns-TA procedure described in Chapter 2. The wavelength of excitation was 355 nm. Kinetic data was not determined for these experiments as the transient signals obtained were weak, and no reliable data could be obtained. The spectra obtained were mainly to observe a decay of the long-lived excited species and what changes the addition of a base has to the long-lived excited species. Three complexes were studies using ns-time resolved spectroscopy; Ru_{bpt}, Ru_{bpybpt} and $Ru_{2,5\text{-}bpp}$. Investigating these three complexes allows for the facile comparison of the effect ligand substitution has on the spectrotemporal evolution of the complex.

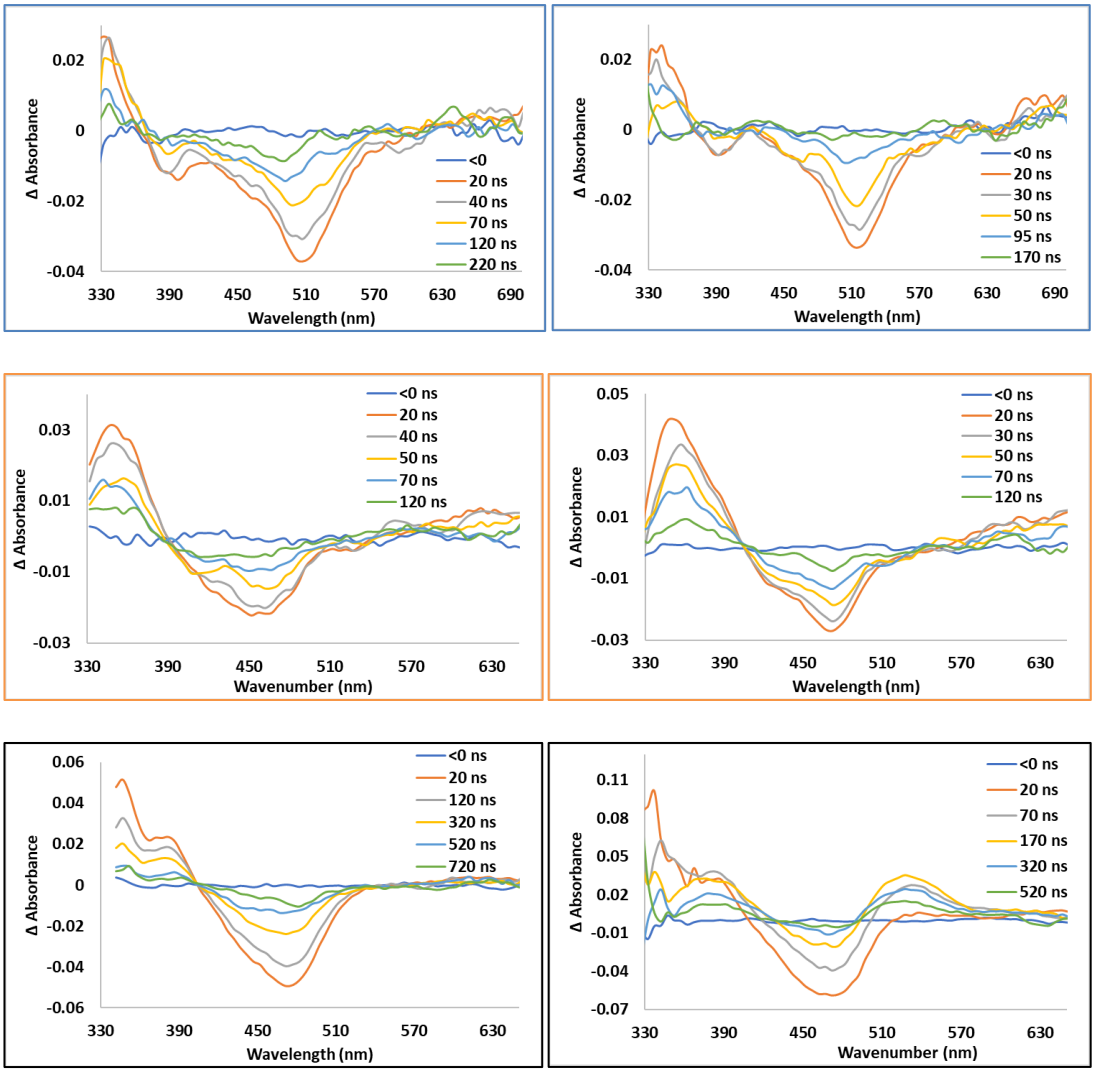

Figure 3.17: Graphs of spectra collected during preliminary ns-TA studies of Ru_{bpt} (top row), $Rubpy_{bpt}$ (middle row) and $Ru_{2,5\text{-}bpp}$ (bottome row), conducted in acetonitrile (left column) and acetonitrile/TEA mix, 3:1 (right column)

In all graphs, in Figure 3.17, the window of detection is shifted to lower wavelengths (vs the ps-TA studies), allowing the ESA at this higher energy to be observed. The top row displays the spectra collect for the Ru_{bpt} complex and at wavelengths <360 nm there is an ESA band present. This ESA band is similar in position, and shape, to that of the $Ru_{2,5\text{-}bpp}$ complex (bottom graphs), which had been assigned to the reduced dceb from previous TA studies by Pan et al.[2] For the $Ru_{2,5\text{-}bpp}$ complex (bottom graphs), the ESA feature related to the reduced BL for the Ru-terpy complex is not present and the two ESA features, at 350 nm and 385 nm, differ in intensity. These spectral differences are possibly explained by 355 nm being the excitation wavelength utilised in these experiments. Whereas, in the study by Pan et al., all ESA bands are present and the ESAs assigned to the reduced dceb ligands (350 nm and 385 nm), are of

equivalent intensity. In their study the excitation wavelength is 480 nm. Therefore, as discussed in Chapter 2, the initial Franck-Condon state is possibly altered, thus, the population distribution upon ISC to the triplet state is different. This is apparent in the graphs concerning the Ru_{bpt} complex, as there is a reduction in the intensity of the ESA at wavelengths >570 nm, previously observed in the ps-TA studies.

On comparison of Ru_{bpt} with Ru_{bpybpt} (the graphs on the top row vs. the middle row), both the ESA and GSB features are inherently different. This was expected due to the stark difference in their electronic absorbance features (Figure 3.16). The UV-Visible spectrum generated by Ru_{bpybpt} is typical of Ru-polypyridyl complexes, such as, $Ru_{2,5\text{-}bpp}$. As there are less features in the visible region and the λ_{max} (440 nm) of the lowest energy transition present is shifted to the blue of that of Ru_{bpt} (510 nm). This then follows through in the TA spectra collected for each complex as observed above.

The addition of the sacrificial agent does not appear to have much effect on either of the bpt complexes (right column of Figure 3.17). It is possible that the diffusion rate is slower than the decay of the excited state features and therefore they do not interact. This could explain the low TON achieved for these complexes (Ru_{bpt} 88 and Ru_{bpybpt} <1 TON). For the $Ru_{2,5\text{-}bpp}$ species, there is the appearance on an ESA overlapping on the lower energy side of the GSB. This feature grows in for up to ~150 ns. It is possible that the change in solvent mix is reflective of the sensitive nature of the ^{3}LMCT excited state of the $Ru_{2,5\text{-}bpp}$ complex.

3.4.1.7 Time-resolved IR Spectroscopy

TRIR experiments in the fingerprint region were conducted in conjunction with TA experiments on all complexes dissolved in solution (CD_3CN) and on the NiO surface. IR features are more susceptible to their environments than UV-Visible features, so it is possible for more information to be gained using this technique to follow the early-time photodynamics using the carboxy groups as reporters. The TRIR data collected corroborates with that collected in the TA experiments, but no additional information was gained. The resulting spectra can be seen in Figure 3.18 below.

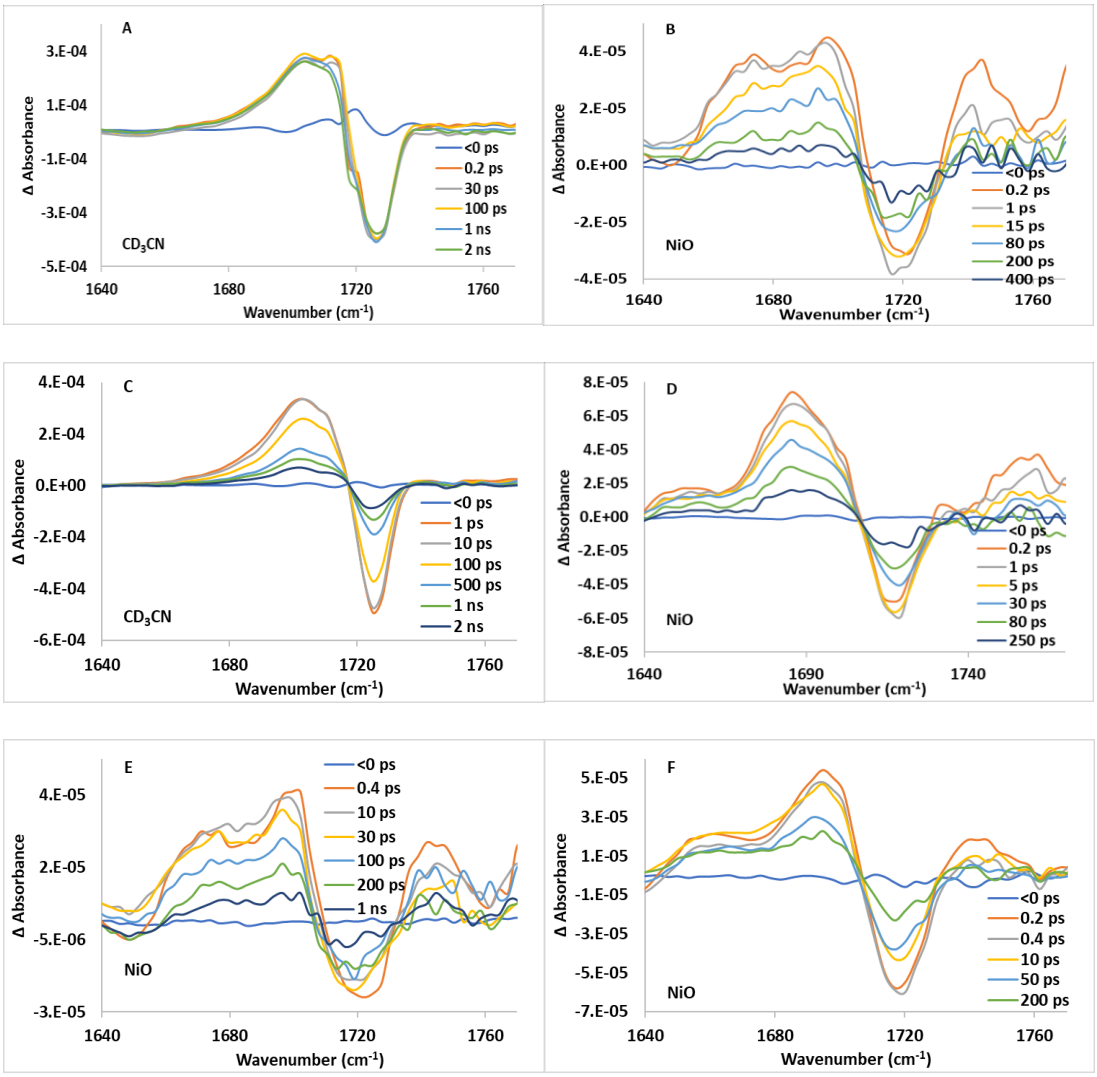

Figure 3.18: Graphs of the absorbance difference TRIR spectra of Ru_{bpt} in CH_3CN (A) and On NiO (B), $RuPd_{bpt}$ in CH_3CN (C) and on NiO (D), $Ru_{2,5\text{-}bpp}$ (E) and $RuPt_{2,5\text{-}bpp}$ (F) on NiO. All with an excitation wavelength of 470 nm

For each sample the GSB of the parent carbonyl band is present, within the time restraints of the instrument. For the solution-based samples the excited species appears shifted by ~30 cm^{-1} to lower energy than the parent band, within the instrumental detection limit. This excited species is assigned to the ^{3}MLCT, as a lesser shift (~14 cm^{-1}) would indicate inter-ligand (π-π^*) transitions.[67] There may be evidence of the excited species pertaining to ligand-centred transitions at ~1710 cm^{-1}, at very early time points, overlapping with the GSB and the dominance of the ^{3}MLCT feature, inhibit confirming presence of this excited state feature.

Once again, a reduction in the lifetime of this ESA is observed upon the addition of the catalytic metal centre (C, D and F) and when the complex is immobilised on the surface of NiO (B,D,E and F) vs. in solution (A and C). The excited state lifetime of the carbonyl band for $RuPd_{bpt}$ is the shortest lived out of this series. For $RuPd_{bpt}$ in CD_3CN (C), the ESA band decays and the corresponding bleach recovers ($\tau \approx 2$ ns). Whereas, for the $RuPt_{2,5\text{-}bpp}$ analogue, the band persists beyond the experimental temporal window of the instruments. The terpyridine complexes were also investigated at longer time delays using the TRMPS application at the RAL facility. The resulting spectra are displayed in Figure 3.19. These were conducted in aerated solutions, and display ESA absorbance over hundreds of nanoseconds, with a reduction in lifetime upon the addition of the Pt catalytic centre as expected.

When each of the complexes are immobilised on the surface of NiO the GSB and ESA follow the same assignment as the solution-based experiments but there appears to be two distinct excited state features present at lower energy (~1660 cm^{-1} and ~1690 cm^{-1}) to the parent band. The higher energy band (~1690 cm^{-1}) is similar to that observed in the solution-based experiments (1700 cm^{-1}). Therefore, this band is possibly due to ^{3}MLCT transitions. The band at ~1690 cm^{-1} is not described in the literature and may be influenced by the presence of surface interactions. There is also a very weak second ESA feature present at higher energy to the bleach in the spectra of the immobilised samples. This feature is tentatively assigned to hole injection on to the NiO as it decays over the same time constants as seen in the TA (< 1 ps).

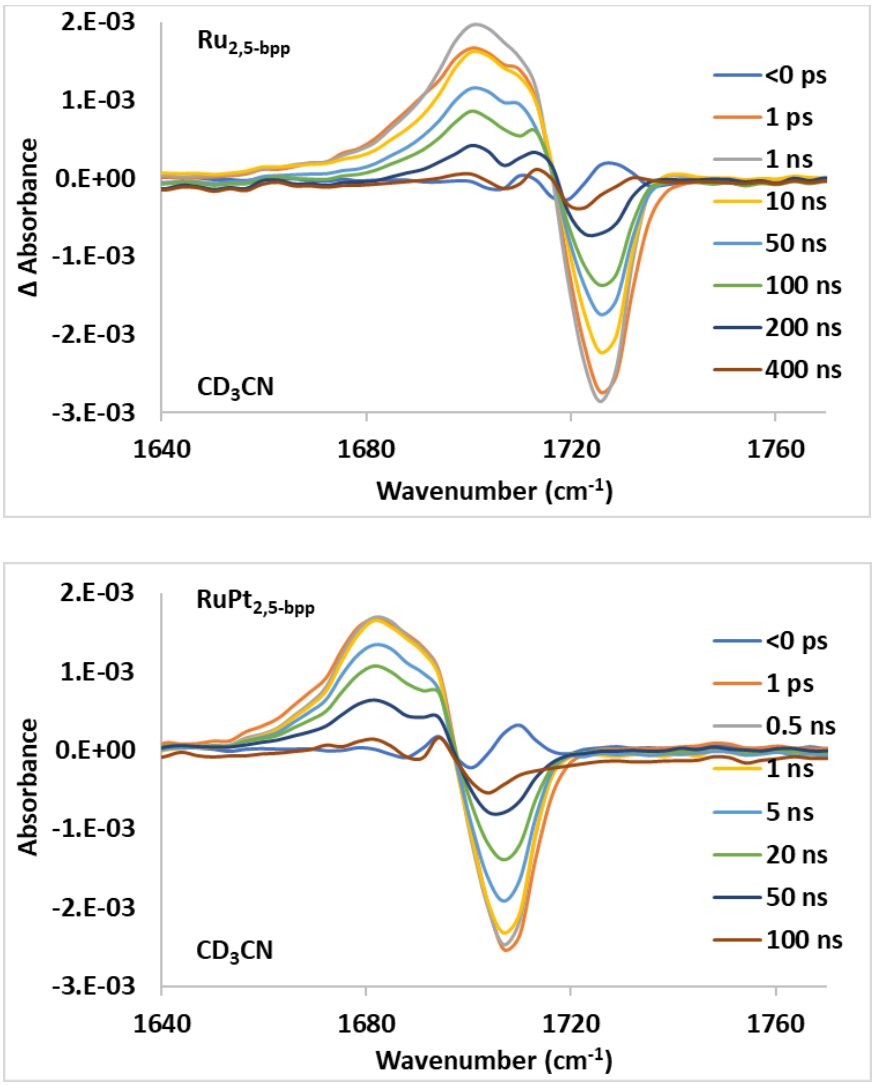

Figure 3.19: Graphs of TRMPS-TRIR spectra of $Ru_{2,5\text{-}bpp}$ (left) and $RuPt_{2,5\text{-}bpp}$ (right) in CD_3CN with an excitation λ of 400 nm

3.4.1.8 Computational studies

The model complexes $[Ru(bpy)_2(bpt)PdCl](PF_6)_2$, $[Ru(dmcb)_2(bpt)PdCl](PF_6)_2$, $[Ru(dmcb)_2(bpt)PdCl(H_2O)](PF_6)_2$ and $[Ru(dmcb)_2(bpt)PdCl](PF_6)$ were used to gain theoretical insight into the dynamics of the $RuPd_{bpt}$ system, to support interpretation of the experimental studies. The dmcb ligand is utilised in place to ease the complexity of the calculations. The calculations were used to fabricate electron density difference maps, which in turn provide information on the origin of the electron. For the bpy based model in acetonitrile the calculations characterised the ^{1}MLCT to be Ru-to-bpt CT state. Whereas, the ^{1}MLCT of the dmcb analogue is a Ru-to-dmcb CT state, as seen with the $RuPt_{2,5\text{-bpp}}$ complex.[2] The aqueous based calculations also predict the ^{1}MLCT state to be Ru-to-dmcb CT in character. Calculations conducted on the triplet state, that is populated from this $^1MLCT_{Ru\rightarrow dmcb}$ state, determined the character of the triplet state is most likely Ru/bpt-to-Pd CT. As the electron density is localised over the Pd moiety, which possibly explains the absence of the ESA typically observed for the reduced peripheral ligand (~380 nm). Figure 3.20 depicts the singlet and triplet excited state electron density difference maps as well as a simplified photophysical scheme of the electron using the dmcb system.

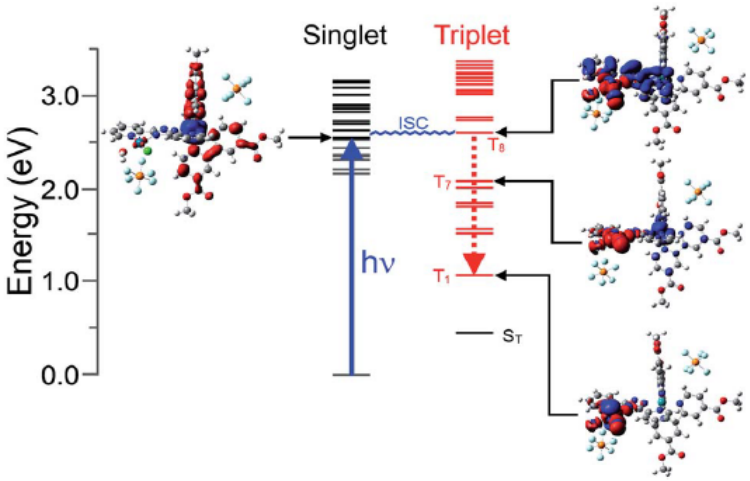

Figure 3.20: Photophysical model for the excitation energy (blue arrow) of $[Ru(dmcb)_2(bpt)PdCl(H_2O)](PF_6)_2$ into its lowest optically accessible singlet excited state (black lines) then inter system crossing (ISC) to the triplet state at T_8 (red lines) and internal conversion to the triplet surface. Electron density difference maps (electron density moves from blue to red) for singlet excited state is on the left and triplet excited state on the right. S_T indicates the singlet state energy at triplet geometry.

3.4.1.9 Photocatalytic Studies

The novel triazole complexes were investigated for their hydrogen generation capabilities under the same conditions as the terpyridine complexes.[1] Only the monomeric Ru_{bpt} complex was found to produce H_2 (88 TON) in the presence of a catalyst. There was no evidence for H_2 generation from the Ru-Pd analogue, even though calculations suggested that following excitation the electron is promoted towards the catalytic centre ($RuPd_{bpt}$). The lack of activity is possibly due to the decomposition of $RuPd_{bpt}$ in the solution mix ($CH_3CN/TEA/H_2O$) or the short lifetime of the complex. It is interesting to compare this complex with $RuPt_{2,5\text{-}bpp}$, as the terpyridine complex yields a TON of 720, under the same conditions.[19] Time resolved transient absorption studies indicates that following excitation of $RuPt_{2,5\text{-}bpp}$ the electron localises on the dceb peripheral ligand, and this is contrary to the directional flow towards the catalytic centre, however relatively high TONs for hydrogen, were observed. In the photoelectrocatalytic experiments the experimental parameters are very different when compared to the solution based photocatalytic experiments. Instead of organic solvent, aqueous solution is utilised, and furthermore the complexes are immobilised on NiO surfaces as opposed to being dissolved in solution. The TA and TRIR results clearly indicate that the kinetic data for the immobilised complexes are very different to that in solution.

3.4.1.10 Photoelectrocatalytic studies

Photoelectrocatalytic studies were conducted by our collaborators, Nils Põldme (Dr. Elizabeth Gibson Research Group) at Newcastle University. Both dinuclear complexes immobilised onto NiO electrodes produced hydrogen under white light illumination with an applied bias. For these immobilised complexes the Gibson group investigated the assemblies under three applied voltages, -0.2 V, 0. 4 V and 0.6 V. Hydrogen was produced at each applied voltage as shown in Figure 3.21. No hydrogen was detected for FTO control experiments, and no hydrogen was detected during the measurements conducted in the dark.

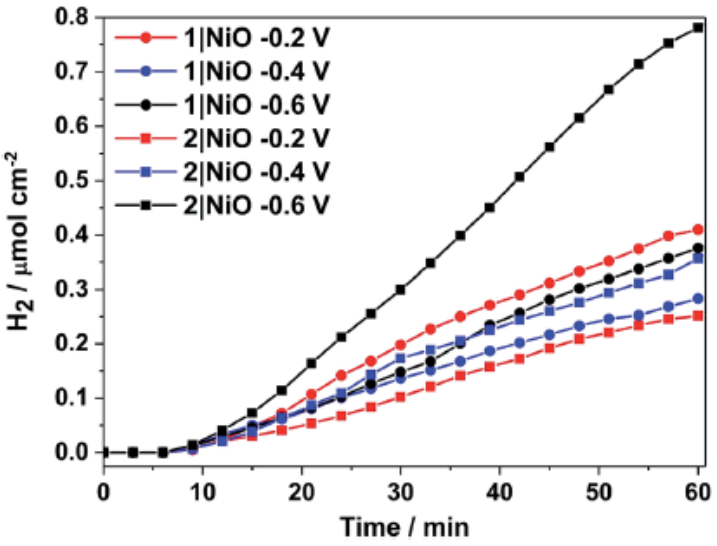

*Figure 3.21: Graph of the amount of hydrogen gas produced over time in photoelectrocatalytic experiments for NiO|RuPd$_{bpt}$ (**1**) and NiO|RuPt$_{2,5\text{-}bpp}$ (**2**) with different applied potentials, under chopped light for the first 10 mins followed by continuous irradiation of white light.*

Although, the terpyridine dinuclear species (Figure 3.21) generated the most hydrogen. It is not certain that the hydrogen produced is generated exclusively from the photocatalyst. XPS experiments found the complex to be decomposing over the course of the experiment. The Pt catalytic centre is released into the solution and deposited on to the NiO electrode, where it is catalytically active and can contribute to the hydrogen generated. Whereas, the triazole dinuclear complex, was determined to be stable over the course of the experiment. Therefore, the values related to the complex are reliable. As seen in the TA and TRIR studies above, the lifetime of each complex is reduced, once bound to the surface. By applying a bias during

photoelectrocatalytic experiments the lifetime of complexes bound to NiO electrodes have been found to increase to >ns timescales.[39] Therefore, this may not be a significant factor for the photoelectrocatalytic experiments. The direction of the electron towards the dceb ligand, which is used as an anchoring ligand on the surface may be of greater concern in photoelectrocatalytic experiments. The photocurrent density generated for the NiO|$RuPd_{bpt}$ system is on par with the current best systems on NiO and ITO, and out performs the others in terms of faradaic efficiency. This is attributed to the $RuPd_{bpt}$ photocatalyst being an intramolecular complex rather than the separate immobilisation of a photosensitiser unit and catalyst moiety or layered deposition of the components in a step-by-step manner, seen employed in these other competing systems.[68] Values pertaining to the NiO|$RuPd_{bpt}$ and NiO|$RuPt_{2,5\text{-bpp}}$ systems are listed in Table 3.1, below.

Table 3.1: Table of photoelectrocatalytic data collected[a]

	NiO|$RuPd_{bpt}$			NiO|$RuPt_{2,5\text{-bpp}}$		
E_{app}/V vs. Ag/AgCl	-0.2	-0.4	-0.6	-0.2	-0.4	-0.6
J_{photo}/μA cm^{-2}	34.8	31.2	12.3	31.8	47.6	43.7
J_{total}/μA cm^{-2}	35.6	34.2	88.2	33.2	52.5	114.7
P_{photo}/%	97.8	91.2	14	95.8	90.7	38.1
η_{Far}/%	88.6	67.5	32.3*	59.1	56.9	44.4*
[H_2]/μmol h^{-1} cm^{-2}	0.41	0.28	0.37	0.25	0.36	0.78
TON	46	31	41	47	68	147

[a] E_{app} is the voltage applied during the experiment, J_{photo} is the average photocurrent (standard deviations not displayed), J_{total} is the photocurrent plus dark current, P_{photo} is the percentage of photocurrent of the total current and η_{Far} is the faradaic efficiency of H_2 production calculated using J_{photo} or in * values J_{total}, TON was calculated by the dye loading (mol cm^{-2}) and [H_2] after an hour.

3.5 Conclusion

In summary, the novel triazole complexes were successfully synthesised and characterised. Photocatalytic studies were conducted on both the monomer (TON 88) and dinuclear analogue (TON <1) in solution. It is not clear why the amount of hydrogen observed in solution for the dinuclear assembly is less than that of the monomer, but the lifetime of the dinuclear complex may play a role. Transient absorption and time-resolved IR were conducted on a number of Ru-polypyridyl complexes, in both acetonitrile and when immobilised on to NiO films. A general trend observed, is a reduction in the lifetime when immobilised on NiO, when comparing to the mono- and di-nuclear complexes.

This chapter spans designing intramolecular systems to studying their dynamics and gaining key insights to what is required to achieve high efficiency and TON. The chapter focuses on the synthesis, characterisation, time resolved studies and both homogeneous and heterogenous photocatalysis for two ruthenium complexes. The results from this research led to first publication using p-DSSCs which used an intramolecular photocatalyst, where photocurrents and efficiencies exceed that currently published in the literature. There is a lot more that must be achieved in this area before there is a commercially viable cell. However, studies like the ones in this chapter provide a deeper understanding of the parameters that are important in designing assemblies for hydrogen generation and these factors can contribute towards progressing research in this field. The knowledge gained here can be used in our strive towards designing noble-metal free photoelectrocatalytic systems for hydrogen generation.

References

[1] T. Kowacs, L. O'Reilly, Q. Pan, A. Huijser, P. Lang, S. Rau, W. R. Browne, M. T. Pryce, J. G. Vos, *Inorganic Chemistry* **2016**, *55*, 2685–2690.

[2] Q. Pan, L. Freitag, T. Kowacs, J. C. Falgenhauer, J. P. Korterik, D. Schlettwein, W. R. Browne, M. T. Pryce, S. Rau, L. González, et al., *Chem. Commun.* **2016**, *52*, 9371–9374.

[3] L. O'Reilly, Q. Pan, N. Das, K. Wenderich, J. P. Korterik, J. G. Vos, M. T. Pryce, A. Huijser, *ChemPhysChem* **2018**, *19*, 3084–3091.

[4] C. Long, J. G. Vos, *Inorganica Chimica Acta* **1984**, *89*, 125–131.

[5] R. Hage, R. Prins, J. G. Haasnoot, J. Reedijk, J. G. Vos, *J. Chem. Soc., Dalton Trans.* **1987**, *0*, 1389–1395.

[6] R. Hage, A. H. J. Dijkhuis, J. G. Haasnoot, R. Prins, J. Reedijk, B. E. Buchanan, J. G. Vos, *Inorg. Chem.* **1988**, *27*, 2185–2189.

[7] B. E. Buchanan, J. G. Vos, M. Kaneko, W. J. M. van der Putten, J. M. Kelly, R. Hage, R. A. G. de Graaff, R. Prins, J. G. Haasnoot, J. Reedijk, *J. Chem. Soc., Dalton Trans.* **1990**, *0*, 2425–2431.

[8] R. Hage, J. G. Haasnoot, J. Reedijk, R. Wang, J. G. Vos, *Inorg. Chem.* **1991**, *30*, 3263–3269.

[9] E. M. Ryan, R. Wang, J. G. Vos, R. Hage, J. G. Haasnoot, *Inorganica Chimica Acta* **1993**, *208*, 49–58.

[10] R. J. Forster, J. G. Vos, T. E. Keyes, *Analyst* **1998**, *123*, 1905–1911.

[11] C. Di Pietro, S. Serroni, S. Campagna, M. T. Gandolfi, R. Ballardini, S. Fanni, W. R. Browne, J. G. Vos, *Inorg. Chem.* **2002**, *41*, 2871–2878.

[12] G. S. Bindra, M. Schulz, A. Paul, S. Soman, R. Groarke, J. Inglis, M. T. Pryce, W. R. Browne, S. Rau, B. J. Maclean, et al., *Dalton Trans.* **2011**, *40*, 10812–10814.

[13] R. Hage, J. G. Haasnoot, H. A. Nieuwenhuis, J. Reedijk, D. J. A. De Ridder, J. G. Vos, *J. Am. Chem. Soc.* **1990**, *112*, 9245–9251.

[14] C. G. Coates, T. E. Keyes, J. J. McGarvey, H. P. Hughes, J. G. Vos, P. M. Jayaweera, *Coordination Chemistry Reviews* **1998**, *171*, 323–330.

[15] Y. Halpin, D. Dini, H. M. Younis Ahmed, L. Cassidy, W. R. Browne, J. G. Vos, *Inorg. Chem.* **2010**, *49*, 2799–2807.

[16] A. C. Lees, C. J. Kleverlaan, C. A. Bignozzi, J. G. Vos, *Inorg. Chem.* **2001**, *40*, 5343–5349.

[17] G. S. Bindra, M. Schulz, A. Paul, R. Groarke, S. Soman, J. L. Inglis, W. R. Browne, M. G. Pfeffer, S. Rau, B. J. MacLean, et al., *Dalton Trans.* **2012**, *41*, 13050–13059.

[18] S. Soman, G. S. Bindra, A. Paul, R. Groarke, J. C. Manton, F. M. Connaughton, M. Schulz, D. Dini, C. Long, M. T. Pryce, et al., *Dalton Trans.* **2012**, *41*, 12678–12680.

[19] N. Das, G. S. Bindra, A. Paul, J. G. Vos, M. Schulz, M. T. Pryce, *Chem. Eur. J.* **2017**, *23*, 5330–5337.

[20] S. Rau, B. Schäfer, D. Gleich, E. Anders, M. Rudolph, M. Friedrich, H. Görls, W. Henry, J. G. Vos, *Angewandte Chemie International Edition* **2006**, *45*, 6215–6218.

[21] B. O'Regan, M. Grätzel, *Nature* **1991**, *353*, 737–740.

[22] O. Kohle, S. Ruile, M. Grätzel, *Inorg. Chem.* **1996**, *35*, 4779–4787.

[23] J. C. Freys, J. M. Gardner, L. D'Amario, A. M. Brown, L. Hammarström, *Dalton Trans.* **2012**, *41*, 13105–13111.

[24] M. Borgström, E. Blart, G. Boschloo, E. Mukhtar, A. Hagfeldt, L. Hammarström, F. Odobel, *J. Phys. Chem. B* **2005**, *109*, 22928–22934.

[25] A. Morandeira, G. Boschloo, A. Hagfeldt, L. Hammarström, *J. Phys. Chem. C* **2008**, *112*, 9530–9537.

[26] A. L. Smeigh, L. L. Pleux, J. Fortage, Y. Pellegrin, E. Blart, F. Odobel, L. Hammarström, *Chem. Commun.* **2011**, *48*, 678–680.

[27] O. Johansson, M. Borgström, R. Lomoth, M. Palmblad, J. Bergquist, L. Hammarström, L. Sun, B. Åkermark, *Inorg. Chem.* **2003**, *42*, 2908–2918.

[28] Z. Ji, G. Natu, Z. Huang, O. Kokhan, X. Zhang, Y. Wu, *J. Phys. Chem. C* **2012**, *116*, 16854–16863.

[29] Z. Ji, Y. Wu, *J. Phys. Chem. C* **2013**, *117*, 18315–18324.

[30] C. A. Kelly, F. Farzad, D. W. Thompson, J. M. Stipkala, G. J. Meyer, *Langmuir* **1999**, *15*, 7047–7054.

[31] M. He, Z. Ji, Z. Huang, Y. Wu, *J. Phys. Chem. C* **2014**, *118*, 16518–16525.

[32] M. Braumüller, M. Schulz, D. Sorsche, M. Pfeffer, M. Schaub, J. Popp, B.-W. Park, A. Hagfeldt, B. Dietzek, S. Rau, *Dalton Trans.* **2015**, *44*, 5577–5586.

[33] M. Bräutigam, J. Kübel, M. Schulz, J. G. Vos, B. Dietzek, *Phys. Chem. Chem. Phys.* **2015**, *17*, 7823–7830.

[34] Y. Pellegrin, L. Le Pleux, E. Blart, A. Renaud, B. Chavillon, N. Szuwarski, M. Boujtita, L. Cario, S. Jobic, D. Jacquemin, et al., *Journal of Photochemistry and Photobiology A: Chemistry* **2011**, *219*, 235–242.

[35] L. D'Amario, L. J. Antila, B. Pettersson Rimgard, G. Boschloo, L. Hammarström, *J. Phys. Chem. Lett.* **2015**, *6*, 779–783.

[36] A. Hallén, M. Bakowski, *Solid-State Electronics* **1989**, *32*, 1033–1037.

[37] F. D. Auret, P. N. K. Deenapanray, *Critical Reviews in Solid State and Materials Sciences* **2004**, *29*, 1–44.

[38] N. Queyriaux, R. A. Wahyuono, J. Fize, C. Gablin, M. Wächtler, E. Martinez, D. Léonard, B. Dietzek, V. Artero, M. Chavarot-Kerlidou, *J. Phys. Chem. C* **2017**, *121*, 5891–5904.

[39] R. J. Dillon, L. Alibabaei, T. J. Meyer, J. M. Papanikolas, *ACS Appl. Mater. Interfaces* **2017**, *9*, 26786–26796.

[40] T. A. Heimer, E. J. Heilweil, *J. Phys. Chem. B* **1997**, *101*, 10990–10993.

[41] A. D. Becke, *J. Chem. Phys.* **1993**, *98*, 5648–5652.

[42] C. Lee, W. Yang, R. G. Parr, *Phys. Rev. B* **1988**, *37*, 785–789.

[43] C. Lee, R. G. Parr, *Phys. Rev. A* **1990**, *42*, 193–200.

[44] P. J. Hay, W. R. Wadt, *J. Chem. Phys.* **1985**, *82*, 270–283.

[45] P. J. Hay, W. R. Wadt, *J. Chem. Phys.* **1985**, *82*, 299–310.

[46] W. R. Wadt, P. J. Hay, *J. Chem. Phys.* **1985**, *82*, 284–298.

[47] G. Scalmani, M. J. Frisch, B. Mennucci, J. Tomasi, R. Cammi, V. Barone, *J. Chem. Phys.* **2006**, *124*, 094107.

[48] J. Tomasi, B. Mennucci, R. Cammi, *Chem. Rev.* **2005**, *105*, 2999–3094.

[49] M. Cossi, V. Barone, R. Cammi, J. Tomasi, *Chemical Physics Letters* **1996**, *255*, 327–335.

[50] M. J. Frisch, G. W. Trucks, H. B. Schlegel, G. E. Scuseria, M. A. Robb, J. R. Cheeseman, G. Scalmani, V. Barone, G. A. Petersson, H. Nakatsuji, X. Li, M. Caricato, A. V. Marenich, J. Bloino, B. G. Janesko, R. Gomperts, B. Mennucci, H. P. Hratchian, J. V. Ortiz, A. F. Izmaylov, J. L. Sonnenberg, D. Williams-Young, F. Ding, F. Lipparini, F. Egidi, J. Goings, B. Peng, A. Petrone, T. Henderson, D. Ranasinghe, V. G. Zakrzewski, J. Gao, N. Rega, G. Zheng, W. Liang, M. Hada, M. Ehara, K. Toyota, R. Fukuda, J. Hasegawa, M. Ishida, T. Nakajima, Y. Honda, O. Kitao, H. Nakai, T. Vreven, K. Throssell, J. A. Montgomery Jr, J. E. Peralta, F. Ogliaro, M. J. Bearpark, J. J. Heyd, E. N. Brothers, K. N. Kudin, V. N. Staroverov, T. A. Keith, R. Kobayashi, J. Normand, K. Raghavachari,

A. P. Rendell, J. C. Burant, S. S. Iyengar, J. Tomasi, M. Cossi, J. M. Millam, M. Klene, C. Adamo, R. Cammi, J. W. Ochterski, R. L. Martin, K. Morokuma, O. Farkas and J. B. Foresman, D. J. Fox, *Gaussian 16, Revision A.03*, Gaussian, Inc., Wallingford CT, **2016**

[51] M. J. Frisch, G. W. Trucks, H. B. Schlegel, G. E. Scuseria, M. A. Robb, J. R. Cheeseman, J. A. Montgomery, Jr., T. Vreven, K. N. Kudin, J. C. Burant, J. M. Millam, S. S. Iyengar, J. Tomasi, V. Barone, B. Mennucci, M. Cossi, G. Scalmani, N. Rega, G. A. Petersson, H. Nakatsuji, M. Hada, M. Ehara, K. Toyota, R. Fukuda, J. Hasegawa, M. Ishida, T. Nakajima, Y. Honda, O. Kitao, H. Nakai, M. Klene, X. Li, J. E. Knox, H. P. Hratchian, J. B. Cross, V. Bakken, C. Adamo, J. Jaramillo, R. Gomperts, R. E. Stratmann, O. Yazyev, A. J. Austin, R. Cammi, C. Pomelli, J. W. Ochterski, P. Y. Ayala, K. Morokuma, G. A. Voth, P. Salvador, J. J. Dannenberg, V. G. Zakrzewski, S. Dapprich, A. D. Daniels, M. C. Strain, O. Farkas, D. K. Malick, A. D. Rabuck, K. Raghavachari, J. B. Foresman, J. V. Ortiz, Q. Cui, A. G. Baboul, S. Clifford, J. Cioslowski, B. B. Stefanov, G. Liu, A. Liashenko, P. Piskorz, I. Komaromi, R. L. Martin, D. J. Fox, T. Keith, M. A. Al-Laham, C. Y. Peng, A. Nanayakkara, M. Challacombe, P. M. W. Gill, B. Johnson, W. Chen, M. W. Wong, C. Gonzalez, and J. A. Pople, *Gaussian 03*, *Revision C.02*, Gaussian, Inc., Wallingford CT, **2004**.

[52] A. R. Oki, R. J. Morgan, *Synthetic Communications* **1995**, *25*, 4093–4097.

[53] B. P. Sullivan, D. J. Salmon, T. J. Meyer, *Inorganic Chemistry* **1978**, *17*, 3334–3341.

[54] R. Hage, Ruthenium and Osmium Complexes Containing Triazole Ligands, PhD, Dublin City University, **1991**.

[55] N. Hirata, J.-J. Lagref, E. J. Palomares, J. R. Durrant, M. K. Nazeeruddin, M. Gratzel, D. D. Censo, *Chemistry – A European Journal* **2004**, *10*, 595–602.

[56] M. Schwalbe, M. Karnahl, S. Tschierlei, U. Uhlemann, M. Schmitt, B. Dietzek, J. Popp, R. Groake, J. G. Vos, S. Rau, *Dalton Trans.* **2010**, *39*, 2768–2771.

[57] C.-Y. Li, C. Su, H.-H. Wang, P. Kumaresan, C.-H. Hsu, I.-T. Lee, W.-C. Chang, Y. S. Tingare, T.-Y. Li, C.-F. Lin, et al., *Dyes and Pigments* **2014**, *100*, 57–65.

[58] R. M. O'Donnell, R. N. Sampaio, G. Li, P. G. Johansson, C. L. Ward, G. J. Meyer, *J. Am. Chem. Soc.* **2016**, *138*, 3891–3903.

[59] K. Y.-D. Tsai, I.-J. Chang, *Inorg. Chem.* **2017**, *56*, 8497–8503.

[60] E. M. Thoresen, D. Balcells, S. Øien-Ødegaard, K. T. Hylland, M. Tilset, M. Amedjkouh, *Dalton Trans.* **2018**, *47*, 2589–2601.

[61] R. Hage, PhD Thesis: Ruthenium and Osmium Complexes Containing Triazole Ligands., PhD, **1991**.

[62] A. C. Lees, B. Evrard, T. E. Keyes, J. G. Vos, C. J. Kleverlaan, M. Alebbi, C. A. Bignozzi, *European Journal of Inorganic Chemistry* **1999**, *1999*, 2309–2317.

[63] C. Brennan, A. Draksharapu, W. R. Browne, J. J. McGarvey, J. G. Vos, M. T. Pryce, *Dalton Trans.* **2013**, *42*, 2546–2555.

[64] S. Sinn, B. Schulze, C. Friebe, D. G. Brown, M. Jäger, J. Kübel, B. Dietzek, C. P. Berlinguette, U. S. Schubert, *Inorg. Chem.* **2014**, *53*, 1637–1645.

[65] N. Kaeffer, C. D. Windle, R. Brisse, C. Gablin, D. Leonard, B. Jousselme, M. Chavarot-Kerlidou, V. Artero, *Chem. Sci.* **2018**, *9*, 6721–6738.

[66] Q. Pan, F. Mecozzi, J. P. Korterik, D. Sharma, J. L. Herek, J. G. Vos, W. R. Browne, A. Huijser, *J. Phys. Chem. C* **2014**, *118*, 20799–20806.

[67] M. K. Kuimova, X. Z. Sun, P. Matousek, D. C. Grills, A. W. Parker, M. Towrie, M. W. George, *Photochem. Photobiol. Sci.* **2007**, *6*, 1158–1163.

[68] B. Shan, A. K. Das, S. Marquard, B. H. Farnum, D. Wang, R. M. Bullock, T. J. Meyer, *Energy & Environmental Science* **2016**, *9*, 3693–3697.

Chapter 4

4 CO_2 photocatalytic reduction using Ru-Re and Porphyrin-Re assemblies

Chapter 4 focuses on the design of assemblies for CO_2 reduction, and a progression from noble metal-based photosensitisers, towards a more sustainable approach using organic based photosensitisers such as porphyrins. In this chapter, the photoreduction of CO_2 is investigated using Ru-Re and porphyrin-Re supramolecular assemblies. A brief synopsis of the state-of-the-art systems for the photocatalytic reduction of CO_2 is provided within this chapter. The porphyrin based supramolecular systems exploit Schiff base chemistry, whereby the catalytic centre is attached to the Schiff base, which is tethered to the photosensitiser. These complexes were successfully synthesised and characterised by ^1H NMR, IR, UV-visible spectroscopy and mass spectrometry. Computational Studies were performed on the singlet and triplet excited states of $RuRe_{bpt}$ to aid in assigning the experimental results obtained from time resolved studies. The excited states are also investigated by time-resolved emission and absorption spectroscopy on the ns - μs timescales.

4.1 Aim

The aim of this chapter is to move towards more sustainable photocatalytic assemblies for light facilitated processes such as hydrogen generation and the reduction of CO_2. This chapter is the first in this thesis to address CO_2 reduction as another approach to combating climate change. Therefore, it aims to provide a brief insight to the surrounding literature of photocatalytically active systems. The monomeric Ru-triazole complex, examined in the previous chapter, is coupled with the known CO_2 reduction catalytic centre -$Re(CO)_3Cl$ through the reaction with the $Re(CO)_5Cl$ precursor. The presence of the carboxy-ester groups in the ruthenium assemblies ensures that immobilisation onto the NiO electrodes remains plausible with this new assembly.

An overall aim of this chapter is to exchange the photosensitising unit from a Ru-polypyridyl complex (as discussed in the previous chapters) to a porphyrin, with both free-base and Zn-centred porphyrins examined. The main objective was to directly attach the photosensitiser to a –$Re(CO)_3$ catalytic centre using a 'Schiff base bridge' and assess the photocatalytic activity of the novel supramolecular photocatalytic assemblies for the reduction of CO_2 to CO. Lastly, the complexes synthesised in this chapter, were studied by ns-μs time-resolved spectroscopy in an attempt to gain an insight into their excited state properties and the possible relationship with photocatalytic potential.

4.2 Introduction

There are many routes to developing solutions to combat climate change in addition to developing routes to renewable forms of energy, such as, hydrogen. The previous chapters of this thesis have focused on the synthesis and the photophysical properties of ruthenium based inorganic assemblies for photo-/photoelectrocatalytic generation of hydrogen. Another approach, which also utilises solar energy, is the photocatalytic reduction of CO_2 to form useful compounds such as CO or methanol. To date many systems have been designed and assessed for CO_2 reduction studies, and the progression path for the development of such dinuclear assemblies for CO_2 reduction reflects that of the hydrogen generation photocatalysts previously discussed in Chapter 1. Again, the general development for these photocatalysts has been an initial focus on intermolecular routes and then towards supramolecular assemblies, which employ both a photosensitising unit and a catalytic moiety followed by immobilisation to semiconducting surfaces. There are several excellent reviews detailing the evolution of CO_2 reduction catalysts.[1–3] Many dinuclear complexes have been developed employing Ru, Ir, Os, Re, Ni, Co, Zn and Mg metal centres.[4–7] Herein, only a few select systems pertaining to the work conducted in this chapter are discussed in detail.

In 2005, the first active dinuclear photocatalyst for CO_2 reduction was published by Ishitani and co-workers and is depicted in Figure 4.1 (top).[8] They compared a number of Ru-Re (PS-Cat) systems for CO_2 reduction capabilities by systematically altering both the peripheral and bridging ligands. The resulting TA spectra generated for their complexes, provided an insight into the electron transfer pathways for these systems. For complexes where higher TON were obtained using intramolecular vs. intermolecular approaches, TA determined was used to confirm that the electron was localised on the Re-end of the bridge following excitation. This provided some mechanistic guidelines to follow for future systems to emulate. Furthermore, they reported that when more conjugated bridges were used less hydrogen (or none) was generated and this was attributed to stronger electronic communication between the metal centres. For the complexes studied, they stated that Ru-based emission is indicative of low metal-metal interaction, but the reduction potential of the complexes is key to the level of photocatalytic activity. High conjugation, within a system, can lower the reduction potential of the catalytic centre. In the same study they also

reported that increased TONs could be obtained by the combined use of TEOA and 1-benzyl-1,4-dihydronicotinamide (BNAH) in the solvent (DMF) mix. The reduction of the excited Ru-unit is improved by using BNAH as the electron donor compared to TEOA, but TA studies found that if both are used, back electron transfer rates are reduced. This is observed as an increase in the lifetimes of the features pertaining to the reduced species in the TA spectra collected.

Ishitani and co-workers also explored how the length of the unconjugated bridging ligand, a variation to the peripheral ligands on the Re-centre and, the use of various electron donors may improve the photocatalytic system.[9–11] Using the photocatalyst depicted in Figure 4.1 (bottom), Ishitani and co-workers investigated (2013) alternative electron donors, which resulted in an increase in the TON from 207 to >3000 for CO. Substitution of BNAH, in the DMF/TEOA/BNAH solvent mix, with 1,3-dimethyl-2-phenyl-2,3-dihydro-1H-benzo[*d*]imidazole (BIH), a better reductant than BNAH (as it is a two-electron donor), led to higher TONs (BNAH is a one-electron donor). This significant enhancement in the amount of CO detected highlights how subtle changes to either the experimental conditions or to the photocatalyst can greatly influence the amount of product detected, and how this research area can develop.

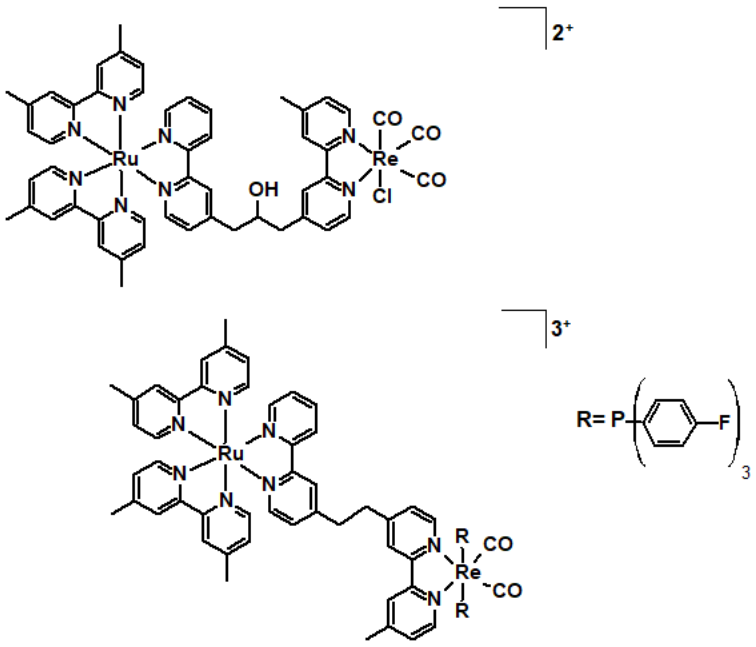

Figure 4.1: Structure of the first active dinuclear photocatalyst for CO_2 reduction (top) and a high TON yielding photocatalyst (bottom)[8,10]

In addition to a myriad of publications where Ishitani and co-workers have performed homogeneous photocatalysis, the group have also immobilised Ru-Re complexes to NiO electrodes, using methylphosphonate anchoring groups (Ru-ReP), and investigated them for their photoelectrocatalytic capabilities, (Figure 4.2 depicts the structures discussed in this section).[12,13] Their Ru-ReP complex selectively produced TON_{CO} = 32 (255 nmol) and no H_2, in their photoelectrocatalytic setup when the photocatalysts was anchored to a NiO electrode.[12] The group have also investigated z-scheme systems using this Ru-ReP immobilised complexes to a NiO photocathode coupled with an oxygen producing photoanode.[14] The activity of the system was determined to be supressed by the photocathodic side of the cell. This was found to be due to the low conductivity of NiO and desorption of the photocatalyst leading to inactivity at the photocathode. Further research on the photocathodic side of the system, enabled an improvement at the photocathode and thus, the amount of CO produced. The NiO-photocatalyst electrode was assembled by first immobilising the mononuclear RuVP species, which is furnished with both methylphosphonate groups and vinyl groups. Subsequently, the vinyl groups undergo electro-polymerisation with that on the Ru-ReV complex. This led to increased absorption and increased stability during irradiation. Therefore, increasing the yield of CO (507 nmol), unfortunately, this also led to H_2 (151 nmol) and HCOOH (120 nmol) production.[13]

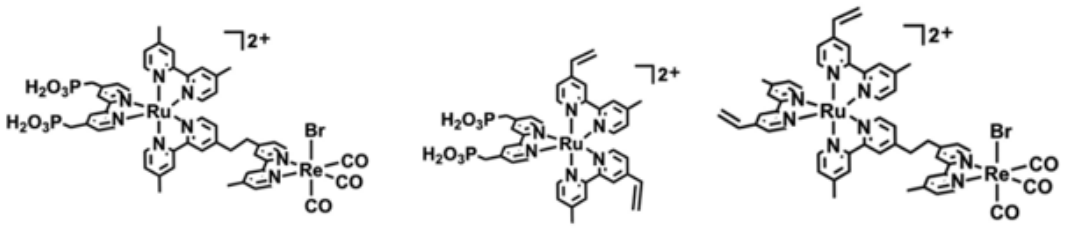

Figure 4.2: Structures of the complexes immobilised to NiO by the Ishitani group[12–14]

Following on from Chapter 3, the work discussed in this chapter involves the Ru_{bpt} mononuclear complex, but with a $[Re(CO)_3Cl]$ unit attached to the triazole bridging ligand, (depicted in Figure 4.3). As the dceb ligands are electron withdrawing, the electron was expected to be localised on the dceb peripheral ligand following ISC after photoexcitation, to generate the triplet state (as previously observed in the corresponding Ru-Pt assemblies).[15] Although, this was not the case for $RuPd_{bpt}$ complex (discussed in chapter 3), as the anionic charge on the deprotonated bpt ligand is shared between the catalytic centre(Pd) and the Ru-moiety. Hage et al., found for their $[(Ru(bpy)_2)_2(bpt)]^{3+}$ that the negative charge on the bridge was delocalised between the two metal centres.[16] Brennan and co-workers, observed a similar effect for $RuRe_{bpybpt}$ complex.[17] Quantum calculations determined that after excitation of $RuPd_{bpt}$ and ISC to the triplet sate, the electron density resides on the bridge of the complex.[18] As discussed in Chapter 3, solution-based photocatalytic experiments concluded that the Ru-triazole-Pd complex was not a promising photocatalyst for hydrogen generation. However, the photoelectrocatalytic studies (carried out following immobilisation) proved the $RuPd_{bpt}$ complex is active for hydrogen generation. These studies prompted us to further investigate similar complexes for CO_2 reduction, by employing the Re-carbonyl catalyst ($RuRe_{bpt}$) instead of the Pd hydrogen evolution catalyst ($RuPd_{bpt}$). This chapter outlines the synthesis of this novel dinuclear complex using literature methods, and includes characterisation and photocatalytic studies.[19] The complex is currently being assessed for photoelectrocatalytic CO_2 reduction, under heterogeneous conditions as the dceb unit facilitates immobilisation to NiO film.

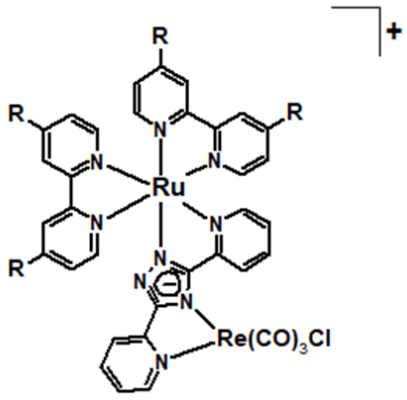

Figure 4.3: Structure of the RuRe complexes examined in this chapter, $RuRe_{bpt}$: R = COOEt and $RuRe_{bpybpt}$: R = H, counter ion for both is PF_6. In the case of the mononuclear analogues (Ru_{bpt}: R = COOEt and Ru_{bpybpt}: R = H), the Re-carbonyl unit

is not present, the structure remains the same otherwise, and the bpt is negatively charged with one PF_6 as the counter ion.

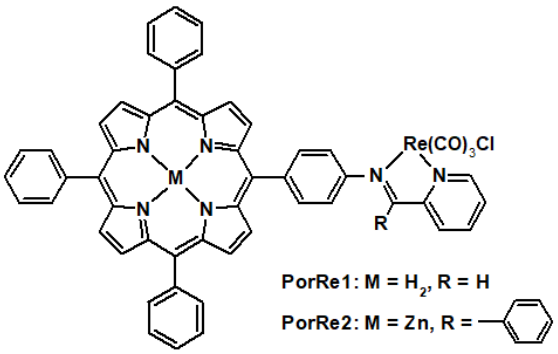

Figure 4.4: Structure of the novel porphyrin-based supramolecular assemblies synthesised in this chapter

This chapter also explores novel porphyrin-metal supramolecular assemblies for photocatalytic CO_2 reduction, (depicted in Figure 4.4). As stated in the first chapter, for photoelectrocatalytic systems to be commercially viable and used globally, it is vital to move away from complexes composed of rare metals and towards more sustainable designs utilising cheaper and abundant components. Porphyrin supramolecular assemblies, where the porphyrin unit is combined with a Re-carbonyl based catalyst (PorRe), have already been successful in photocatalytic CO_2 reduction, with TON_{CO} of > 300 reported (Figure 4.5: top).[20] These type of assemblies are mostly synthesised using a porphyrin with an amine linker as the bridge to a bipyridyl-based Re-carbonyl moiety, as depicted in Figure 4.5. They were also the first supramolecular complexes to be immobilised onto p-type semiconductors for the photoelectrocatalytic reduction of CO_2 and achieved initial TON of 10 for CO production.(Figure 4.5: bottom).[21] This was then improved to a TON_{CO} of 122 with the co-immobilisation of the photocatalyst with 5,10,15,20-tetra(4-carboxy)phenylporphyrinatozinc (ZnTCPP), acting as an electron reservoir for the Zn-porphyrin-Re-photocatalyst. As the photocatalyst harvests the electrons stored on the monomeric ZnTCPP for the catalytic reduction of CO_2.

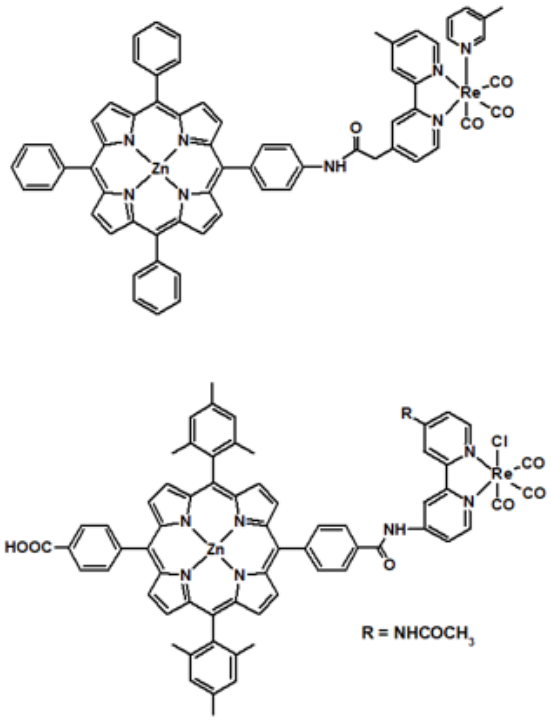

Figure 4.5: Structure of the highly active porphyrin-Re complex for photocatalytic CO_2 reduction (top)[20] and structure of the first supramolecular assembly to be immobilised to a p-type semiconductor (NiO) for photoelectrocatalytic CO_2 reduction (bottom)[21]

Direct attachment of the catalytic moiety to the porphyrin, by a Schiff base/imine reaction, has not yet been explored as an approach in developing photocatalysts for the reduction of CO_2. It is a synthetically simplistic method of one pot type synthesis and the properties of the complex can be altered/tuned easily by varying the R group on the imine bridge/catalytic metal centre (Figure 4.4).[22] Following on from the previous chapters, in which hydrogen photo-evolution is the focus, a Pt/Pd catalytic centre can be attached in the same manner of a Schiff base/imine reaction forming a porphyrin-Pt/Pd photocatalyst.[23] The substitution of pyridyl groups on the porphyrin macrocycle, in place of the phenyl group, allows the complex to be immobilised to semiconducting materials. Pyridine anchoring groups have already been utilised in n-type DSSCs with TiO_2 photoanodes sensitised with porphyrin systems and on NiO p-type semiconductors with organic photosensitisers.[24–26] The vast potential for synthetic tuning of these type complexes is on par with that of Ru-polypyridyl complexes, hence the long library of porphyrin-based assemblies to date.

4.3 Experimental

4.3.1 Materials

As described in Chapter 2 and Chapter 3, unless otherwise stated.

4.3.2 Equipment

As described in Chapter 2 and Chapter 3, unless otherwise stated.

4.3.3 Synthesis

The synthesis for $[Ru(dceb)_2(bpt)](PF_6)$ monomer is described in Chapter 3. $[Ru(bpy)_2(bpt)Re(CO)_3Cl](PF_6)$ ($RuRe_{bpybpt}$) and $RuRe_{bpt}$ were synthesised following literature procedures (or a modification thereof).[17] 5-(4-nitrophenyl)-10,15,20-triphenyl porphyrin, 5-(4-aminophenyl)-10,15,20-triphenyl porphyrin[27] and the metalation of amino-porphyrin (Zn)[28] were carried out following literature methods. Formation of the imine/Schiff base porphyrin-metal systems were conducted following modified literature procedures.[22]

$[Ru(dceb)_2(bpt)Re(CO)_3Cl](PF_6)$ ($RuRe_{bpt}$). 50 mg $[Ru(dceb)_2bpt](PF_6)$ was dissolved in 30 mL ethanol and purged with nitrogen for 30 min. A 1.1 equivalent of $Re(CO)_5Cl$ was added. The reaction was degassed by vacuum before being left under a constant flow of nitrogen. The reaction was brought to reflux temperature for 6 hours. The solvent was reduced and the solid was filtered by vacuum filtration and washed with diethyl ether. Yield 25 mg. (0.02 mmol, 40 %). ^{1}H-NMR (600 MHz, acetonitrile-d3) δ[ppm] = 1.23 (t, 3 H), 1.32 (t, 3 H), 1.36 (td, 6 H), 4.27 (q, 2 H), 4.38 (q, 2 H), 4.43 – 4.50 (m, 4 H), 7.35 (td, 1 H), 7.47 (d, 1 H), 7.50 (dd, 1 H), 7.55 (m, 2 H), 7.72 (d, 1 H), 7.77 (dd, 1 H), 8.03 (td, 1 H), 8.04 – 8.17 (m, 5 H), 8.25 (d, 1 H), 8.48 (d, 1 H), 8.75 (s, 1 H), 8.78 (s, 1 H), 9.05 (s, 1 H), 9.13 (s, 1 H), 10.31 (d, 1 H).

5-(4-nitrophenyl)-10,15,20-triphenyl porphyrin (NO_2-TPP). To 60 mL propionic acid, 4-nitrobenzaldehyde (302 mg, 2 mmol, 1 equiv.) and benzaldehyde (613 µL, 6 mmol,3 equiv.) were added and stirred for an hour at 120 °C. Dropwise freshly distilled pyrrole (555 µL, 8 mmol, 4 equiv.) was added and the reaction was left to stir at 120 °C for a

further hour. The solvent is then removed, and the crude is purified by column chromatography on silica column with chloroform:petroleum ether (6:4) as eluent.

5-(4-aminophenyl)-10,15,20-triphenyl porphyrin (NH_2-TPP). To 20 mL of chloroform NO_2-TPP (80 mg, 121 mmol) and 20 mL of $SnCl_2$ in conc. HCl were added along with 20 mL acetic acid. The reaction was stirred and heated at 70-80 °C overnight. 2 M NaOH (150 mL) was used to neutralise the solution and stop the reaction. The solution was then washed with water (2 x 100 mL) and dried over $MgSO_4$ and filtered. Column chromatography was then used with a silica column and chloroform as solvent.

Porphyrin-Re complexes. Pyridine-2-carboxaldehyde (0.012 mL, 0.125 mmol) and 1 equiv. of the amino-porphyrin were dissolved in ethanol (15 mL) and brought to reflux temperature for an hour. 1 equiv. of $Re(CO)_5Cl$ was added to the reaction mixture, and it was stirred at reflux temperature for a further 8 hours. The solution was then cooled to room temperature and the solvent removed. The remaining solid was dried under vacuum and then washed with diethyl ether to give the pure compound.

PorRe1: Yield 105 mg (0.102 mmol, 82%), [M]+ ion at 1243.2659 m/z corresponding to $C_{53}H_{35}ClN_6O_3Re$

PorRe2: Yield 90 mg (0.08 mmol, 64 %).

4.4 Results and Discussion

4.4.1 Ruthenium polypyridyl based complexes

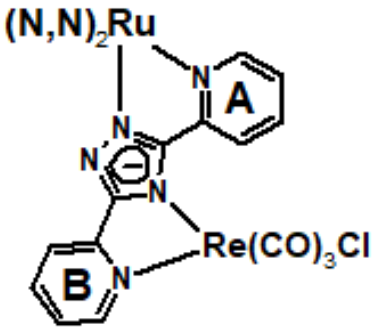

Figure 4.6: Structure of dinuclear complex with the pyridyl triazole rings denoted A or B

$RuRe_{bpt}$ was successfully synthesised following modification of a literature method and characterised by ^{1}H NMR, COSY NMR, elemental analysis and other spectroscopic techniques. Figure 4.6 highlights the ring nomenclature used throughout the following sections. The structure of mononuclear analogues of these complexes are the same as their dinuclear equivalents without the Re-catalytic unit, as seen for Ru_{bpt} in Chapter 3.

4.4.1.1 ^{1}H NMR and COSY-NMR spectroscopy

For the $RuRe_{bpt}$ complex, it was not possible to assign all of the protons present in the spectrum, in Figure 4.7, due to overlapping of the peaks pertaining to dceb-based and bpt-based protons. The COSY NMR, depicted in Figure 4.8, is as expected based on similar complexes reported in the literature.[29] As many of the peaks overlap it was difficult to accurately assign all resonances. If the dceb ligand was deuterated it would be extremely beneficial to ensure the correct assignment of each peak. A downfield shift of the protons in ring B on the bpt (Figure 4.6), is an indication of metalation, as seen in the case of $RuPd_{bpt}$ in Chapter 3.

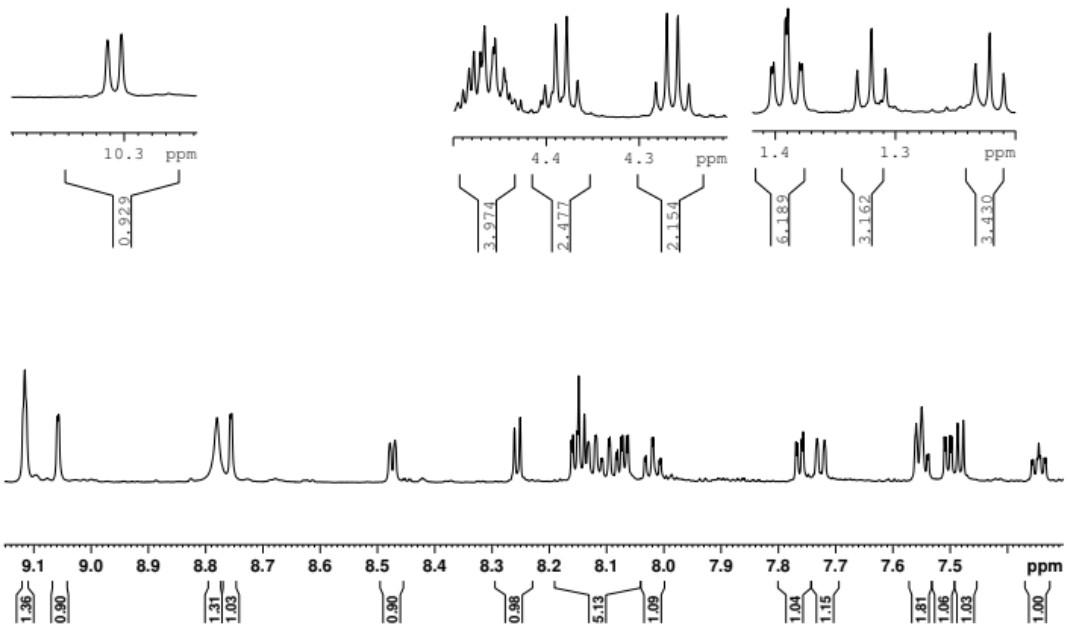

Figure 4.7: ^{1}H NMR spectrum of $RuRe_{bpt}$ in CD_3CN

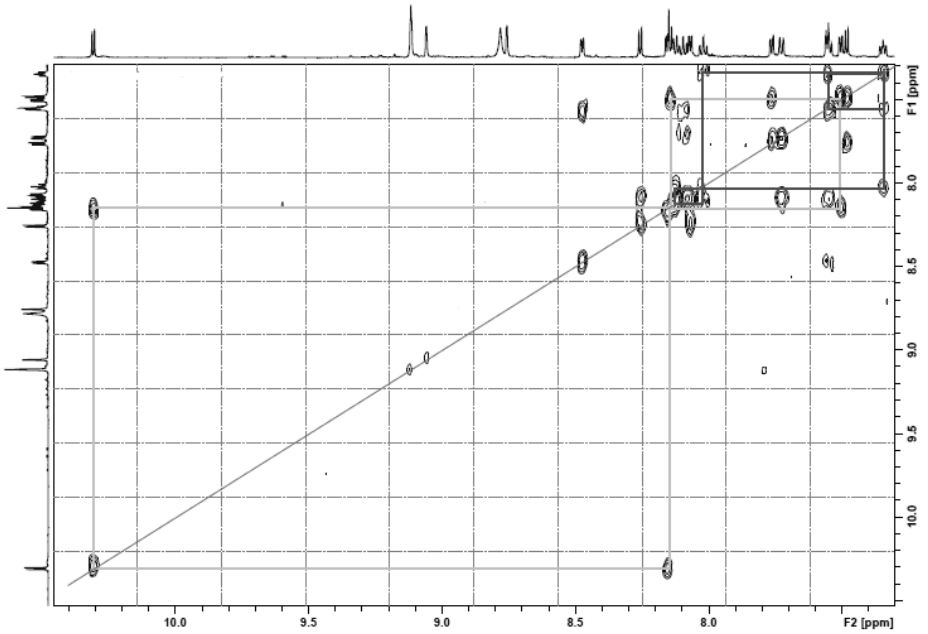

Figure 4.8:COSY NMR spectrum of $RuRe_{bpt}$ in CD_3CN

The COSY-NMR of the aliphatic region, in Figure 4.9, highlights the non-equivalence of the ester-based protons, on the dceb ligands, due to spatial interaction with the Re-carbonyl catalyst. Although, the COSY NMR allows for coupling of the CH_2 and CH_3 on one end of the dceb ligand. It is not possible to assign the protons in full to specific dceb ligands.

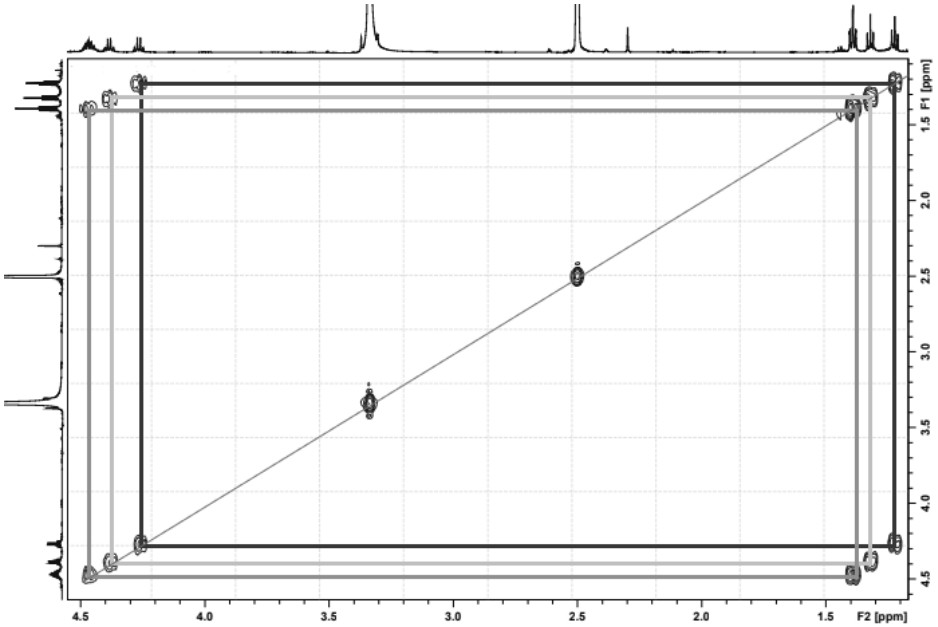

Figure 4.9: COSY-NMR spectrum of the aliphatic region of $RuRe_{bpt}$ in CD_3CN

In the case of $RuRe_{bpybpt}$, the presence of structural isomers and their individual distinct spectra lead to a complicated ^1H NMR (not shown).[17] No attempt was made to separate these isomers as previous studies showed no difference in the spectroscopic or electrochemical properties between the isomers.[17,30]

4.4.1.2 IR spectroscopy

The presence of the three IR bands related to Re-CO stretching (~2100-1700 nm) vibrations was also an indication of successful synthesis of the dinuclear species. The carbonyl stretching frequencies of the two RuRe complexes in acetonitrile are summarised in Table 4.1 with the corresponding spectra displayed in Figure 4.10.

Table 4.1:The CO stretching frequencies of the RuRe complexes synthesised in this chapter (IR spectra were obtained in in acetonitrile)

Complex	νCO (cm^{-1})		
$RuRe_{bpt}$	2019	1909	1887
$RuRe_{bpybpt}$	2021	1911	1897
*Re_{bpt}	2012	1904	1879

*In THF From reference [17]

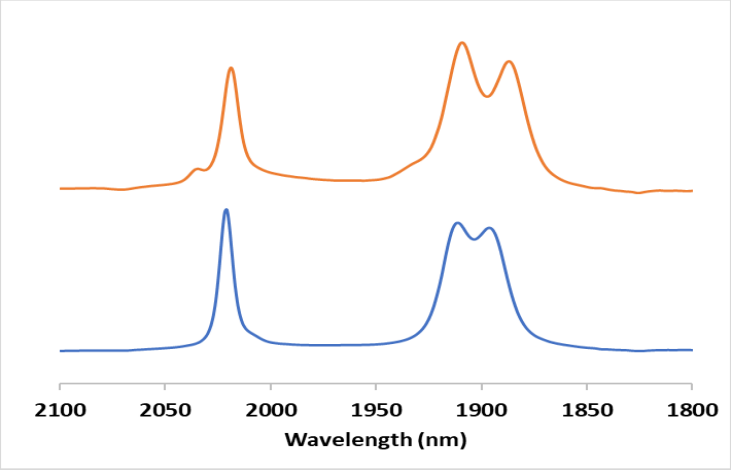

Figure 4.10: Graph of the IR spectra obtained in acetonitrile for $RuRe_{bpt}$ (orange line) and $RuRe_{bpybpt}$ (blue line). Both spectra were subjected to background subtraction of the reference spectrum in acetonitrile.

The position, and the number of IR stretching modes observed for the $RuRe_{bpybpt}$ complex are in agreement with the IR spectra previously reported by Brennan with νCO at higher frequency than that of the Re-triazole monomeric species $[Re(CO)_3(bpt)Cl]^-$ (displayed in Table 4.1 as Re_{bpt}).[17] As the charge is shared across the metal centres in the RuRe complexes, the electron density on the Re-carbonyl moiety is reduced from that of Re_{bpt}. Therefore, the carbonyl bands are located at higher energy as there is a reduction in the back-bonding interaction between Re and carbonyl ligands.[17]

4.4.1.3 UV-Visible spectroscopy

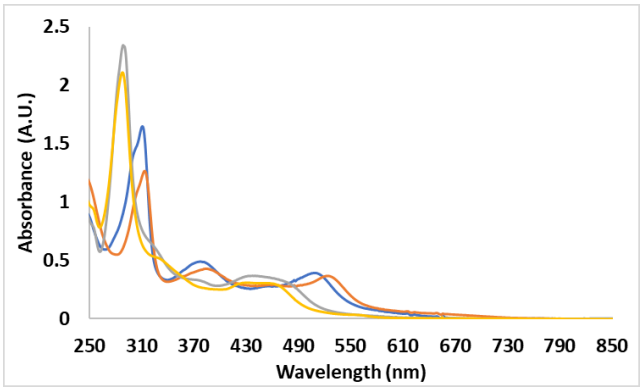

Figure 4.11: UV-Visible spectra of Ru_{bpt} (blue line) and $RuRe_{bpt}$ (orange line), Ru_{bpybpt} (grey line) and $RuRe_{bpybpt}$ (yellow line) in acetonitrile with absorbance ~0.36 at 355 nm.

In Figure 4.11, the UV-Visible spectra of the mono- and di-nuclear Ru-triazole complexes (Ru_{bpt}, $RuRe_{bpt}$, Ru_{bpybpt} and $RuRe_{bpybpt}$) are displayed. Assignment of the features of the spectra are consistent with other Ru-based complexes.[17,29,31] the features observed below 350 nm are assigned to ligand-centred π-π* transitions, those above 350 nm are typical of ^{1}MLCT transitions, with the furthest red feature assigned to the lowest energy ^{1}MLCT. At a glance, there is a clear electronic effect due to the presence of the carboxy-ester groups on the peripheral bpy ligands in Ru_{bpt} and $RuRe_{bpt}$. The features corresponding to the LC transitions experience a red shift, from ~290 nm to ~310 nm, upon the addition of the carboxy-ester groups. This has been seen in many complexes when comparing bpy and dceb analogues.[31–33] The bands in the region 350 – 650 nm displays the additional features observed for the Ru_{bpt} complex (discussed in Chapter 3) and are present in the spectrum for the $RuRe_{bpt}$ complex, as seen for the equivalent dinuclear $RuPd_{bpt}$ complex (Chapter 3). These are possibly due to the electron withdrawing effect of the dceb ligands and the asymmetry of the anionic bpt ligand.[34,35] There is a slight redshift of the spectrum generated for $RuRe_{bpt}$ on comparison with the mononuclear complex (λ_{max} 525 nm from 510 nm). Although, the trend with bpt dinuclear species is normally a blueshift on comparison to the monomer, as seen with $RuPd_{bpt}$ in Chapter 3 and with the homo-dinuclear $[(Ru(bpy)_2)_2(bpt)]^{3+}$.[36] This is also observed with $RuRe_{bpybpt}$, it is blue shifted compared to Ru_{bpybpt} with the addition of the Re-carbonyl unit. The blueshift is attributed to the distribution of the negative charge on the bpt ligand between the two metal centres.

4.4.1.4 Emission spectroscopy

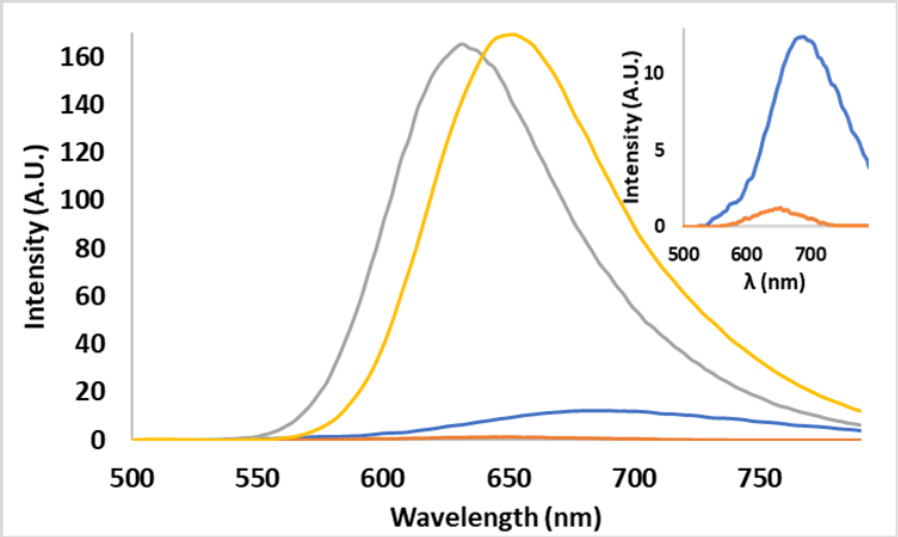

Figure 4.12: Graph of the emission spectra collected for Ru_{bpt} (blue line), $RuRe_{bpt}$ (orange line), compared to that of $[Ru(dceb)_2(2,5\text{-}bpp)](PF_6)_2$ (yellow line) and $[Ru(dceb)_3](PF_6)_2$, (grey line) all in acetonitrile, with an excitation wavelength of 355 nm and OD at this point ~0.36. The insert is a close-up of the blue and orange line.

The emission spectra for the $RuRe_{bpt}$ complex and the corresponding mononuclear analogue can be seen in Figure 4.12, which highlights the effect of ligand substitution of a dceb ligand, in $Ru(dceb)_3$, for 2,5-bpp ($Ru_{2,5\text{-}bpp}$) or bpt (Ru_{bpt}). When terpyridine (2,5-bpp) is introduced ($Ru_{2,5\text{-}bpp}$) , the only effect is that the λ_{max} is shifted slightly to the red by 20 nm. Whereas, there is a clear reduction in the emission intensity upon the introduction of the bpt ligand and a further red shift of the λ_{max} from 630 nm ($Ru(dceb)_3$) to 690 nm for Ru_{bpt}. When the Re-carbonyl unit is attached ($RuRe_{bpt}$), the emission is blue shifted 40 nm, in comparison with that of the parent Ru_{bpt}. The emission intensity is quenched, almost entirely, with the addition of the Re-carbonyl. RuRe complexes with emission spectra have previously been reported, by Vogler and Kisslinger, for a $[Ru(bpy)_2(bipyrimidine)Re(CO)_3Cl](PF_6)_2$ complex.[37] The emission of their complex was only visible in the solid state and at low temperature (77 K) and the λ_{max} = 774 nm, close to the λ_{max} of $[(Ru(bpy)_2)_2(bipyrimidine)](PF_6)_4$ (769 nm). The similar positioning of the λ_{max}, enabled them to conclude the emission was from the Ru→bipyrimidine transition state. Similar observations have previously been reported for the $RuRe_{bpybpt}$ (λ_{max} 635 nm) and the homonuclear $[(Ru(bpy)_2(bpt))_2]^-$ (λ_{max} 675 nm) complexes.[17,36] Table 4.2 displays the emission λ_{max} of the Ru-based complexes. In both RuRe complexes ($RuRe_{bpt}$ and $RuRe_{bpybpt}$), the emission λ_{max} is

centred at wavelengths >600 nm (Table 4.2). This suggests the emission is based on the Ru-metal centre and not the Re-centre. According to Ishitani and co-workers, Ru-based emission is indicative of limited metal-to-metal interaction, which they found to increase the TON in CO_2 reduction experiments involving RuRe complexes.[8]

Table 4.2: Table of the λ_{max} of the emission spectra for several Ru-polypyridyl complexes in acetonitrile.

Complex	Emission λ_{max} (nm)
Ru_{bpt}	690
$RuRe_{bpt}$	650
$*Ru_{bpybpt}$	675
$*RuRe_{bpybpy}$	635
$*RuRu_{bpybpt}$	648
$*Ru(bpy)_3$	615
$Ru_{2,5\text{-}bpp}$	650
$Ru(dceb)_3$	630

*The values for the bpy-based complexes have been taken from ref [17].

4.4.1.5 Computational Studies

These studies were carried out by Prof. Conor Long in a similar manner to that described in Chapter 3. As seen in Chapter 3, the complexes modelled used dmcb, instead of the dceb ligands to simplify the calculations.

The simulated UV-Visible absorbance spectrum for the model complex $[Ru(dmcb)_2(bpt)Re(CO)_3Cl]^-$ is displayed in Figure 4.13. The quantum calculations carried out on this model complex describe the lowest singlet excited state (ES1), populated by an excitation wavelength just below 600 nm, to be Ru-to-dmcb charge-transfer character, involving only one dmcb ligand. Whereas, the intense transition, populated by photons just below 500 nm, is a Ru-to-dmcb charge-transfer state, involving both dmcb ligands. Ru-polypyridyl complexes undergo ISC from the singlet to the triplet state within the first few hundred femtoseconds, competing with IC to the lowest singlet state. Therefore, population of the triplet state is generally from the initially populated singlet state determined by the excitation wavelength. For ease of comparison, the triplet excited state populated by the lowest singlet excited state, was also investigated and found to be a Ru-to-Re charge-transfer state, with some electron density residing on the peripheral ligands. The simulated UV-visible spectrum of the triplet state, in Figure 4.14, was generated for the complex to aid with the interpretation of the TA recorded. The spectrum generated displays an intense absorbance in the mid-IR region (800-2300 nm), that is beyond the window measured in the TA studies. It also shows a relatively intense absorption with a λ_{max} of ~700nm. In the TA studies discussed later there is no evidence for this absorption following excitation of $RuRe_{bpt}$.

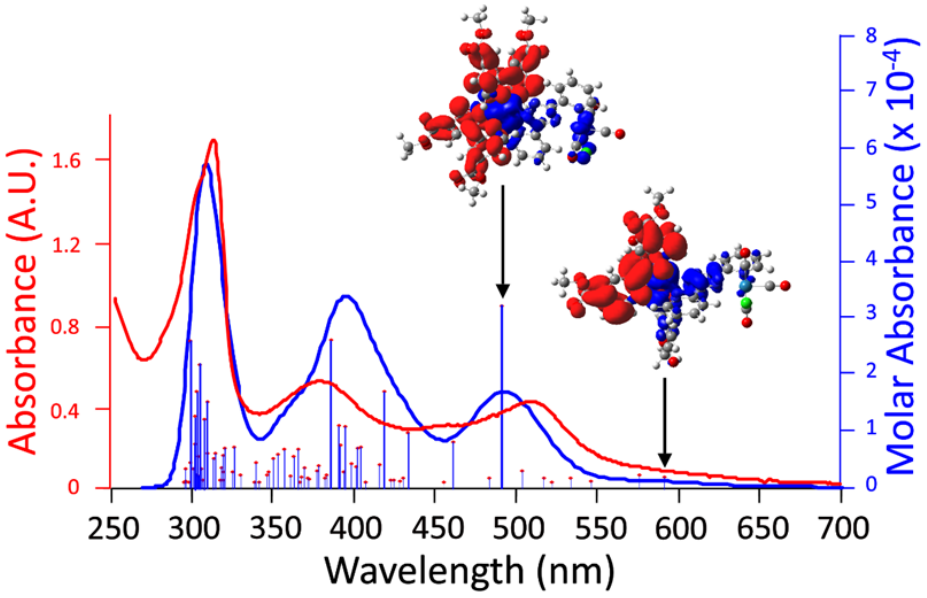

Figure 4.13: Graph of the experimental (red) and theoretical (blue) UV-Visible absorbance spectra in acetonitrile for $RuRe_{bpt}$ and $[Ru(dmcb)_2(bpt)Re(CO)_3Cl]^-$, respectively. The inserts are the electron density difference maps of the model complex in the singlet excited state ES1 (right) and ES8 (left).

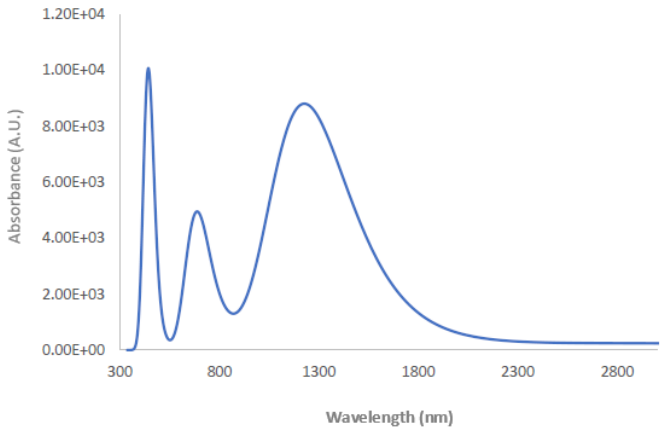

Figure 4.14: Graph of the simulated UV-Visible absorbance spectrum of the triplet excited state of the RuRe-dmcb complex in acetonitrile

The above-mentioned computational studies prompted an investigation of the loss of the Cl^- anion on the model complex and the effect this had on the simulated results. The calculations determined the Franck Condon state of this complex (without Cl^-) is significantly Ru-to-dmcb charge-transfer in character. Population of the triplet state from this singlet state leads to substantial Ru-to-Re charge-transfer. The electron density difference maps of the singlet and triplet energies are presented in Figure 4.15.

The UV-Visible spectrum simulated for this state, in Figure 4.16, resembles the experimental electronic absorbance spectrum of $RuRe_{bpt}$ (Figure 4.11). The TA spectra, which is a difference spectrum of the ground state to excited state at different time intervals after excitation, therefore, would be expected to be minimal as the ESA and GSB overlap significantly. This is comparable to the TA findings discussed in the next section.

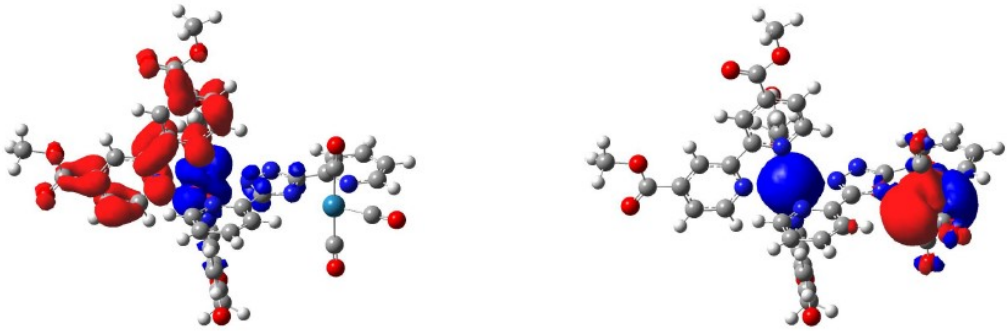

Figure 4.15: Electron density difference maps of $[Ru(dmcb)_2(bpt)Re(CO)_3]^{2-}$ in the singlet excited state (left) and triplet excited state (right), where the electron density moves from blue to red.

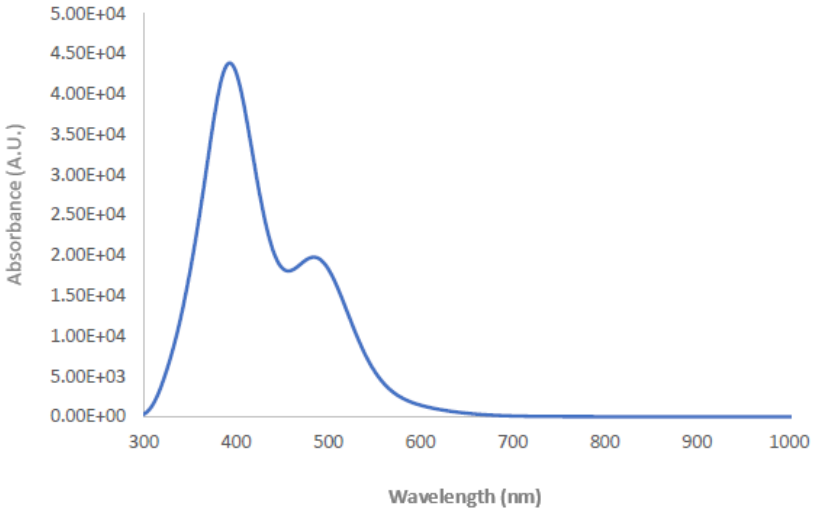

Figure 4.16: Graph of the simulated triplet excited state UV-Visible absorbance spectrum of $[Ru(dmcb)_2(bpt)Re(CO)_3]^{2+}$

4.4.1.6 ns-Transient Absorption Spectroscopy

The TAS set-up was previously described in chapter 2. The sample was prepared by dissolving the complex in dry acetonitrile and purging with CO_2 gas for ~20 min. The excitation wavelength employed was 355 nm, with a sample absorbance of ~0.36 at this wavelength.

The TA spectra obtained following excitation of $RuRe_{bpt}$ showed minimal spectral features and hence, have not been included. In these spectra there is an extremely weak GSB between ~400-600 nm and a very weak ESA at wavelengths >600 nm. Both features are too weak to extract any information from them. The lack of any prominent spectral features indicates that, following excitation, this complex forms a non-emissive excited state that regenerates the parent, or a complex with an absorption profile similar to the parent absorbance spectrum, which could result from loss of the Cl ligand as indicated by the computational studies. There was no evidence in the TA spectra for the 'usual' ^{3}MLCT that is usually observed for bpy-Ru complexes which persists for hundreds of nanoseconds.

The computational studies also suggest that once the complex is in the triplet excited state the electron density resides, almost solely, on the Re-metal unit (Figure 4.15). This suggests that the reduction in emission experienced with these complexes is more likely due to the electron density residing at the catalytic centre.

Similar experiments were performed using the $RuRe_{bpybpt}$ complex, and analogous to the dceb counterpart, the emission intensity of the dinuclear species is substantially reduced compared to the Ru-mononuclear complex. In contrast to the dceb analogues, transient signals were observed in the TAS experiments (Figure 4.17), following excitation of the sample at 355 nm in acetonitrile. The experiments were performed in CO_2 saturated solutions. The transient signal for this complex at 370 nm, decays over ~ 120 ns, which agrees with the recovery of the parent absorption at ~ 460 nm. These transient features are assigned to the ^{3}MLCT which is typical of ruthenium compounds. The ESA at <400 nm is attributed to the LC transitions typical of $Ru(bpy)_2$ complexes, such as, that seen in the TA spectra for the $Ru(bpy)_2$(2,5-bpp) complex (discussed in Chapter 2).[15] There is also another ESA >500 nm, but were weak in

intensity. Ishitani and co-workers, observed similar TA spectra for their complex, depicted in Figure 4.1 (top), dissolved in argon saturated DMF, with λ_{exc} = 532 nm.[8]

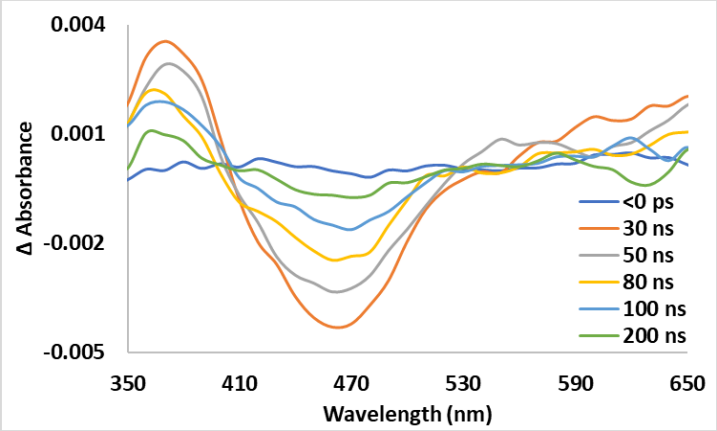

Figure 4.17: Graph of the absorbance difference TA spectra for $RuRe_{bpybpt}$ in CO_2 saturated acetonitrile, obtained following excitation of solution with an absorbance of ~0.36 at 355nm. .

4.4.1.7 Photocatalytic Studies

Photocatalytic studies were performed on both dinuclear RuRe complexes in CO_2 saturated solvent mixtures with acetonitrile:TEOA and DMF:TEOA (2:1) under a CO_2 atmosphere. It is important, in photocatalytic studies focusing on CO_2 reduction using metal carbonyl catalytic centres, such as the systems explored within this chapter, to account for the possible loss of one (or more) of the carbonyl groups on the complex, and that these do not contribute to the TON of any CO produced. Therefore, when calculating the TON of CO produced, a TON of above 3, in the case of -$Re(CO)_3$ systems, must be achieved for the system to be considered as photocatalytically active. Unfortunately, no CO was detected for either of the RuRe complexes under the photocatalytic conditions used. Previously in Chapter 2 the effect of the experimental conditions used greatly influences the TON of the product produced, therefore it is possible that other conditions may be more suited for these complexes. The use of BIH as a stronger donor would be interesting to explore. Whereas in Chapter 3, although, the related dinuclear RuPd complex is unsuccessful in hydrogen production under the selected homogenous conditions, it performs well in a p-type photoelectrochemical cell (p-PEC), once bound to the surface of a NiO electrode. This may be the case with the RuRe complexes also and there are currently being assessed for photoelectrocatalytic CO_2 reduction in a collaborator's laboratory.

4.4.2 Porphyrin based complexes

The second part of this chapter focuses on replacing the ruthenium photosensitising unit with an organic unit, which led to the synthesis of the two compounds in Figure 4.18 (PorRe1 and PorRe2). This work is in the early stages of investigation and therefore, only preliminary results are discussed. Following the synthesis, the complexes were characterised using mass spectrometry, and a range of spectroscopic techniques including ^{1}H-NMR, UV-vis, luminescence and others. Outlined in Figure 4.18 is the synthetic pathway used for the porphyrin-Re complexes. Initially, the porphyrin unit is synthesised, which was done using a well-established process the Adler method, which involves heating the requisite aldehydes and pyrrole together in propionic acid at reflux temperatures for 8 hours.[38] During the synthesis of the target porphyrin, in Figure 4.18, a number of different porphyrins form, including tetraphenylporhyrin, mononitrobenzenetriphenylporphyrin, and the di-, tri, and tetranitro-porphyrin analogues, therefore column chromatography is used to separate the target complex. Following column chromatography, the next step involves reduction of the nitro-group to an amine using $SnCl_2$. Once again, column chromatography is used to obtain the target compound pure. If metalation of the porphyrin ring is required, it can be carried out by using the corresponding metal acetate as a metalating agent. In this chapter, Zn is the metal centre of the porphyrin ring for complex **PorRe2**, therefore Zn acetate was utilised. At this stage column chromatography is employed again to separate the starting materials from product. To synthesis the porphyrin-imine-Re photocatalyst, a one-pot reaction is carried out, where an aldehyde or ketone is added to the nitroporphyrin. The $Re(CO)_5$ is then added to the reaction mixture, which yields the Porphyrin-$Re(CO)_3$ supramolecular assembly.

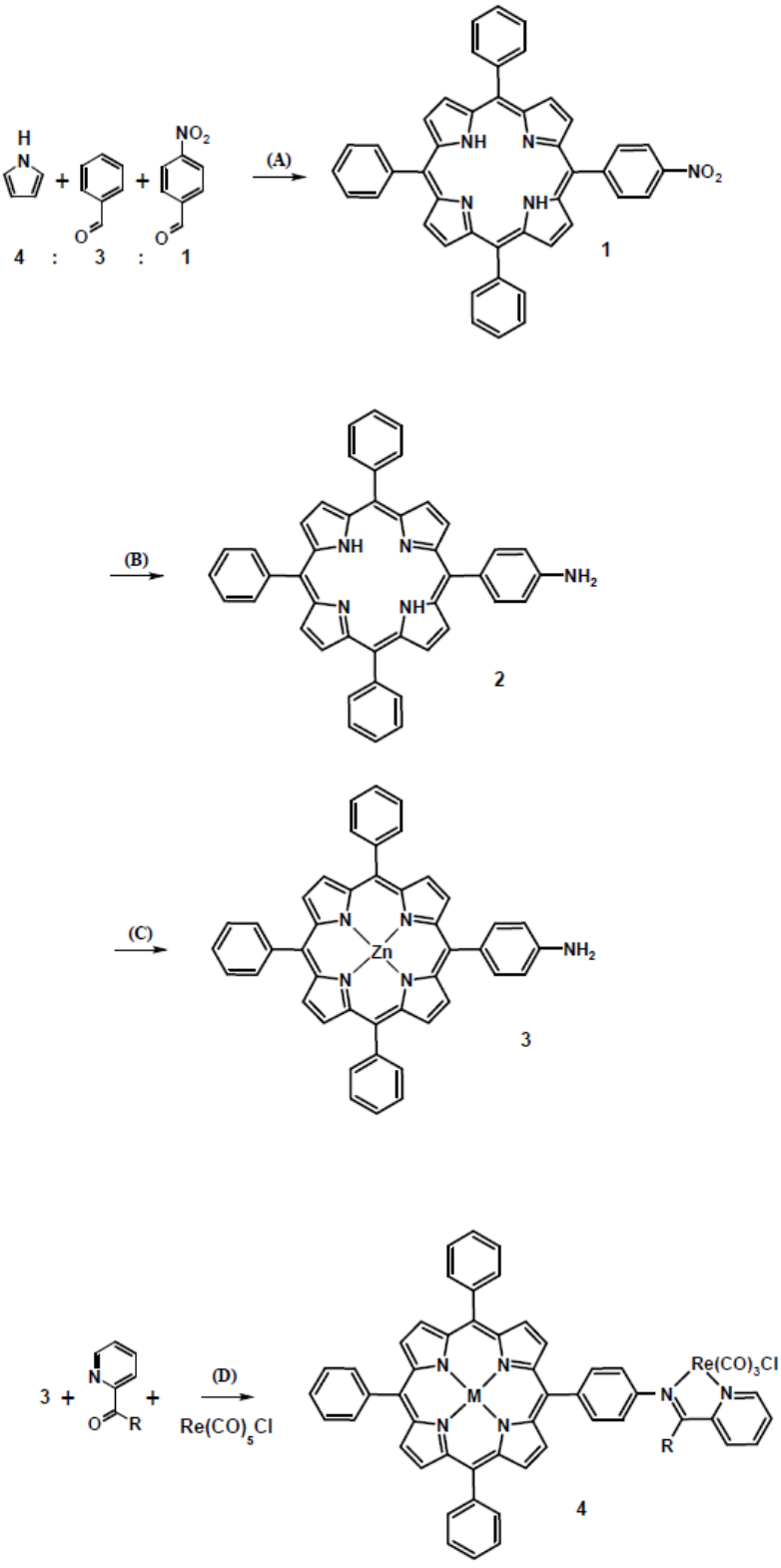

Figure 4.18: General reaction scheme for the synthesis of the porphyrin-Re complexes. (A) = propionic acid at reflux temperature for 1 h, (B) = chloroform and $SnCl_2$ in HCl and acetic acid, stirred overnight at 70°C (C) = DCM:MeOH (3:1) and Zn acetate, stirred at room temperature for 1 h, (D) = MeOH at reflux temperature overnight, (note M = Zn when R = phenyl ring and M = H_2 when R = H).

4.4.2.1 ^{1}H NMR Spectroscopy

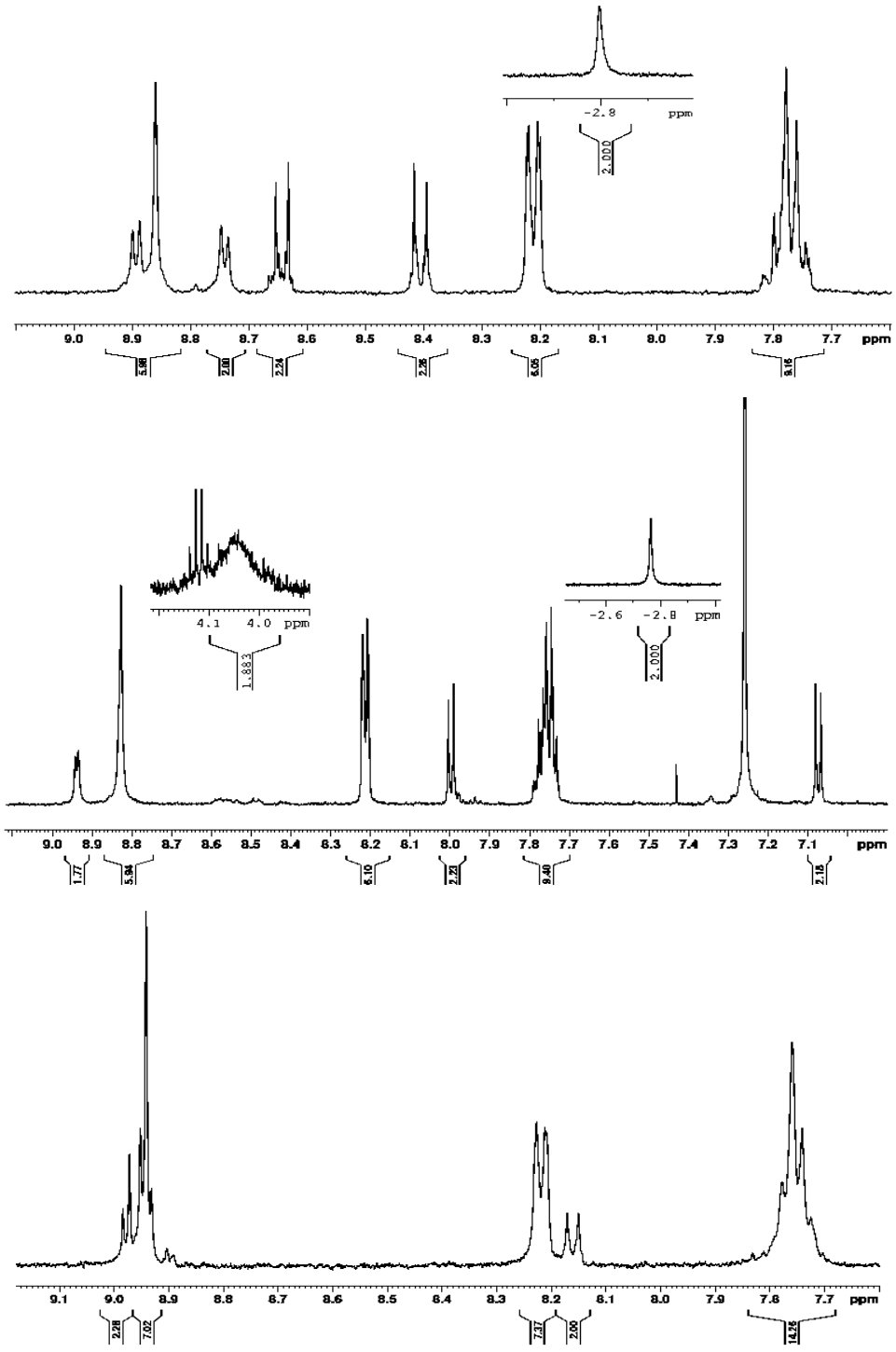

*Figure 4.19: Graphs of the ^{1}H-NMR spectra collected for complex **1** (top), **2** (middle) and **3** (bottom) (as seen in the reaction scheme above) in CD_3Cl.*

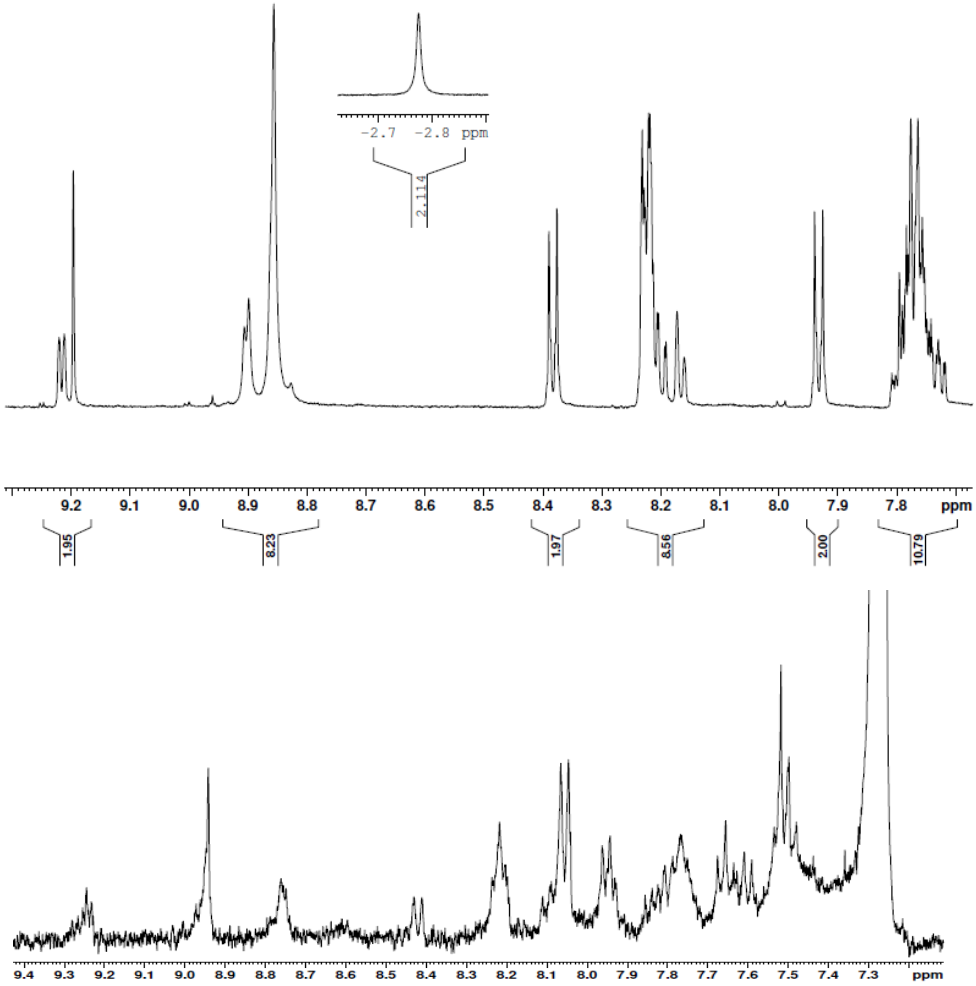

Figure 4.20: Graphs of the ^{1}H NMR spectra of the supramolecular porphyrin-Re complexes ***PorRe1*** *(top) and* ***PorRe2*** *(bottom) in CD_3Cl.*

The above proton NMR spectra displayed in Figure 4.19 and Figure 4.20, demonstrates the synthetic pathway and the NMR spectra of the porphyrin-Re complexes synthesised and studied in this chapter.

4.4.2.2 UV-Visible and Emission Spectroscopy

The UV-Visible absorbance spectra for the 2 porphyrin-Re complexes are displayed in Figure 4.21. The typical Soret (~350-450 nm) and Q bands are clear in the UV-vis spectra for both complexes.[39] The Soret band is attributed to a strong transition between the ground state (S_0) and the second excited state (S_2). The Q bands are attributed to quasi-allowed transitions between the ground state and the first singlet excited state (S_1). For the free-base porphyrin, **PorRe1**, the characteristic 4 Q bands are present between 480 nm and 700 nm. Whereas, for the Zn metallated **PorRe2,** the metalation of the porphyrin centre increases the symmetry, and this is evident by the reduction in the number of Q bands from four to two. **PorRe2** also has a further absorbance towards the red region in the spectrum which is not usually observed for porphyrins. This extreme red absorbance may be due to aggregation of the complex, although, reducing the concentration did not remove the absorbance centred ~800 nm.

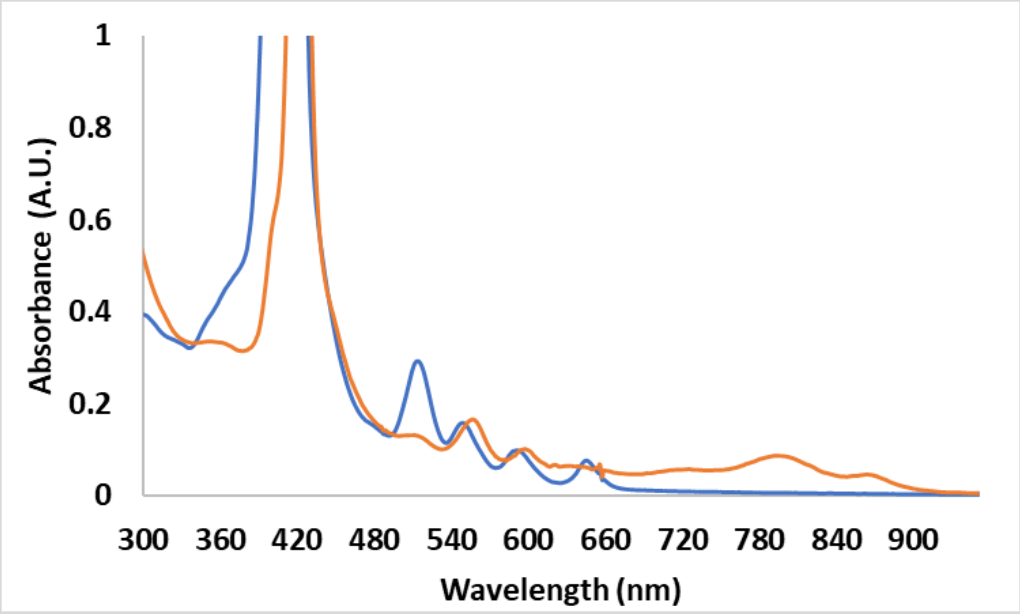

*Figure 4.21: Graph of the electronic absorbance spectra for **PorRe1** (blue line) and **PorRe2** (orange line) in acetonitrile.*

The emission spectra for the two supramolecular assembles are displayed in Figure 4.22. Both complexes give rise to the typically observed emission spectra reported for the precursor free-base/metallo-Zn amino-porphyrin and other porphyrin-Re complexes.[39,40] The emission intensity however is lower for the Zn complex due to the presence of Zn in the porphyrin ring.[40] Both porphyrins exhibit lower intensity than that typically recorded for metal-free porphyrins such as TPP (not shown below).

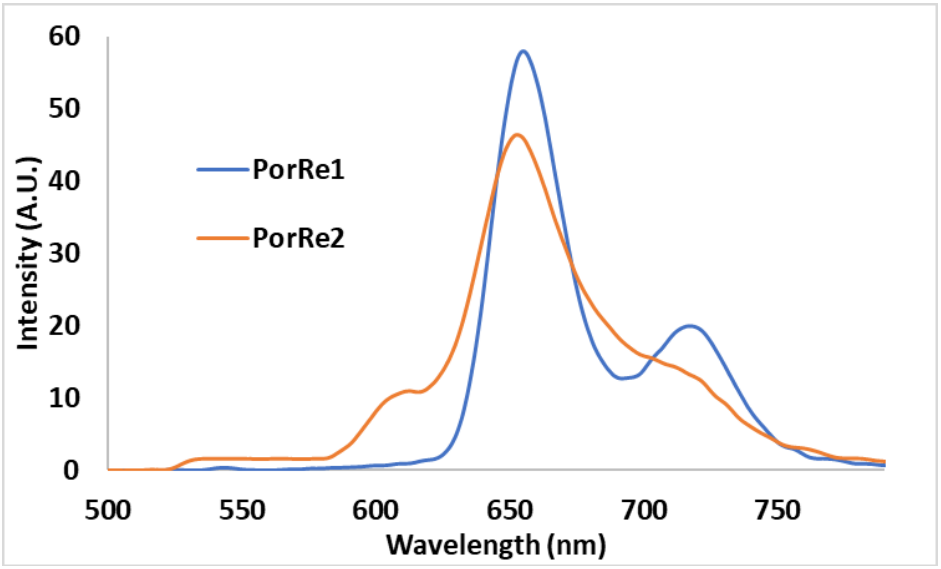

Figure 4.22: Graph of the emission spectra for PorRe1 (blue line) and PorRe2 (orange line) with an excitation wavelength of 355 nm in acetonitrile (samples are isoabsorptive with an absorbance of 0.2 at 355 nm).

4.4.2.3 Preliminary ns-Transient Absorption and Time-resolved Photoluminescence Spectroscopy

The photophysical properties of both porphyrin-Re complexes was probed using nanosecond-TAS, and time resolved luminescence following excitation at 355 nm. Figure 4.23 displays the TA spectra collected for the **PorRe1** complex and Figure 4.24 displays that for the **PorRe2** complex. Both graphs show that bleaching of the Soret band between ~390-450 nm occurs following excitation. As, the Soret band is intense spectra cannot be collected in the region 390 nm to 440 nm, therefore, the bleach is not displayed in either graph. Both systems give rise to transient signals on both sides of the GSB of the Soret band (there is some overlap of the GSB with ESA). The ESA, to the lower energy side of the Soret parent bleach (at ~ 470 nm), is attributed to the excited state Soret band in both complexes. Also evident in the transient absorption spectra are the GSB of the first, and most intense, Q band for both complexes, ~520 nm for **PorRe1** and ~560 nm for **PorRe2**. Figure 4.23 also clearly displays the excited state absorbance of the Q bands, all red shifted in their excited state. The band at higher energy to the Soret bleach, observed in both graphs, is attributed to the same excited species. Unfortunately, reliable kinetics could not be extracted for this feature due to its low intensity. The lifetime of the excited state at ~470 nm was measured for both complexes and found to be ~4 μs for **PorRe1** and ~7 μs for **PorRe2**. The longevity of the excited state indicates that in the TA studies this species is assigned to a porphyrin-based triplet excited state. Whereas, in the time-resolved photoluminescence experiments conducted with these complexes (maps of the emission decay are given in Figure 4.25), the signals are assigned to the singlet excited state with a lifetime of ~13 ns **PorRe1** and ~9 ns for **PorRe2**. Alessio and co-workers conducted similar ns-TA studies on their mono- and tetra-Re-carbonyl appended free-base mono- and tetra-pyridyl porphyrins, $[Re(CO)_3(bpy)(4'MPyP)][CF_3SO_3]$ and $[(Re(CO)_3(bpy))_4(4'TPyP)][CF_3SO_3]_4$.[41] They also observe a broad feature from ~460 – 520 nm that overlaps with a GSB at 515 nm. Their ESA are assigned to a triplet species as the features decay over hundreds of microseconds, in both the porphyrin-Re assemblies and the parent porphyrin macrocycles.

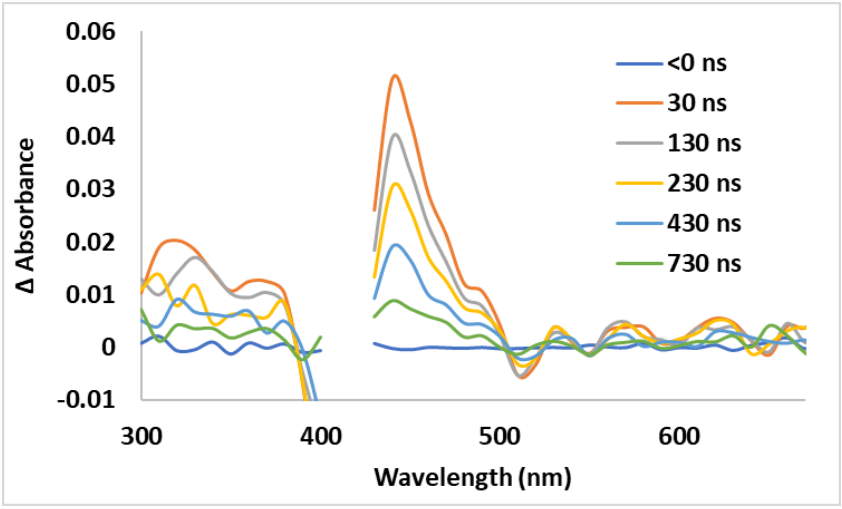

Figure 4.23: TA spectra collected for PorRe1 in CO_2 saturated acetonitrile (using 355 nm excitation and an absorbance of ~0.36).

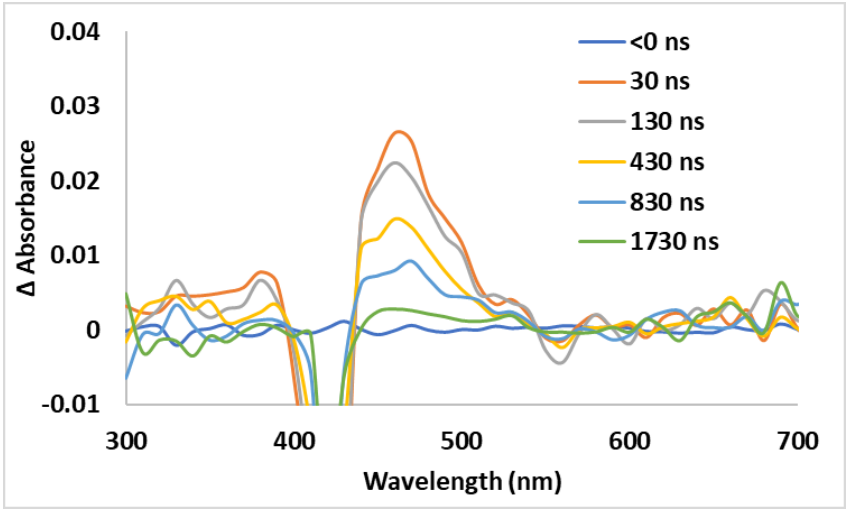

Figure 4.24: TA spectra collected for PorRe2 in CO_2 saturated acetonitrile (using 355 nm excitation with an absorbance of ~0.36).

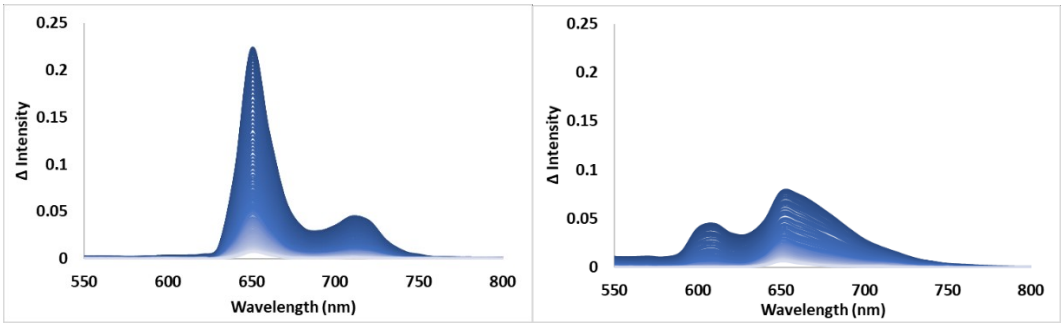

Figure 4.25: The time-resolved photoluminescence spectra for PorRe1 (left) and PorRe2 (right) with excitation wavelength of 355 nm, Dark blue → light blue is after excitation → 50 ns.

4.4.2.4 Preliminary Photocatalytic Studies

Photocatalytic studies were conducted on **PorRe1** under the same conditions as the RuRe complexes, using solvent mixtures using with acetonitrile:TEOA and DMF:TEOA (2:1) under a CO_2 atmosphere. When the head space in the vials was checked for CO, no peaks were observed in the chromatograms to indicate the photoreduction of CO_2 to CO under the experimental conditions employed. Ishitani and co-workers have reported enhanced photocatalytic activity when BIH is added to the DMF:TEOA solvent mix, and this was also tried, but again no CO was detected.[11] It is possible there is CO in the solution, or another CO_2 conversion product such as formic acid may have been generated but the solutions were not analysed for this.

The UV-Visible spectra of the **PorRe1** complex was monitored prior to and following irradiation at 407 nm in the photocatalytic experiments (Figure 4.26). It is clear from the spectra, that the presence of BIH results in decomposition of the complex. No difference was recorded between the irradiated and dark sample when the solvent mix contained DMF/TEOA. Metalation of the porphyrin ring, as done with **PorRe2**, was thought to increase the stability of the complex. Changes in the electronic absorbance spectrum of porphyrin-Re assemblies have been reported previously by Perutz and co-workers, due to the hydrogenation of a porphyrin to a chlorin and/or ligand substitution on the Re-carbonyl.[20,42] These indicate that the Q band region of the spectrum is best to monitor changes occurring, inferring that the changes are only seen in at the Q bands. Whereas, in the systems studied in this chapter, the Soret band diminishes.

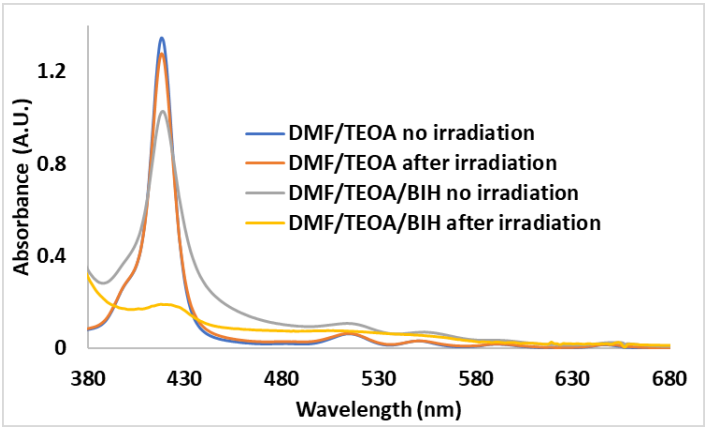

*Figure 4.26: Graph of UV-Visible spectra of **PorRe1** before and after photocatalysis under different conditions with an irradiation wavelength of 407 nm*

4.5 Conclusions

In conclusion, this chapter compares the photocatalytic activity for ruthenium vs porphyrin based supramolecular assemblies for CO_2 reduction. The mononuclear Ru-triazole complex, from Chapter 3, and a Re-carbonyl catalytic centre were successfully combined to yield the $RuRe_{bpt}$ photocatalyst. This was confirmed by NMR spectroscopy and the presence of the rhenium carbonyl was confirmed using IR spectroscopy. Although, TA experiments and computational methods corroborated that excitation of $RuRe_{bpt}$ populates the triplet state. The lifetime of this state is significantly lower than optimum for CO_2 reduction, with near full recovery of the GSB occurring within the first 50 ns. The complex was unsuccessful in reducing CO_2 to CO under the conditions examined. As seen with the $RuPd_{bpt}$ complex in Chapter 3, it is possible that the photocatalytic ability will improve under heterogenous conditions.

This chapter also examined the possibility of moving away from rare metals by incorporating a porphyrin macrocycle as the photosensitising unit on the supramolecular photocatalyst. The Re-carbonyl meatal centre was attached through a Schiff base reaction on the imine bridge. TA experiments proved these systems have a long-lived triplet states. Yet, the free-base complex, PorRe1, was unsuccessful for CO_2 reduction under the photocatalytic conditions used. It was assumed that TEOA alone was not sufficient to reduce the excited porphyrin, therefore, BIH was used in conjunction with TEOA during photocatalysis. Unfortunately, PorRe1 was found to decompose under these conditions. PorRe2 may be more stable, due to the metalation of the porphyrin ring and the presence of the phenyl group in place of a hydrogen atom on the imine bridge. The phenyl group was added to avoid CO_2 insertion at this position on the PorRe1 complex.

References

[1] S. Nahar, M. F. M. Zain, A. A. H. Kadhum, H. A. Hasan, M. R. Hasan, *Materials (Basel)* **2017**, *10*, DOI 10.3390/ma10060629.

[2] X. Liu, S. Inagaki, J. Gong, *Angewandte Chemie International Edition* **2016**, *55*, 14924–14950.

[3] A. Coleman, C. Brennan, J. G. Vos, M. T. Pryce, *Coordination Chemistry Reviews* **2008**, *252*, 2585–2595.

[4] N. Komatsuzaki, Y. Himeda, T. Hirose, H. Sugihara, K. Kasuga, *BCSJ* **1999**, *72*, 725–731.

[5] A. Gabrielsson, F. Hartl, H. Zhang, J. R. Lindsay Smith, M. Towrie, Vlček Antonín, R. N. Perutz, *J. Am. Chem. Soc.* **2006**, *128*, 4253–4266.

[6] Y. Tamaki, K. Koike, T. Morimoto, Y. Yamazaki, O. Ishitani, *Inorg. Chem.* **2013**, *52*, 11902–11909.

[7] Y. Kuramochi, O. Ishitani, *Inorg. Chem.* **2016**, *55*, 5702–5709.

[8] B. Gholamkhass, H. Mametsuka, K. Koike, T. Tanabe, M. Furue, O. Ishitani, *Inorg. Chem.* **2005**, *44*, 2326–2336.

[9] K. Koike, S. Naito, S. Sato, Y. Tamaki, O. Ishitani, *Journal of Photochemistry and Photobiology A: Chemistry* **2009**, *207*, 109–114.

[10] Y. Tamaki, K. Watanabe, K. Koike, H. Inoue, T. Morimoto, O. Ishitani, *Faraday Discuss.* **2012**, *155*, 115–127.

[11] Y. Tamaki, K. Koike, T. Morimoto, O. Ishitani, *Journal of Catalysis* **2013**, *304*, 22–28.

[12] G. Sahara, R. Abe, M. Higashi, T. Morikawa, K. Maeda, Y. Ueda, O. Ishitani, *Chem. Commun.* **2015**, *51*, 10722–10725.

[13] R. Kamata, H. Kumagai, Y. Yamazaki, G. Sahara, O. Ishitani, *ACS Appl. Mater. Interfaces* **2018**, DOI 10.1021/acsami.8b05495.

[14] G. Sahara, H. Kumagai, K. Maeda, N. Kaeffer, V. Artero, M. Higashi, R. Abe, O. Ishitani, *J. Am. Chem. Soc.* **2016**, *138*, 14152–14158.

[15] Q. Pan, L. Freitag, T. Kowacs, J. C. Falgenhauer, J. P. Korterik, D. Schlettwein, W. R. Browne, M. T. Pryce, S. Rau, L. González, et al., *Chem. Commun.* **2016**, *52*, 9371–9374.

[16] R. Hage, A. H. J. Dijkhuis, J. G. Haasnoot, R. Prins, J. Reedijk, B. E. Buchanan, J. G. Vos, *Inorg. Chem.* **1988**, *27*, 2185–2189.

[17] C. Brennan, Synthesis and Characterisation of Mononuclear and Dinuclear Rhenium Carbonyl Complexes., PhD, Dublin City University, **2007**.

[18] N. Põldme, L. O'Reilly, I. Fletcher, J. Portoles, I. V. Sazanovich, M. Towrie, C. Long, J. G. Vos, M. T. Pryce, E. A. Gibson, *Chemical Science* **2019**, *10*, 99–112.

[19] K. Kalyanasundaram, M. K. Nazeeruddin, *J. Chem. Soc., Dalton Trans.* **1990**, *0*, 1657–1662.

[20] C. D. Windle, M. W. George, R. N. Perutz, P. A. Summers, X. Z. Sun, A. C. Whitwood, *Chem. Sci.* **2015**, *6*, 6847–6864.

[21] Y. Kou, S. Nakatani, G. Sunagawa, Y. Tachikawa, D. Masui, T. Shimada, S. Takagi, D. A. Tryk, Y. Nabetani, H. Tachibana, et al., *Journal of Catalysis* **2014**, *310*, 57–66.

[22] K. Chanawanno, J. Caporoso, V. Kondeti, S. Paruchuri, T. C. Leeper, R. S. Herrick, C. J. Ziegler, *Dalton Trans.* **2014**, *43*, 11452–11455.

[23] C. Shiju, D. Arish, N. Bhuvanesh, S. Kumaresan, *Spectrochimica Acta Part A: Molecular and Biomolecular Spectroscopy* **2015**, *145*, 213–222.

[24] D. Daphnomili, G. Landrou, S. P. Singh, A. Thomas, K. Yesudas, B. K, G. D. Sharma, A. G. Coutsolelos, *RSC Adv.* **2012**, *2*, 12899–12908.

[25] J. Cui, J. Lu, X. Xu, K. Cao, Z. Wang, G. Alemu, H. Yuang, Y. Shen, J. Xu, Y. Cheng, et al., *J. Phys. Chem. C* **2014**, *118*, 16433–16440.

[26] K. Ladomenou, T. N. Kitsopoulos, G. D. Sharma, A. G. Coutsolelos, *RSC Adv.* **2014**, *4*, 21379–21404.

[27] C. Ringot, N. Saad, R. Granet, P. Bressollier, V. Sol, P. Krausz, *Journal of Porphyrins and Phthalocyanines* **2010**, *14*, 925–931.

[28] M. Gardner, A. J. Guerin, C. A. Hunter, U. Michelsen, C. Rotger, *New Journal of Chemistry* **1999**, *23*, 309.

[29] R. Hage, J. G. Haasnoot, J. Reedijk, R. Wang, J. G. Vos, *Inorg. Chem.* **1991**, *30*, 3263–3269.

[30] R. Hage, Ruthenium and Osmium Complexes Containing Triazole Ligands, PhD, Dublin City University, **1991**.

[31] T. Kowacs, Q. Pan, P. Lang, L. O'Reilly, S. Rau, W. R. Browne, M. T. Pryce, A. Huijser, J. G. Vos, *Faraday Discuss.* **2015**, *185*, 143–170.

[32] G. S. Bindra, M. Schulz, A. Paul, S. Soman, R. Groarke, J. Inglis, M. T. Pryce, W. R. Browne, S. Rau, B. J. Maclean, et al., *Dalton Trans.* **2011**, *40*, 10812–10814.

[33] T. Kowacs, L. O'Reilly, Q. Pan, A. Huijser, P. Lang, S. Rau, W. R. Browne, M. T. Pryce, J. G. Vos, *Inorg. Chem.* **2016**, *55*, 2685–2690.

[34] K. Y.-D. Tsai, I.-J. Chang, *Inorg. Chem.* **2017**, *56*, 8497–8503.

[35] E. M. Thoresen, D. Balcells, S. Øien-Ødegaard, K. T. Hylland, M. Tilset, M. Amedjkouh, *Dalton Trans.* **2018**, *47*, 2589–2601.

[36] R. Hage, *Ruthenium and Osmium Complexes Containing Triazole Ligands: Synthesis, Structures, Electrochemical, and Photophysical Properties*, **1990**.

[37] A. Vogler, J. Kisslinger, *Inorganica Chimica Acta* **1986**, *115*, 193–196.

[38] A. D. Adler, F. R. Longo, J. D. Finarelli, J. Goldmacher, J. Assour, L. Korsakoff, *The Journal of Organic Chemistry* **1967**, *32*, 476–476.

[39] B. L. Auras, V. A. Oliveira, H. Terenzi, A. Neves, B. A. Iglesias, *Photochem. Photobiol. Sci.* **2016**, *15*, 564–579.

[40] T. Gatti, P. Cavigli, E. Zangrando, E. Iengo, C. Chiorboli, M. T. Indelli, *Inorg. Chem.* **2013**, *52*, 3190–3197.

[41] M. Ghirotti, C. Chiorboli, M. T. Indelli, F. Scandola, M. Casanova, E. Iengo, E. Alessio, *Inorganica Chimica Acta* **2007**, *360*, 1121–1130.

[42] C. D. Windle, M. V. Câmpian, A.-K. Duhme-Klair, E. A. Gibson, R. N. Perutz, J. Schneider, *Chem. Commun.* **2012**, *48*, 8189–8191.

Chapter 5

5 The Photophysics of Boron-dipyrromethene (BODIPY) Polymers

Chapter 5 introduces boron-dipyrromethene (BODIPY) polymers. This chapter opens with an insight into the background of BODIPY based compounds in particular focusing on photo-driven applications. In this chapter, two BODIPY-polymers and their monomeric BODIPY precursors are studied using both TRIR and TA spectroscopies spanning the pico-second to nano-second time scales. The pico-second studies were conducted at the Central Laser Facility, at the Rutherford Appleton Laboratory, in the U.K. The polymers were assessed for their ability to generate singlet oxygen, and for hydrogen generation in solution and under heterogeneous conditions when immobilised on NiO. The latter studies were carried out in collaboration with the Gibson Group from Newcastle University.

5.1 Aim

The predominant aim of this chapter was to investigate the early-time (picosecond) photodynamics of two BODIPY polymers and assess their ability to act as photosensitisers for both hydrogen generation and also singlet oxygen generation. However, to fully understand the photophysics of the polymers, the BODIPY precursors were also studied. The TA and TRIR studies were carried out both in solution and also when the polymers were immobilised onto NiO, as the polymers were assessed for photoelectrocatalytic hydrogen evolution. Usually BODIPYs have high fluorescence quantum yields with negligible triplet state formation unless heavy atoms are incorporated, however the polymers discussed here generate singlet oxygen and therefore have the potential to act as singlet oxygen delivery systems.

5.2 Introduction

BODIPY dyes are derivatives of 4,4-difluoro-1,3,5,7-tetramethyl-4-bora-3a,4a-diaza-s-indacene. Structurally, BODIPYs are based on half of a porphyrin macrocycle, such as those discussed in Chapter 4. The BF_2 unit increases the robustness and rigidity of the structure, which in turn increases the fluorescence yield of the complex. The π-conjugation of the system is expressed with strong absorbances in the UV-Visible region. The photophysical properties and therefore, the underlying electron dynamics can be manipulated by varying the substituents on the BODIPY core, in the positions indicated in Figure 5.1.

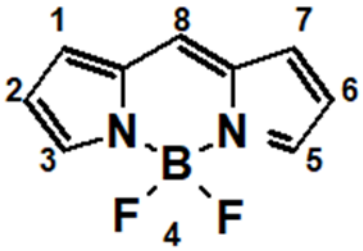

Figure 5.1: Structure of the BODIPY core with the indicated sites for substitution, 8 is also referred to as the meso position.

BODIPY dyes have been extensively examined since initially synthesised, reported by Treibs and Kreuzer in 1968,[1] and this has led to a wide library of BODIPY-based compounds with varying functionalities and applications.[2,3] The optical properties of BODIPYs are highly tuneable through synthetic modifications on the BODIPY core, inciting the synthesis of a long list of compounds with varying photo-driven applications. These applications include bio-sensing, photodynamic therapy and solar energy conversion. Bio-sensing usually employs monomeric BODIPY systems, which utilises the high fluorescence quantum yields coupled with negligible triplet state formation usually observed for BODIPY dyes.[4] Whereas, applications in areas such as photodynamic therapy, which causes cell death through $^1O_2$ production, or as photosensitisers/photocatalysts for hydrogen generation, require BODIPY-based systems where population of a triplet state occurs.[5–7] Population of a triplet state via ISC is generally only possible in BODIPY based systems furnished with heavy atoms, such as, iodine, or the attachment of metal complexes.[8] However, recent multi-chromatic BODIPY complexes have been reported where triplet states are populated

in the absence of toxic heavy atoms, by triplet-triplet energy transfer (TTET) or, the more topical process, singlet fission (SF).[9–11]

The heavy atom effect is seen in many systems, including the Ru-based complexes discussed in this thesis. The presence of heavy atoms leads to the phenomenon known as spin-orbit coupling, which enhances ISC to the triplet state. The enhancement of ISC from singlet to triplet excited state results in a decrease in emission intensity.[12] TTET or triplet-triplet annihilation (TTA) occurs when the triplet state is populated by transfer from another triplet state within the molecule (intramolecular conversion) or between separate entities (intermolecular).[9,10,13,14] This transfer mechanism, therefore, eradicates the original triplet excited state (annihilation) in favour of the new triplet excited state on the BODIPY. Singlet fission is the process of the excited singlet state splitting to two triplet states within the same molecule. This occurs in the absence of heavy atoms and when the triplet energy levels are half or less than that of the excited singlet state.[11]

Montero and co-workers recently (2018) reported the photophysics of a BODIPY dimer and used TA spectroscopy to identify the photodynamic pathway leading to formation of a triplet state, in a heavy atom free BODIPY dimer. They proposed that the triplet state is populated following a singlet fission mechanism in the dye (Figure 5.2).[11] The TA kinetic data collected for the dimer in $CHCl_3$ was used to confirm that a triplet excited state (^{3}ES) formed, following direct conversion from a singlet excited state (^{1}ES, $\tau_1 \approx 16.2$ ps) with the grow in of the ^{3}ESA ($\tau_2 \approx 391$ ps) denoted as TT (for the separate triplet states), which relaxed to give charge separated triplet states that persist on the micro-second timescale (T..T, $\tau_3 \gg 1$ ns). They used ns-TA to investigate the long τ_3 lifetime and found it to be 386 μs in N_2 saturated $CHCl_3$, the longest reported to date for a BODIPY derivative. In addition to lifetimes, a high singlet oxygen quantum yield ($\Phi\Delta = 0.75$) was reported, which confirms population of a triplet state in this dimer.

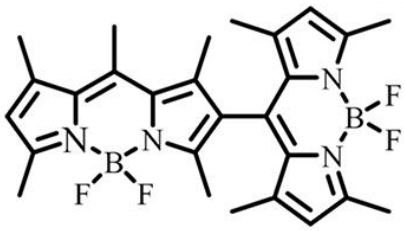

Figure 5.2: Structure of the dimeric-BODIPY complex studied by Montero et al (the BODIPYS are attached via a 2-8 orientation).[11]

Gibson and co-workers have led the way for BODIPY-based photosensitisers immobilised onto p-type semiconducting films, such as NiO semiconductors. In 2014, the group examined the early-time photodynamics of a BODIPY system (Figure 5.3: top) in solution and when anchored onto a NiO film via the carboxy appendage.[15] They compared TA spectra collected for solution-based experiments to those for surface-based experiments (immobilised systems) (Figure 5.3). From the solution (CH_2Cl_2) based TA experiments, they were able to assign the ESA features to both a ^{1}ESA and ^{3}ESA species, based on the lifetime, with the ^{1}ESA at ~450 nm decaying within ~400 ps, together with a new feature at ~425 and 650 nm, assigned as to a ^{3}ESA which persisted for hundreds of nanoseconds ($\tau_{425} \approx 730$ ns in air, $\tau_{425} \approx 860$ ns in Ar). The TA spectral features suggest that the ^{3}ES is localised on the BODIPY moiety.

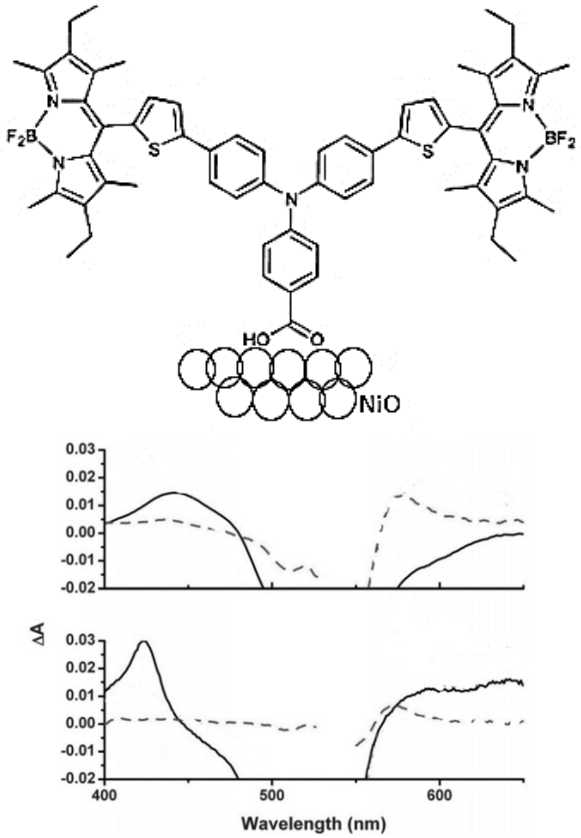

Figure 5.3: Structure of BODIPY dye investigated by the Gibson group as a p-type photosensitiser immobilised on NiO semiconductor and the corresponding TA spectra collected in CH_2Cl_2 (block line) and immobilised to NiO (dashed line), 10 ps (top graph) and 2 ns (bottom graph) after excitation at 532 nm, (adapted from reference [15])

Once the compound was immobilised onto NiO, the spectral features reduced in intensity. This was also seen for the Ru-complexes discussed in Chapter 3. It is most likely due to a lower concentration of the immobilised sample on the NiO. The broad ESA, between 400-470 nm is representative of a ^{1}ESA. Whereas, the ESA feature at ~575 nm, present within a few ps, is comparable with the spectroelectrochemical studies of the complex, and suggest the generation of a reduced species. This ESA is present throughout the experiment and during ns-TA, and was assigned to the oxidised NiO and reduced complex, leading to formation of a charge separated state (NiO^+|$BODIPY^-$), which with a lifetime $\tau_{575nm} \approx 180$ ns. The lifetime of the charge-separated state is three times longer than that observed in the BODIPY-free analogue (where cyano groups replace the BODIPY moieties).[16] The group have gone on to investigate systematic synthetic changes to the BODIPY-dye and how this alters the kinetics of the system in solution and when immobilised on the surface of NiO

films.[17,18] The group have also employed TRIR to further probe the charge transfer processes of the compound, depicted in Figure 5.3, and the BODIPY-free analogue, both in solution and on the surface of NiO films.[19] This method enabled a deeper comprehension of the dynamics involved in these compounds. The TRIR data are in agreement with the kinetics obtained using TA spectroscopy, but no further kinetic information was gained for the experiments carried out. A bleach was observed at 1543 cm^{-1} (which is a BODIPY-based ground state) and the corresponding ESA at 1525 cm^{-1}, was assigned as a triplet excited state localised on the BODIPY moiety. This ESA band decayed over the same time scale as observed in the TA experiments with a lifetime of $\tau \approx 760$ ns. The Gibson group investigated both DCM and acetonitrile as solvents for the TRIR study. This showed that the band representative of the BODIPY localised ^{3}ES was not present in acetonitrile samples. The absence of this band is due to the increased polarity of acetonitrile stabilising the charge transfer state and populating a lower energy level.

In this chapter, TA and TRIR spectroscopic techniques were used to probe the photophysical properties in the BODIPY dyes, depicted in Figure 5.4 and Figure 5.5. The polymeric analogues were investigated using both TRIR and TA in solution studies and using TA when the polymers were adsorbed on NiO films. As the use of BODIPY chromophores for applications in DSSCs continues to grow,[3] BODIPY-based polymers are another approach. Since the first conjugated BODIPY-based polymer was reported by Herrmann and co-workers in 2009,[20] a number of BODIPY polymers have since been synthesised.[21] Although, there has been a number of publications focusing on the synthetic approaches for these polymers, no time resolved studies have been reported to date. The following section introduces the time resolved studies performed and the results tentatively suggest that the triplet states are populated via singlet fission (SF).

5.3 Materials

The compounds and polymers examined in this chapter were synthesised by other members of the DCU group following known methods with minor adjustments to that reported in the literature.[22,23] The synthetic routes for the BODIPY polymers and the monomeric precursors are given in the following figures:

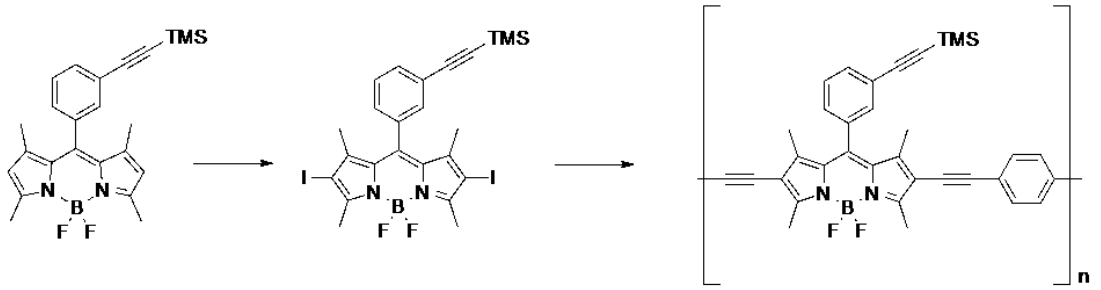

Figure 5.4: General schematic of the reaction steps for the synthesis of TMS-BODIPY polymer (BODIPY → Di-iodo-BODIPY → Polymer).

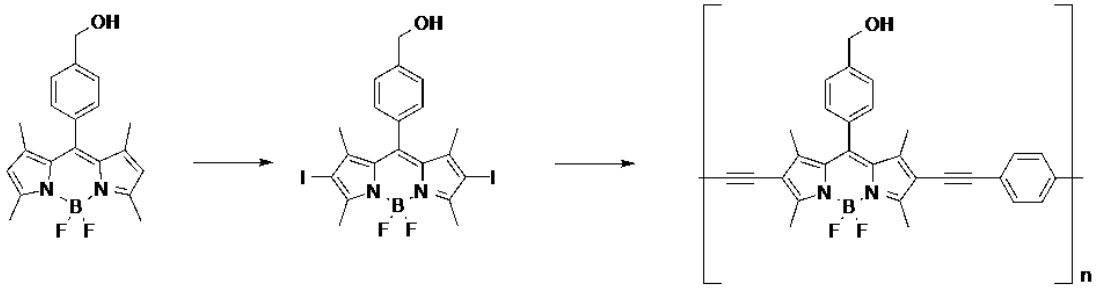

Figure 5.5: General reaction schematic for the synthesis the $HOCH_2$-BODIPY polymer (BODIPY → Di-iodo-BODIPY → Polymer).

5.4 Results and Discussion

5.4.1 UV-Vis and Emission Spectroscopy

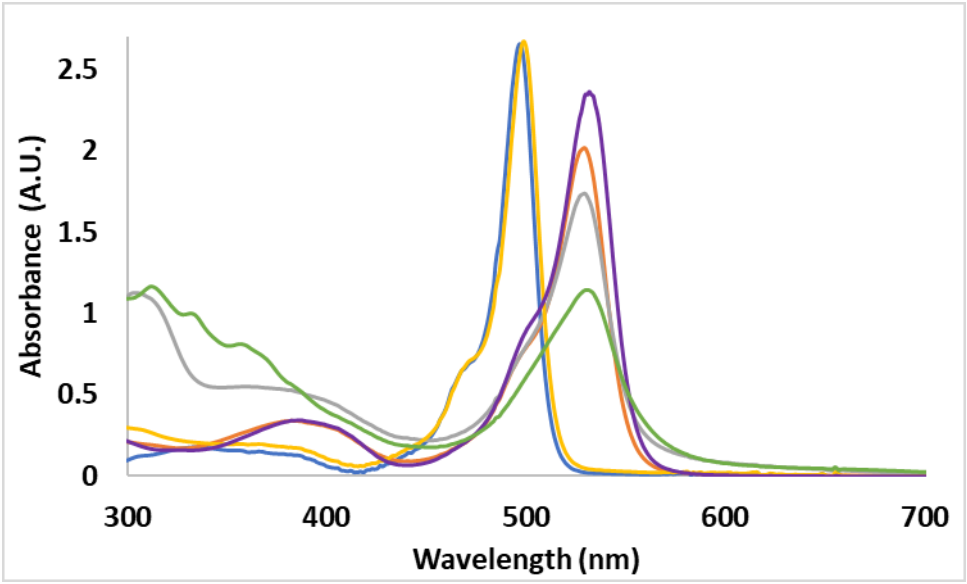

Figure 5.6: UV-Vis. absorbance spectra of HO-BODIPY (blue line), TMS-BODIPY (yellow line), HO-CH_2-di-iodo (orange line), TMS-di-iodo-BODIPY (purple line), HOCH_2-BODIPY-polymer (grey line) and TMS-BODIPY-polymer (green line) in acetonitrile.

Displayed in Figure 5.6 are the UV-Visible spectra for the BODIPY-dyes in CH_3CN. The monomeric BODIPY dyes have a strong absorbance just below 500 nm. This absorbance is attributed to the intense $S_0 \rightarrow S_1$ π-π* transition on the dipyrromethene core. The shoulder on the blue side of the intense feature (~465 nm) is due to vibronic coupling of this transition. The weaker absorbance ~360 nm is due to the weaker $S_0 \rightarrow S_2$ π-π* transition. These absorbance features are red shifted by ~30 nm when the hydrogen atoms at the 6 position of the pyrrole units are replaced with iodine, yielding the diiodo-BODIPY. For the dyes studied the λ_{max} of the absorbance is dependent on the substituents in the 2 and 6 position (H vs I). Caruso and co-workers, reported that the main contributing factor to the location of the λ_{max} was in fact the bulkiness of the substituents on the BODIPY frame.[24] In our studies a redshift in absorbance is experienced with the addition of iodine at the 2 and 6 positions, as seen for other iodine furnished BODIPY compounds.[25] The same is observed upon polymerisation, with a red shift in the λ_{max} for the polymers. The broadening of the polymeric species is due to increased π-conjugation and has been reported for other BODIPY-polymers.[20]

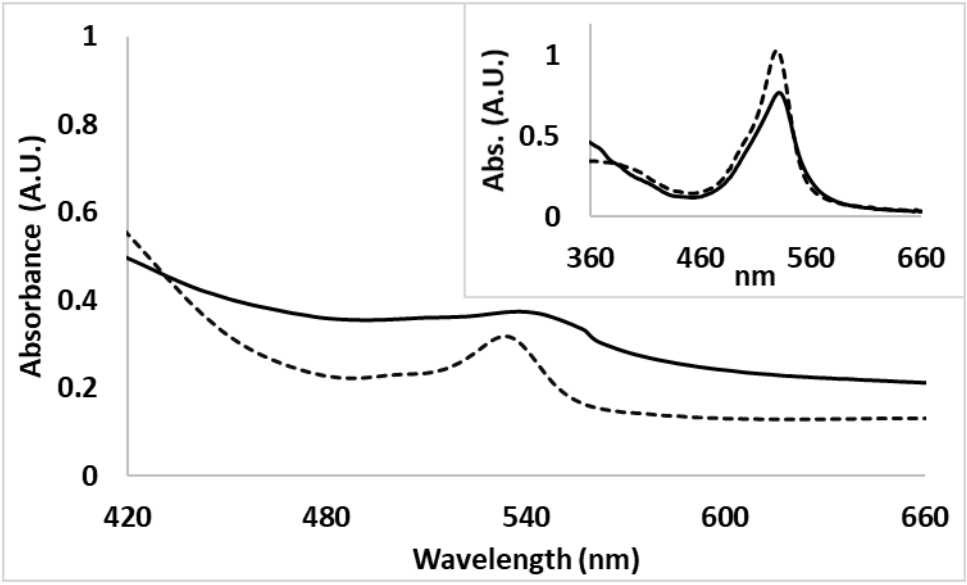

Figure 5.7: Graph of the UV-visible absorbance spectra for the $HOCH_2$-polymer (dashed line) and TMS-BODIPY-polymer (block line) immobilised on NiO film. Insert are the UV-visible spectra of the polymers in CH_3CN.

In Figure 5.7, the UV-vis spectra for the polymers when immobilised on NiO and dissolved in acetonitrile solution are displayed. The spectral features are maintained following immobilisation but shifted to the red by ~10 nm to that of the solution spectra. This is shift towards the red when immobilised onto the NiO was previously observed with the Ru-complexes in Chapter 3.

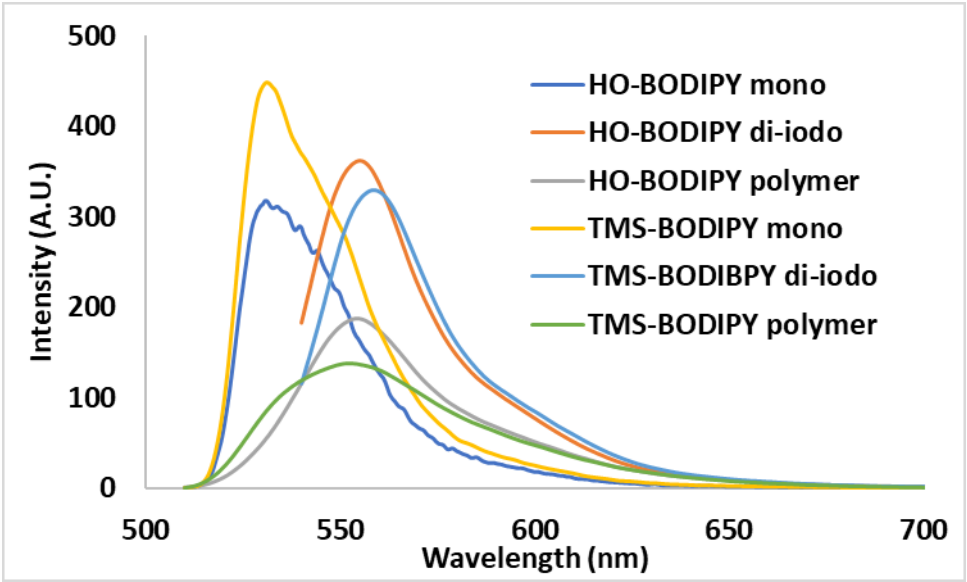

Figure 5.8: The emission spectra for all BODIPY-based compounds in DCM with an excitation wavelength of 500 nm for the non-halogenated monomers and polymer compounds and 520 nm for di-iodo compounds (O.D. of ~0.2 at λ_{exc} for all samples).

The emission spectra for the monomeric precursors and the corresponding BODIPY-polymers are displayed in Figure 5.8. The emission maxima occur at similar wavelengths to that reported for other BODIPY dyes.[25] The diiodo BODIPY dyes are much less emissive when compared to their H-analogue, due to ISC and population of the triplet state. When the emission spectra for the monomeric precursors are compared to the polymers, the emission spectra for the polymers are further reduced and broadened.

5.4.2 ps-TA Spectroscopy Studies

The BODIPY dyes and polymers were studied using both time-resolved transient absorption and time-resolved infrared spectroscopy in acetonitrile and dichloromethane and these results are presented in this section. Additionally, the polymers were immobilised onto NiO, and investigated using TAS. In Figure 5.9, the compounds investigated were dissolved in dichloromethane, while in Figure 5.10, the experiments were performed in acetonitrile and the spectra are less intense, therefore it was difficult to extract reliable kinetic data and only the spectral features are discussed for these experiments in Figure 5.10.

For the spectra displayed in Figure 5.9, Figure 5.10 and Figure 5.11, there is a GSB, for each BODIPY present within the instrumental response time (200 fs) and this bleach corresponds to the $\lambda_{max.}$ in the electronic absorbance spectra (as seen in Figure 5.6) for all compounds. The GSB also overlaps with the stimulated emission (SE) of the BODIPY dye on the lower energy side of the GSB. The features observed in the spectra, in Figure 5.10, are weak when compared to the spectra in Figure 5.9 or Figure 5.11. This may be due to solvent, excitation wavelength or the experimental setup (the experiments in Figure 5.10 and Figure 5.11 were carried out during different research trips to the Central Laser Facility).

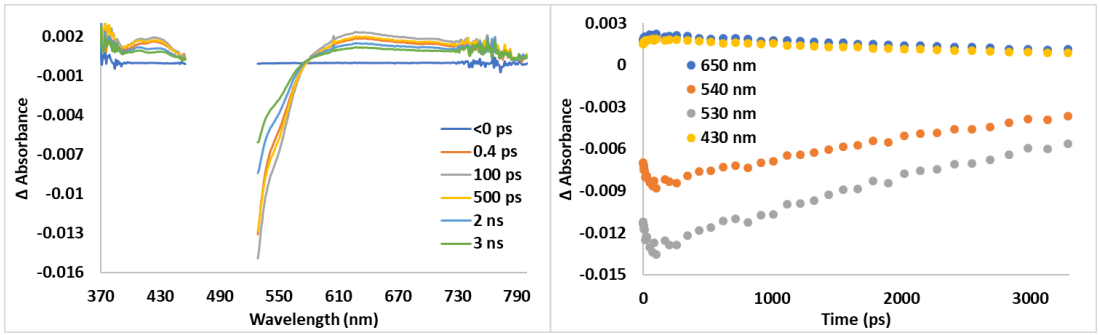

A

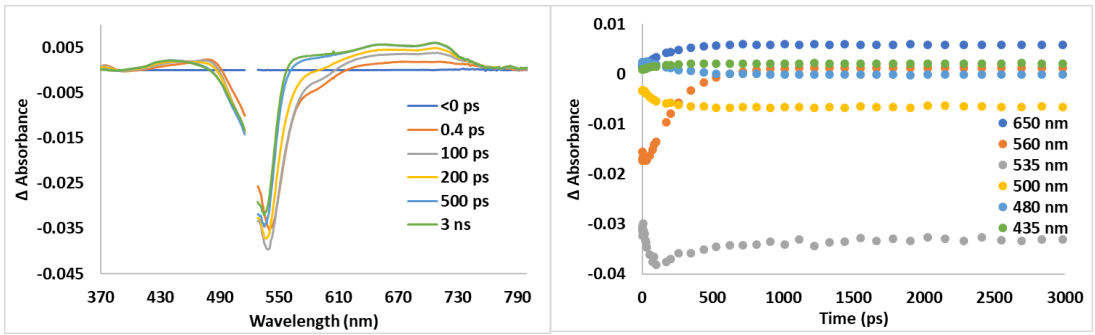

B

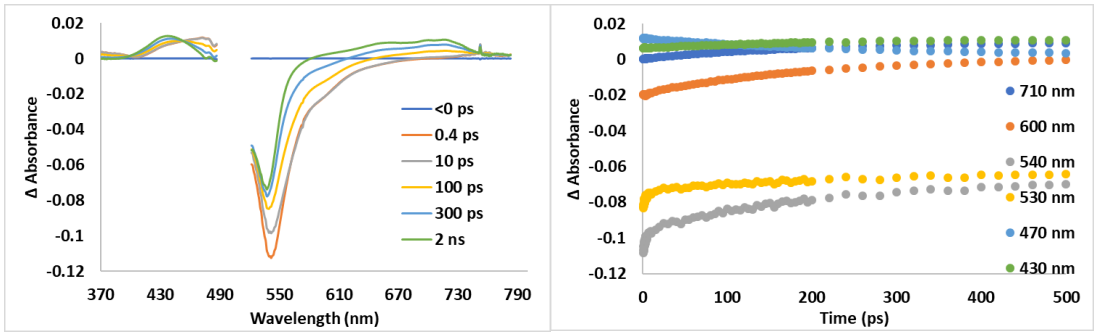

C

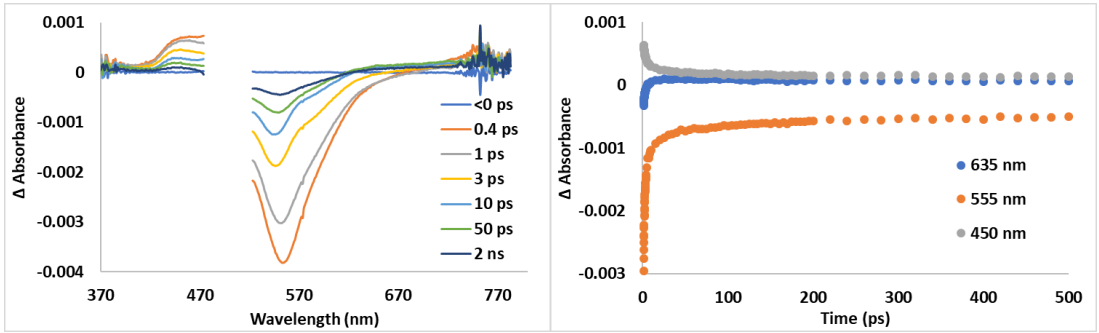

D

*Figure 5.9: The spectra on the left hand side depict the TA spectra collected following excitation of the TMS-BODIPY dyes: (**A**) TMS-BODIPY (**B**) TMS- Diiodo-BODIPY (using 525 nm excitation) and that of the TMS-BODIPY-Polymer in DCM (**C**) and the TMS-BODIPY-Polymer immobilised on a NiO film (**D**) (following excitation using 520 nm). The break in the graph is due to the notch of the excitation wavelength. The corresponding kinetic traces at stated wavelengths for each system are displayed in the right hand side.*

At a glance, the TA spectra collected for the TMS-based BODIPY dyes, and corresponding polymer dissolved in DCM and when absorbed onto NiO films appear similar (Figure 5.9). In summary, all the spectra collected exhibit GSB at ~ 540 nm, (within the response time of the instrument), which corresponds to the maximum absorbance in the electronic absorbance spectra for these compounds (UV-visible spectra are given in Figure 5.6). The compounds and polymers also display ESA features. Another feature in all the spectra is stimulated emission (SE), and this feature overlaps on the red side of the GSB for all BODIPYs (emission spectra are provided in Figure 5.8).

Displayed in Figure 5.9: A, are the TA spectra collected up to 3 ns for the monomeric TMS-BODIPY. Following photolysis, in addition to the GSB, ESA features are observed both at 430 nm, and to the low energy side of the GSB extending from 610-730 nm. Over the time frame of the experiment the ESA features begin to decay, together with a recovery of the parent bleach. The early-time kinetics were extracted for this halogen free BODIPY dye by analysing the ESA features at 430 nm and 650 nm, and both appear to follow the same kinetics. The features decay monoexponentially, with $\tau \approx 4$ ns. Recovery of the GSB also occurs with $\tau \approx 4$ ns, concurrent with the ESA features. Based on the lifetimes, and the similarities of these transient signals with that in the literature, these ES are assigned to population of a singlet excited state.[17]

In the case of the halogenated analogue, TMS-diiodo-BODIPY (Figure 5.9: B), differences are evident in the kinetics, and the spectrotemporal evolution of the signals are also different. Similar to the H-analogue, following photolysis, a negative bleach at ~ 550 nm, which corresponds to the GSB, together with an ESA at 435, 480, and a broad absorption spanning 560 – 730 nm is observed. The ESA at 480 nm decays with a $\tau \approx 225$ ps, which is concomitant with the rate of recovery (SE) at 560 nm, with $\tau \approx$ 230 ps. This indicates these features are related to the singlet excited state (^{1}ES). The broad ESA feature at wavelengths greater than 560 nm grows in with a $\tau \approx 230$ ps. This ESA persists over the timeframe of the experiment (3 ns, which is the limit of detection for the pico second set-up), with no decay evident. Gibson and co-workers have assigned a similar broad ESA, in their TA experiments where they studied triphenylamine-BODIPY sensitisers, to a charge separated state.[17] This is unlikely for the monomeric BODIPY compounds reported in this Thesis and the signals

observed on the nanosecond time scale are tentatively assigned to a T_1 state. In addition to the broad ESA, over the same time frame an ESA also forms at 435 nm, but as it overlaps with the ^{1}ES, reliable kinetic data could not be determined. Assignment of the ESA features to a T_1 state has previously been reported by Zhao and co-workers for iodine-containing BODIPY compounds, which are similar to the BODIPYs reported here.[13] Zhao's halogenated BODIPY compounds were examined by ns-TA and the excited features experience long-lived lifetimes up to ~66 μs. They assign the long-lived ESA features to a T_1 state as a charge separated state is unlikely and DFT calculations conducted by the Zhao group supported this assignment. In our experiments, there is little recovery of the GSB feature up to 3 ns. An isosbestic point is evident at 480 nm, which confirms the triplet state is formed directly from the singlet state. In the BODIPY system, the presence of iodine contributes to enhanced ISC from the singlet to the triplet state, and the feature at 435 nm is assigned to a T_1 state, reported by Zhang an co-workers for a diiodo-BODIPY compound (discussed below).[26]

It is important to note, the overlapping of features on both sides of the GSB, with the singlet excited state on the blue side (centred ~480 nm) and the SE on the low energy side. Therefore, the SE contributes to the kinetic data extracted at ~540 nm. Whereas, at ~530 nm there is less of a contribution from the SE, this can be seen by a comparison of the corresponding kinetic traces provided in Figure 5.9: B. Due to this, it was not possible to determine reliable kinetics for the GSB. The assignment of the spectral TA features to both singlet and triplet states, their related kinetics and the proposed mechanism followed for population of the triplet state are all characteristic for diiodo-BODIPY compounds and agree with that reported in the literature.[13,26]

Displayed in Figure 5.9: C, are the TA spectra for the corresponding TMS-BODIPY-polymer (see Figure 5.4 for structure). Similar to the previous two BODIPYs discussed, the kinetics appear to be mono-exponential kinetics, other than the GSB (which is masked both SE and also an ES feature). For the TMS-BODIPY polymer following excitation, a negative feature is evident at ~ 545 nm which corresponds to the GSB, together with ESA signals at 430, 470 and a broad absorption at greater than 600 nm. Over the timeframe of the experiment (2 ns) the GSB reduces by ~ 30%, but it is difficult to determine what portion is recovery of the parent polymer or SE. The kinetics for SE extracted at 600 nm translates to a rate of recovery of the SE with $\tau \approx$

206 ps. The ESA feature at 470 nm has a similar lifetime, with $\tau \approx 239$ ps, and is assigned to a singlet excited state. As this signal decays, a further ESA feature ~430 nm grows in with $\tau \approx 221$ ps. An isosbestic point is evident at 455 nm in the TA spectra, which indicates that the feature at 470 nm is the precursor to the long-lived features at 430 and at longer wavelengths greater than 600 nm. The latter forms, over a similar timeframe with $\tau \approx 201$ ps. The ESA features at 430 nm and at greater than 600 nm persist longer than 3 ns and remain at the same intensity for the duration of the experiment and is attributed to population of the triplet excited state. As the decay of the feature at 470 nm is equivalent to the grow in of other features at 430 nm, this indicates population of a triplet state from the singlet state, as seen the dimeric BODIPY reported by for Montero and colleagues, (discussed above and is depicted in Figure 5.2).[11] In the halogen free dimeric BODIPY reported by Montero and colleagues, they suggested that the triplet state is populated via a singlet fission mechanism. It is likely that the same mechanism applied for the BODIPY polymer discussed here but decay associated spectra (DAS), are required as this approach characterises the weight of each time constant. The monoexponential rates extracted in this Thesis refer to the conversion of the singlet excited state to a triplet, with no evidence for relaxation of any TT states to T..T (charge-separated states) which was suggested by Montero and co-workers. It is possible that the rates are homogenous and therefore appear as one. It is also possible that the broad ESA to the red side of the GSB, may be indicative of a relaxed TT to T..T charge separated state. Tentatively the mechanism for formation of the triplet states observed here is assigned to a SF mechanism but further studies are required to confirm this assignment.

The TA spectra for the TMS-BODIPY polymer immobilised on NiO film are displayed in Figure 5.9: D, and while the features observed in the UV-vis spectra are also similar to that previously observed in solution, they are significantly reduced in intensity. This is possibly due to the amount of the polymer present on the film, and has also been observed by other groups.[15,17,19] However, when the transient signals are analysed the kinetics are quite different. As observed with the solution studies, following photolysis a GSB is evident at ~560 nm together with an ESA at ~450 nm. While there appears to be a weak signal between ~650 – 700 nm, indicative of the reduced BODIPY unit, reliable kinetic data could not be extracted.[17] The ESA at 450 nm is much shorter lived, than any ESA features in the solution studies for this

compound. A similar observation was also recorded for the Ru-complexes when immobilised onto NiO films, which were previously discussed in chapter 3. This observation, where the lifetimes for the BODIPY polymer are significantly reduced following immobilisation on NiO, also agrees with previous findings from the Gibson group (discussed above).[15,17,19] They have also reported that phenylamine-BODIPY dyes when anchored on NiO, form a reduced $BODIPY^-$ species following excitation, with an absorbance ~580 nm.[17] The ESA at 450 nm is present within the instrumental response time and it decays biexponentially, with $\tau_1 \approx 3$ ps and $\tau_2 \approx 74$ ps. This is possibly due to the rapid electron injection from the NiO to the polymer, followed by recombination.[17] Although the characteristic ESA associated with the reduced BODIPY anion does not appear to be present in the spectra (~580 nm), however, it is possible the bleach and SE mask the weak signal.[17] The recovery of the GSB at ~555 nm was tri-exponential ($\tau_1 \approx 2$ ps, $\tau_2 \approx 66$ ps and $\tau_3 >> 2$ ns). This may imply formation of a charge-separation state giving rise to TMS-$polymer^-$|NiO^+ which recombines on the picosecond time scale in addition to population of the triplet state which is the long-lived species that is observed in solution.

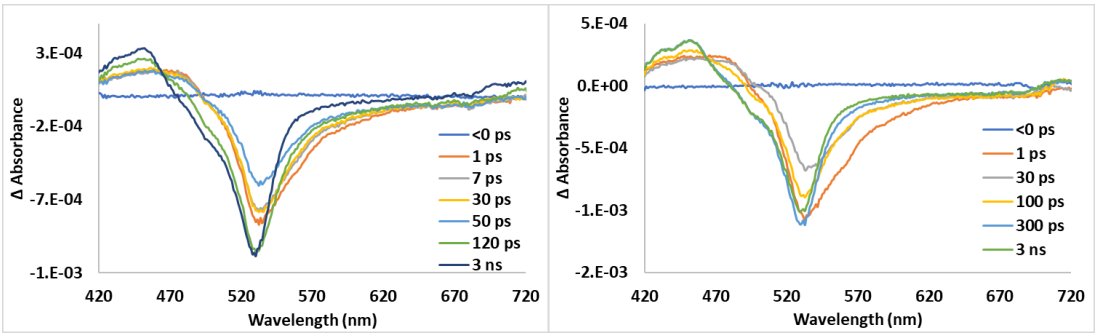

Figure 5.10: The TA spectra collected for (A), HOCH$_2$-diiodo-BODIPY (B), HOCH$_2$-BODIPY-polymer in CD$_3$CN using an excitation wavelength of 400 nm. The spectra were carried out at the Central Laser Facility, RAL, U.K., using the same setup as discussed in Chapter 3.

The spectra displayed in Figure 5.10 were performed in CDCN, and when compared to the spectra in Figure 5.9 and Figure 5.11, which were performed in dichloromethane, the transient signals in Figure 5.10 are substantially weaker. This difference with solvents has previously been reported by Flamigni and co-workers. They reported that the intensity of the excited state absorption features for the BODIPYs in acetonitrile were much weaker in their TA studies.[27] They compared the TA spectra of BODIPY dyes dissolved in CH$_3$CN and in toluene. They found that the TA spectra of their dyes dissolved in CH$_3$CN were reduced by ~50% to that when the studies were performed in toluene. They suggested the polarity of the solvent to play a role in the electron dynamics, with stabilisation of the excited state occurring with decreased solvent polarity, contributing to lower internal conversion rates.

Following photolysis of the HO-CH$_2$-diiodo-BODIPY a weak ESA on the high energy side of the GSB at ~480 nm forms together with depletion of the parent at ~520 nm. The ESA decays in less than 150 ps, giving rise to a further ES, at ~450 nm, that persists on the nanosecond time scale. SE is also evident at ~570 nm which corresponds with the fluorescence spectrum for this compound. As the ESA at 480 decays, the band at 450 nm forms, and as discussed in the previous section, these excited state features are assigned to a ^{1}ES that is the precursor to the ^{3}ES which persists on the nanosecond time scale.

The features of the diiodo-BODIPY complexes (in Figure 5.9, Figure 5.10 and Figure 5.11), and the spectrotemporal evolution, signify population of the triplet state from

the singlet. This is most likely due to the presence of the iodine resulting in "the heavy atom effect" also seen with metallated complexes, such as the Ru-based complexes discussed in this thesis. This phenomenon has also been reported for other BODIPYs furnished with iodine or bromine atoms.[6,28,29] Zhang and co-workers investigated solvent effects on their diiodo-BODIPY derivative, with a phenyl group in the *meso* position.[26] They report similar spectral findings in their TA spectra, with a GSB ~540 nm and three ESA features at ~346, 471 and 716 nm, in all solvents used (hexane, heptane, toluene, 1,4-dioxane, and dimethyl sulfoxide). The window of the spectra in Figure 5.9, Figure 5.10 and Figure 5.11, is cut-off at 370, 420 and 370 nm, respectively, therefore missing the higher energy band at ~346 nm, which they assigned to the ^{1}ES. Zhang and co-workers also observed an ESA feature at 471 nm which shifts to higher energy (450 nm) as it decays with an isosbestic point at 453 nm. This isosbestic point remains for the length of the experiment, confirming that ISC from the $S_1 \rightarrow T_1$ is occurring.

Similar features and kinetics are also observed for the $HOCH_2$-BODIPY-polymer, in Figure 5.10: B, as that previously discussed for the TMS analogue. Again, following excitation of the polymer, an ESA is evident at 470 nm, together with a GSB (which is partially masked by SE). As the ES at 470 nm decays, a new band grows in at 430 nm that persists on the nanosecond timescale. In addition, an isosbestic point is evident at 465 nm, which again indicates that the ^{1}ES at 470 nm is the precursor to the ^{3}ES at 430 nm. The recovery of the SE at ~570 nm over 3 ns reflects the lifetime of the initially populated singlet state. On the time scale of the experiment the GSB at ~ 520 nm does not appear to recover.

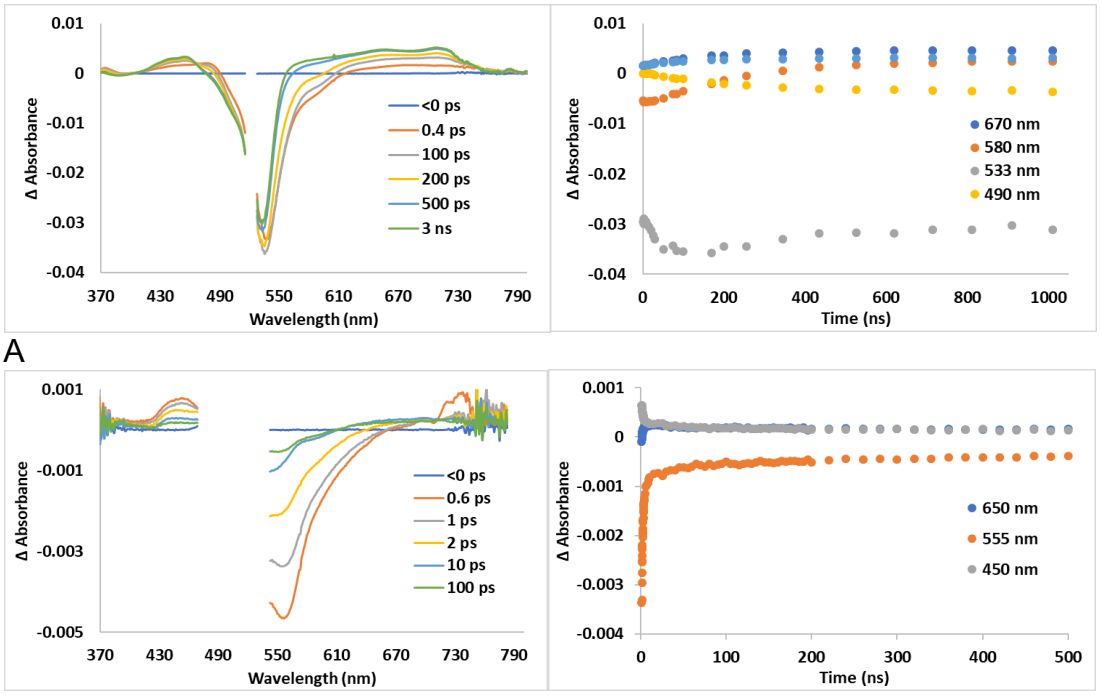

Figure 5.11: TA spectra collected following excitation of (A) the HOCH$_2$-BODIPY Polymer in d$_2$-DCM and the corresponding kinetic traces, (excitation wavelength of 525 nm) and (B) when the polymer was immobilised on NiO films (an excitation wavelength of 505 nm was used).

The HO-BODIPY polymer was also studied, in dichloromethane solution and when immobilised on NiO (Figure 5.11). As described for the TMS-BODIPY polymer very similar spectral changes were observed in the TA experiments following excitation of the HO-BODIPY polymer. As observed with the solution studies, following photolysis a GSB is evident at ~ 580 nm together with an ESA at ~ 490 nm. The ESA at 490 nm decays over $\tau \approx 234$ ps, with the growth of a new band at 450 nm, together with a broad absorption at greater than 600 nm over $\tau \approx 167$ ps, the slight difference in τ values recorded is due to the ESA at lower energy overlapping with SE and GSB. The SE partially masks the GSB at ~570 nm. As observed for the TMS-polymer the transient species that decay on the picosecond time scale are assigned to a singlet state, which subsequently populate the triplet state that persists on the nanosecond time scale. As before the mechanism is tentatively attributed to SF, but further analysis is required to confirm this assignment.

The TA spectra for the HO-CH$_2$-BODIPY polymer immobilised on NiO film are displayed in Figure 5.11: B, and as observed for the TMS-BODIPY immobilised on NiO, the transients observed are much weaker than that in solution, and the life times

are significantly shorter. As observed with the TMS-polymer, following photolysis a GSB is evident at ~555 nm together with an ESA at ~440 nm. There is a weak signal between ~660 – 700 nm, but reliable kinetic data could not be extracted. Following excitation, the ESA at 450 nm is present within the instrumental response time and it decays tri exponentially, with $\tau_1 \approx$ 1.5 ps, $\tau_2 \approx$ 59 ps and $\tau_3 >>$ 2 ns. This is possibly due to the rapid electron injection from the NiO to the polymer and recombination.[17] The recovery of the GSB at ~555 nm was triexponential ($\tau_1 \approx$ 1.7 ps, $\tau_2 \approx$ 58 ps and $\tau_3 >>$ 2 ns). Again, these results may indicate a charge-separated state giving rise to, TMS-polymer$^-$|NiO$^+$ that recombines on the picosecond time scale together with population of a triplet state that persists on the nanosecond timescale.

5.4.3 ns-Transient Absorption

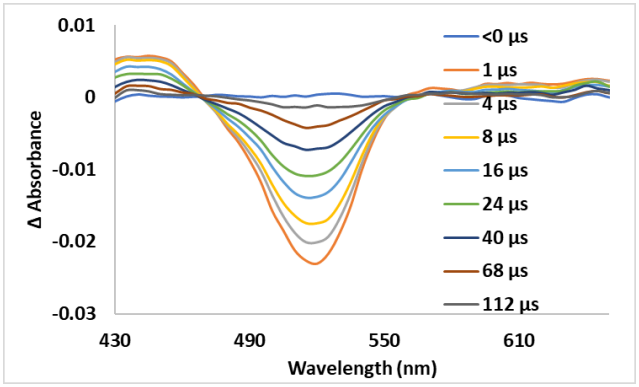

Figure 5.12: TA spectra obtained following laser flash photolysis (λ_{exc} 355 nm) of the TMS-BODIPY-polymer in acetonitrile under an argon atmosphere. The sample was degassed using 3-cycles of freeze-pump-thaw. The absorbance at the excitation wavelength was ~0.36 nm.

Laser flash photolysis was performed on both polymers in acetonitrile on the nanosecond time scale to probe the long-lived species previously observed in the picosecond studies. The experiments discussed in the previous section, provided evidence for a transient species that persisted on the nanosecond time scale, however these laser flash photolysis experiments confirm that this species decays on the micro-second time base. The spectra in Figure 5.12 demonstrate that following excitation a GSB occurs at 540 nm together with an ESA at ~ 440 nm. The feature at 440 nm decays with $\tau \approx 60$ µs, which is the same as the life time for recovery of the parent bleach and is assigned to the lifetime for the ^{3}ES. The corresponding HO-BODIPY-polymer has a reduced lifetime for the triplet state of $\tau \approx 30$ µs. These lifetimes are similar to those reported in the literature for other triplet states in dimeric BODIPYs where lifetimes ranging 0.2 – 45 µs were reported, and these varied with both the solvent and also the point of attachment of the two BODIPY units on the BODIPY core.

5.4.4 ps-Time-resolved IR Spectroscopy

TRIR studies were also performed on the TMS- and $HOCH_2$-BODIPY polymers in deuterated dichloromethane and deuterated acetonitrile using the ULTRA facility at the Central Laser Facility in the Rutherford Appleton Laboratories. The spectra collected from these experiments are displayed in Figure 5.13 and Figure 5.14. TRIR is useful in providing both lifetimes and structural information. In the following section, only the solution studies are discussed, as no transient signals were observed when the polymer were immobilised on the NiO.

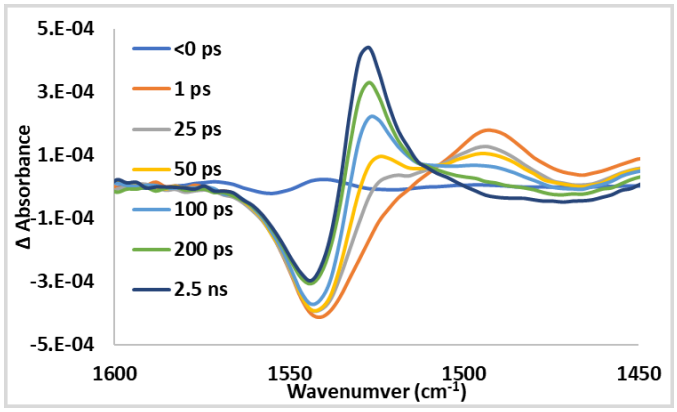

A

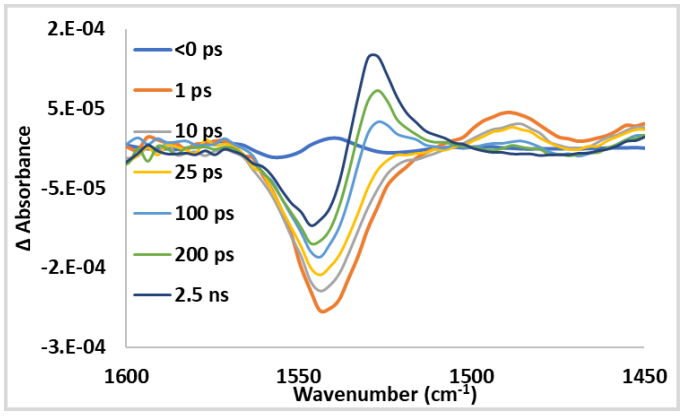

B

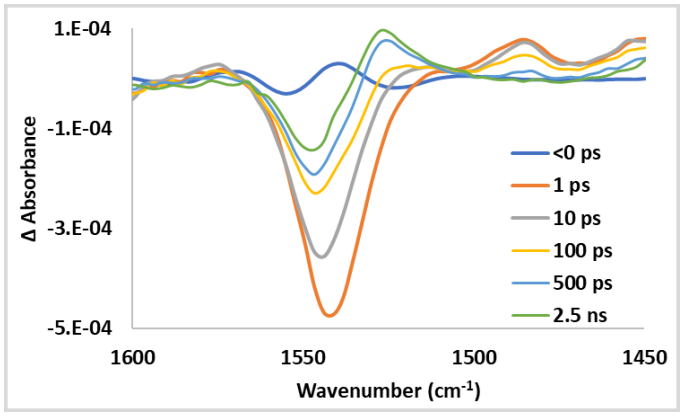

C

Figure 5.13: TRIR spectra for (A) TMS-diiodo-BODIPY, (B) TMS-BODIPY-polymer in CD_3CN and (C) the TMS-BODIPY polymer in d_2-DCM, (excitation wavelength = 525 nm)

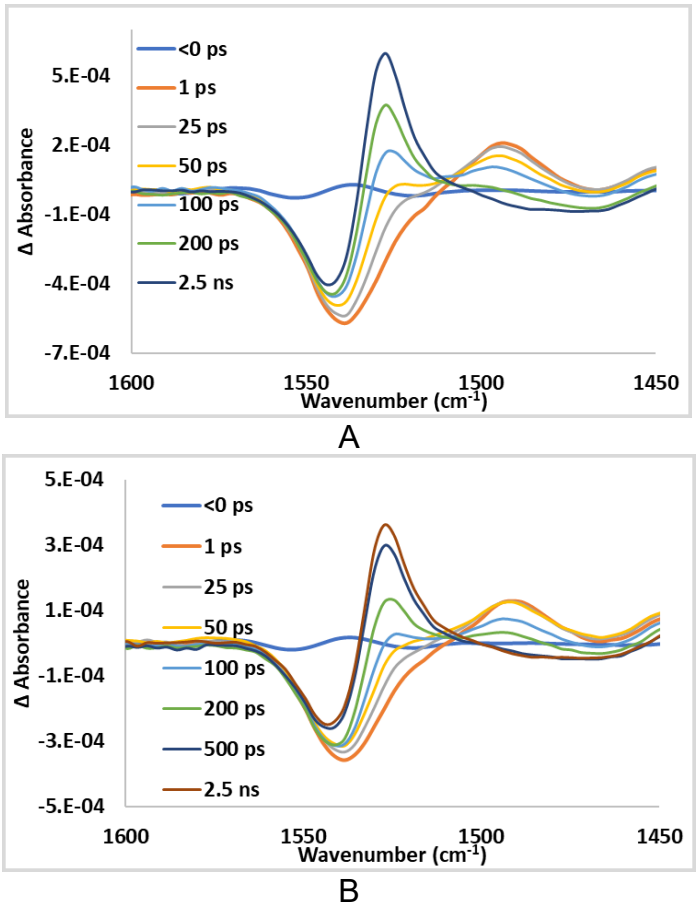

Figure 5.14: : TRIR spectra collected for the (A) HO-CH_2-BODIPY-polymer in CD_3CN and (B)in d_2-DCM (following λ_{exc} = 525 nm).

Figure 5.13 and Figure 5.14, display the TRIR spectra collected for the TMS and HO-BODIPY polymers, in the region 1600 – 1450 cm^{-1}. Following excitation at 525 nm, a GSB is observed at ~1540 cm^{-1}, assigned to both ν(C=N), ν (C=C) vibrations in all spectra.[29] The GSB is present within the instrumental response (200 fs) together with a new absorption centred at higher frequency at ~1490 cm^{-1}.[30] In all spectra, and in both solvents, the stretching vibration at ~1490 cm^{-1} decays over ~300 ps, together with the formation of a new band at ~1527 cm^{-1} which grows in over a similar timeframe. The timeframe for the decay of the ES species following excitation mirrors that observed in the TA experiments, and therefore, the new stretching vibration at ~1490 cm^{-1} is assigned to a singlet excited state, and is the precursor to the triplet state, assigned to the stretching vibration at ~1527 cm^{-1}. An isosbestic point between the two ESA in all spectra is consistent with that seen in the TA, and confirms that the triplet state forms following initial population of the singlet state. The lifetime for the triplet state could not be determined in the TRIR studies, as it was not possible to collect data beyond 2.5 ns. Gibson and co-workers have previously, carried out solution studies on

a phenylamine-BODIPY, using TRIR, and similarly to the results for the BODIPY polymers presented here, observed a bleach at 1543 cm^{-1}, together with a new band at 1507 cm^{-1}, which was assigned to a ^{1}ES.[19] They reported that this ^{1}ES decayed, with the formation of a band that grew in over 400 ps at 1525 cm^{-1} which they attributed to a ^{3}ES with a lifetime of 760 ns. This lifetime is much shorter, than observed for the BODIPY polymer where with the aid of TA, we obtained a lifetime of 60 μs.

Both Figure 5.13 and Figure 5.14 give a comparison of the evolution of the spectral features of the HO- and TMS BODIPY polymers in different solvents (CD_3CN vs. d_2-DCM). While the kinetics are similar in both solvents, in deuterated DCM, the intensity of the ESA are lower than when the experiments are carried out in acetonitrile. This observation has been previously reported for diiodo-BODIPY complexes investigated by TA in different solvents.[26] The lower intensity for the ^{3}ESA band in DCM solutions, may also be due to an overlapping of the GSB bleach with ^{3}ES. Also included in Figure 5.13 is the TMS-diiodo-BODIPY dye. The kinetics and spectral features in the TRIR for the TMS-diiodo-BODIPY similar to that of the polymers, with a GSB, and a stretching vibration at ~1490 cm^{-1} (assigned to a ^{1}ES), which decays over 400 ps, with a corresponding growth of the band at ~1527 cm^{-1}. Overall the spectrotemporal evolution observed in the TRIR experiments agree with the TA, and the presence of the band at ~1527 cm^{-1} assigned to a triplet state, is tentatively thought to occur via a SF mechanism. However, as outlined in the TA section further analyses are required to confirm this mechanism.

5.4.5 Singlet Oxygen Studies

The $^1O_2$ quantum yield (Φ_Δ) was investigated for all the BODIPY compounds in acetonitrile and in dichloromethane using an excitation wavelength of 470 nm and $[Ru(bpy)_3](PF_6)_2$ as a standard (for the ruthenium standard the $^1O_2$ quantum yields are known and are: $\Phi_\Delta = 0.57$ in acetonitrile and $\Phi_\Delta = 0.52$ in CH_2Cl_2). As expected, the quantum yield for $^1O_2$ in the non-halogenated BODIPY monomers is very low. For the diiodo and polymer BODIPYs, population of the triplet state occurs and, therefore, $^1O_2$ is generated. Table 5.1 lists the Φ_Δ obtained for the BODIPYs in both solvents. From Table 5.1, it is clear that the diiodo-BODIPYs yield the highest Φ_Δ in this study. This was expected as the presence of the halogens enhance ISC, thereby populating the triplet state. The values obtained for the polymers are ~50% less (or lower) than that of the halogenated monomeric precursors. Zhang investigated a range of dimeric BODIPY species for singlet oxygen generation.[31] They reported that the dimeric species attached in a 2-2' orientation on the BODIPY core generated quantum yields for singlet oxygen, which are lower than observed in this study ($\Phi_\Delta = 0.053$ in toluene, $\Phi_\Delta = 0.047$ in CCl_4 and $\Phi_\Delta = 0.04$ in n-hexane). Similarly, to the studies presented in this thesis, an ^{3}ESA was observed in the TA experiments, with lifetimes of 43 μs for 2-2' linked dimers. Zhang concluded the that the modest singlet oxygen quantum yields were due to the 2-2' linking of the BODIPY dimer as this performed the worse out of their series of differently orientated BODIPY dimers, even though 2-2' had a comparable or longer ^{3}ES lifetimes than the other orientations in their series. The solvent is also known to influence singlet oxygen quantum yields and Zhang reported an increase in Φ_Δ as the solvent polarity increased, and stated that the polar solvent enhanced intramolecular charge transfer to the triplet state.[31] This trend with solvent polarity is in the opposite direction to the BODIPY dyes studied in this chapter, with the Φ_Δ values decreasing with the solvent polarity. However, this observation is more in agreement with a recent study by Montero and co-workers who published a $\Phi_\Delta = 0.75$ in CH_3Cl and only 0.25 in acetonitrile, (for the dimeric BODIPY dye in Figure 5.2). They attributed this variation in Φ_Δ to an increase in spectrotemporal evolution in acetonitrile, and the lower intensity of the ^{3}ES signals inferred less molecules were populating the TT state.[11] The TA signals recorded in acetonitrile (Figure 5.10) appear less intense than those in DCM, however this is not mirrored in the TRIR,

therefore based on the results presented this rationale is not a plausible rationale for the increase in Φ_Δ in a less polar solvents.

Table 5.1: Table of corresponding $^1O_2$ Quantum Yields for BODIPY-based complexes in aerated acetonitrile and dichloromethane with an excitation wavelength of 470 nm and absorbance at this wavelength of ~0.2, reference $[Ru(bpy)_3](PF_6)_2$.

Complex	CH_3CN	DCM
TMS BODIPY	0.013	0.004
TMS di-iodo-BODIPY	0.597	1.187
TMS-BODIPY-polymer	0.129	0.323
HO-CH_2-BODIPY	0.005	0.015
HO di-iodo-BODIPY	0.805	1.199
HO-CH_2-BODIPY-polymer	0.232	0.540

5.4.6 Preliminary Photocatalytic Studies

Preliminary photocatalytic experiments were conducted with HO-CH_2-BODIPY. Following the intermolecular photocatalytic procedures described in Chapter 2, with a deaerated solvent mix including acetonitrile, triethylamine and water (ratio; 12:6:1) and an equimolar amount of K_2PtCl_4 as the catalyst. In these studies when the head space was analysed, no hydrogen was detected using GC. Recent studies within the group and by others,[12] indicate that these polymers decompose rapidly under the photocatalytic conditions used, hence the lack of hydrogen observed. However, preliminary experiments performed by collaborators at Newcastle, suggest that under photoelectrocatalytic conditions where the polymers are immobilised on NiO together with a Pt catalyst hydrogen is produced.

5.5 Conclusion

In summary, time-resolved techniques were used to identify both singlet and triplet excited states and the related kinetics of these polymers. TA and TRIR spectroscopy have been used to compare the spectrotemporal evolution of both the halogen-free and halogenated monomeric BODIPYs and their polymeric analogues. The dyes were studied in both dichloromethane and acetonitrile solutions, also when immobilised on the surface of NiO films. This chapter demonstrates the importance of time resolved-techniques in investigating electron transfer dynamics and assigning the various processes at both early and late timescales (in this case spanning ps-us time scales). Although, long-lived triplet lifetimes were achieved and studied for the polymeric systems, preliminary hydrogen photogeneration was unsuccessful, due to decomposition of the polymers. While the monomers do not produce singlet oxygen (unless there is a heavy atom present) the studies do confirm that the polymers can be used as singlet oxygen delivery systems. The combination of time resolved techniques was used to tentatively assigned the mechanism for singlet oxygen generation to occur via singlet fission.

References

[1] A. Treibs, F.-H. Kreuzer, *Justus Liebigs Ann. Chem.* **1968**, *718*, 208–223.

[2] A. Loudet, K. Burgess, *Chem. Rev.* **2007**, *107*, 4891–4932.

[3] S. P. Singh, T. Gayathri, *Eur. J. Org. Chem.* **2014**, *2014*, 4689–4707.

[4] G. Ulrich, R. Ziessel, A. Harriman, *Angew. Chem. Int. Ed.* **2008**, *47*, 1184–1201.

[5] Y. Cakmak, S. Kolemen, S. Duman, Y. Dede, Y. Dolen, B. Kilic, Z. Kostereli, L. T. Yildirim, A. L. Dogan, D. Guc, et al., *Angew. Chem. Int. Ed.* **2011**, *50*, 11937–11941.

[6] A. Kamkaew, S. H. Lim, H. B. Lee, L. V. Kiew, L. Y. Chung, K. Burgess, *Chem. Soc. Rev.* **2012**, *42*, 77–88.

[7] J. Bartelmess, A. J. Francis, K. A. El Roz, F. N. Castellano, W. W. Weare, R. D. Sommer, *Inorg. Chem.* **2014**, *53*, 4527–4534.

[8] J. A. Anshori, T. Slanina, E. Palao, P. Klán, *Photochem. Photobiol. Sci.* **2016**, *15*, 250–259.

[9] W. Wu, X. Cui, J. Zhao, *Chem. Commun.* **2013**, *49*, 9009–9011.

[10] K. Chen, W. Yang, Z. Wang, A. Iagatti, L. Bussotti, P. Foggi, W. Ji, J. Zhao, M. Di Donato, *J. Phys. Chem. A* **2017**, *121*, 7550–7564.

[11] R. Montero, V. Martínez-Martínez, A. Longarte, N. Epelde-Elezcano, E. Palao, I. Lamas, H. Manzano, A. R. Agarrabeitia, I. López Arbeloa, M. J. Ortiz, et al., *J. Phys. Chem. Lett.* **2018**, 641–646.

[12] L. Dura, M. Wächtler, S. Kupfer, J. Kübel, J. Ahrens, S. Höfler, M. Bröring, B. Dietzek, T. Beweries, *Inorganics* **2017**, *5*, 21.

[13] W. Wu, H. Guo, W. Wu, S. Ji, J. Zhao, *J. Org. Chem.* **2011**, *76*, 7056–7064.

[14] Z. Wang, J. Zhao, A. Barbon, A. Toffoletti, Y. Liu, Y. An, L. Xu, A. Karatay, H. G. Yaglioglu, E. A. Yildiz, et al., *J. Am. Chem. Soc.* **2017**, *139*, 7831–7842.

[15] J.-F. Lefebvre, X.-Z. Sun, J. A. Calladine, M. W. George, E. A. Gibson, *Chem. Commun.* **2014**, *50*, 5258–5260.

[16] P. Qin, J. Wiberg, E. A. Gibson, M. Linder, L. Li, T. Brinck, A. Hagfeldt, B. Albinsson, L. Sun, *J. Phys. Chem. C* **2010**, *114*, 4738–4748.

[17] G. H. Summers, J.-F. Lefebvre, F. A. Black, E. S. Davies, E. A. Gibson, T. Pullerits, C. J. Wood, K. Zidek, *Phys. Chem. Chem. Phys.* **2016**, *18*, 1059–1070.

[18] F. A. Black, A. Jacquart, G. Toupalas, S. Alves, A. Proust, I. P. Clark, E. A. Gibson, G. Izzet, *Chem. Sci.* **2018**, *9*, 5578–5584.

[19] F. A. Black, C. A. Clark, G. H. Summers, I. P. Clark, M. Towrie, T. Penfold, M. W. George, E. A. Gibson, *Phys. Chem. Chem. Phys.* **2017**, *19*, 7877–7885.

[20] F. E. Alemdaroglu, S. C. Alexander, D. Ji, D. K. Prusty, M. Börsch, A. Herrmann, *Macromolecules* **2009**, *42*, 6529–6536.

[21] B. M. Squeo, V. G. Gregoriou, A. Avgeropoulos, S. Baysec, S. Allard, U. Scherf, C. L. Chochos, *Prog. Polym. Sci.* **2017**, *71*, 26–52.

[22] B. Ghosh, M. D. R. I. Amado-Sierra, D. Holmes, R. E. Maleczka, *Org. Lett.* **2014**, *16*, 2318–2321.

[23] S. Zhang, Y. Wang, F. Meng, C. Dai, Y. Cheng, C. Zhu, *Chem. Commun.* **2015**, *51*, 9014–9017.

[24] S. Banfi, G. Nasini, S. Zaza, E. Caruso, *Tetrahedron* **2013**, *69*, 4845–4856.

[25] S. Wanwong, P. Surawatanawong, S. Khumsubdee, S. Kanchanakungwankul, J. Wootthikanokkhan, *Heteroat. Chem.* **2016**, *27*, 306–315.

[26] Q. Zhou, M. Zhou, Y. Wei, X. Zhou, S. Liu, S. Zhang, B. Zhang, *Phys. Chem. Chem. Phys.* **2017**, *19*, 1516–1525.

[27] B. Ventura, G. Marconi, M. Bröring, R. Krüger, L. Flamigni, *New J. Chem.* **2009**, *33*, 428–438.

[28] T. Yogo, Y. Urano, Y. Ishitsuka, F. Maniwa, T. Nagano, *J. Am. Chem. Soc.* **2005**, *127*, 12162–12163.

[29] S. H. Lim, C. Thivierge, P. Nowak-Sliwinska, J. Han, H. van den Bergh, G. Wagnières, K. Burgess, H. B. Lee, *J. Med. Chem.* **2010**, *53*, 2865–2874.

[30] S. Schoder, S. Kord Daoroun Kalai, H.-U. Reissig, *Chem. – Eur. J.* **2017**, *23*, 12527–12533.

[31] X.-F. Zhang, *Dyes Pigments* **2017**, *146*, 491–501.

Chapter 6

6 Future Work

Chapter 2 described a series of intermolecular photocatalytic hydrogen evolution experiments with a Ru-tris diphenylphenanthroline photosensitiser under varying conditions (catalyst; solvent mix; sacrificial agent; water content; etc.). This was part of a broader study, with collaborators across different research groups, on the effect of reaction conditions and reagents, measurement techniques and light sources on the outcome of photocatalytic water splitting for hydrogen evolution. A manuscript is in preparation.

Chapter 3 follows on from decades of research into hydrogen generating photocatalysts capable of immobilisation on to NiO semiconducting electrodes to be employed in photoelectrocatalysis of hydrogen from water. To progress from the work in this chapter other photocatalysts, with systematic synthetic changes, need to be investigated on the surface and evaluated for their performance. This will aid further in understanding the electron dynamics of sensitised semiconductors. This work has already begun, in collaboration with the Gibson Group in Newcastle University. It is also of interest to conduct surface-based time-resolved studies with an applied bias, as this would more accurately describe the conditions of photoelectrocatalytic experiments.

Chapter 4 is a mainly preliminary studies and there is a lot more research into the systems and their workings under varied experimental conditions for CO_2 reduction in solution. Also, exploring the systems immobilised to a NiO electrode and investigating their photoelectro-capabilities.

Chapter 5 examined the photodynamics of a range of BODIPY-based monomeric and polymer complexes by time-resolved techniques and for their singlet oxygen production abilities. There is a manuscript in preparation for these studies. Also, we are looking to progressing towards photocatalytic material by attaching a catalytic moiety either along the polymer chain or in the meso position of the BODIPY and allowing for the possibility of photocatalytic hydrogen generation. In turn, these

systems will be investigated by time-resolved techniques to gain insights into their electron dynamics.